I. TWO-PHASE FLOW IN VERTICAL AND ANNULAR FLUIDIZED BEDS

II. UNSTEADY DISTURBANCES IN AXIAL COMPRESSORS

Thesis by

Blair Allen Folsom

In Partial Fulfillment of the Requirements

for the Degree of

Doctor of Philosophy

California Institute of Technology

Pasadena, California

1974

(Submitted May 24, 1974)

ACKNOWLEDGMENTS

The writer wishes to express his deepest gratitude to Dr. W. Duncan Rannie for his sound judgment and guidance during the course of this work. The many hours spent discussing and analyzing the problems described in this thesis are greatly appreciated.

Special thanks is also due to Mr. F. T. Linton for his help in constructing several of the apparatuses and for preparation of most of the figures in Part II.

Appreciation also goes to Messrs. Ervin Adler, John Allingham, Mark Bohn, and James Stana for their help in various phases of the project.

The writer wishes to acknowledge the financial assistance of the Aerospace Research Laboratories at Wright Patterson Air Force Base, the General Electric Foundation, United States Steel Corporation, the State of California, Byron Jackson Pump Division of Borg-Warner Corporation, and the California Institute of Technology.

This thesis is dedicated to the writer's wife, Patricia. Her continuous encouragement and support and typing of the manuscript are greatly appreciated.

ABSTRACT

Part I is a study of vertical and annular fluidized beds. The vertical fluidized bed was used to determine the responses of a total head probe and an electromagnetic probe to the average velocity through the bed. Both probes indicated velocities substantially higher than the calculated average fluid velocity for the suspension. The fluidized bed consisted of glass beads suspended in water flow and had an aspect ratio of 20. The average concentration distribution was measured over the height of the bed as well and was found to be constant within one tube diameter of the top and bottom of the bed.

The annular fluidized bed consisted of a suspension of small nylon spheres in a vortex-sink flow of water in a special annular chamber. The velocity distribution was deduced from pressure measurements in the flat side walls and the concentration distribution of particles was measured with a special optical meter. The drag coefficient of the particles and the wall shear stress were calculated from the measurements. At low concentrations the side-wall boundary layers had a major effect on motion of the particles. At higher concentration the drag coefficient of the particles was found to have approximately the same value as for a vertical fluidized bed at the same concentration and Reynolds number. The wall shear stress coefficient was found to be of the same order of magnitude as for channel flow at the same Reynolds number.

Part II is an analytical study of unsteady disturbances in an axial compressor. The blade forces were represented as a continuous distribution of body forces acting on the fluid and the equations of

motion were linearized. Only axial variations in the mean flow were considered and the disturbances were limited to planar pressure and entropy waves. A numerical integration gave results that depended on frequency and indicated that the largest velocity fluctuations inside the compressor always occurred at either the front or rear. Two related problems were also considered. Disturbances were superimposed on the flow through a duct with a restriction, similar to a blade row, and the reflected and transmitted waves were determined as functions of frequency. The response of turning vanes, treated as an actuator disc, to small disturbances was also determined.

TABLE OF CONTENTS

LIST OF FIGURES

PART I-A

PART I-B

PART I--APPENDICES

PART I

TWO-PHASE FLOW IN VERTICAL AND ANNULAR FLUIDIZED BEDS

SUMMARY

Part I of the thesis is an account of a study originally aimed at better understanding of the mechanics of flow of a slurry. The principal difficulty in any investigation of slurries is that of making definitive measurements in the two-phase flow. Hence, the first goal of this study was to develop an instrument that would measure the velocity of one component of the flow--the fluid phase. An electromagnetic velocity probe was developed with a vertical fluidized bed as a calibration device. Unfortunately, the velocity as determined by the probe could not be correlated in a physically meaningful way with the known fluid velocities in the suspension, so this development was dropped.

The vertical fluidized bed used for the calibration of the probe was well suited for answering some questions regarding uniformity of concentration distribution of particles. Hence, advantage was taken of its existence to make careful measurements of concentration distribution, even though this was not the primary aim of the investigation.

A device with annular flow, a vortex-sink combination with both circulating and radial flow, was constructed for study of particle suspensions by static pressure measurements in the side walls. Experiments on the first rather crude annular chamber gave considerable promise and a more elaborate system was constructed for better quantitative measurements. An optical device for measuring concentration of particles by attenuation of a light beam was also developed. It was hoped that it would be possible to measure an effective viscosity of

the suspension in shear flow. The usefulness of the apparatus for this purpose was disappointing, although many other aspects of the flow proved very interesting.

Electromagnetic Velocity Probe Development

The original goal of this research was not the study of fluidized beds, but instead the development of an instrument to measure the local velocity of the liquid phase of a slurry flowing in a pipe. Although many investigators have measured the overall properties of slurries, very few have even attempted to measure any local properties because of instrumentation problems. The instrumentation so far available measures only overall momentum or heat transfer characteristics of the mixture, not the individual phases, or can be used only in very dilute slurries by tracking individual particles optically.

After a detailed survey of measurement methods, the most promising instrument seemed to be the electromagnetic flowmeter. This instrument originally conceived by Faraday in the nineteenth century but only recently made workable by Kolin (Kolin (1944, 1945, 1954, 1969, 1970), Kolin and Wisshaupt (1963)), is currently used for the metering of flow of liquids and slurries in pipes. The advantage of the electromagnetic flowmeter for two-phase flow is that it measures only the velocity of an electrically conducting medium. If a slurry is composed of an electrically conducting liquid phase such as water and an electrically insulating solid phase such as glass or sand, then only the motion of the liquid phase would affect an electromagnetic instrument.

It was decided to design and build an electromagnetic velocity probe and test it first on pure liquid and second on two-phase (solid,

liquid) flow. The design and construction of the probe and associated electronics are discussed in Appendix A.

The tests on pure liquid yielded a linear calibration curve relating the meter reading to velocity. The next step was the measurement of the velocity in a vertical fluidized bed. A vertical fluidized bed consists of a tube with its axis mounted vertically. The tube is partially filled with solid particles resting on a screen near the bottom of the tube. Fluid of lower density than the particles is pumped through the screen and flows upward past the solid particles. If the velocity of the fluid is sufficiently high, the particles become hydrodynamically supported and lift away from their neighbors. At this point the bed of particles is said to be fluidized. This medium was chosen to test the electromagnetic velocity probe because it is a two-phase (solid, liquid) flow configuration in which the average velocities of the solid and liquid phases are known.

The results of the measurements were disappointing. Although the meter reading seemed related to the average velocity, the magnitude of the velocity as calculated from the liquid calibration curve was much too high. Either the meter was not reading the proper velocity or the average velocity in the fluidized bed was not the calculated value. In any case, it was clear that the probe could not be used to measure the velocity of the liquid phase of a slurry correctly.

Vertical Fluidized Bed

At this point the goal of the research was changed to a study of the local properties of fluidized beds.

There is disagreement in the literature as to the vertical concentration distribution in a fluidized bed. Some investigators have agreed that the concentration should be uniform except in small regions near the bottom and the top. Others, as a result of attempts to measure the concentration distribution, have reported large variations over the bed height. To clear up this point, the fluidized bed used in the electromagnetic velocity probe calibration was modified to measure concentration. Static pressure taps were drilled in the wall of the column and fluidized beds of several concentrations were carefully measured. The results indicate quite uniform concentration throughout the height of the bed, within experimental error. Measurements were difficult to interpret very close to top or bottom.

Another question that is not answered in the literature concerns the velocity profile in a fluidized bed. It can be argued that the velocity of the liquid should be essentially constant up to within one particle radius of the tube wall, but no measurements have been made. The measurements with the electromagnetic velocity probe had shown this to be roughly true if the meter readings are taken as measures of velocity. As a further check, traverses were made with a total head probe and a static pressure probe across several fluidized beds. The pressures were measured with reference to wall pressure taps. The results confirmed the electromagnetic velocity probe readings and indicated essentially constant mean velocity up to within one particle radius of the wall.

Annular Fluidized Bed

The problem with all of these local measurements is that while it is relatively easy to develop a device to measure some property of two-phase flow, it is very difficult to determine precisely how the property measured is related to the important parameters of the flow. There is, however, a two-phase flow configuration in which it is possible to measure local properties with simple wall pressure taps without placing probes or other devices into the flow. This configuration is an annular fluidized bed (a term coined by the writer). An annular fluidized bed consists of a cloud of particles suspended hydrodynamically in annular vortex-sink flow. It is the direct rotational analog of a vertical fluidized bed. In a vertical fluidized bed, the particles are suspended by a balance between the force of gravity and the drag of the fluid flowing upward past the particles. In an annular fluidized bed, the particles are suspended by a balance between the centrifugal force of the particles rotating around the axis of the vortex and the drag of the fluid flowing inward past the particles. Thus, a suspension of particles is created.

Similar configurations have been reported in the literature for a fluid alone (Lewellen, 1971) and for configurations involving particles. The colloid core nuclear reactor uses a gaseous vortex-sink flow with high swirl to retain small radioactive particles and to transfer the heat of fission to the gas (Jackomis and Turman (1970), Poblawski and Toms (1971), and Anderson, Hasinger, and Turman (1971)). The cyclone separator is another example of vortex flow with particles (Fletcher, Gyarmathy, and Hasinger (1966), and Pinchak (1967)).

The advantage of the annular fluidized bed for making two-phase flow measurements is that the average velocity of the particles in the radial direction is known to be zero, and the radial velocity of the fluid can be deduced rather easily from continuity considerations. In addition, the average tangential velocities of the solid particles and the liquid must be nearly equal at each radius and can be deduced from knowledge of the static wall pressure as a function of radius.

Knowledge of the first derivative of circulation with respect to radius allows calculation of the shear stresses on cylindrical surfaces if the motion is two-dimensional. If the shear stresses are known one can calculate an effective viscosity of the suspension. Thus, simple measurements taken from pressure taps have the potential of measuring both local velocities and viscosities.

In order to test the feasibility of such measurements, a small annular fluidized bed was constructed using the same test loop as before. Pressure gradients were measured with wall pressure taps for both pure liquid flow and flow with two kinds of particles. The results were encouraging even though the apparatus was small and suffered from lack of symmetry. It was clear that the particles were indeed hydrodynamically suspended, and the crude measurements showed a large effective viscosity in the presence of the particles and negligible viscosity with no particles present. It was assumed that the shear stresses on the flat side walls were negligible in comparison.

Based on these results, it was decided to construct a substantially larger apparatus to make more accurate measurements. The new apparatus consisted of an entirely new flow circuit and was almost an

order of magnitude larger, in most respects, than the smaller annular fluidized bed. In order to measure concentration distribution, an optical concentration meter was developed and calibrated. This instrument measures the attenuation of a light beam passing through the suspension. It was calibrated on a small vertical fluidized bed of nylon balls in water.

Measurements over a range of operating parameters were made for water and for suspensions of ground nylon balls in water. In analyzing these data, it became obvious that the derivative of circulation with respect to radius was not due to shear stresses on cylindrical surfaces alone, but that the wall shear stress on the side walls was also playing an important role. It can be argued that in the configuration used here the wall shear stress is probably much larger than the shear stress on cylindrical surfaces. This eliminates the possibility of calculating an effective viscosity for the suspension, but does allow the determination of the wall shear stress as a function of the operating parameters of the annular fluidized bed.

The wall shear stress was also calculated for the case of laminar flow of pure liquid. This problem has been examined by many other investigators, all with the assumption that the radial flow outside the boundary layer is zero. Here the analysis was extended to include non-zero radial flow outside the boundary layer.

Because of the similarity between annular and vertical fluidized beds, measurements made on a vertical fluidized bed can be used to predict the concentration distribution in an annular fluidized bed. The data are converted to a form relating the drag coefficient of the particles

to the local velocity and concentration. This relationship is then used in the hydrodynamic equilibrium equation for the annular bed to calculate the concentration as a function of radius.

In the interest of brevity, a number of the analyses performed in connection with these studies have not been reported in this thesis. Among the subjects not recorded here are the design and development calculations for the flow circuit and associated instrumentation, the detailed description of experimental procedure, and the analyses of certain fluid mechanical problems necessary to accomplish the work.

PART I-A

VERTICAL FLUIDIZED BEDS

CHAPTER I

INTRODUCTION

If a tube with a screen across one end is partially filled with a solid granular material of uniform size and placed with its axis vertically, the solid particles will pile up at the bottom of the tube against the screen so as to form a packed bed. If provision is then made to pump a fluid of lower density than the particles upward through the tube from the bottom and the flow rate of the fluid is slowly increased from zero, the following phenomena will take place. First there is no motion of the particles as the fluid flows through the interstices. As the flow rate is increased further, the particles experience drag from the fluid flowing through the spaces between the particles and begin to move. Finally, when the drag on each particle is equal to its weight, the particles are lifted up off their neighbors and the bed is said to be on the onset of fluidization. If the velocity is increased, the drag of the fluid on the particles becomes greater, lifting the particles further. Thus, the bed will expand until the velocity in the spaces is just large enough to support the particles. Further increase in flow rate expands the bed to a new equilibrium height.

So, for a given flow rate there will be an equilibrium concentration of particles in the fluidized bed. If the velocity is increased, the concentration at equilibrium will decrease and the bed will expand. The particles move around in an apparently random manner in response to the movement of their neighbors and the fluid. This motion is highly turbulent. It is not uncommon for the particles to collide with each

other and with the tube walls. These collisions may produce an audible clicking noise.

The top of most fluidized beds is characterized by a distinct surface of discontinuity. Beneath this surface there is a high concentration of particles, and above it there are no particles. The surface is not stationary, but undulates and boils much like the air-water interface in a pan of rapidly boiling water. Occasionally a few particles will migrate above the surface, but they later sink and become a part of the suspension again. The stability of the surface is a function of the concentration of the particles in the bed. The lower the concentration, the more the surface undulates.

Fluidized beds are widely used in industry and exist in nature as quicksand. The high turbulence level in a fluidized bed and the large surface area of the particles are useful in certain heat transfer processes and in catalytic reactions. For a more detailed discussion of the general characteristics of vertical fluidized beds, the reader is referred to several of the recent books on the subject (Zabrodsky (1966), Davidson and Harrison (1963), Zenz and Othmer (1960), and Leva (1959)).

The next two chapters describe experiments carried out by the writer to measure some basic parameters of fluidized beds. The first chapter deals with the concentration distribution of particles in a fluidized bed of uniform particles. The subsequent chapter deals with local measurement of conditions inside the fluidized bed.

CHAPTER II

CONCENTRATION DISTRIBUTION MEASUREMENTS

A. Background

1. Phenomenological Theory

Despite the widespread use of fluidized beds, the hydrodynamics are not fully understood. Fluid mechanics has been unable, so far, to describe completely the turbulent flow of a liquid around a sphere. Thus, the possibility of merely extrapolating single particle knowledge to obtain fundamental understanding of a fluidized bed with thousands of particles seems hopeless. Most of what is known about fluidized beds is empirical aided by so-called phenomenological theories which are helpful in correlating results of measurement.

One question that remains unanswered in the literature is the nature of the concentration distribution in the vertical direction. It is expected that the local conditions in a fluidized bed would determine the equilibrium concentration of particles. The basic equation for a fluidized bed is essentially a momentum balance equating the submerged weight of the particles to the hydrodynamic drag of the fluid flowing past the particles. The drag of the fluid flowing past the particles should be a function of the local velocity through the spaces between the particles and the characteristics of the particles themselves. Thus, there should be a one to one correspondence between the flow rate per unit cross-sectional area of the bed and the local concentration. Appendix B presents some of these relationships in detail.

Thus, for a fluidized bed of uniform particles, the average

concentration should be constant everywhere in the bed. If a region of high concentration (uniform across the cross-section) developed at some position, that region would expand due to the increased lift and return to the proper concentration.

Of course, the flow is different near the top and bottom of the bed, and the concentration would not be expected to be constant in those regions. At the top of the bed there is a discontinuity in concentration, and the local velocity of the fluid must be lower above the surface than below. Hence a particle will not be supported in the fluid of lower vertical velocity above the surface of discontinuity, and if displaced upward will fall back. At the bottom of the bed there is a screen, and it is possible that some particles may be partially supported by the screen. The screen also limits the vertical motion of particles adjacent to it, thus changing the flow conditions locally. Except for small regions near the bottom and top of the bed, the concentration should be constant. The length of the regions in which the concentration varies may be a function of diameter of the bed, average concentration of particles in the main part of the bed, and the fluid and particle characteristics. Thus, if a bed with a large height-to-diameter ratio were constructed, the region in which the concentration varies would be small compared to the overall height of the bed.

2. Existing Experimental Evidence

The only work done so far to measure concentration profile in a fluidized bed was done by McMichael in 1963. He used two methods to measure concentration. First, the wall tap method, in which static

pressure taps were used to measure pressure versus depth and the results converted to concentration versus depth by the assumption that the particles were fully suspended. Second, an electrical technique whereby a probe with two electrodes was lowered into the fluidized bed and the resistance between the two electrodes was measured and converted to an equivalent concentration. Although the height-to-diameter ratio for McMichael's experiments was not reported directly, it can be calculated to be between 1.0 and 2.0 from data presented in his thesis.

With such a low height-to-diameter ratio, it is extremely difficult to produce a bed that is one-dimensional. Willus (1970) found large circulating currents in the fluidized beds he constructed with height-to-diameter ratios of about 5.0. He also had difficulty in eliminating stationary circulating eddies in beds of substantially higher height-to-diameter ratios. His problems were solved by stabilizing the flow at the inlet to the fluidized bed by a packed bed of small particles beneath the supporting screen.

Thus, it is very possible that strong eddies existed in the fluidized beds measured by McMichael. If this were the case, the conditions were not uniform across the fluidized bed cross-section and local concentration measurements obtained with his electrical probe would not be expected to agree with the concentration calculated from the wall pressure taps.

The results of McMichael's experiments indicated a very strong concentration gradient even in beds of nearly uniform particle size. In addition, as expected, the results of the two different concentra-

tion measurements did not fully agree. Also, the total pressure drop across the bed was less than the equivalent weight of the bed per unit area. This indicates that not all of the particles were supported and thus that the bed was not fully fluidized. These considerations cast some doubt on the profiles of concentration versus depth that he obtained.

McMichael also derived a one-dimensional model for a fluidized bed and applied it to his results to obtain insight into the diffusion coefficient and solid particle average velocity.

However, the low height-to-diameter ratio, the lack of agreement of the independent concentration measurements, and the lack of total fluidization in the bed make any such detailed analysis of the data questionable.

The net result is that there has been no satisfactory determination of concentration as a function of depth for fluidized beds of high aspect ratio. However, the assumption of uniform concentration is fundamental to many of the correlations of fluidized bed operating parameters. It is important, then, to justify the assumption of uniform concentration by experiment in light of the conflicting phenomenological theory and past experiments.

Experiments were performed to measure the concentration as a function of height for fluidized beds of high aspect ratios. The following sections will first describe the experimental apparatus and procedures and then the actual results.

B. Apparatus and Procedure

The basic apparatus was designed and constructed by Willus. The reader is referred to his thesis for a more detailed description. Some modifications were necessary to accommodate the different working fluid, water, and to accomplish the experiments necessary here. The most important modifications to Willus's apparatus are the addition of a calibration system for the orifice plate and the construction of a new test section and the associated instrumentation. Figure II.1 is a photograph of the complete apparatus.

Willus's system for calibration of the orifice plate was quite satisfactory for the low flow rate he used. However, the experiments performed here needed substantially more flow than before. Consequently, an additional flow loop was constructed. This new loop allowed rapid switching of the flow from a test tank to a tank on a balance. Thus, accurate measurements of the flow rate could be made by weighing the tank before and after flow had been pumped into it for a measured time period.

The new test section is a fluidized bed made of acrylic plastic of the same dimensions as Willus's. It mounts on the top of Willus's lower stabilizing bed and extends upward to join the rest of the flow circuit at the top.

The test section consists of 3 sections of 4-inch inside diameter cast acrylic plastic tubing and a probe holder made out of a solid block of acrylic plastic and bored to 4-inch inside diameter to match the tubing. The total length of the column is 95 inches. Each of the sections of tubing is equipped with an acrylic plastic

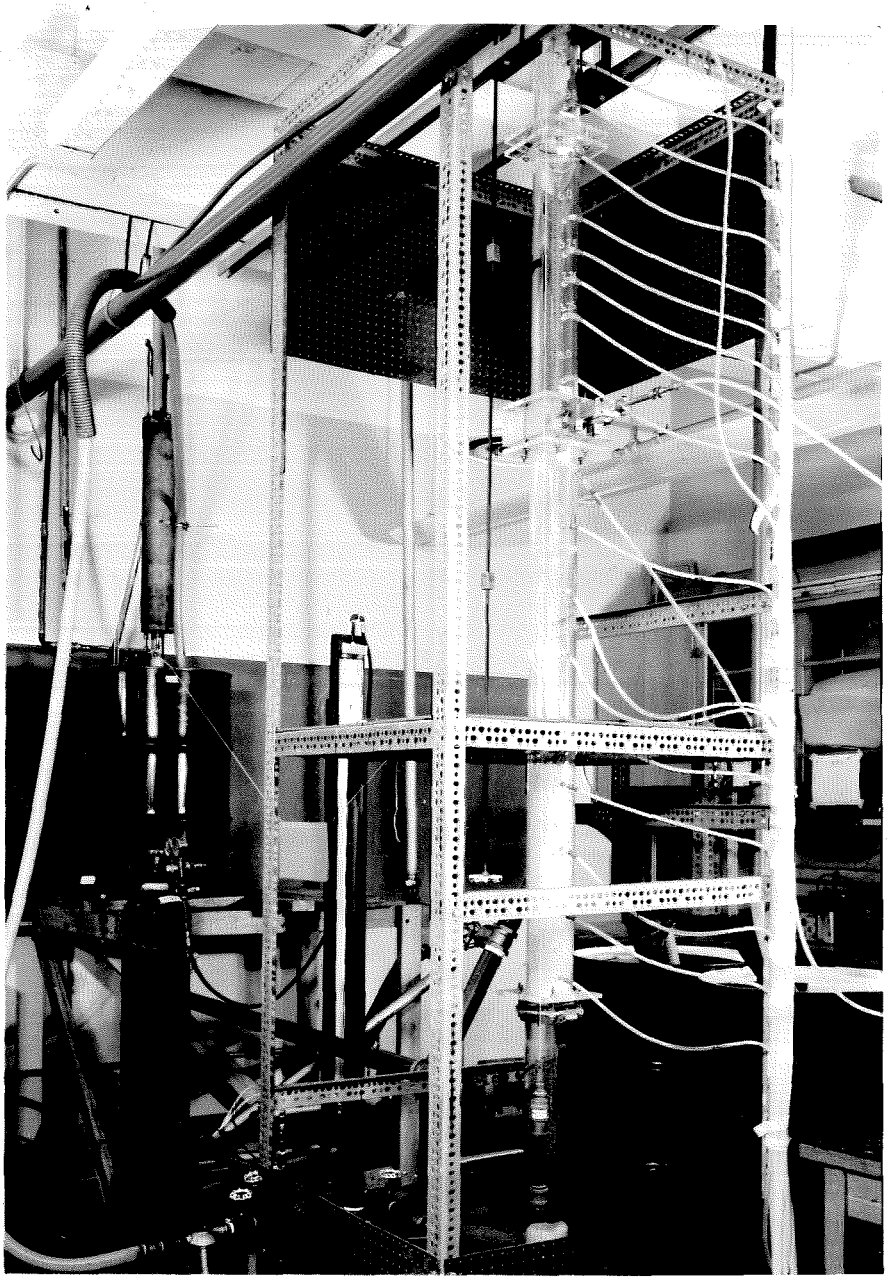

Figure II.1. Photograph of Vertical Fluidized Bed Apparatus.

flange at each end. The bolt pattern of the flanges matched that of the flanges for the flow circuit and the probe holder so that the acrylic tubing and probe holder could be arranged in any permutation. Since the tubing sections are of different length, it is possible to locate the probe holder in any of seven heights above the lower screen.

The probe holder is designed to move a probe horizontally across a diameter of the bed. A micrometer screw is used to position the probe to within ± 0.001 inch of any desired position. Provision is also made for rapid removal of the probe without disassembly of the whole test section. The probe holder is used in the experiments described in the next chapter.

Each of the 3 acrylic sections has several wall pressure taps located in a vertical line 15 degrees away from the moving probe axis. Eighteen taps in all are provided each with a 0.050-inch diameter hole. The taps at the end of each acrylic section are located so that if that end of the section were placed adjacent to the probe holder, the wall tap would be 4.0 inches beneath the supporting shaft for the probe. Directly opposite these wall taps at the end of the sections are additional wall taps, 6 in all. Thus, if a probe whose tip is 4.0 inches from the supporting rod is used, then the static wall taps at the end of the lower sections will be on the same level as the probe tip. The static taps are inclined 15 degrees to the direction of travel of the probe tip so that there will be no interference between probe tip and wall tap as the probe approaches the wall. The distances between each pair of pressure taps in the vertical direction was measured to within ± 0.001 inch.

There are 8 mesh screens located both below and above the test section. These screens serve to contain the glass beads used in the upper fluidized bed. The bed is filled or emptied of beads through the hole left upon removal of the probe.

The test section is supported by a steel framework bolted to the ceiling and floor. The flange on the upper acrylic section is supported by the framework and the bottom rests on the floor. Provision has been made for leveling and moving the base of the test section to achieve vertical alignment against a plump bob.

Each of the 18 wall pressure taps located in a line is connected to one tube of an 18 tube common top manometer especially constructed for the purpose. The space above the water level in the tubes is filled by pressurized nitrogen gas from a high pressure bottle. In this manner, the pressures at various depths within the bed are determined relative to the pressure above the bed. The scale on the manometer was divided into 0.05-inch increments.

The beads used for the fluidized bed were the same as those Willus used. Namely, Kimble kimax glass beads with an average diameter of 0.236 inch and density of 138 pounds per cubic foot, or a specified gravity of 2.21 relative to water. Most of the beads were quite spherical, although a few were of odd shape.

To determine the pressure as a function of depth, the test section was filled with a measured amount of beads and the probe was removed leaving the bed unobstructed. The test section was then filled with water, and each of the 18 manometer tubes purged to remove air bubbles. A zero check was used to detect any air bubbles present

in the long connecting tubes. The flow was then started and the bed expanded to a height of about 82 inches. After an equilibrium state was reached, the orifice plate head loss and the bed height were recorded, and the 18 manometer tubes were read. A second check of bed height and orifice plate head loss was then made. The entire procedure was repeated to obtain a comparison of readings. Two fluidized beds of different concentrations were examined in this manner.

The height-to-diameter ratio for these fluidized beds was slightly more than 20. This, coupled with the packed bed beneath the lower end of the fluidized bed greatly reduced the circulation problems described earlier.

C. Calculations and Results

If the particles in a fluidized bed are fully suspended, the pressure drop, ΔP, across a portion of the bed height, ΔX, will be:

$$\Delta P = g\left[C(\rho_s - \rho_l) + \rho_l\right]\Delta X \tag{2.1}$$

where wall friction has been neglected. Now if the pressure drop is measured by the difference in height of manometer tubes filled with the working fluid, ΔH, then:

$$\Delta P = \rho_l\, g\, \Delta X + \rho_l\, g\, \Delta H \tag{2.2}$$

Thus:

$$C = \frac{\Delta H}{\Delta X}\,\frac{\rho_l}{\rho_s - \rho_l} \tag{2.3}$$

Local concentration was calculated for each pair of adjacent pressure taps in each run by the equations above. The results in the

form of concentration versus bed depth are plotted in Figures II.2 and II.3. Runs 1 and 2 (in Figure II.2) were essentially the same fluidized bed measured at different times. Similarly, Runs 3 and 4 (Figure II.3) were also almost identical. The average concentration for Runs 1 and 2 was about 14 percent. The average concentration for Runs 3 and 4 was about 29 percent.

The large variations from point to point in Figures II.2 and II.3 are due to the fact that ΔH for each 2 pressure taps was accurate to $\pm$ 0.10 inch, and ΔH between taps was nominally about 1 inch for Runs 1 and 2, and 2 inches for Runs 3 and 4. Hence the values of concentration calculated are accurate to $\pm$ 10 percent for Runs 1 and 2 and $\pm$ 5 percent for Runs 3 and 4.

Aside from what appears to be experimental errors, there seems to be no variation of concentration with vertical position. If the concentration is indeed constant, then a plot of head against vertical position should produce a straight line of slope $C \frac{\rho_s - \rho_l}{\rho_l}$. The plots of head against vertical position for Runs 1, 2, 3, and 4 are presented in Figures II.4 and II.5. Note that the slope of the data in each case matches a straight line almost perfectly. The straight lines in the graphs were calculated from the data using the least-squares method. The lines were extrapolated to the bottom and top of the bed to give the total bed height and head drop across the bed assuming that there were negligible end effects. The bottom of the bed was taken as the top of the supporting screen, and the top of the bed was taken as that point where the head was the same as the static head measured above the bed.

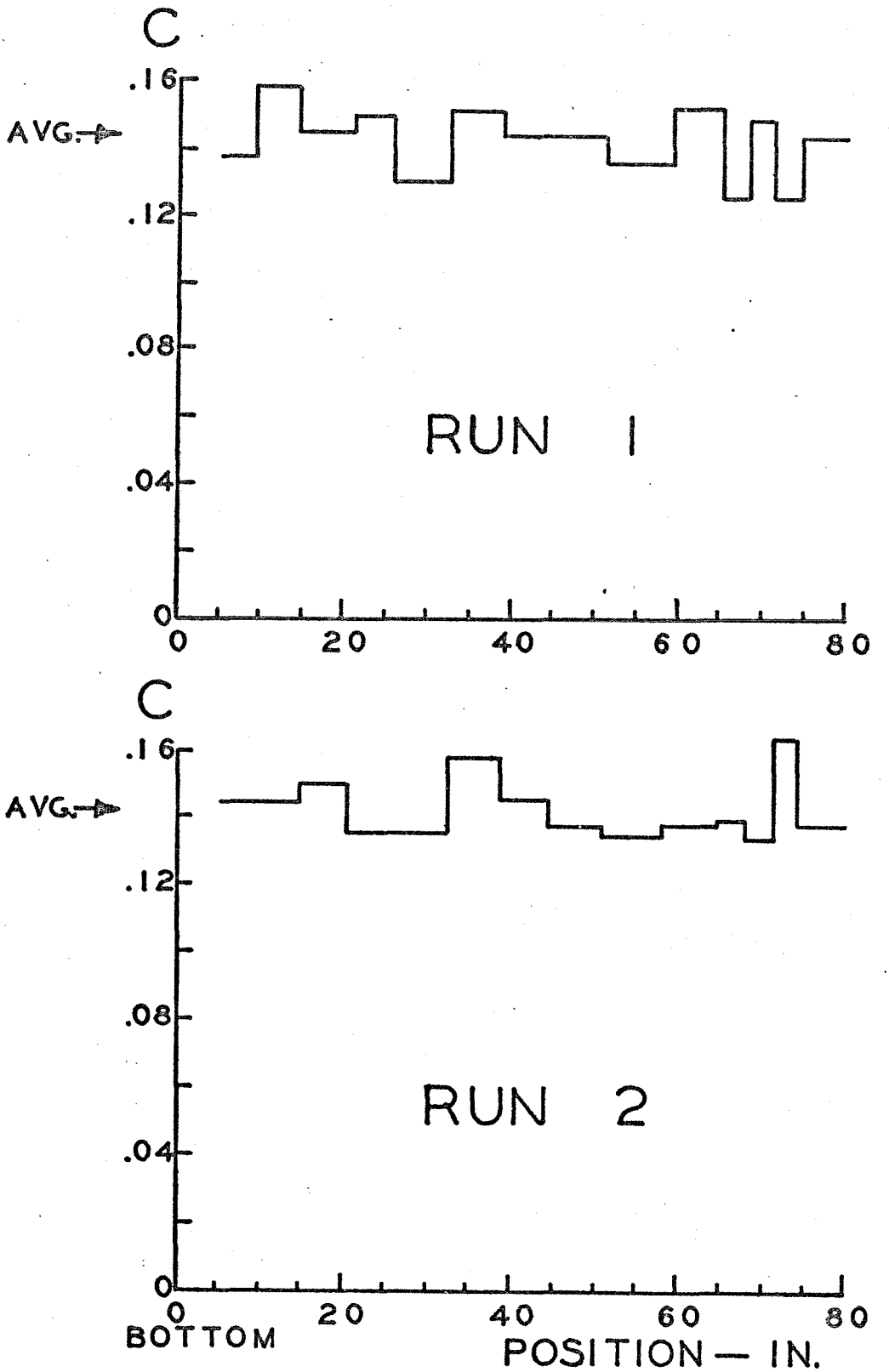

Figure II.2. Concentration Versus Vertical Position for Runs 1 and 2.

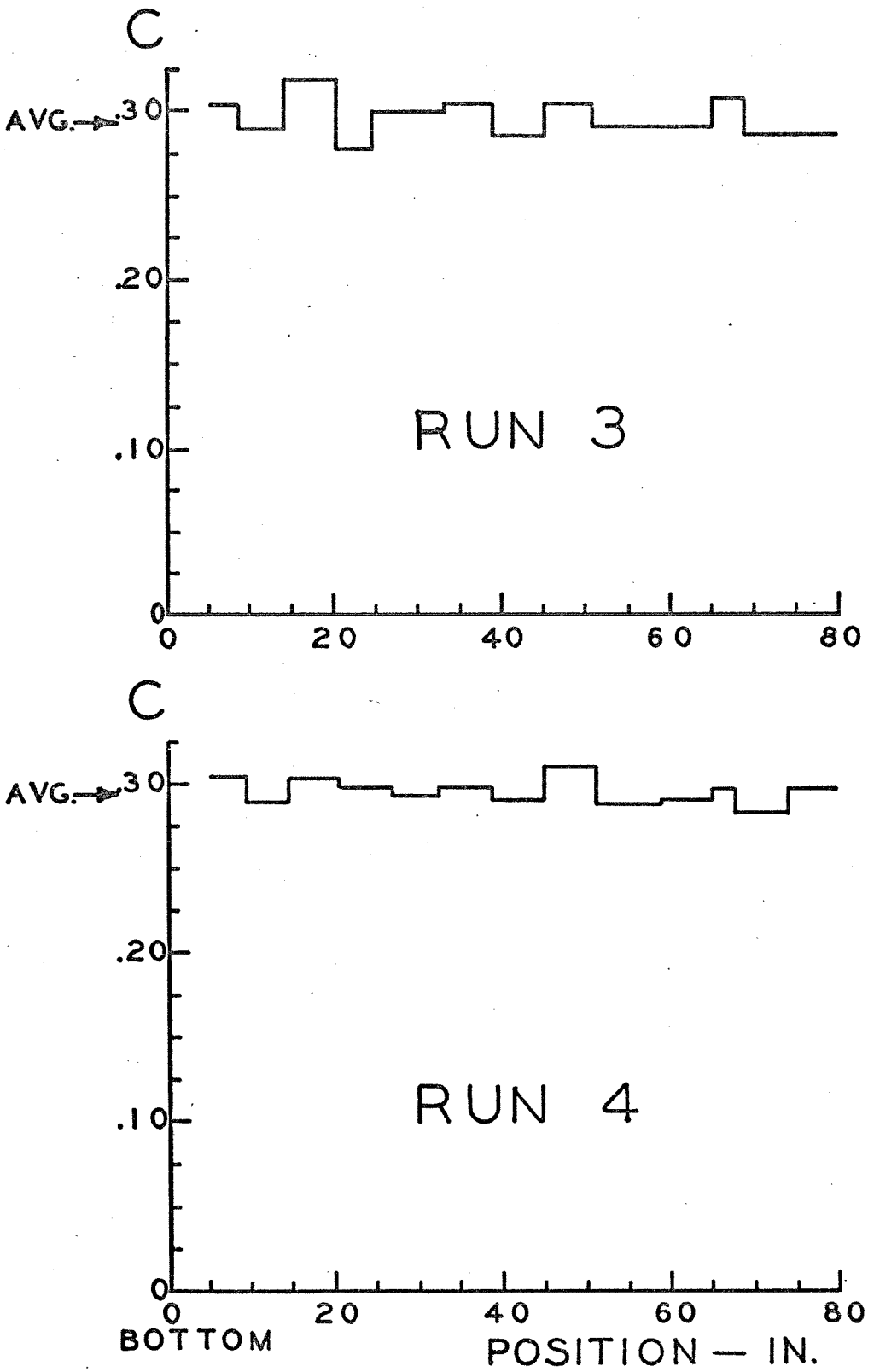

Figure II.3. Concentration Versus Vertical Position for Runs 3 and 4.

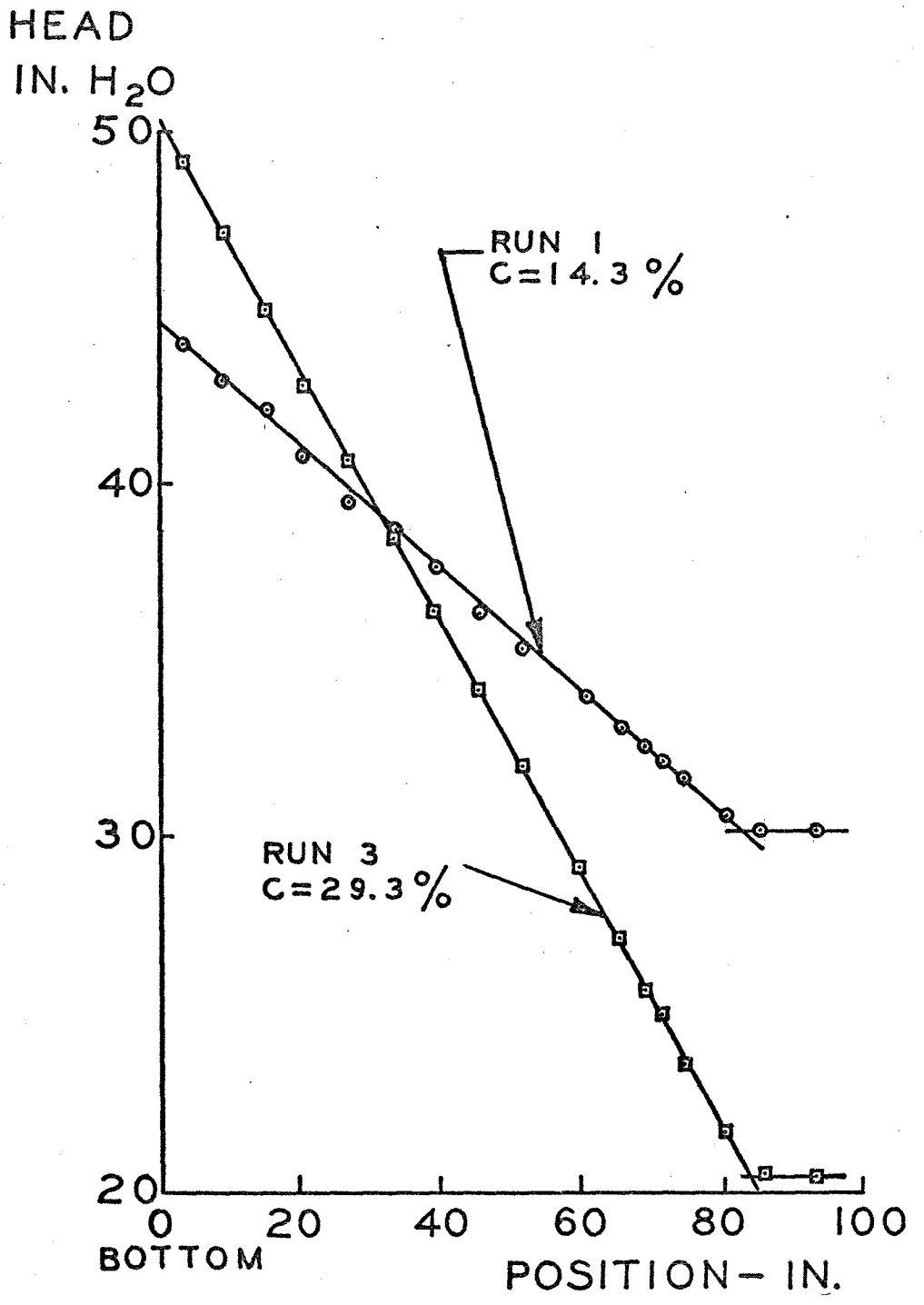

Figure II.4. Head Versus Vertical Position For Runs 1 and 3.

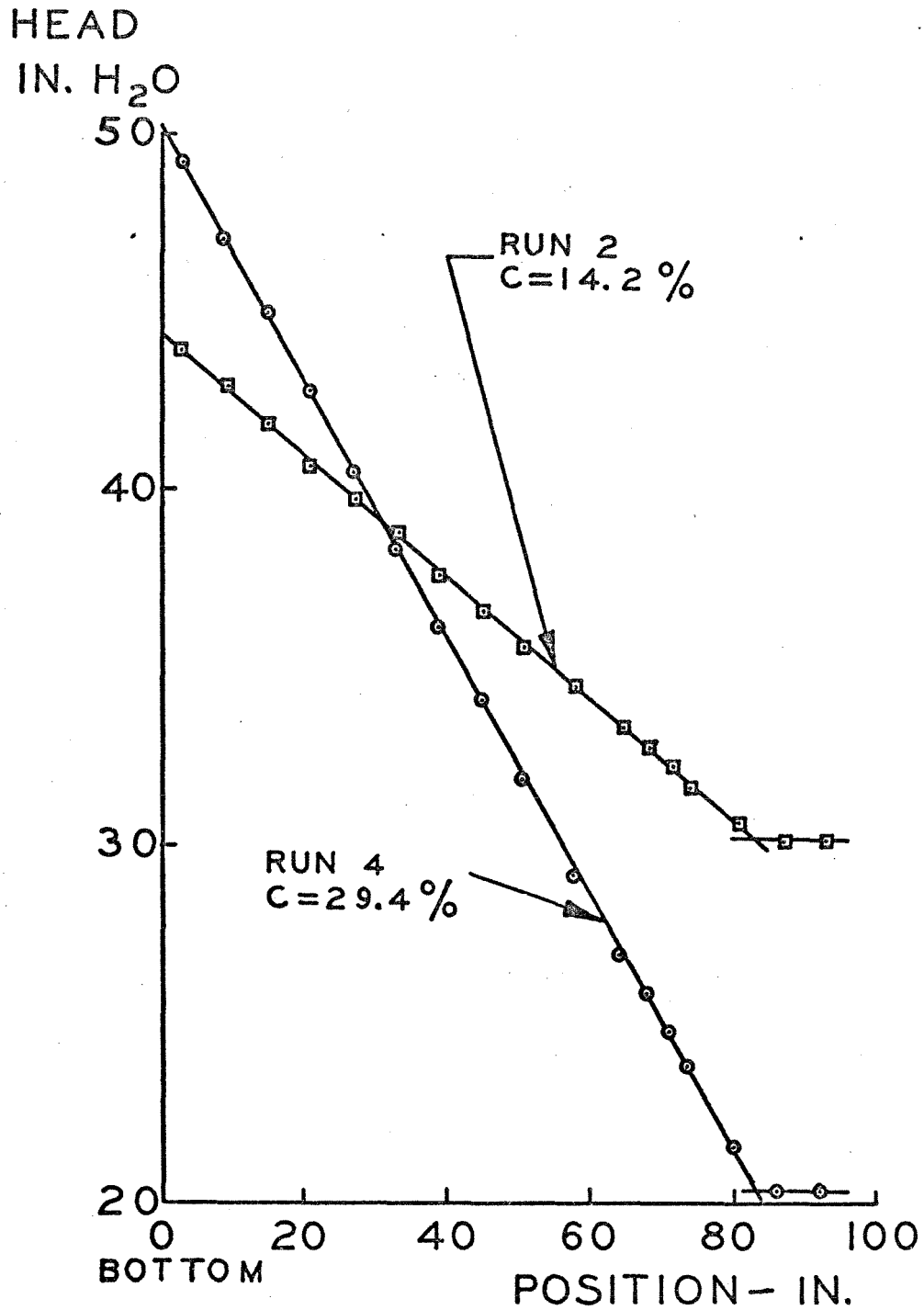

Figure II.5. Head Versus Vertical Position for Runs 2 and 4.

The head drop across the bed can also be calculated from the volume of the particles in the bed, V.

$$\Delta H = \frac{V}{A} \frac{\rho_s}{\rho_l} \tag{2.4}$$

where A is the cross-sectional area of the bed.

The results of these calculations are displayed in Table II.1. In each case, the two values of ΔH agree within experimental error. This means that the bed was fully fluidized. It also means that the concentration variation near the ends of the beds was very small. Of course, the manometer data cannot be used to measure the concentration within a few inches of the top, or bottom, and so there may be some concentration variation in these regions.

To be strictly accurate, one must also take into account the pressure drop due to wall friction. Because of the high shear gradient near the wall of the tube, it is expected that the pressure drop due to friction would be at least as large as that for fully developed turbulent flow at the superficial average velocity in an equivalent length of pipe. This pressure loss of pure fluid is also shown in Table II.1. Note that this value is significantly less than the experimental error. Thus, it is not possible to determine wall friction for a fluidized bed from these data.

Another effect that may be measurable is the pressure changes at the ends of the bed due to momentum change of the fluid entering or leaving the restricted cross-section of the fluidized bed. The magnitude of the effect is difficult to calculate since the momentum of the fluid within the bed is not known accurately. However, assuming

Table II.1. Properties of Fluidized Beds--Concentration Measurement.

RUN NUMBER	1	2	3	4	Probe at 1.50	Probe at 0.1
$\bar{C}$ Percent From Least-Squares Analysis	14.29	14.20	29.32	29.44	29.63	29.65
ΔH_{GRAPH} From Least-Squares Plot	14.25	14.29	29.57	29.64	29.26	29.27
Expected Accuracy of ΔH_{GRAPH}	± .70%	± .70%	± .34%	± .34%	± .34%	± .34%
$\Delta H_{CALC.}$ From Volume of Beads Calculation	14.12	14.12	29.46	29.46	29.46	29.46
$\Delta H_{CALC.}$ Expected Accuracy	± 1.09%	± 1.09%	± .87%	± .87%	± .87%	± .87%
$\Delta H_{GRAPH} - \Delta H_{CALC.}$	.13	.17	.11	.18	-.20	-.19
$\Delta H_{GRAPH} - \Delta H_{CALC.}$ as a Percent of ΔH_{GRAPH}	.91%	1.19%	.37%	.61%	-.67%	-.64%
ΔH_{PIPE} For Fully Developed Turbulent Pipe Flow at Superficial Velocity	.035	.035	.084	.084	.084	.084
ΔH_{PIPE} as a Percent of ΔH_{GRAPH}	.25%	.25%	.28%	.28%	.28%	.28%

that at the top of the bed the velocity changes from the average velocity in the spaces to the average velocity in the tube, the net result for all 4 runs is a head rise of about 0.048 inch of water. This magnitude is within the range of the experimental error present in the manometers. Consequently, it may be neglected.

It must be noted that the concentration could not be measured closer than about 2 inches from the ends of the bed. Since the concentration appeared uniform elsewhere, the possible region of concentration variation is limited to those 2 inches or less than 3 percent of the bed height on each end.

Since the fluidized bed used by Willus was almost identical to the ones examined here, it can safely be assumed that his assumption of uniform concentration was justified.

However, these results tend to negate the premise of McMichael that strong concentration gradients exist in fluidized beds of uniform particles. In the experiments performed here, there was no sign that any variation existed. The concentration gradients measured by McMichael are probably due to his short bed height and the presence of circulating eddies.

CHAPTER III

LOCAL VELOCITY MEASUREMENTS

A. Background

As stated in the summary, the original intent of this study was to develop some means of measuring the velocity of the liquid phase of two-phase (solid, liquid) flow. The difficulty in obtaining such measurements is that, in general, both the particles and the fluid affect any sort of a probe that is used. Thus, if a reading is obtained, it is not clear what quantity is being measured. It was hoped that an electromagnetic velocity probe would eliminate this problem and be sensitive to the fluid properties only. However, the experiments described herein show that it is impossible to calibrate the electromagnetic velocity probe in the presence of the particles of a fluidized bed. Tests with a total head probe indicated that its response was similar to the electromagnetic velocity probe. The results of these tests provide information about the local conditions in fluidized beds. Thus, the work reported in this chapter will be directed more toward an understanding of the fluid mechanics of fluidized beds than the development of an electromagnetic velocity probe.

To understand the significance of measurements made with a probe in a fluidized bed, it is necessary to know the effect of the presence of the probe on the behavior of the fluidized bed. It is expected that any asymmetric distortion of the flow will tend to cause circulating currents. Such distortion could be caused by the presence of a probe in the flow. In order to determine the magnitude of this

effect, a static pressure probe was used to traverse a fluidized bed. The results of the pressures measured as a function of position were used to estimate the magnitude of the distortion caused by the probe.

It is expected that the velocity in a fluidized bed is nearly a constant independent of position on a cross-section in the absence of circulating eddies. Since the particles are supported by the fluid velocity, a velocity profile of the sort present in fully developed flow in a pipe would produce circulation of particles up in the center and down on the periphery. Such fluidized beds are called spouting beds and have been observed in gas fluidized beds and in liquid fluidized beds where the inlet conditions were not uniform.

Now the velocity must be zero on the tube wall. So if no circulating eddies are present, the velocity must drop from the average value to near zero in a thin region close to the wall surface (for non-spouting beds). If the particles adjacent to the wall are not moving downward, the region of rapid velocity change must be limited to a region within one particle radius of the wall.

The experiments performed in this chapter involve the use of an electromagnetic velocity probe and a total head probe to measure the velocity profiles for several fluidized beds. Of course, the measurements are not really of the velocity, but are assumed to be closely related to it.

The following sections will first describe the instruments used in these experiments, and then report the results.

B. Apparatus and Procedures

1. Instrumentation

Three different probes were constructed to measure various parameters. The electromagnetic velocity probe is described in detail in Appendix A. It is shaped much like a total head probe. It is 0.25 inch in diameter and extends downward from the probe stem about 5 inches. The sensing area is located on the sides of the cylinder 4.0 inches beneath the probe stem. Figure III.1 is a photograph of the probe in its holder, and the associated electronics.

A total head probe was also constructed. It is 0.125 inch in diameter and has a hemispherical nose which extends 4.0 inches beneath the probe stem.

In addition, a static pressure probe was constructed. It is also 0.125 inch in diameter and has its sensing holes 4.0 inches beneath the probe axis.

The pressures sensed by these last two probes are only about 0.1 inch of water. Consequently, a micromanometer was constructed to measure these pressures accurately. Figure III.2 is a photograph of the micromanometer. This micromanometer is of the inverted type, and is designed to measure small differential pressures in water systems. The manometric fluid is 1-pentanol. This fluid was chosen because of the excellent meniscus it has in contact with water, and because its specific gravity relative to water is about 0.815 at room temperature. This means that the head measured in inches by the micromanometer will be 5.405 times the actual head in inches of water. The manometer tubes are 0.5-inch inside diameter precision bore glass tubing. The

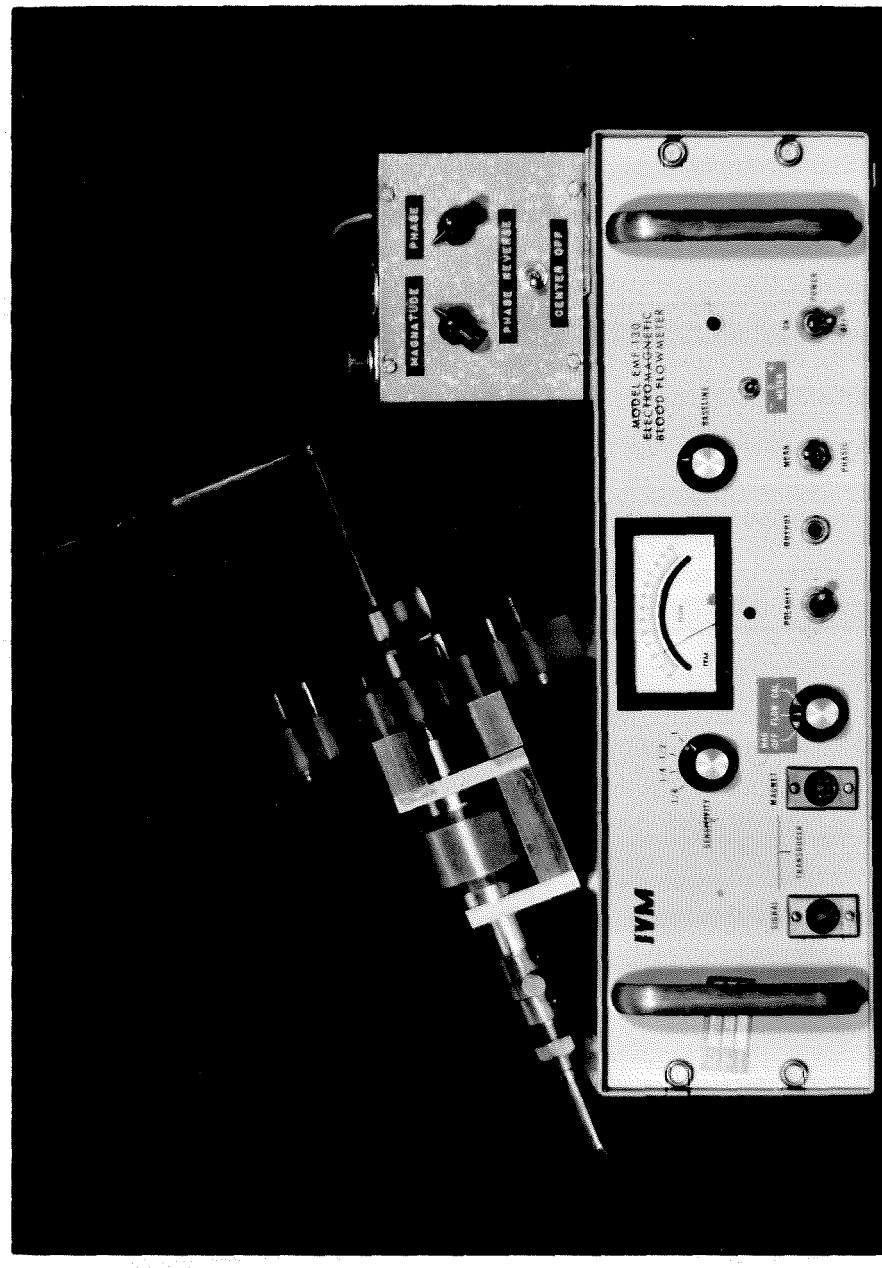

Figure III.1. Photograph of the Electromagnetic Velocity Probe and Electronics.

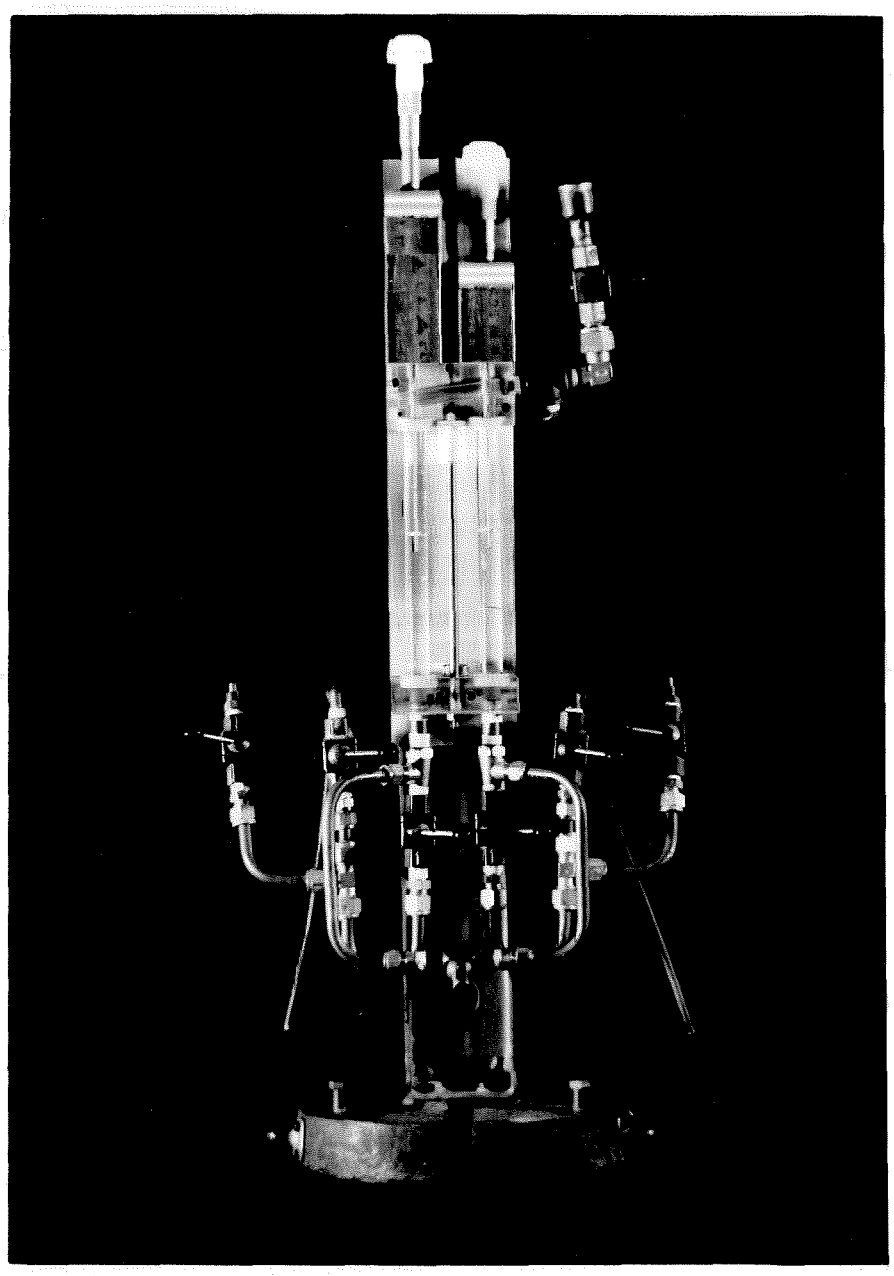

Figure III.2 Photograph of the Micromanometer.

different heights of the manometer tubes are measured by contact of sharpened rods, positioned by micrometer screws, with the surface. The various valves in the photograph are used to fill the system, bleed out air, zero the manometer, etc.

2. Procedures

The procedures involved in each of the experiments will now be presented. The tests with total head and static tubes were designed to detect any change in flow brought about by the insertion of a probe into a fluidized bed, and to measure the velocity profile as determined from a total pressure tube within the bed. In each experiment the micromanometer was used to measure pressure differences. These pressure differences were extremely small and of the order of 0.1 inch of water. Great care was taken to insure that thermal gradients and slight misalignment did not reduce the accuracy of the measurements. The micromanometer has a theoretical accuracy limit of $\pm$ 0.00002 inch of water head. However, the repeatability was limited to about $\pm$ 0.0005 inch of water due to zero drift problems and variable meniscus characteristics.

The precise procedure used to obtain a measurement was too long and involved to repeat here. Basically, the instrument was zeroed both before and after each measurement, and the measurement itself was made by reading the heights of sharpened rods positioned at the fluid-fluid interfaces with micrometer screws.

All pressure taps were located almost precisely 4.000 inches beneath the center of the probe stem axis. Slight errors were introduced due to gasket compressibility and the finite size of the

pressure holes. However, the maximum deviation was less than 0.010 inch. So the tip of the total head tube, the static hole on the static tube and the two wall taps were essentially at the same height.

Several experiments were performed and the following measurements were taken for one fluidized bed:

1. The pressure difference between wall taps as the total head tube moved across test section
2. The pressure difference of each wall tap with respect to the static probe as it moved across the test section
3. Pressure difference between total head tube and average of wall taps as total head tube moved across the test section

In a second fluidized bed, the difference between total head and one wall pressure tap was measured as a function of probe position. The orifice plate head loss and the water temperature were also measured. For each of these measurements the probes were carefully aligned with the test section axis.

To obtain additional data on the effect of the probes on the flow, the total head probe was inserted in the fluidized bed at various locations and the concentration as a function of depth was measured with the wall pressure taps.

The electromagnetic velocity probe was calibrated first in flow of pure water. The probe was mounted in the probe holder facing upstream and the system filled with tap water. It was subsequently

found that the noise present in the laboratory environment was at such a high level that no satisfactory measurements could be taken. Consequently, table salt was added to the tap water to make a solution of 1.0 percent by weight and the electrodes were platinized.

Following these steps, the probe was seen to respond in a predictable manner to flow. However, there were large drifts in the zero flow reading with time and temperature. These problems were eliminated by allowing several hours for the electronic system to come to equilibrium, maintaining the water temperature constant within 1°F. and zeroing the meter before and after each reading. No glass beads were used in this test so that only water flowed through the test section. With the probe inserted into the test section, and immersed in quiescent water, the meter reading was noted as the probe was moved across the cross-section and yawed to nearly 90°. No measurable change in the zero reading was obtained. Next the flow was started and maintained fixed at a certain value. The probe was then again moved across the cross-section and severely yawed. The results were no change of meter reading with respect to position and little sensitivity to yaw. So it was concluded that the presence of the wall near the probe did not affect its reading and that the probe was relatively insensitive to yaw.

The next step was to calibrate the probe against velocity. To do this the probe was positioned in the center of the test section and carefully aligned with the test section axis. The meter was zeroed, and then the flow was started. Flow through the test section was monitored by the orifice plate and was kept constant as the probe

meter reading was taken. The flow was then stopped and another zero reading was taken and the zero drift noted. Only runs with low or zero zero-drift were recorded.

Because of the stabilizing effect of the lower bed, the velocity profile was essentially square, and the velocity of flow past the probe could be determined from the flow rate divided by the cross-sectional area of the tube.

The electromagnetic velocity probe was then used to measure the velocity profiles of 6 different fluidized beds. The procedure was similar to that used for pure liquid flow except that the probe was moved across the test section diameter to determine a velocity profile. The average concentration for each bed was obtained by dividing the volume of the beads, determined by water displacement, by the total volume of the bed. As for the liquid alone, the flow was stopped before and after each run so that an accurate zero was obtained.

C. Calculations and Results

1. Effect of Probe Position on Concentration Distribution

Measurements of pressure versus depth were taken for a bed almost identical to those in Runs 3 and 4 above. The total head probe was placed in the probe holder and positioned at two different positions. First at 1.5 inches from the wall, and second at 0.1 inch from the wall. In both cases the probe support extended across more than half the bed. The data of local concentration versus vertical position are shown in Figure III.3, and the pressure versus position data are shown in Figure III.4. The data were analyzed as before and results are in Table II.1.

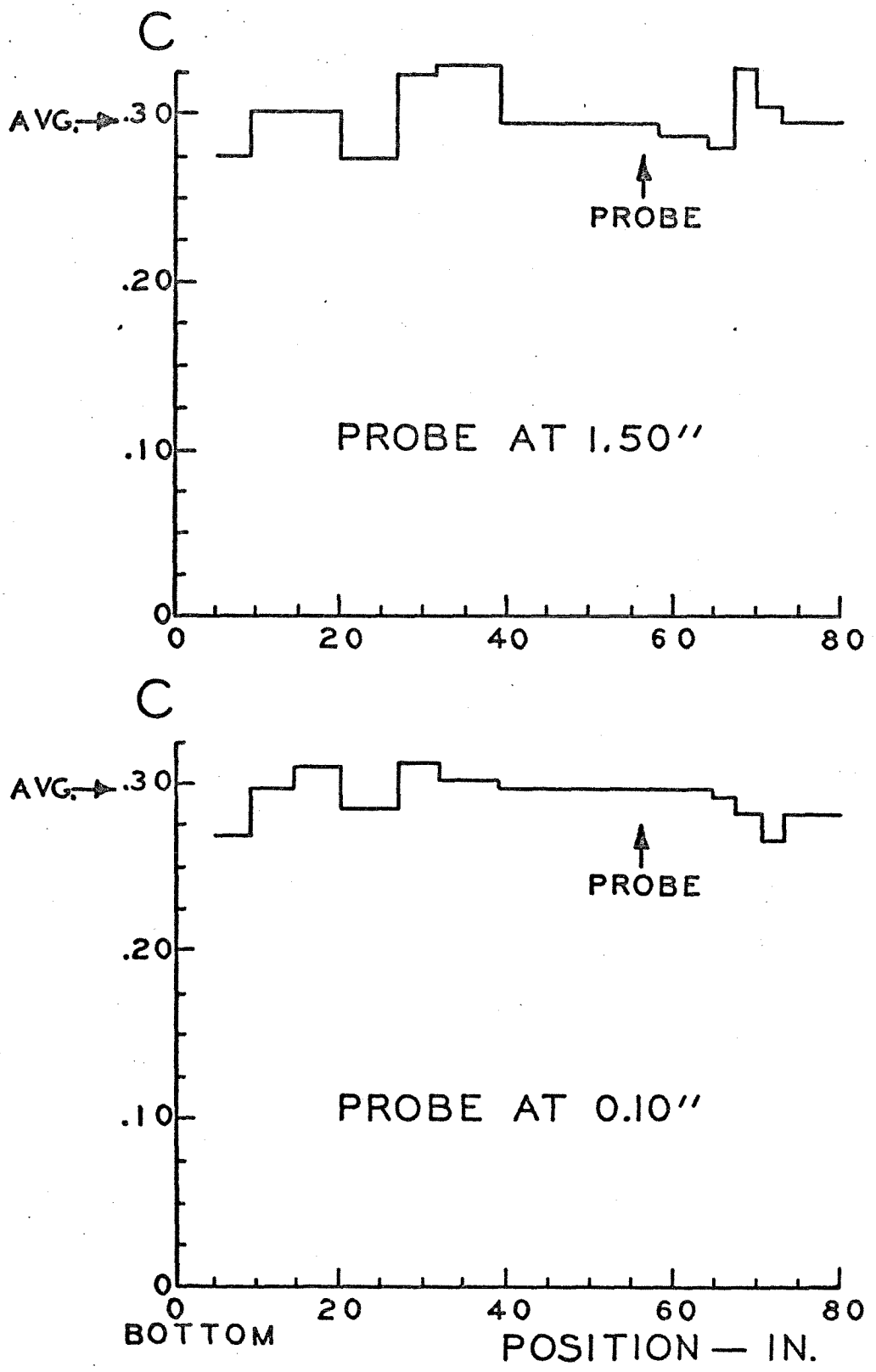

Figure III.3. Concentration Versus Vertical Position with Probe.

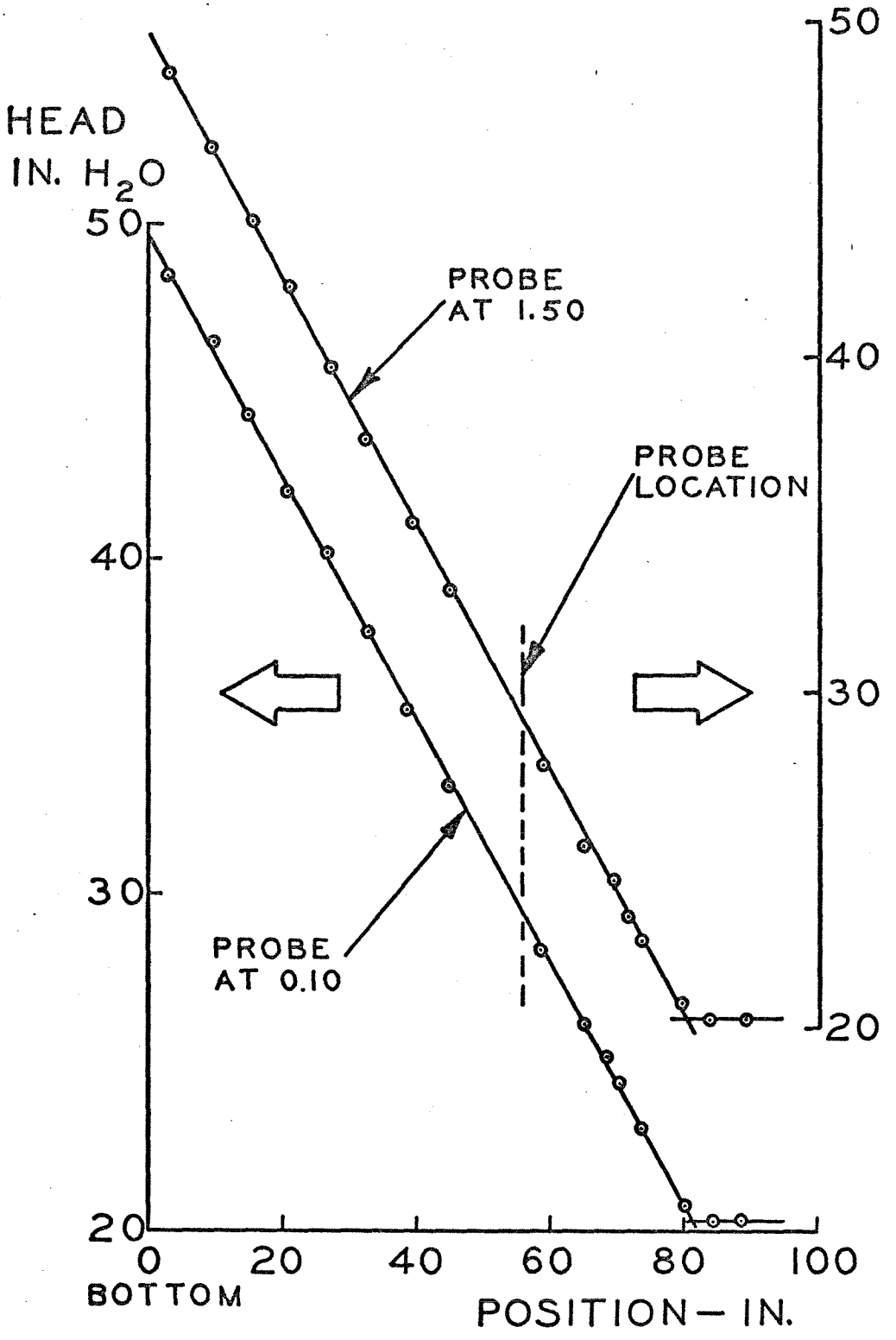

Figure III.4. Head Versus Vertical Position with Probe.

Figure III.3 shows that the concentration distribution is again essentially constant. Note that the concentration at the probe location is very nearly the average concentration for the entire bed. Figure III.4 shows that a straight line again fits the data quite accurately and that there do not seem to be any irregularities near the probe. Also, Table II.1 shows that the ΔH values again agree within experimental error.

On the basis of these tests, it can be concluded that the presence of the probe does not measurably affect concentration distribution in the bed.

2. Effect of Probe Position on Static Pressure

Even though there is no change in bed concentration locally due to the presence of a probe immersed in the bed, it is still possible that a probe could cause local bending of the streamlines around the probe stem and the probe itself, thus altering the velocity profile. If such bending of the streamlines was great enough to significantly change the flow condition in the neighborhood of the probe, it would be expected that the static pressures measured by two opposing wall taps, and the static probe itself would not agree. However, the absolute value of the difference in static pressure itself could not be used to determine the curvature of the streamlines because of the presence of the particles.

For such pressure measurements to be satisfactory, it is necessary that both static wall taps and the holes in the static pressure probe be at the same elevation. Otherwise the gradient of the static pressure with depth would be measured rather than any deviation

of the flow.

Three separate experiments were performed to measure these pressures as a function of probe position. The average bed conditions maintained for each experiment were:

Bed Height	=	82 ± 1 inch
Height of probe tip above bottom of bed	=	50.785 inches ± 0.010
Volume of beads	=	5008 cubic centimeters
Concentration (average)	=	29.5 ± 0.4 percent

First, the difference in pressure between the two opposite wall taps was measured. Second, the difference in pressure between the stem side pressure tap and the static probe was measured. Third, the difference in pressure between the far side wall tap and the static probe was measured. Several measurements were taken at each probe position. The average values and ranges of each measurement are shown in Figure III.5.

These results show several things. First, the variation of pressure in each data point is large compared with the mean value of pressure difference at that probe position. This is primarily due to long-term fluctuations in the pressure. These fluctuations had a time period of about 30 seconds or more in some cases and prevented the micromanometer from reaching an equilibrium position. They may have been caused by a resonance of the micromanometer and some forcing function in the pumping circuit. Hence, several measurements were taken in an attempt to determine an average. However, these fluctuations are so large compared to their average that the average is

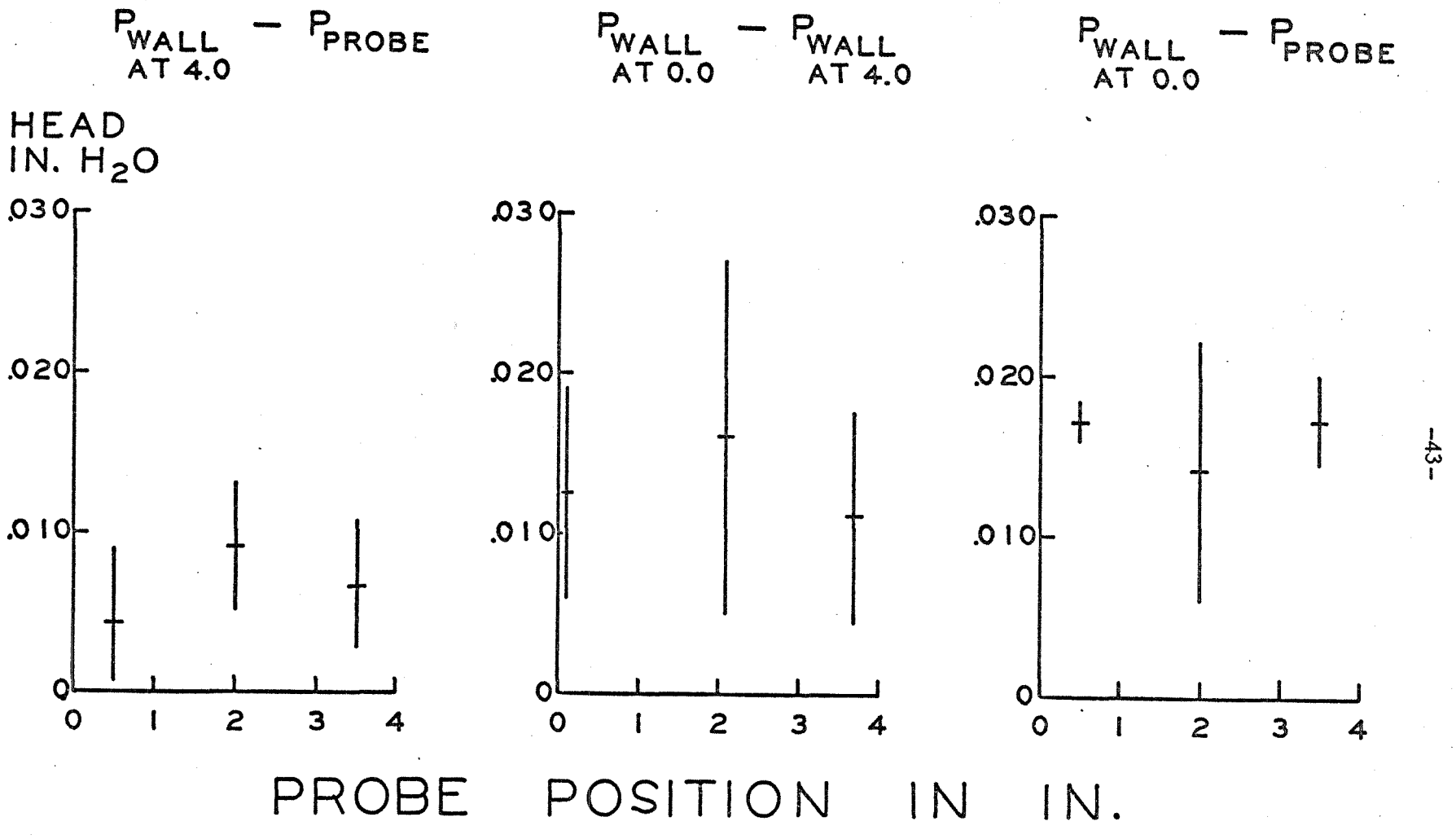

Figure III.5. Results of Static Pressure Measurements.

really meaningless.

The second point is that there seems to be no trend in the measurements as the probe moves across the bed at x = 3.5, the probe is almost totally withdrawn from the bed, and at x = .5 it extends almost all the way across the bed. At the middle position, x = 2.0, one would expect to find a large deviation between the three pressure taps, because x = 2.0 is an asymmetric position where the probe stem covers half of the bed. However, the data show no such result.

The third point is that there seems to be a bias in each set of pressure measurements so that one tap always has a higher pressure than the other. This is undoubtedly due to inaccuracies in the heights of the wall taps and static probe tip. Even slight misalignment of the bed with vertical or slightly overcompressed gaskets could produce differences in heights between the various pressure taps great enough to account for all the differences noted here (0.015 inches).

Fourth, if one examines the difference in average values of static pressure differences as a function of probe position, the largest variation is in the two wall taps and amounts to 0.005 inch of water. Now as it will be seen later, when a total head tube is placed in the bed, the nominal difference between total and static pressures is about 0.16 inch of water. So the variation of the static pressure as the probe moves is only about 3 percent of the total minus static pressure for the flow.

On the basis of these pressure measurements and the concentration measurements mentioned above, it can be concluded that the presence of a probe in a fluidized bed does not measurably change the flow.

3. Velocity Profiles Measured With Total Head Probe

Pressure surveys were done on two fluidized beds with the total head probe. The difference between the pressure at the tip of the probe and the pressure at the static wall taps was measured.

The tip of the total head probe pointed downward and was located at the same elevation as the wall pressure taps used above. The pressure surveys were done using the micromanometer to measure the difference in head between the total head tube and the two wall taps manifolded together.

The pressure difference measured was converted to velocity by the use of Bernoulli's equation in the standard manner. The density was taken as that of the fluid, water. Figure III.6 contains plots of the calculated velocity as a function of probe position. The size of each data point is approximately the range of static pressure imbalance noted above. Table III.1 lists the important parameters for each bed and the results of these calculations. The measured average velocity is calculated as the linear average of the velocities measured.

In examining these results, it must be remembered that the velocity calculated from the difference between total and static head is not necessarily the local fluid velocity. It is well known that the total head minus static head can be used to calculate velocity in an infinite fluid providing that the Reynolds number based on diameter of the probe is greater than about 200. However, the presence of particles in a fluidized bed can be expected to alter the calculated velocity. To

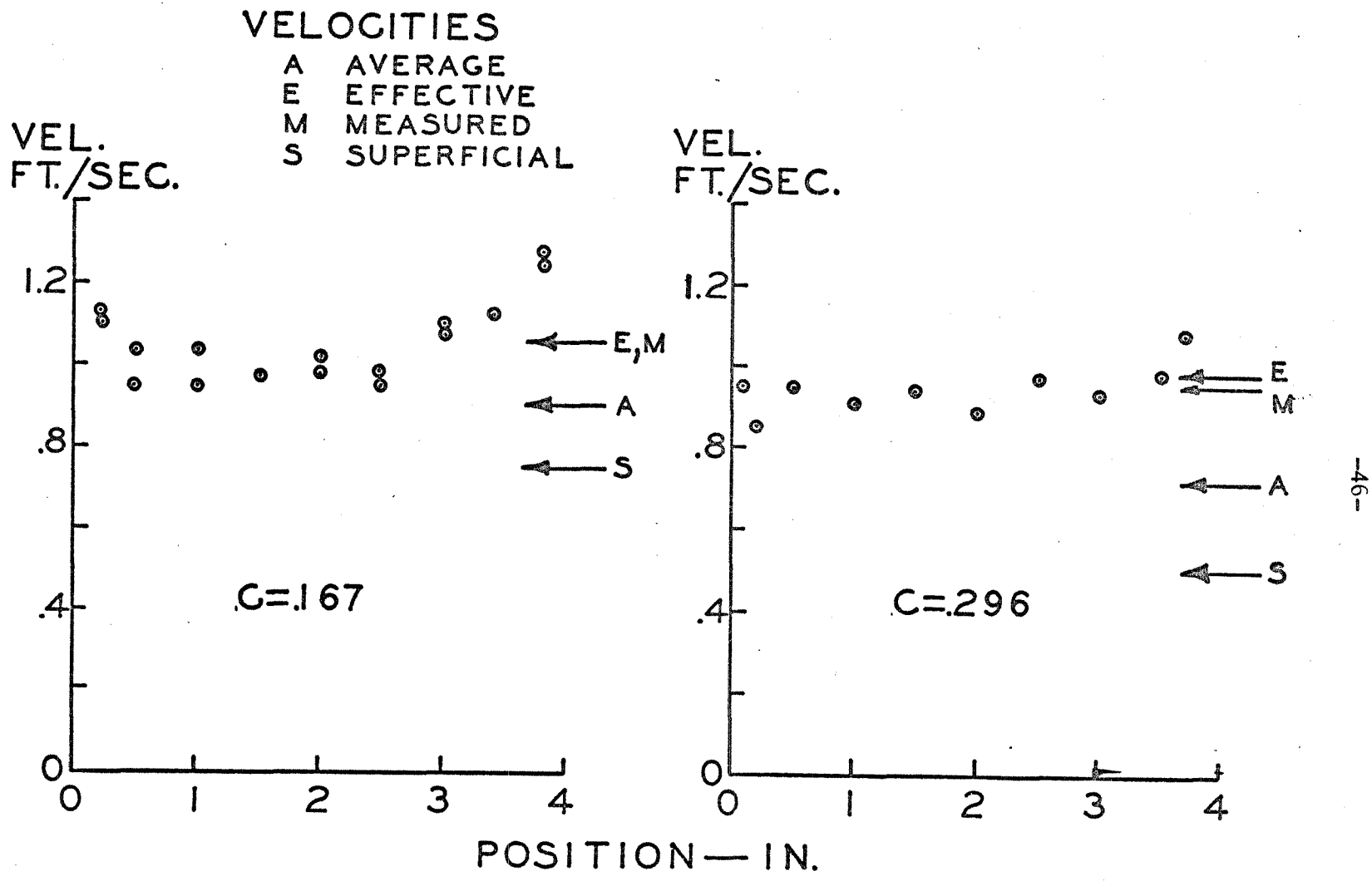

Figure III.6. Velocity Profiles with Total Head Probe.

Table III.1. Properties of Fluidized Beds--Total Head Surveys.

PARAMETER	RUN		UNITS
	1	2	
Bed Height	82	82	inches
Probe Distance From Bottom	52	52	inches
Volume of Solid Particles	5008	2820	$Cm.^3$
Average Concentration	.296	.167	By Volume
Superficial Velocity = U_S	.508	.753	ft./sec.
Average Velocity = $U_A = \frac{U_S}{1-C}$	.722	.904	ft./sec.
Effective Velocity = $U_S(1-C)^{-1.89}$	.986	1.064	ft./sec.
Measured Average Velocity	.946	1.055	ft./sec.
Estimated Turbulence Level = $\sqrt{\overline{U'^2}}/\overline{U}$ (see text)	.49	.35	

first order, one would expect that the calculated velocity would be close to the average velocity of the fluid around the particles. Appendix B discusses the meaning of the average velocity in a fluidized bed in terms of the hydrodynamics of flow around the particles. The average velocity of the fluid in the spaces is $U_A = \frac{U_s}{1-C}$ where U_s is the superficial velocity (the flow rate divided by cross-sectional area) and C is the volume concentration of particles. An effective velocity, U_E , is defined such that the drag coefficient based on this velocity is constant independent of concentration. U_E is found to be of the form $U_E = U_s (1-C)^{\frac{1-2m}{2}}$ where m is a function of a Reynolds number of the flow. For high Reynolds numbers, such as the experiments reported here, $m = 2.39$. The reader is referred to Appendix B for a detailed discussion of these velocities.

The average velocity and the effective velocity have been calculated for each fluidized bed. The results appear in Table III.1 and are shown in Figure III.6. Note that in both cases the velocity calculated from the total minus static head is significantly greater than the average velocity. However, it is almost identical, on the average, to the effective velocity. There are two possible reasons for this.

The first reason is that the turbulence level may be very high. For isotropic turbulence in one-dimensional flow over a total head probe, it can be shown from the averaged momentum equation that the velocity calculated, $\bar{V}$ will be

$$\bar{V} \approx \left[\bar{U}_a^2 + 3 \overline{U'^2} \right]^{1/2} \qquad (3.1)$$

where $\overline{v_a}$ is the average velocity of the fluid with respect to the probe, and $\overline{v'^2}$ is the average of the square of the turbulent part (Goldstein, 1936). The turbulence in a fluidized bed is probably not isotropic because the flow is similar to flow of a fluid in a pipe. Nevertheless, the isotropic turbulence assumption will probably not be too far off. So assuming isotropic turbulence in a fluidized bed, the turbulence level, $\frac{\sqrt{\overline{v'^2}}}{\overline{v}}$, may be calculated from the known average velocity, $v_a = \frac{v_s}{1-\epsilon}$, and the measured velocity $\overline{V}$. This has been done for the two fluidized beds analyzed here. The results, shown in Table III.1, indicate extremely high turbulence levels of the order of 0.40. Although these levels are high in comparison to typical values for pure fluid flow in a pipe, they are quite reasonable for a fluidized bed. If the probe were located in the wake of a particle, the local velocity would be near zero. If it were located adjacent to a particle, the local velocity would be much higher than the average. If the probe saw a sinusoidal fluctuating velocity of minimum magnitude zero and of maximum magnitude $2\overline{v_a}$, then the turbulence level can be calculated to be 0.707. In addition, Willus used an optical technique to follow individual particles in fluidized beds. His results indicated that the turbulent velocities of the particles in a fluidized bed of 12 percent concentration ranged from zero up to the superficial velocity of the fluid. If the turbulence level in the liquid phase is roughly the same as the solid phase, the turbulence levels calculated here seem reasonable. Thus, it is quite possible that the velocity measured is higher than the average velocity because of the high turbulence level.

The second reason why the measured velocity should be higher than the average velocity is that the probe may only see higher than average velocities. The particles used in this experiment were almost twice as large as the probe diameter. It is conceivable then that the particles could orient themselves in some particular configuration that caused the probe tip to be almost continually immersed in the high velocity region adjacent to the particles. This is certainly possible. However, this was not observed experimentally. Since the test section was transparent, the flow around the probe could be observed quite well when the probe was close to the sides of the tube. The particles seemed to move at random with respect to the probe tip.

The magnitude of the measured velocity will be discussed again in comparison with the electromagnetic velocity probe experiments.

The velocity profiles in Figure III.6 show that the conditions are essentially the same all the way across the tube. Measurements were not made very close to the wall because of problems with particles becoming trapped between the probe and the wall. Neither profile shows any tendency for the velocity to go to zero near the wall. Of course, the velocity must be zero on the tube wall, so that in the region near the wall (within one particle radius) the velocity must drop rapidly to zero.

There seems to be a tendency in both plots in Figure III.6 for the velocity to be higher on the right than on the left. This was noted to a much higher degree with the electromagnetic velocity probe experiments described later. This tendency is probably due to slight misorientation of the vertical axis of the tube, and the presence of

weak circulating eddies.

4. Velocity Profiles Measured With Electromagnetic Velocity Probe

The calibration curve for the electromagnetic velocity probe in pure liquid is shown in Figure III.7. Thirty-four separate data points were taken at various flow rates with the probe located in the center of the tube. Velocity was determined from the flow rate through the orifice plate assuming a square velocity profile.

A least-squares analysis was used to correlate the data to a straight line, and the result is shown in Figure III.7. The correlation coefficient for the data was 0.9976, indicating a nearly perfect fit. The analysis presented in Appendix A predicts that the meter reading will be linearly related to the velocity. The fact that the fitted straight line, when extrapolated, does not go through zero velocity at zero meter reading does not mean that there is a zero offset. On the contrary, the meter was zeroed before and after each data point was taken. This does not pose a problem in that the instrument is not sensitive enough to make accurate readings possible in this range.

As an additional check of repeatability, 14 more data points were taken, and the results compared favorably with the calibration curve. Of the 14, 10 or about 70 percent were within 4 percent of the calibrated value. This then sets the limits of accuracy for the electromagnetic velocity probe on pure liquid.

Next, the probe was used to measure the velocity profile in fluidized beds. Six different beds were examined. The average

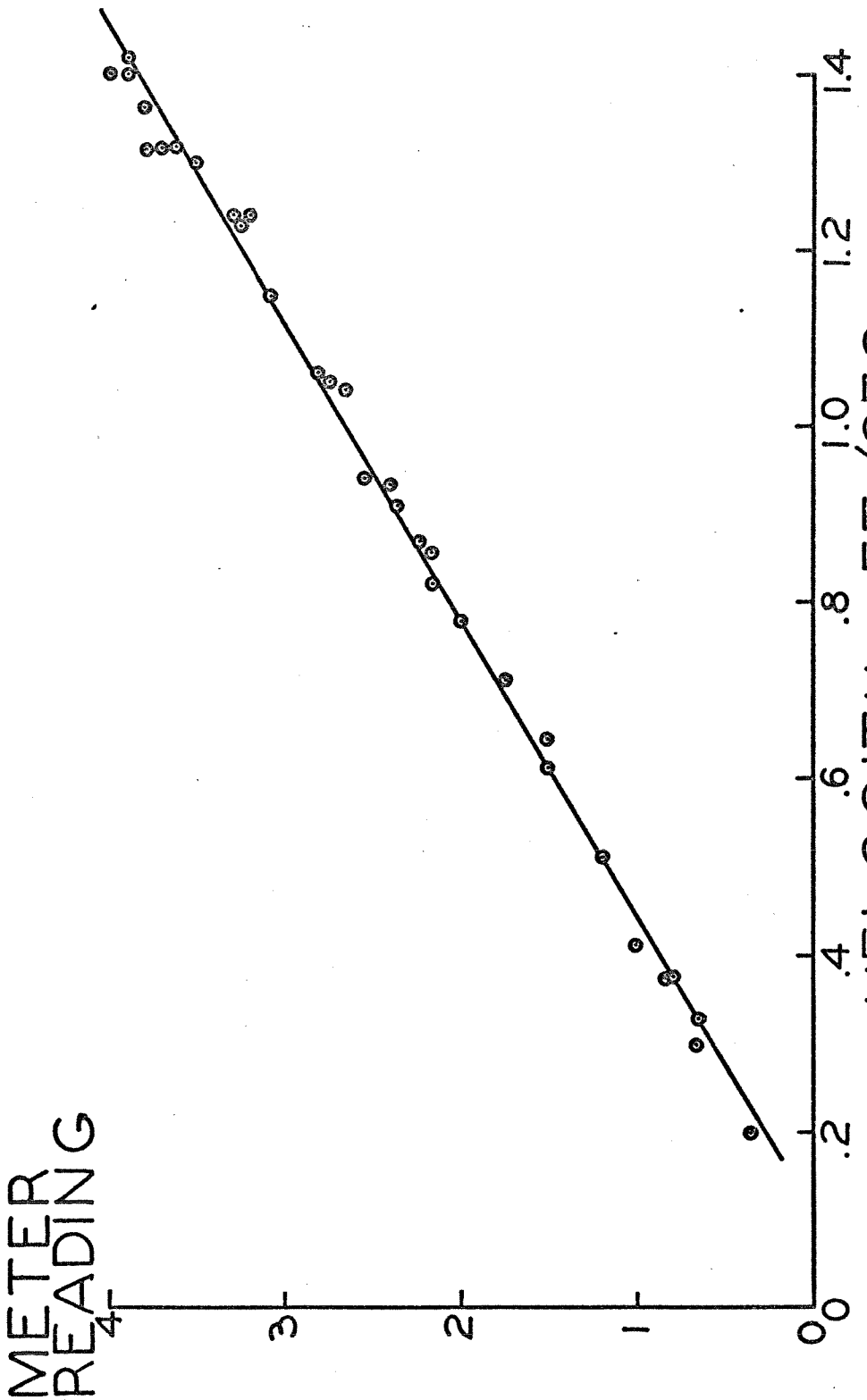

Figure III.7. Calibration Curve for the Electromagnetic Velocity Probe.

characteristics of each bed are shown in Table III.2. For each bed, the sequence of moving the probe across the bed was random so that no time dependent variables were measured. In addition, at least 12 data points were taken for each bed, and for most probe positions two readings were taken at different times.

The calibration curve was used to convert the meter readings to velocities. These velocities are plotted as a function of probe position for each bed in Figure III.8.

Examination of these velocity profiles reveals that except for Run 2, C = 35.15 percent (the highest concentration), the velocity profiles are definitely not square, but are "inverted". That is, the velocity near the outside of the tube is greater than the velocity near the center. Of course, on the tube wall the velocity must be zero because of viscosity.

The point of lowest velocity was always on the left side of the middle. Thus, the average velocity as measured by the probe was greater on the right side than on the left side. Now if the assumptions that the particles always move with constant velocity with respect to the liquid and that the net flow of solids across the whole cross-section is zero are applied here, the result is a net flow of particles up on the right side and down on the left side. This is a circulation of particles, or an eddy.

This result was borne out somewhat by inspection of the bed during operation. Because of the high concentration, one could only see a short distance inside the tube. It was noted, however, that there was some tendency for particles to go up on the right side and

TABLE III.2.

RESULTS OF VELOCITY MEASUREMENTS

RUN NUMBER	1	2	3	4	5	6	UNITS
Average Concentration	.249	.352	.140	.200	.166	.140	
Bed Height	82	58	82	57.5	69.5	82	inches
Volume of Solid Particles	4200	4200	2370	2370	2370	2370	$Cm.^3$
Superficial Velocity	.578	.411	.800	.657	.734	.800	ft./sec.
Average Velocity	.769	.634	.930	.821	.880	.930	ft./sec.
Effective Velocity	.993	.933	1.064	1.002	1.034	1.064	ft./sec.
Measured Average Velocity	1.146	.982	1.037	1.078	1.112	1.120	ft./sec.

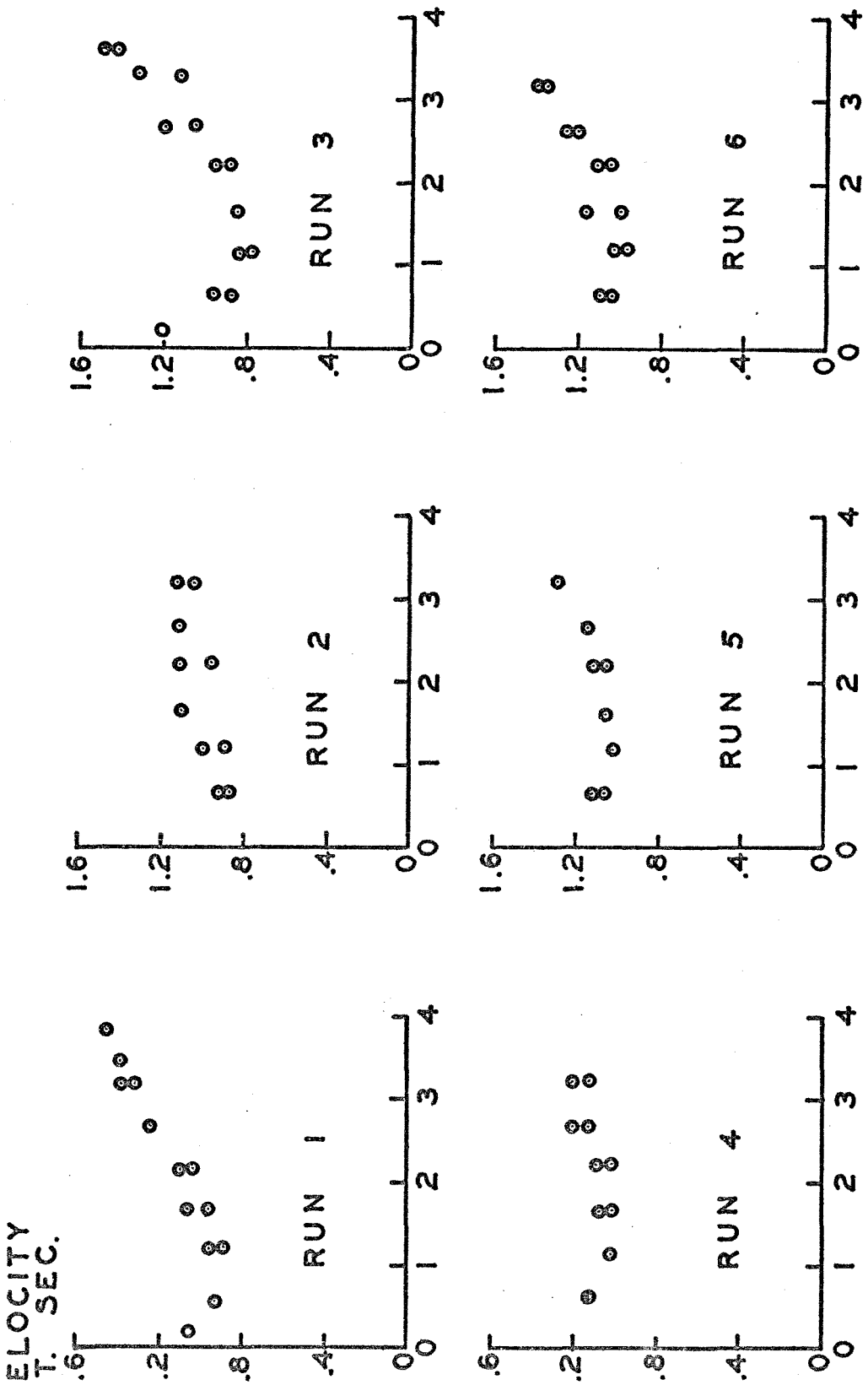

Figure III.8. Velocity Profiles with Electromagnetic Velocity Probe.

down on the left side as the measurements predict. This is not to say, however, that all the particles on the right side were going up and all the particles on the left side were going down. On the contrary, the motion seemed to be quite random with particles moving in all directions. This tendency was evident in the motion of a few colored beads identical in all respects to the others, but colored brown. These beads were seen to have a tendency to move up on the right side and down on the left side. Of course, these observations must not be taken as representative of the whole flow as they were confined to the region near the surface of the tube.

Run 2 does not show the same pronounced inverted velocity profile as the others, but still has higher velocity measurements on the right side.

The reason for the presence of these "eddies" is puzzling. One would expect that since the probe was located more than 10 diameters from the bottom of the bed, and since the bed was carefully aligned, no eddies would exist in the vicinity of the probe. If an eddy were induced by the blockage created by the probe stem, the static pressure measurements mentioned above should have shown this. And if the probe stem nevertheless did cause an eddy, it should be up on the left side (no stem) and down on the right side (stem side) and be affected by probe position.

It may be suspected by the reader that this anomaly is created by some special characteristic of the probe which gives it erroneous signals. This is a distinct possibility. However, the measurements with a total head probe also give the inverted profile.

Runs 3 and 6 were made at the same average concentration, but on different days. The results shown in Figure III.8 point out the experimental errors in the measurements. Although the superficial velocity, bed height, and concentration were identical for both runs, the velocity profiles were somewhat different. However, the overall shape of velocity profile is the same for each run. The deviation in average velocity measured by the probe for the two runs was 7.4 percent of the higher of the two averages.

The question again arises as to why the velocity measured is greater than the average velocity. The argument of high turbulence level does not apply here because the electromagnetic velocity probe responds linearly to velocity so that on the average, turbulent fluctuations have no effect.

Figure III.9 is a plot of the ratio of measured velocity to superficial velocity against voidage (1.0 minus the concentration) on logarithmic coordinates. Both the total head probe data and the electromagnetic velocity probe data are shown. The effective and average velocities are also shown. The result is that the velocities measured by both probes correlate quite well with the effective velocity.

The electromagnetic velocity probe has its sensing areas on the cylindrical side surface. Because of this, it can be argued that the sensing area may never be immersed in the low velocity wake area behind each particle. This would result in a higher velocity measurement than the average velocity.

Several other arguments could be postulated to attempt to

LOGARITHMIC
COORDINATES

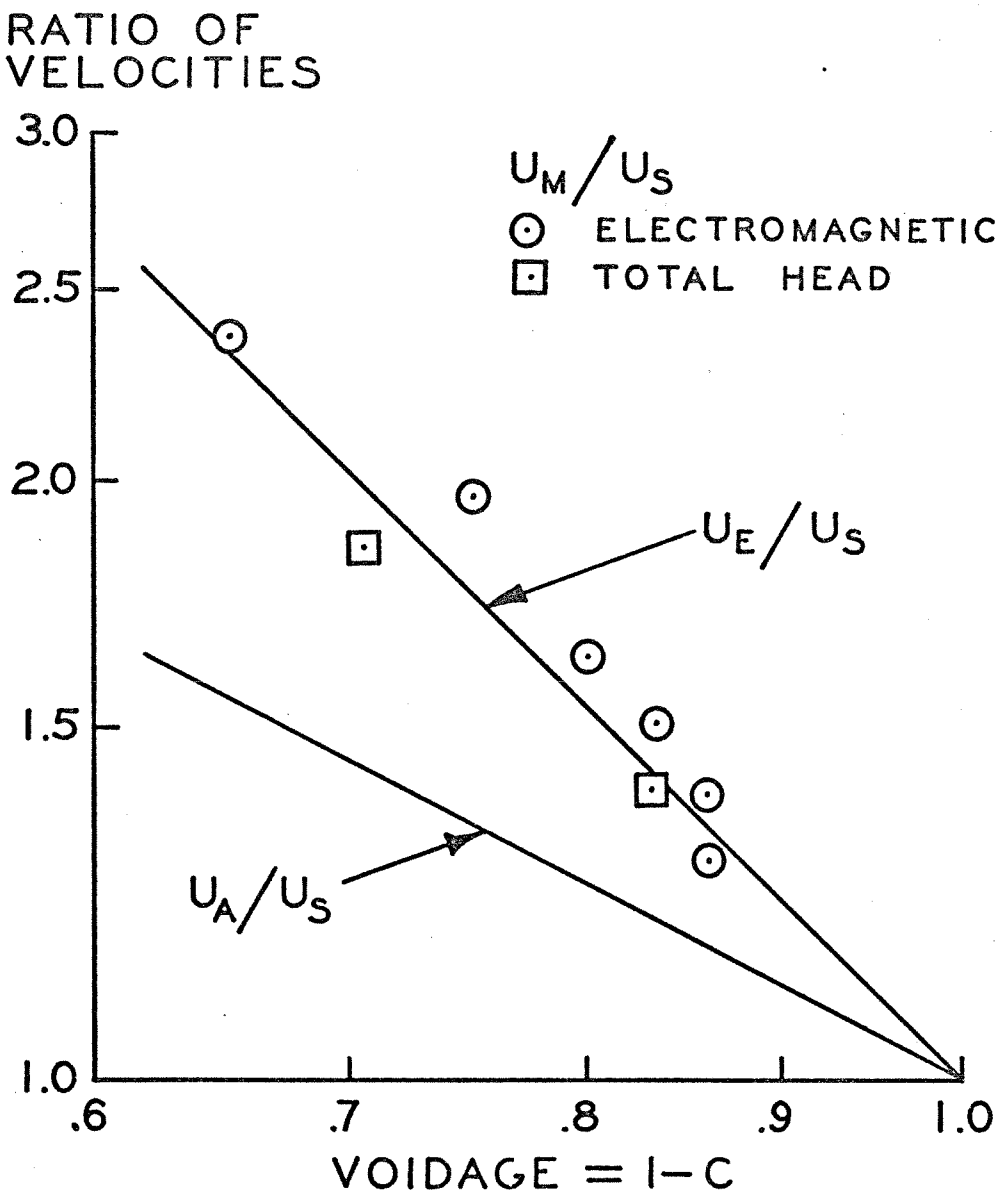

Figure III.9. Correlation of Probe Measurements with Voidage.

explain these results. But the net result is still the same: For the fluidized beds used here, the average velocity across the bed as measured by either a total head probe or an electromagnetic velocity probe correlates quite well with the effective velocity.

The question arises as to the suitability of the use of total head and electromagnetic velocity probes in fluidized beds and other two-phase (solid, liquid) flow configurations. The suitability of these instruments is determined solely by the information that the investigator wishes to glean from the experiment. Several investigators at the M.I.T. Hydrodynamics Laboratory (Elata and Ippen (1961), Daily and Chu (1961), Daily and Shen (1964), Daily and Roberts (1964)) have attempted to measure velocity profiles for slurries flowing in pipes with total head probes where the particles were small compared to the probe diameter. These measurements, when integrated across the cross-section, correlated quite well with the flow rates through the pipes. In addition, electromagnetic flowmeters have been used, as described in Appendix A, to monitor the flow rates of industrial slurries and blood.

It appears that the probes used here are suitable for measuring a velocity in a fluidized bed and it appears to be the effective velocity from these limited experiments. However, such probes do not measure the average velocity of the fluid phase.

CHAPTER IV

CONCLUSION

On the basis of the experiments reported above, several conclusions can be drawn.

There is no evidence to suggest that the concentration of uniform particles in a fluidized bed with high aspect ratio is other than constant over the entire height of the bed. The measurements performed here on two water fluidized beds of different concentration show the concentration to be uniform within the limits of experimental error up to less than one tube diameter of the ends of the bed. Although no direct measurements were made closer than this to the ends of the bed, the maximum possible region of concentration variations at each end is less than 3 percent of the total bed height. The results obtained by McMichael indicating large concentration gradients in fluidized beds of low aspect ratio are thus not typical of fluidized beds with high aspect ratio.

Although fluidized beds are very susceptible to recirculating eddies, it is still possible to insert a probe into a fluidized bed without causing eddies. The probe used here had a horizontal stem which partially blocked the cross-section. Nevertheless, the measurements indicated no perceptible change in fluidized bed characteristics as the probe was moved across the bed.

An electromagnetic velocity probe can be constructed to measure the local velocity in a liquid. However, it cannot be calibrated to measure the average velocity of the liquid phase of a suspension unless the concentration of particles is known.

Both the electromagnetic velocity probe constructed here and a total head probe measure the same velocity in fluidized beds. In the limited experiments performed here, the average velocities measured correlated well with the effective velocities of the fluidized beds. (The effective velocity is defined as the local velocity necessary to support a single isolated particle.)

Finally, the velocity profiles as measured by both the electromagnetic velocity probe and the total head probe showed no tendency of the velocity to drop to zero near the tube walls. Since measurements were made up to within one particle diameter from the tube wall, the region in which the velocity of the fluid drops to zero must be limited to a thin layer less than one particle diameter thick adjacent to the wall. The rest of the cross-section has essentially constant fluid velocity.

PART I-B

ANNULAR FLUIDIZED BEDS

CHAPTER I

INTRODUCTION

An annular fluidized bed consists of a high concentration of particles hydrodynamically suspended in a confined vortex-sink flow. Such flow may be produced in a cylindrical tank with short axial length where fluid is introduced at the periphery with swirl and allowed to pass out through a cylindrical screen located near the axis. In the annulus between the screen and the outer cylindrical wall, the flow is basically a two-dimensional vortex combined with a sink. A particle heavier than fluid will tend to move with the fluid and as it moves around the axis, a centripetal force is required to hold it in a circular path. This is supplied by the drag of the radial component of the flow over the particle. The particle moves under the action of these forces until it reaches a state of equilibrium where the pressure and drag forces exerted by the fluid just balance the centripetal force necessary for a circular orbit. Ideally a single particle will have a circular equilibrium orbit.

If many particles are introduced into the flow the drag coefficient for the cloud of particles will be greater, resulting in a smaller equilibrium radius. Thus, a cloud of particles distributes itself such that there is a concentration gradient from zero at a large radius to higher concentrations at smaller radii.

The purposes of this study are two-fold. The first is to describe the operating characteristics for annular fluidized beds. Although the current applications of this device are few, the potential applications are great. The annular fluidized bed is useful in many of

the situations where vertical fluidized beds are currently employed. Like the vertical fluidized bed, the annular fluidized bed provides great particle surface area for heat transfer and catalysis. However, compared to the vertical fluidized bed, everything is speeded up. In the vertical fluidized bed the flow rate of fluid is limited by the gravitational force acting on the particles. In an annular fluidized bed the analogous force is the centrifugal force on a particle moving in its orbit. This may be made as small or large as desired.

The second purpose is to obtain measurements of various parameters of the flow that will be useful in other two-phase flow situations. The annular fluidized bed provides a simple way of measuring the drag coefficient for particles in a cloud over a range of concentrations. Since the particles distribute themselves so that there is a concentration gradient, measurement of the concentration and the velocities as functions of radius allow direct calculation of the drag coefficient for a cloud. The concentration may be deduced from optical measurements, and the velocities can be calculated from wall static pressure data.

It is also possible to measure the wall shear stress. As stated in the summary, it was originally thought possible to measure the effective viscosity of the suspension from calculating the shear stress on annular surfaces. However, the wall shear stress affects the flow much more than the shear stress on cylindrical surfaces. Consequently, the effective viscosity of the particle cloud cannot be determined. The measurement of the wall shear stress involves the second derivative of pressure with respect to radius. While such

differentiation is difficult and subject to large experimental error, it can be performed approximately. Thus, the wall shear stress may be correlated with the concentration of the suspension.

This part of the thesis has three principal sections. The first part provides the analytical background. The flow without particles is examined for irrotational and laminar viscous flow in two dimensions, and the side-wall boundary layer is examined in three dimensions. The behavior of single particles in irrotational flow is also considered. Both the equilibrium orbit for a single particle and the stability of that orbit are examined. For clouds of particles, the relationship between drag coefficient and concentration distribution is derived, and the effects of wall shear stress on the circulation are determined.

The second section describes the experiments. Two annular fluidized beds were constructed. The first was designed only to verify the principle of operation, and the second was substantially larger and more complex. The experiments included studies of the circulation distribution with and without particles and the distribution of concentration as a function of radius.

The third section correlates the results of the experiments with the analysis to obtain the drag coefficient and wall shear stress as a function of concentration.

CHAPTER II

ANALYTICAL CONSIDERATIONS

A. Vortex-Sink Flow Between Parallel Plates

1. Two-Dimensional Potential and Laminar Flow

To understand the operation of an annular fluidized bed, it is necessary to study the behavior of the flow when no particles are present. In the vertical fluidized bed analog, this would consist of studying the flow of pure fluid in a vertical pipe. Here it consists of describing the flow in a vortex-sink contained between parallel side walls.

This flow will be discussed in two sections. In this section, the equations for potential and laminar flow in two dimensions will be developed. The axial variation is neglected. In the next section the three-dimensional problem will be considered by examining the boundary layers along the side walls.

The equations of motion for steady two-dimensional, axisymmetric flow of a fluid with constant density may be written down directly

Continuity
$$\frac{1}{r}\frac{\partial}{\partial r}\left(r V_r\right) = 0 \tag{2.1}$$

Radial Momentum
$$V_r\frac{\partial V_r}{\partial r} - \frac{V_\theta^2}{r} = \frac{-1}{\rho}\frac{\partial P}{\partial r} + \nu\left[\frac{\partial^2 V_r}{\partial r^2} + \frac{1}{r}\frac{\partial V_r}{\partial r} - \frac{V_r}{r^2}\right] \tag{2.2}$$

Tangential Momentum
$$V_r\frac{\partial V_\theta}{\partial r} + \frac{V_r V_\theta}{r} = \nu\left[\frac{\partial^2 V_\theta}{\partial r^2} + \frac{1}{r}\frac{\partial V_\theta}{\partial r} - \frac{V_\theta}{r^2}\right] \tag{2.3}$$

where V_r and V_θ are the velocities in the radial and tangential directions respectively, r is the radius from the axis, P is the static pressure, ρ is the fluid density and ν is the kinematic viscosity.

Equation 2.1 may be integrated directly to give

$$V_r = -\frac{Q}{2\pi r} \tag{2.4}$$

where Q is the volumetric flow rate radially inward per unit length along the axis.

Combining Equations 2.3 and 2.4 yields

$$\frac{d^2V_\theta}{dr^2} + \frac{1}{r}\frac{dV_\theta}{dr}\left[1 + \frac{Q}{2\pi\nu}\right] + \left[\frac{Q}{2\pi\nu} - 1\right]\frac{V_\theta}{r^2} = 0 \tag{2.5}$$

If ν is a constant, then Equation 2.5 has the solution

$$V_\theta = \frac{A}{r} + Br^{1-\frac{Q}{2\pi\nu}} \tag{2.6}$$

Using the Equations 2.4 and 2.6, Equation 2.2 may be rearranged to give:

$$\frac{1}{\rho}\frac{dP}{dr} = \frac{V_\theta^2 + V_r^2}{r} \tag{2.7}$$

Several cases can now be examined. Consider first irrotational flow where $\nu = 0$ and $Q \neq 0$. Then the solution becomes

$$V_r = \frac{-Q}{2\pi r} \tag{2.4}$$

$$V_\theta = \frac{A}{r} \tag{2.8}$$

and Equation 2.7 may be integrated

$$\frac{1}{\rho}\frac{dP}{dr} = \frac{A^2 + \left(\frac{Q}{2\pi}\right)^2}{r^3} \tag{2.9}$$

$$P = P_1 + \frac{\rho\left[A^2 + \left(\frac{Q}{2\pi}\right)^2\right]}{2}\left[\frac{1}{r_1^2} - \frac{1}{r^2}\right] \tag{2.10}$$

where $\rho = \rho_1$ at $r = r_1$. Also,

$$\frac{V_\theta}{V_r} = -\frac{2\pi A}{Q} \tag{2.11}$$

So for irrotational flow $\frac{V_\theta}{V_r}$ will be a constant, and a plot of pressure versus $\frac{1}{r^2}$ will result in a straight line.

For the viscous case, $\nu \neq 0$, neither of these statements are true.

Here,

$$\frac{V_\theta}{V_r} = \frac{-2\pi}{Q}\left[A + B r^{2 - \frac{Q}{2\pi\nu}}\right] \tag{2.12}$$

and

$$\frac{1}{\rho}\frac{d\rho}{dr} = \frac{1}{r^3}\left[A + B r^{2-\frac{Q}{2\pi\nu}} + \left(\frac{Q}{2\pi}\right)^2\right] \tag{2.13}$$

For a flow with unknown viscosity, the viscosity may be determined experimentally from pressure measurements. Equation 2.7 can be rewritten as

$$r V_\theta = \left[r^3 \frac{1}{\rho}\frac{d\rho}{dr} - \left(\frac{Q}{2\pi}\right)^2\right]^{1/2} \tag{2.14}$$

Now note that

$$\frac{1}{r}\frac{d}{dr}\left(r V_\theta\right) = B\left(2 - \frac{Q}{2\pi\nu}\right) r^{-\frac{Q}{2\pi\nu}} \tag{2.15}$$

Therefore

$$\frac{1}{r}\frac{d}{dr}\left[r^3 \frac{1}{\rho}\frac{d\rho}{dr} - \left(\frac{Q}{2\pi}\right)^2\right]^{1/2} = B\left(2 - \frac{Q}{2\pi\nu}\right) r^{-\frac{Q}{2\pi\nu}} \tag{2.16}$$

The left hand side of Equation 2.16 may be calculated from measurement of pressure as a function of radius. Call this function F .

$$F = \frac{1}{r}\frac{d}{dr}\left[r^3 \frac{1}{\rho}\frac{dp}{dr} - \left(\frac{Q}{2\pi}\right)^2\right]^{1/2} \qquad (2.17)$$

If F is plotted against radius, a straight line of slope $-\frac{Q}{2\pi\nu}$ will result. Thus, ν may be determined. Note that for the irrotational case, $F \equiv 0$.

This method can be extended to include the determination of local viscosity where the viscosity varies slowly with radius. F can be evaluated at several radii within a small range and the viscosity can be determined as above.

This experiment is very difficult to perform accurately for several reasons. First, it is difficult to produce a truly axisymmetric flow. In the typical experimental apparatus for vortex-sink flow the fluid enters tangentially through a finite number of vanes. These vanes produce potential effects extending throughout the fluid. In addition, there is some momentum loss associated with friction on the vane surfaces giving wakes within the fluid. Both of these effects produce variations in velocities and pressures which affect the value of the viscosity calculated. Clearly, the difficulty of the problem is decreased as the number of vanes increases.

The second difficulty is that the determination of viscosity involves the calculation of the second derivative of pressure with respect to radius. The calculation of derivatives from discrete data by a finite difference technique involves measuring the differences between experimental data points. If pressures are measured at unit intervals, then the derivatives may be calculated from:

$$\frac{\partial P}{\partial r} = \frac{P_{i+1} - P_i}{\Delta r} \tag{2.18}$$

$$\frac{\partial^2 P}{\partial r^2} = \frac{P_{i+1} + P_{i-1} - 2P_i}{\Delta r} \tag{2.19}$$

If the pressure taps are close together, then the pressure differences measured become the order of magnitude of the experimental errors involved. If the pressure taps are far apart, then the finite difference technique becomes a poor approximation of the derivatives.

The third problem is that it is difficult to construct a vortex-sink combination that does not exhibit three-dimensional effects. If the axial separation of the walls is small, then the side-wall boundary layer will dominate the flow; if large, then it is difficult to maintain uniform flow along the entire length, and slight non-uniformities may result in radial circulating currents. The problem of the side-wall boundary layer is discussed in the next section.

2. Side-Wall Boundary Layer

Background

If a potential vortex and sink is created between two flat parallel plates, there will be a pressure gradient generated as shown in Equation 2.9. In the main flow, this gradient is balanced by the momentum of the rotating flow. However, the fluid in the boundary layers on the side walls is moving much slower than the main fluid, hence, the pressure gradient will tend to accelerate the boundary layer flow inward. Thus, a three-dimensional boundary layer with secondary flow is produced. This secondary flow tends to entrain some of the normal potential radial flow from the main stream, thus altering its characteristics. If the total radial flow is small to begin with, it is

possible that all of the radial flow will occur as secondary flow in the wall boundary layers or even radial outflow could occur in the middle of the channel. Clearly the ratio of circulation to radial flow, or $\frac{V_\theta}{V_r}$, must play a major role in determining the effect of the boundary layer on the main flow.

The velocity of the fluid locally in the boundary layer may be resolved into two parts (the radial velocity and the tangential velocity), just as in the main flow. The tangential component can be expected to drop from the free stream value to zero in a monotonic fashion due to friction on the wall. The radial component of velocity can also be expected to go from the free stream value to zero on the wall due to friction. However, it will not be a monotonic function due to the accelerating effect of the pressure gradient. If the tangential velocity in the free stream is assumed to be several times the radial velocity, then the radial acceleration due to pressure gradient will be largest where the tangential velocity is smallest (i.e., at the wall). This results in a radial velocity component which may be larger than in the free stream. Now these two effects (first the friction acting on the radial velocity and second the friction acting on the tangential velocity and the response of the radial velocity to the resultant reduction in momentum) are really two independent effects. For flow over a flat plate, the rate of growth of the boundary layer is a function of the free stream velocity. Different free stream velocities result in different growth rates. Similarly, it is expected that the growth of the boundary layers due to the two effects mentioned above would be different due to the different magnitudes of the velocity components.

Several investigators have studied flows quite similar to the one examined here. All have used the momentum integral method introduced by von Karman. Taylor (1950) examined the problem of a swirl atomizer where flow enters a conical chamber tangentially at the large end and passes out an orifice located at the small end. The problem of flow over a flat plate is a special case where the cone angle is 180°. He assumed zero radial flow and a potential vortex for the main flow. He also assumed that the boundary layer thicknesses in the radial and tangential directions were the same.

Cooke (1952) extended Taylor's method to include two boundary layer thicknesses, but still assumed that the main flow had zero radial velocity. Cooke stated, "The algebraic and numerical work is heavy".

Mack (1962, 1963) extended Taylor's work to include free stream velocities of the form $V_\theta \propto \frac{1}{r^n}$ with $V_r = 0$ for a flat plate. Like Taylor, he used only one boundary layer thickness.

Lewellen and Rott (1966) discussed a solution similar to Mack's and attempted to predict circulation reduction in the main flow. A second report by Lewellen (1971) gives an excellent summary of all of the work to date and attempts to treat the turbulent case as an extension of the laminar case with a different form of wall friction.

Method of Solution

The method used here is similar to that of Cooke in that two separate boundary layer thicknesses are used, but, in addition, the flow outside the boundary layer is taken as a two-dimensional potential vortex and sink. It will be seen that this added condition of having

the radial velocity in the main flow non-zero greatly increases the complexity of the solution.

The equations of motion for the boundary layer may be written directly and simplified using the usual boundary layer approximations. Taking the axial direction as X ,

Continuity
$$\frac{1}{r}\frac{\partial}{\partial r}\left(r V_r\right) + \frac{\partial V_x}{\partial x} = 0 \tag{2.20}$$

Radial Momentum
$$\frac{\partial}{\partial r}\left(V_r^2\right) + \frac{1}{r}\left(V_r^2 - V_\theta^2\right) + \frac{\partial}{\partial x}\left(V_r V_x\right) = \nu \frac{\partial^2 V_r}{\partial x^2} - \frac{1}{\rho}\frac{dP}{dr} \tag{2.21}$$

Tangential Momentum
$$\frac{\partial}{\partial r}\left(V_r V_\theta\right) + \frac{\partial}{\partial x}\left(V_x V_\theta\right) + \frac{2 V_r V_\theta}{r} = \nu \frac{\partial^2 V_\theta}{\partial x^2} \tag{2.22}$$

The equation of motion in the axial direction has been neglected. Now integrate these equations across the boundary layer, taking the boundary layer thickness as δ and letting all the velocities equal zero at $X = 0$. The continuity equation, Equation 2.20, becomes:

$$V_x\Big|_\delta = -\frac{1}{r}\frac{d}{dr}\left[r\int_0^\delta V_r\, dx\right] + V_r\Big|_\delta \frac{d\delta}{dr} \tag{2.23}$$

This may be used to simplify the integrated radial and tangential equations. The results after some manipulation are:

$$\frac{1}{r}\frac{d}{dr}\left[r\int_0^\delta V_r^2\, dx\right] - \frac{1}{r}\int_0^\delta V_\theta^2\, dx - \frac{V_r|_\delta}{r}\frac{d}{dr}\left[r\int_0^\delta V_r\, dx\right] = \tag{2.24}$$

$$\nu\left[\frac{\partial V_r}{\partial x}\Big|_\delta - \frac{\partial V_r}{\partial x}\Big|_0\right] - \frac{\delta}{\rho}\frac{dP}{dr}$$

$$\frac{1}{r^2}\frac{d}{dr}\left[r^2\int_0^{\delta} V_r V_\theta \, dx\right] - \frac{V_\theta|_\delta}{r}\frac{d}{dr}\left[r\int_0^{\delta} V_r \, dx\right] = \nu\left[\frac{dV_\theta}{dx}\bigg|_\delta - \frac{dV_\theta}{dx}\bigg|_0\right] \tag{2.25}$$

The flow outside the boundary layer is taken as a potential vortex and sink so that if $V_{\theta\infty}$ and $V_{r\infty}$ are the components of velocity outside the boundary layer

$$V_{\theta\infty} = \frac{\Gamma}{2\pi r} \tag{2.26}$$

$$V_{r\infty} = \frac{-Q}{2\pi r} \tag{2.27}$$

where Γ and Q are the circulation and flow rate per unit thickness. Now define δ_θ as the boundary layer thickness associated with the tangential velocity and the component of the radial velocity due to the pressure gradient, and δ_r as the boundary layer thickness associated with the frictional part of the radial velocity profile. The boundary conditions on the velocity profiles are

$$V_\theta = 0\,, \quad V_r = 0 \qquad AT \quad X = 0$$

$$V_\theta = V_{\theta\infty}, \; V_r = V_{r\infty} \qquad FOR \quad X > \delta_\theta \; AND \; \delta_r$$

An additional condition can be found by putting $X = 0$ in the tangential momentum equation, Equation 2.22, with the result $\frac{d^2 V_\theta}{dx^2}\Big|_{x=0} = 0$. These conditions are satisfied by

$$V_\theta = V_{\theta\infty} F\left(\frac{x}{\delta_\theta}\right) \tag{2.28}$$

$$V_r = V_{r\omega}\left[F\left(\frac{x}{\delta_r}\right) + \beta G\left(\frac{x}{\delta_\theta}\right)\right] \tag{2.29}$$

where

$$F(\xi) = 2\xi - 2\xi^3 + \xi^4 \qquad 0<\xi<1, \quad F(\xi)=1 \quad \xi>1 \tag{2.30}$$

$$G(\xi) = \frac{1}{6}\xi(1-\xi)^3 \qquad 0<\xi<1, \quad G(\xi)=0 \quad \xi>1 \tag{2.31}$$

β may be determined by solving the radial momentum equation, Equation 2.21, at $X = 0$.

$$\beta = \frac{Q}{2\pi U}\left(\frac{\delta_\theta}{r}\right)^2\left[\left(\frac{\Gamma}{Q}\right)^2 + 1\right] \tag{2.32}$$

Figure II.1 is a plot of V_θ and V_r with $\frac{\delta_r}{\delta_\theta}$ taken as 0.3 and β taken as 200. Note that the "hump" part of the radial velocity is produced by a term involving δ_θ and not δ_r. Also note that at $X=\delta_\theta$ $\frac{\partial V_\theta}{\partial x} = 0$, and at $X = \delta_\theta$ $\frac{\delta_r}{\delta_\theta} < 1$ or $X = \delta_r$ $\frac{\delta_r}{\delta_\theta} > 1$, $\frac{\partial V_r}{\partial x} = 0$. Consequently, the terms involving $\frac{\partial V_\theta}{\partial x}\Big|_\delta$ and $\frac{\partial V_r}{\partial x}\Big|_\delta$ in Equations 2.24 and 2.25 are zero. This means that there is no momentum exchange due to friction with the main flow.

The values of V_θ and V_r from Equations 2.28 and 2.29 are now substituted into Equations 2.24 and 2.25. The integrals can be evaluated providing that the relative magnitudes of δ_θ and δ_r are known. It will be shown later that δ_r is always less than δ_θ. Defining $\gamma = \frac{\delta_r}{\delta_\theta}$, the equations, after some manipulations, become:

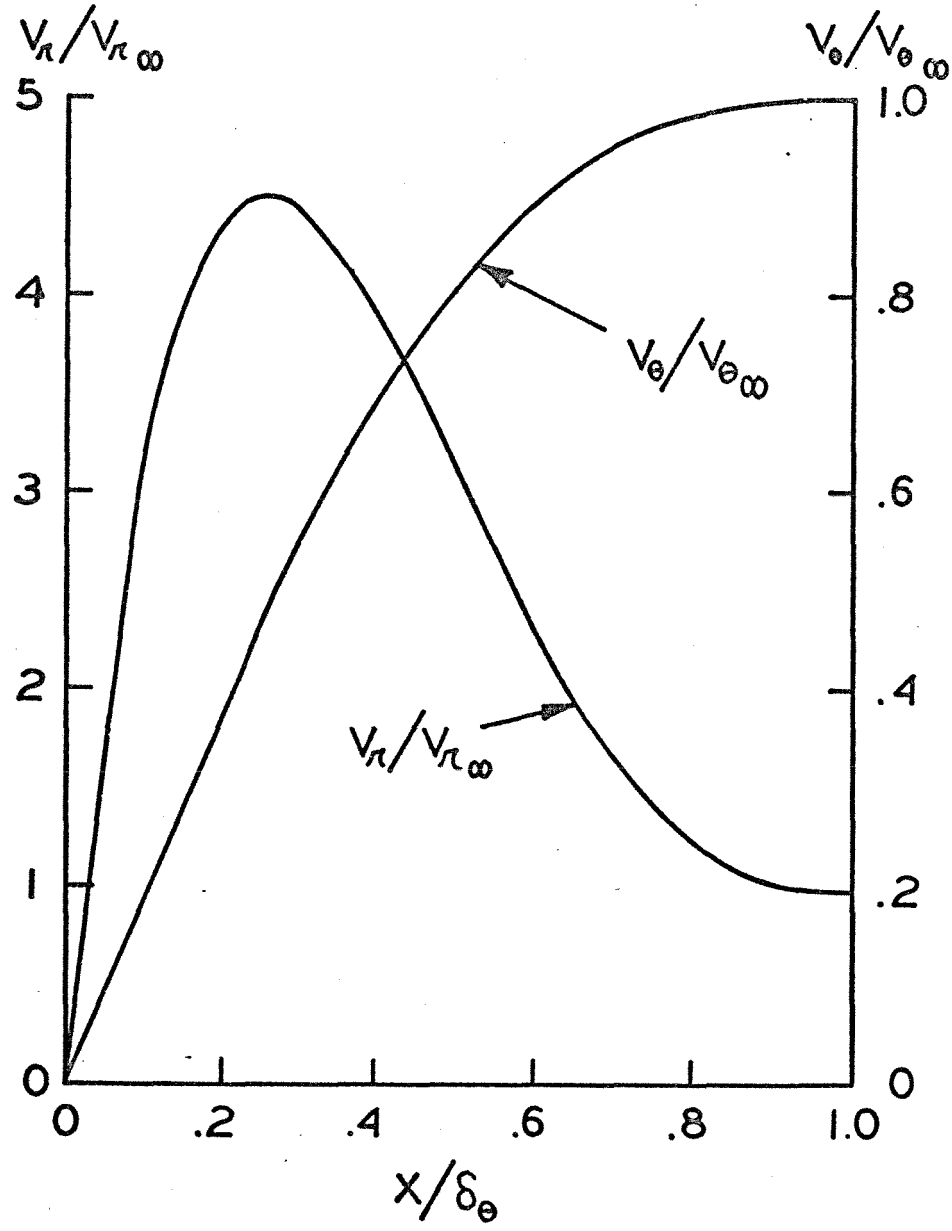

Figure II.1. Velocity Profiles Within Boundary Layer.

$$\frac{d}{d\eta}\left\{\delta_\theta\left[-\beta^2\int_0^1 G^2(\xi)\,d\xi+\beta\gamma\left(\int_0^1 G(\gamma\xi)\,d\xi-2\int_0^1 G(\gamma\xi)F(\xi)\,d\xi\right)\right.\right.$$
$$\left.\left.+\gamma\left(\int_0^1 F(\xi)\,d\xi-\int_0^1 F^2(\xi)\,d\xi\right)-\beta\int_\gamma^1 G(\xi)\,d\xi\right]\right\} \qquad (2.33)$$
$$+\delta_\theta\left[\frac{\Gamma^2}{Q^2}\left(\int_0^1 F^2(\xi)\,d\xi-1\right)+\gamma\int_0^1 F^2(\xi)\,d\xi+\beta^2\int_0^1 G^2(\xi)\,d\xi-\gamma\right.$$
$$\left.+2\beta\gamma\int_0^1 G(\gamma\xi)F(\xi)\,d\xi+2\beta\int_\gamma^1 G(\xi)\,d\xi\right]=\frac{-1}{\frac{Q}{2\pi v}\frac{\delta_\theta}{\eta}}\left[\frac{2}{\gamma}+\frac{\beta}{6}\right]$$

and tangential

$$\frac{d}{d\eta}\left\{\delta_\theta\left[\beta\left(\int_0^1 G(\xi)\,d\xi-\int_0^1 F(\xi)G(\xi)\,d\xi\right)+1-\int_\gamma^1 F(\xi)\,d\xi\right.\right.$$
$$\left.\left.+\gamma\left(\int_0^1 F(\xi)\,d\xi-\int_0^1 F(\gamma\xi)F(\xi)\,d\xi-1\right)\right]\right\}=\frac{-2}{\frac{Q}{2\pi v}\frac{\delta_\theta}{\eta}} \qquad (2.34)$$

The integrals in these equations can be evaluated from Equations 2.30 and 2.31. They become merely power series in γ. Evaluating the integrals, performing the differentiation, and defining $\zeta^2=\frac{Q}{2\pi v}\left(\frac{\delta_\theta}{\eta}\right)^2$ and $Y=\frac{\eta}{\eta_0}$ yields

Tangential

$$\frac{Y}{2}\frac{d(\zeta^2)}{dY}\left\{\frac{11}{1008}\left[\left(\frac{\Gamma}{Q}\right)^2+1\right]\zeta^2+\frac{3}{10}-\frac{3}{10}\gamma+\frac{2}{15}\gamma^2-\frac{3}{140}\gamma^4+\frac{1}{180}\gamma^5\right\}$$
$$+Y\zeta^2\frac{d\gamma}{dY}\left\{-\frac{3}{10}+\frac{4}{15}\gamma-\frac{3}{35}\gamma^2+\frac{1}{36}\gamma^4\right\}= \qquad (2.35)$$
$$-\frac{11}{3024}\left[\left(\frac{\Gamma}{Q}\right)^2+1\right]\zeta^4-\left[\frac{3}{10}-\frac{3}{10}\gamma+\frac{2}{15}\gamma^2-\frac{3}{140}\gamma^4+\frac{1}{180}\gamma^5\right]\zeta^2-2$$

Radial

$$\frac{Y}{2}\frac{d\zeta^2}{dY}\left\{-\frac{5}{9072}\left[\left(\frac{\Gamma}{Q}\right)^2+1\right]\zeta^4+\left[-\frac{1}{90}+\frac{1}{15}\gamma^2-\frac{1}{14}\gamma^3-\frac{9}{280}\gamma^4-\frac{1}{180}\gamma^5\right]\left[\left(\frac{\Gamma}{Q}\right)^2+1\right]\zeta^2\right\}$$

$$+Y\zeta^2\frac{d\gamma}{dY}\left\{\left[\left(\frac{\Gamma}{Q}\right)^2+1\right]\left[\frac{2}{45}\gamma-\frac{1}{14}\gamma^2+\frac{3}{70}\gamma^3-\frac{1}{108}\gamma^4\right]\zeta^2+\frac{37}{315}\right\}= \tag{2.36}$$

$$-\frac{1}{120}\left[\left(\frac{\Gamma}{Q}\right)^2+1\right]\zeta^4+\left\{\frac{79}{315}\left[\left(\frac{\Gamma}{Q}\right)^2+1\right]+\frac{3}{10}\gamma-\frac{263}{630}\right\}\zeta^2-\frac{2}{\gamma}$$

The algebra required in performing the above steps is straightforward, but tedious.

These equations point out several features of this analysis. First, the term $\left[\left(\frac{\Gamma}{Q}\right)^2+1\right]$ is the only way in which the conditions of the main flow affect the solution. Since $\left[\left(\frac{\Gamma}{Q}\right)^2+1\right]$ occurs only in some terms, its value will determine the solution, and a different numerical integration must be performed for each value.

Second, since δ_θ and $\frac{Q}{2\pi\nu}$ never occur explicitly, but always in the form $\zeta^2=\left(\frac{\delta_\theta}{r}\right)^2\frac{Q}{2\pi\nu}$ it follows that a solution for one value of $\left[\left(\frac{\Gamma}{Q}\right)^2+1\right]$ will be valid for all values of flow rate, viscosity, and size of apparatus.

Third, the factor $\frac{Q}{2\pi\nu}$ is effectively a Reynolds number. Since Q is the flow rate per unit thickness in the main flow,

$$Q=2\pi r V_{r\infty} \tag{2.37}$$

$$\frac{Q}{2\pi\nu}=\frac{rV_{r\infty}}{\nu} \tag{2.38}$$

Thus, this Reynolds number is based on radius and radial velocity.

Equations 2.35 and 2.36 are a pair of first order, linear differential equations with variable coefficients of the form

Tangential $$A\frac{\partial \zeta^2}{\partial Y} + B\frac{\partial \gamma}{\partial Y} = C \tag{2.39}$$

Radial $$D\frac{\partial \zeta^2}{\partial Y} + E\frac{\partial \gamma}{\partial Y} = F \tag{2.40}$$

where A, B, C, D, E, and F are functions of Y, ζ^2, γ, and $\left[\left(\frac{\Gamma}{\varphi}\right)^2+1\right]$.

These equations can be rearranged so that

$$\frac{\partial \zeta^2}{\partial Y} = \frac{CE-BF}{AE-BD} \tag{2.41}$$

$$\frac{\partial \gamma}{\partial Y} = \frac{AF-CD}{AE-BD} \tag{2.42}$$

Equations 2.41 and 2.42 may be integrated numerically from $\zeta = 0$. The initial conditions appropriate here are $\delta_\theta = 0$ and $\delta_\eta = 0$ at $Y = 1$. The proper value of γ may be determined by evaluating Equations 2.35 and 2.36 for small values of ζ. The result is $\gamma = 1.0$.

However, the initial condition for $\frac{\partial \gamma}{\partial Y}$ requires a further expansion of Equations 2.35 and 2.36 to second order terms. The result is that $\frac{\partial \gamma}{\partial Y}$ is negative and provides a satisfactory starting point for the numerical process.

The numerical work was carried out for $\frac{V_{\theta\infty}}{V_{\eta\infty}} = 15$. This value was chosen because it could easily be produced in the experimental apparatus described later. The viscosity was taken as that of water at room temperature.

After the solution had progressed a short distance, the denominator in Equations 2.41 and 2.42 went to zero. This means that Equations 2.39 and 2.40 were essentially the same and that only one of $\frac{\partial \zeta^2}{\partial Y}$ or $\frac{\partial \gamma}{\partial Y}$ could be obtained. The solution was continued by choosing

a fixed value of γ such that the solutions of the two equations were approximately the same. The best value of γ turned out to be $\gamma = 0.3$.

Figure II.2 is a graph of $\zeta Y = \frac{\delta_\theta}{r_0}\left(\frac{Q}{2\pi v}\right)^{1/2}$ against Y. The point at which the solution broke down was at $Y = 0.98$. For $Y < 0.98$ the two lines are the solutions to the radial and tangential equations with $\gamma = 0.3$. Note that γ starts off at 1.0 and drops rapidly to 0.3 at $Y = 0.98$ and continues at $\gamma = 0.3$ for the rest of the solution. However, the solutions were not sensitive to the value of γ. Following the same method, a solution to the problem with $\Gamma = 0$ was obtained. In this case, the "hump" in the radial velocity profile goes to zero and only one boundary layer thickness, $\delta = \delta_r$, remains. These simplifications give an equation which can be integrated directly. The result is:

$$\zeta^2 = \left(\frac{\delta}{r}\right)^2 \frac{Q}{2\pi v} = \frac{20}{3}\left[1 - Y^{\frac{189}{37}}\right] \tag{2.43}$$

Comparison of Results With Other Investigators

Both of these solutions are similar in form to those of Taylor and Cooke. Both Taylor and Cooke assumed that $Q = 0$ in the main flow and found that the solution could be expressed as

$$F(Y) = \left(\frac{\delta}{r}\right)^2 \frac{\Gamma}{2\pi v} \tag{2.44}$$

For Taylor's work, $\delta_r = \delta_\theta$, and for Cooke's work $\frac{\delta_r}{\delta_\theta} = \gamma > 1$ and

$$\gamma = \gamma(Y) \tag{2.45}$$

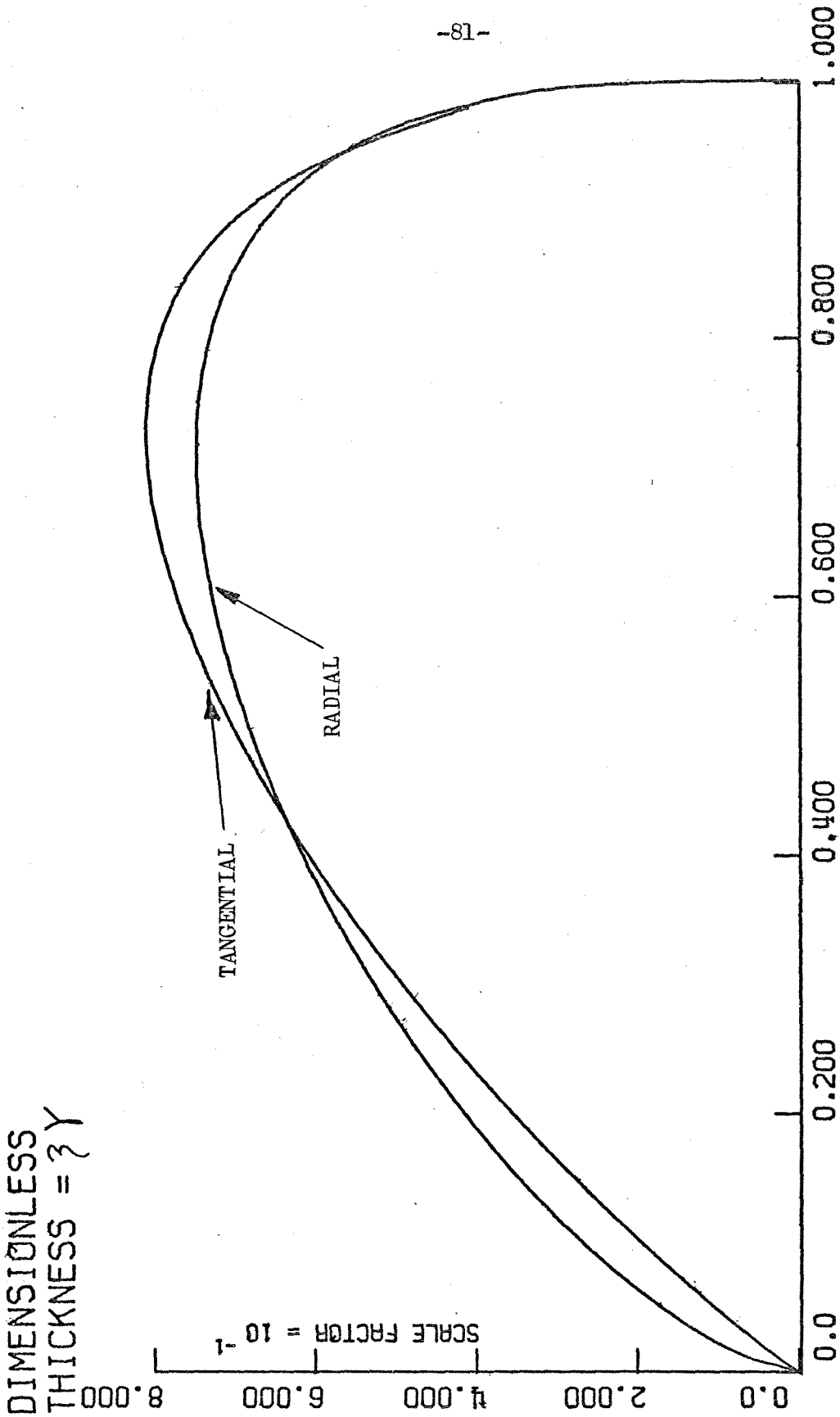

Figure II.2. Results of Numerical Integration.

In the present work the case of $\Gamma = 0$ gave

$$\zeta^2(\gamma) = \left(\frac{\delta}{r}\right)^2 \frac{Q}{2\pi\nu} \tag{2.46}$$

and the case of $\frac{\Gamma}{Q} \neq 0$ gave

$$\zeta^2\left(\gamma, \frac{\Gamma}{Q}\right) = \left(\frac{\delta_e}{r}\right)^2 \frac{Q}{2\pi\nu} \tag{2.47}$$

Thus, all results are of the same form. Figure II.3 is a plot of $\frac{\delta}{r_o}\left(\frac{\Gamma}{2\pi\nu}\right)^{1/2}$ for all of the work mentioned above. The plot for the case of $\frac{\Gamma}{Q} = 0$ was evaluated by noting that

$$\frac{\delta}{r_o}\left(\frac{\Gamma}{2\pi\nu}\right)^{1/2} = \frac{\delta}{r_o}\left(\frac{Q}{2\pi\nu}\right)^{1/2}\left(\frac{\Gamma}{Q}\right)^{1/2} \tag{2.48}$$

and letting $\frac{\Gamma}{Q} = 15$. In effect, this is equivalent to evaluating the solution at the same radial flow rate as the case where $\frac{\Gamma}{Q} = 15$ for comparison with the rest of the results. Alternately the graph could be expressed as $\frac{\delta}{r_c}\left(\frac{Q}{2\pi\nu}\right)^{1/2}$ as a function of γ, but that would require a similar argument to the one above for the case where $\frac{\Gamma}{Q} = \infty$.

Figure II.3 shows that the value of $\frac{\Gamma}{Q}$ does indeed play a significant role in determining the boundary layer thickness. If one considers Cooke's solution to be more precise than Taylor's due to the additional variable γ, then the result is that decreasing $\frac{\Gamma}{Q}$ from infinity to 15 holding Γ constant results in a slight thickening of the overall boundary layer. In addition, further decreasing $\frac{\Gamma}{Q}$ to zero holding Q constant results in almost doubling the boundary layer thickness.

Another comparison to the work of other investigators can be made by considering the amount of flow in the boundary layer. Defining

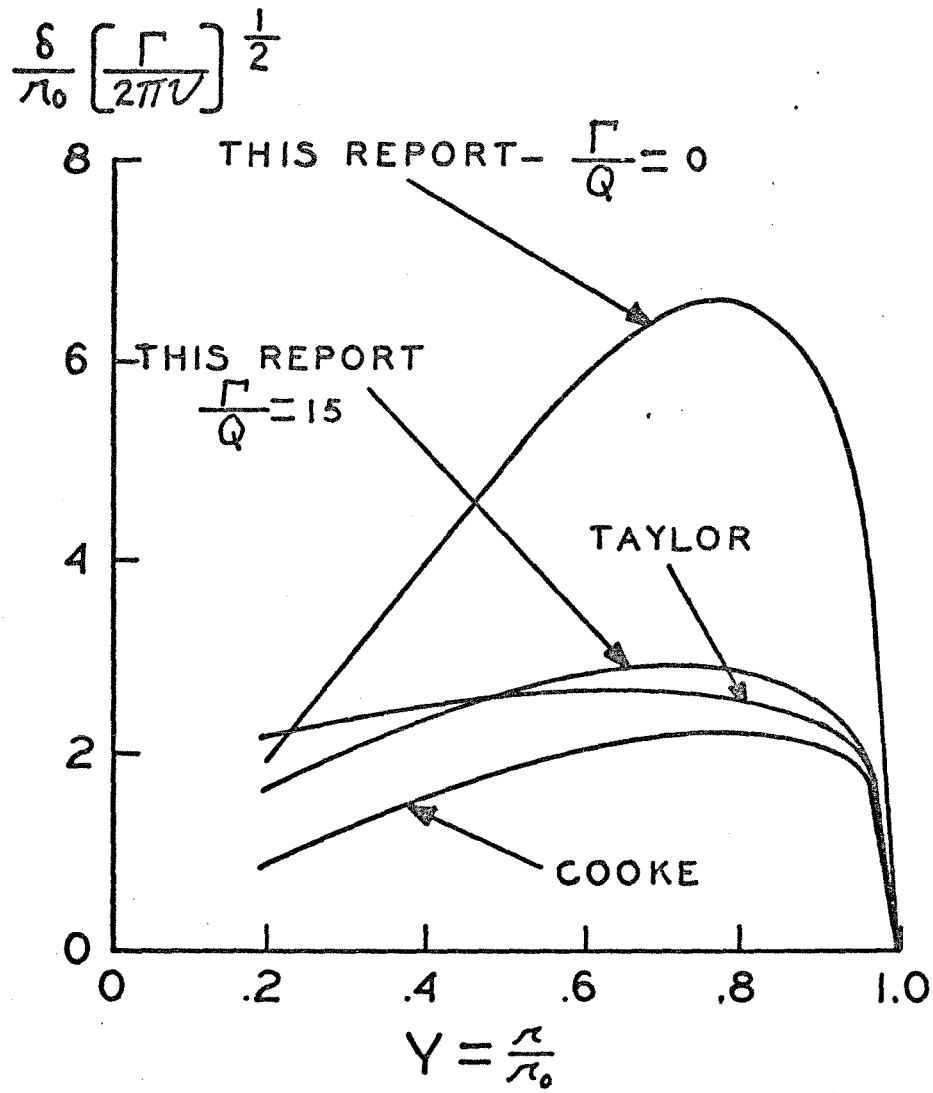

Figure II.3. Comparison of Boundary Layer Thicknesses from Several Investigators.

this flow as Q_B ;

$$Q_B = -2\pi r \int_0^{\delta} V_r \, dx \tag{2.49}$$

and using the form of V_r from Equation 2.29,

$$Q_B = -2\pi r \, V_{r\infty} \int_0^{\delta} \left[F\left(\frac{x}{\delta_r}\right) + \beta G\left(\frac{x}{\delta_\theta}\right) \right] dx \tag{2.50}$$

Evaluating the integral, one finds

$$Q_B = Q \, \delta_\theta \left\{ 1 - \frac{3}{10}\gamma + \frac{1}{120}\left[\left(\frac{\Gamma}{Q}\right)^2 + 1 \right] \gamma^2 \right\} \tag{2.51}$$

which can be put into the form

$$\frac{Q_B}{\Gamma r_0} \left(\frac{\Gamma}{2\pi\nu}\right)^{1/2} = \left(\frac{Q}{\Gamma}\right)^{1/2} Y \left\{ 1 - \frac{3}{10}\gamma + \frac{1}{120}\left[\left(\frac{\Gamma}{Q}\right)^2 + 1 \right] \gamma^2 \right\} \tag{2.52}$$

Lewellen, assuming $\frac{\Gamma}{Q} = \infty$, found for the laminar case,

$$\frac{Q_B}{\Gamma r_0} \left(\frac{\Gamma}{2\pi\nu}\right)^{1/2} = 1.26 \left[1 - Y^{4/3} \right]^{3/4} \tag{2.53}$$

and for the turbulent case

$$\frac{Q_B}{\Gamma r_0} \left(\frac{\Gamma}{2\pi\nu}\right)^{1/2} = 0.1323 \left(\frac{\Gamma}{2\pi\nu}\right)^{0.3} \left[1 - Y \right] \tag{2.54}$$

Figure II.4 is a plot of Equations 2.52, 2.53, and 2.54. Note the close agreement of the results for the laminar cases. For the turbulent case it has been assumed that $\frac{\Gamma}{2\pi\nu}$ = 500. The turbulent case is somewhat suspect due to the uncertainties in the expression Lewellen used for wall shear stress.

The results of a specific example have been worked out. It is assumed that the boundary layer starts at zero thickness at a 12-inch radius, the fluid is water flowing at 100 G.P.M., the axial length of

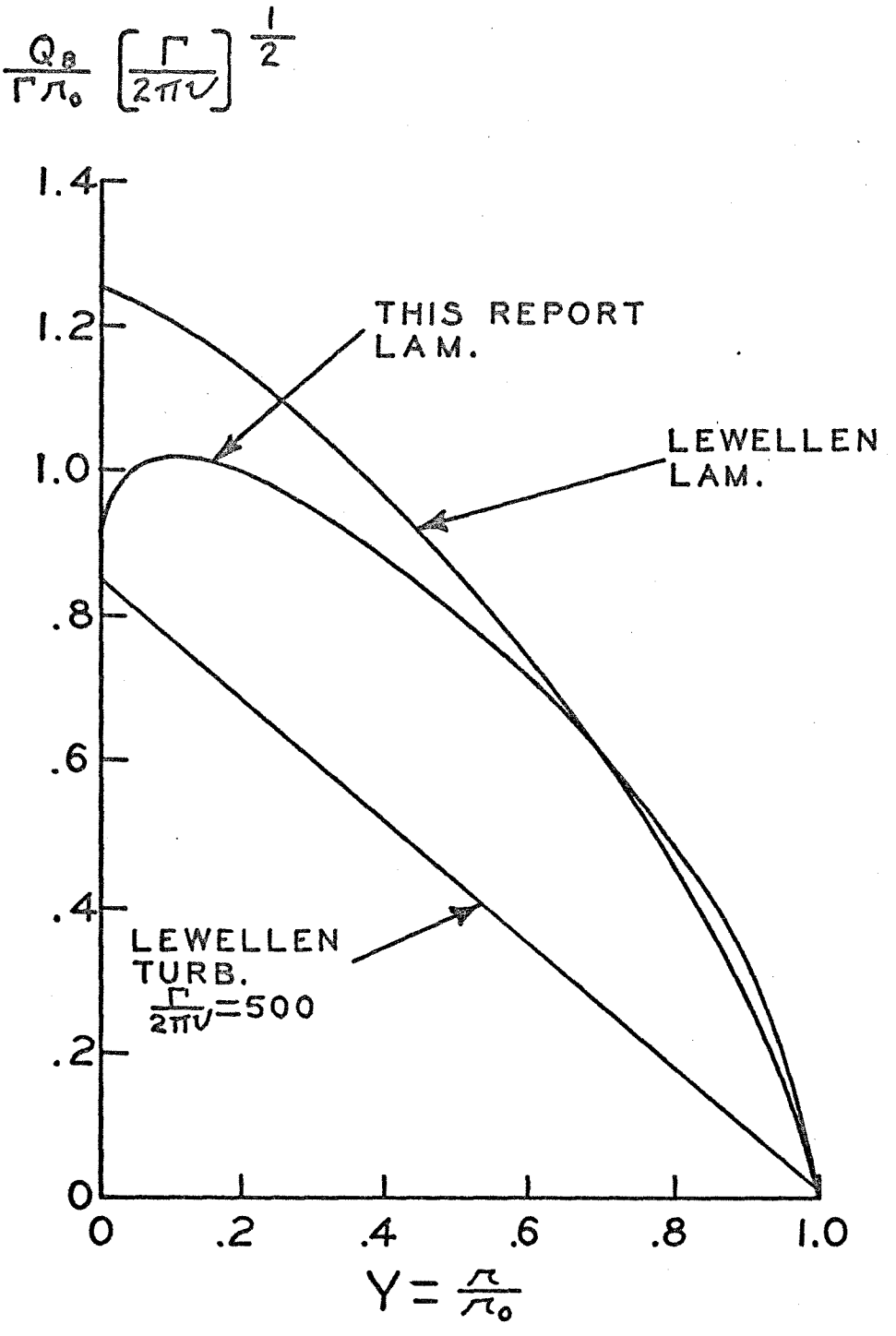

Figure II.4. Radial Flow in the Boundary Layer.

the chamber is 1.6 inches, and that $\frac{\Gamma}{Q} = 15$. The important parameters are:

$$r_o = 12 \quad \text{INCHES}$$

$$\frac{\Gamma}{Q} = 15$$

$$\frac{Q}{2\pi\nu} = 2.47 \times 10^4$$

The results have been expressed as: the boundary layer thickness, δ_θ, as a function of reduced radius, Y; the ratio of flow in the boundary layer, Q_B, to the total flow rate as a function of Y; and the ratio of maximum radial velocity in the boundary layer to the radial velocity in the main flow, $V_{r\infty}$, as a function of Y. Figure II.5 graphs these results.

As expected, the maximum radial velocity in the boundary layer is always greater than the free stream value, and even though the tangential velocity is 15 times as great as the radial velocity in the free stream, the radial velocity in the boundary layer may be equal or greater than the tangential velocity in the free stream. For this problem the secondary flow, Q_B, approaches 20 percent of the total flow rate for low values of Y. Thus, the phenomenon of zero or outward radial flow in the main flow, due to large secondary flow, does not occur. The boundary layer thickness is seen to grow rapidly and reach a maximum of about 0.06 inch, which is still small compared to the gap between the walls of the chamber.

In summary, the investigation of laminar vortex-sink flow between parallel plates shows that there are two separate regions of

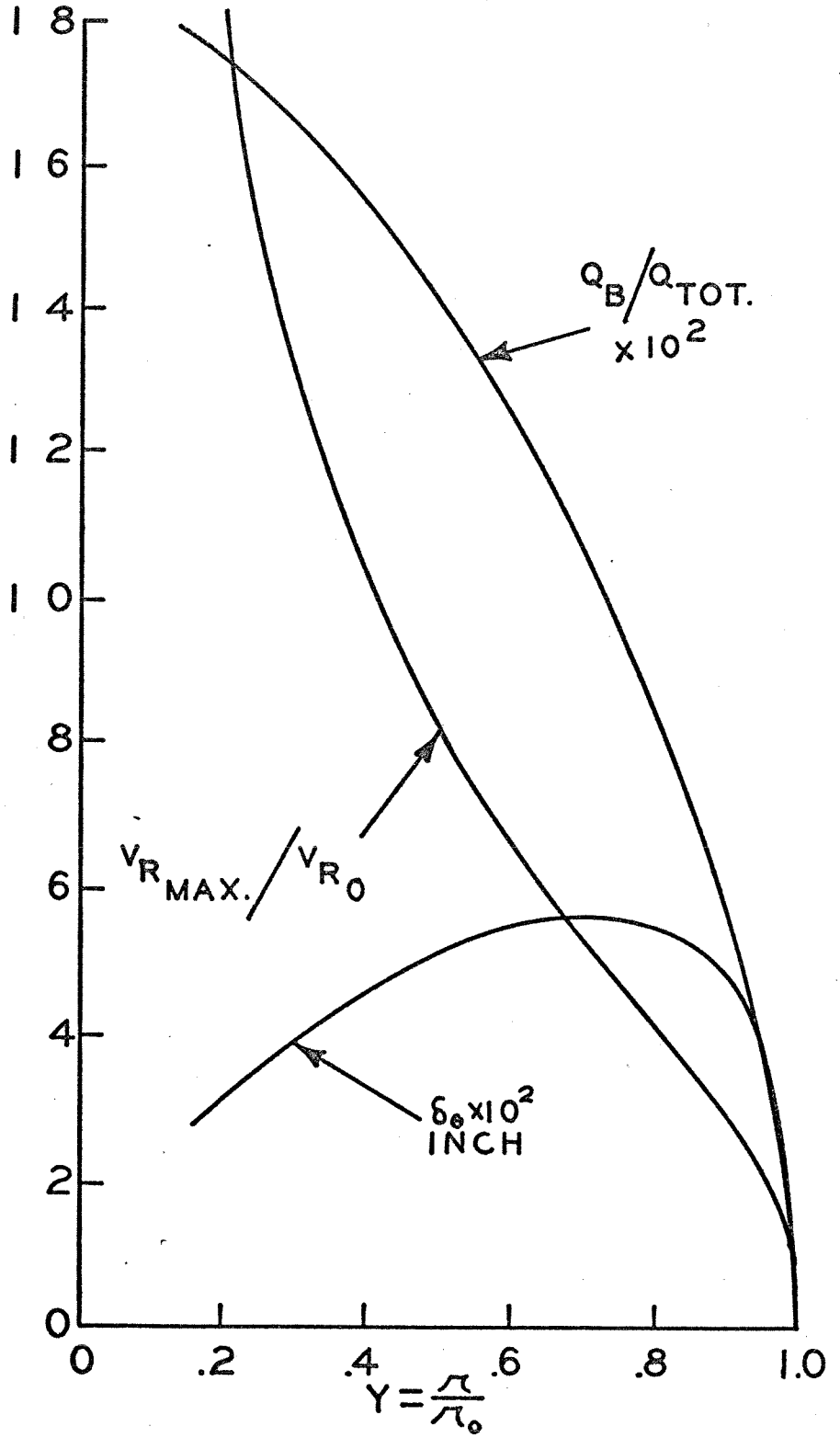

Figure II.5. Boundary Layer Characteristics for a Specific Problem.

flow. The main flow consists of a two-dimensional solution to the equations of motion and results in essentially constant circulation for low viscosity.

The secondary flow consists of strong radial flow in the boundary layers along the flat plate sides. This flow can be quite large depending upon the particular case analyzed.

It is important to note that although the solution obtained here compares closely with similar analyses carried out by other investigators, it is limited in application. There are two reasons why the solution may be unsatisfactory.

First, in the course of the analysis, it was assumed that at the outside of the boundary layer, the shear rates vanished. Thus the only means by which the main flow can exchange momentum with the boundary layer is entrainment. This means that the circulation in the main flow can never change (except through viscous shear stresses acting on cylindrical surfaces). It will be seen later in the experimental work that the circulation does change for flow without particles thus casting suspicion on the analysis here.

Second, the analysis here is only valid for laminar flow. Rosenhead (1963) in his book on laminar boundary layers has stated some criteria for transition to turbulent flow based on three-dimensional boundary layers on swept wings. Converting his notation to the notation used here, it is found that transition is expected when the parameter $\frac{V_{R\,MAX}\,\delta_\theta}{\nu} = 175$. In the example studied above, this occurs at $y \approx 0.95$. Thus, based on this criterion, nearly the whole flow would be turbulent.

Also, Lewellen (1971) states that turbulent flow is expected in a confined vortex when, in our notation, $\frac{\Gamma}{2\pi\nu} > 1.5\times10^{4}$. In the problem worked here, $\frac{\Gamma}{2\pi\nu} = 3.7\times10^{5}$. So turbulent flow is predicted by this criterion also.

An analysis for turbulent flow was not attempted since uncertainties associated with the shear stress terms make any turbulent analysis, such as Lewellen's, of questionable validity.

B. Behavior of Single Particles in Vortex-Sink Flow

1. Particle Orbits at Equilibrium

This section is devoted to a study of the behavior of a particle in vortex-sink flow where the viscous forces (except for viscous drag on the particle) are zero. First the equilibrium orbit of a particle will be obtained by making a force balance. In the next section the stability of this orbit will be considered.

If a particle were allowed to move with the local tangential velocity along a circle of constant radius, it would see a radial velocity inward. The drag of the radial flow on the particle would generate a force inward, but since the particle is moving in a circle, there is an acceleration force outward. If conditions were just right, no additional forces would be necessary for the particle to move in this circular orbit. The three identifiable forces acting on the particle are as follows.

First, since the particle is moving in a circle, there is an acceleration force, F_A, such that:

$$F_A = \rho_s \frac{4}{3}\pi a^3 \frac{V_\theta^2}{r} \tag{2.55}$$

where ρ_s is the particle density, a is the particle radius, V_θ is the local tangential velocity at r, the radius of the orbit.

Second, if C_D is the drag coefficient, ρ_f is the fluid density, and V_r is the local radial velocity, then the drag force is:

$$F_D = C_D \frac{1}{2} \rho_f V_r^2 \pi a^2 \tag{2.56}$$

It has been assumed here that the particle is small so that the radial velocity V_r is essentially constant over the particle.

The third force is the force due to pressure. This may be evaluated by integrating the force due to pressure over the surface of the particle. Since the flow is assumed irrotational, Equation 2.10 gives the local pressure, and the resultant force may be expressed as

$$F_p = 2\pi \rho_f (V_\theta^2 + V_r^2) r^2 \frac{a}{r} \left\{ \frac{1}{\frac{a}{r}\left[1 - \left(\frac{a}{r}\right)^2\right]^{1/2}} \tan^{-1}\left[\frac{\frac{a}{r}}{\left[1 - \left(\frac{a}{r}\right)^2\right]^{1/2}} \right] - 1 \right\} \tag{2.57}$$

If $\frac{a}{r}$ is small then

$$F_p = -\left[\frac{4}{3}\pi a^3\right]\left[\frac{\rho_f (V_\theta^2 + V_r^2)}{r}\right]\left[1 + \frac{4}{5}\left(\frac{a}{r}\right)^2 + \cdots\right] \tag{2.58}$$

The first factor is the volume of the particle. The second factor is the pressure gradient at the center of the particle, and the third factor contains corrections for the variation of the pressure gradient over the particle.

Taking a first order approximation of this equation and summing all of the forces yield:

$$\rho_s \frac{4}{3}\pi a^3 \frac{V_\theta^2}{r} - C_D \frac{1}{2} \rho_f V_r^2 \pi a^2 - \left(\frac{4}{3}\pi a^3\right)\left[\frac{\rho_f (V_\theta^2 + V_r^2)}{r}\right] = 0 \tag{2.59}$$

After some rearrangement this becomes

$$C_D = \frac{8}{3}\frac{a}{r}\left[\left(\frac{V_\theta}{V_r}\right)^2\left(\frac{\rho_s}{\rho_L}-1\right)-1\right] \tag{2.60}$$

Now for laminar flow in the vortex, C_D will be close to the drag coefficient of a single particle in an infinite medium. So C_D will be a function of the Reynolds number of flow over the sphere.

$$C_D = C_D\left(\frac{2aV_r}{\nu}\right) \tag{2.61}$$

or

$$C_D = C_D\left[\left(\frac{rV_r}{\nu}\right)\left(\frac{2a}{r}\right)\right] \tag{2.62}$$

where we introduce the Reynolds number $\frac{Q}{2\pi\nu}$ (see Equation 2.38).

Rearranging Equation 2.60;

$$\frac{r}{a} = \frac{8}{3}\frac{\left(\frac{V_\theta}{V_r}\right)^2\left(\frac{\rho_s}{\rho_L}-1\right)-1}{C_D\left[\left(\frac{Q}{2\pi\nu}\right)\left(\frac{2a}{r}\right)\right]} \tag{2.63}$$

This equation determines the equilibrium particle position as a function of the vortex parameters. Implicit in this analysis is $\frac{r}{a} >> 1$. It is clear that no equilibrium orbit exists when the numerator of Equation 2.63 is zero or negative. So for equilibrium orbits:

$$\left(\frac{V_\theta}{V_r}\right)^2\left(\frac{\rho_s}{\rho_L}-1\right)-1 > 0 \tag{2.64}$$

or

$$\frac{\rho_s}{\rho_L} > 1 + \left(\frac{V_r}{V_\theta}\right)^2 \tag{2.65}$$

It is obvious that particles that are lighter than the fluid will be swept into the center. However, Equation 2.65 states that some particles even heavier than the fluid will also be swept into the center. This effect can be quite substantial. For example, if $\frac{V_\theta}{V_r} = 1$, then $\frac{\rho_s}{\rho_f} > 2$ for equilibrium.

Equation 2.63 also shows that the equilibrium radius of the particle is proportional to the particle radius for any given vortex. Thus, the problem scales linearly.

Figure II.6 is a graphical representation of Equation 2.63 where the drag coefficient has been taken from Zenz and Othmer (1960). The drag coefficient for $\frac{Q}{2\pi\nu} > 10^4$ was taken equal to 0.45. Note that the small values of $\left[\left(\frac{V_\theta}{V_r}\right)^2\left(\frac{\rho_s}{\rho_f}-1\right)-1\right]$ and $\frac{r}{a}$ correspond to the large values of $\frac{Q}{2\pi\nu}$ which produce constant C_D. This is the reason for the convergence of the curves.

In the above analysis, it has been assumed that the radial acceleration of the particle in its equilibrium orbit is large compared to gravity. However, even if gravity is a small effect, its presence is bound to perturb the particle slightly from its equilibrium orbit. The next section will examine the response of the particle to such perturbations.

2. Stability of Particle Position

Consider now the problem of a single particle moving in an equilibrium circular orbit. Let the Reynolds number for flow over the particle, $\frac{Q}{2\pi\nu}$, be small enough so that the drag on the particle may be expressed as Stokes drag--linear in velocity. The equations of motion may be written down directly. In the radial direction, using

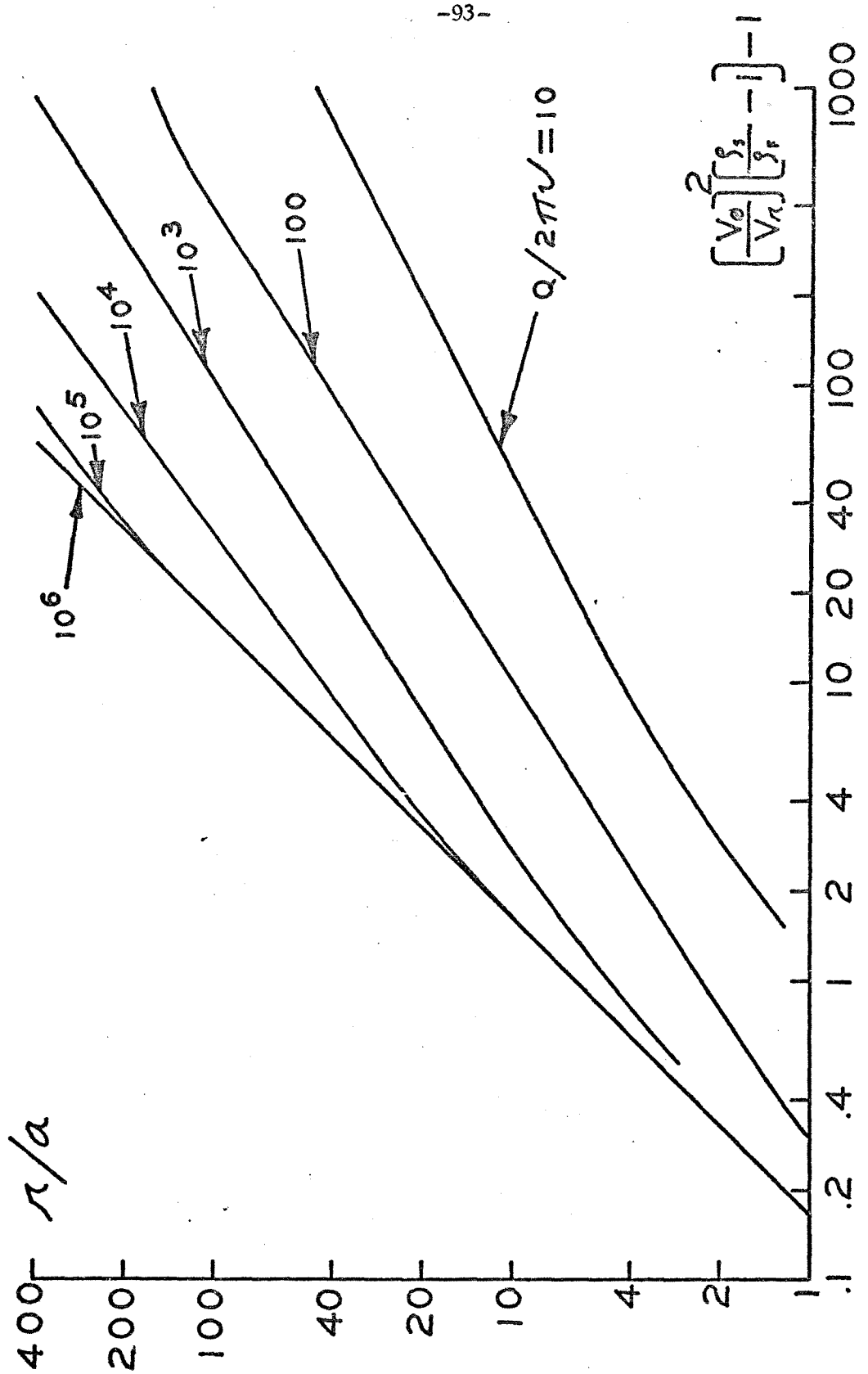

Figure II.6. Equilibrium Orbits of a Single Particle.

dots to denote $\frac{d}{dt}$, the equation is:

$$m_a\left(\ddot{r} - r\dot{\theta}^2\right) = 6\pi\mu a\left(V_r - \dot{r}\right) - m_a \frac{\rho_f}{\rho_s} \frac{r_o^2\left(V_{\theta_o}^2 - V_{r_o}^2\right)}{r^3} \tag{2.66}$$

where m_a is the effective mass of the particle, r and θ are the coordinates of the particle, and the zero subscript refers to conditions at the equilibrium position r_o. The term on the left is the acceleration of the particle times its mass; the first term on the right is the drag force; and the last term is the pressure force.

Similarly, the tangential equation is:

$$m_a\left(2\dot{r}\dot{\theta} + r\ddot{\theta}\right) = 6\pi\mu a\left(V_\theta - r\dot{\theta}\right) \tag{2.67}$$

The term on the left is the acceleration times the particle mass, and the term on the right is the drag force.

Now define:

$$\tau = \frac{6\pi\mu a}{m_a} \tag{2.68}$$

$$X = \frac{\rho_f}{\rho_s}\left[1 + \left(\frac{V_\theta}{V_r}\right)^2\right] \tag{2.69}$$

$$\frac{\alpha}{\tau} = \frac{2V_\theta}{r_o} \tag{2.70}$$

and let r and $\dot{\theta}$ be equal to their equilibrium values plus a small perturbation.

$$r = r_o + r' \tag{2.71}$$

$$\dot{\theta} = \frac{V_{\theta_o}}{r_o} + \dot{\theta}' \tag{2.72}$$

Substituting these quantities into Equations 2.66 and 2.67 yields the following two equations after some manipulation.

$$\ddot{\pi}' + \frac{1}{\tau}\dot{\pi}' - \frac{1}{2}\left(\frac{\alpha}{\tau}\right)^2(1+x)\pi' - 2\frac{\alpha}{\tau}\pi_0\dot{\theta}' = 0 \qquad (2.73)$$

$$\pi_0\ddot{\theta}' + \frac{1}{\tau}\pi_0\dot{\theta}' + \frac{\alpha}{\tau^2}\pi' + 2\frac{\alpha}{\tau}\dot{\pi}' = 0 \qquad (2.74)$$

The zero order terms were dropped because they constitute the determination of the equilibrium radius, and the higher order terms were dropped because the perturbations were assumed small.

These equations are satisfied by perturbations of the form

$$\pi' = A\, e^{\frac{\lambda}{\tau}x} \qquad (2.75)$$

$$\pi_0\theta' = B\, e^{\frac{\lambda}{\tau}x} \qquad (2.76)$$

Substituting,

$$A\left[\lambda^2 + \lambda - \frac{\alpha^2}{2}(1+x)\right] - B\,\frac{\alpha\lambda}{\tau^2} = 0 \qquad (2.77)$$

$$A\left[\alpha(1+\lambda)\right] + B\left[\lambda(1+\lambda)\right] = 0 \qquad (2.78)$$

The condition for solution is that the determinant of the coefficients is zero: this reduces to

$$\lambda(\lambda+1)\left[\lambda^2 + \lambda + \frac{\alpha^2}{2}(1-x)\right] = 0 \qquad (2.79)$$

The roots of this equation are:

$$\lambda = 0 \qquad (2.80)$$

$$\lambda = -1 \qquad (2.81)$$

$$\lambda = -\frac{1}{2}\left\{1 \pm \left[1 - 2\alpha^2(1-x)\right]^{1/2}\right\} \qquad (2.82)$$

Because of the nature of Equations 2.75 and 2.76, unstable roots correspond to $\lambda > 0$. The only possible unstable roots occur in Equation 2.82 if $X > 1$.

Comparison of Equation 2.69 with Equation 2.65 will reveal that the condition $X > 1$ corresponds to $\frac{r}{a}$ at equilibrium less than zero. So all of the equilibrium orbits obtained in the last section are stable to small perturbations providing the flow is laminar.

The turbulent case is much harder to analyze. The difficulty lies in evaluating the direction of the drag force in the presence of the perturbations.

The motion of a single particle in a circular orbit is difficult to observe for two reasons. One reason involves the secondary flow in the boundary layer. Because of this secondary flow the local value of $\frac{V_\theta}{V_r}$ is smaller in the boundary layer than in the main flow. Also, since the equilibrium position of a particle is quite sensitive to $\frac{V_\theta}{V_r}$, if a particle wanders into the boundary layer, it will be swept inward toward the center. If it then falls out of the boundary layer, it will move outward in a spiral until it reaches its equilibrium position or until it is again caught in the boundary layer. Now because at every radius (except very small radii) the boundary layer is increasing in thickness, it follows that there must be a small axial component of velocity toward the wall everywhere except midway between the two side walls. So the entrainment of particles in the boundary layer is inevitable.

A second reason is that the flow in the vortex-sink may be turbulent. To obtain laminar flow it is necessary to use a high value

of $\frac{V_\theta}{V_r}$ and a low value of $\frac{Q}{2\pi\nu}$. This combination results in a large value of $\frac{r}{a}$ which means either a large apparatus or extremely small particles, and, in addition, if $\frac{V_\theta}{V_r}$ is large in a large apparatus, it is difficult to maintain laminar flow.

C. Behavior of Clouds of Particles in Vortex-Sink Flow

1. Concentration Distribution

It has been shown above that it is possible for a single particle immersed in vortex-sink flow to be entirely hydrodynamically supported by the flow. This section will discuss the phenomena associated with concentrations high enough so that the particles may be treated as a cloud similar to the vertical fluidized bed analog. First, the equilibrium orbits of the particles will be determined. The method is again a force balance taking into account the change in drag coefficient due to the non-zero concentration. Second (in the next section), the effect of the particles on the flow will be discussed. The effect is a reduction of circulation due to wall shear stress.

In the last section above it was found that individual particles immersed in two-dimensional vortex-sink flow had circular orbits. It is reasonable to assume that with higher concentrations, the same phenomenon occurs. The only difference is that the pressure gradient in the bed must include the effects of the mass of the particles, and the drag force must be appropriate for radial flow through a cloud.

Consider the equations of motion for the liquid component alone. If one assumes that there are no viscous shear forces due to the liquid or particles, the equations of motion are:

Continuity $$\frac{1}{r}\frac{d}{dr}(r V_r) = 0 \qquad (2.83)$$

Radial Momentum $$\rho_L V_r \frac{dV_r}{dr} - \rho \frac{V_\theta^2}{r} = -\frac{dP}{dr} \qquad (2.84)$$

Tangential Momentum $$V_r \frac{dV_\theta}{dr} + \frac{V_r V_\theta}{r} = 0 \qquad (2.85)$$

These equations are of the same form as Equations 2.1, 2.2, and 2.3 except that the meaning of V_r, V_θ, and ρ must be different. Here V_r is taken as the superficial radial velocity. This is the flow rate per unit area if no particles were present. The definition is completely analogous to the superficial velocity in a vertical fluidized bed. Strictly speaking, the term $\rho_L V_r \frac{dV_r}{dr}$ in Equation 2.84 should include the actual velocity of the fluid in the radial direction which is higher than the superficial velocity, V_r. A better approximation would be $\frac{V_r}{1-\epsilon}$, the average velocity. However, the term in question is not very large if $\frac{V_\theta}{V_r} >> 1$ and so the form given is a satisfactory approximation providing the concentration is not too large. V_θ is the actual velocity of the liquid and particles in the tangential direction and ρ is the actual density of the mixture.

Equation 2.83 may be integrated directly just as before to give:

$$V_r = -\frac{Q}{2\pi r} \qquad (2.86)$$

where Q is the volumetric flow rate per unit area. Equation 2.85 may also be integrated directly and it yields

$$V_\theta = \frac{A}{r} \qquad (2.87)$$

Now noting that:

$$\rho = c(\rho_s - \rho_\ell) + \rho_\ell \tag{2.88}$$

and combining Equations 2.84, 2.86, 2.87, and 2.88:

$$\frac{dP}{dr} = \frac{\rho_\ell}{r}\left[V_\theta^2 + V_r^2 + c\,V_\theta^2\left(\frac{\rho_s - \rho_\ell}{\rho_\ell}\right)\right] \tag{2.89}$$

Now assume hydrodynamic support of an individual particle just as before. The same three forces can now be evaluated in terms of the above equations.

The force due to acceleration is exactly the same as before.

$$F_A = \rho_s \frac{4}{3}\pi a^3 \frac{V_\theta^2}{r} \tag{2.90}$$

The force due to viscous drag is

$$F_D = -C_{D_s} \frac{1}{2}\rho_\ell V_r^2 \pi a^2 \tag{2.91}$$

where C_{D_s} is the drag coefficient based on superficial velocity. Because of the close analogy with a vertical fluidized bed, it is assumed that C_{D_s} is the same as that for vertical fluidized beds. This has been evaluated in Appendix B as

$$C_{D_s} = C_{D_o}(1-c)^{1-2m} \tag{2.92}$$

where C_{D_o} is based on the conditions when no particles are present. Thus, C_{D_o} is a function of $R_\ell = \left(\frac{Q}{2\pi\nu}\right)\left(\frac{2a}{r}\right)$ just as before.

If the particles are small, then the force due to pressure can be determined from the pressure gradient in Equation 2.89.

$$F_p = -\frac{4}{3}\pi a^3 \frac{\rho_L}{r}\left(V_\theta^2 + V_r^2 + C V_\theta^2 \frac{\rho_s - \rho_L}{\rho_L}\right) \qquad (2.93)$$

Summing these forces yields:

$$\rho_s \frac{4}{3}\pi a^3 \frac{V_\theta^2}{r} - C_{D_s}\frac{1}{2}\rho_L V_r^2 \pi a^2 - \frac{4}{3}\pi a^3 \frac{\rho_L}{r}\left(V_\theta^2 + V_r^2 + C V_\theta^2 \frac{\rho_s - \rho_L}{\rho_L}\right) = 0 \qquad (2.94)$$

and after some rearrangement

$$C_{D_s} = \frac{8}{3}\frac{a}{r}\left[(1-C)\left(\frac{V_\theta}{V_r}\right)^2 \frac{\rho_s - \rho_L}{\rho_L} - 1\right] \qquad (2.95)$$

Using Equation 2.92 for C_{D_s} and rearranging:

$$\frac{r}{a} = \frac{8\left[(1-C)\left(\frac{V_\theta}{V_r}\right)^2 \frac{\rho_s - \rho_L}{\rho_L} - 1\right]}{3(1-C)^{1-2m} C_{D_0}\left(\frac{Q}{2\pi\nu}\frac{2a}{r}\right)} \qquad (2.96)$$

This equation is the generalization of Equation 2.63 for non-zero concentration and allows the calculation of a concentration profile versus radius. As before, for a given vortex-sink geometry, the radius of the particle is linearly related to the radius of the orbit at a given concentration.

Now for Reynolds number, $\frac{Q}{2\pi\nu}\frac{2a}{r}$, greater than 500, $m = 2.39$, and in addition, if the Reynolds number is less than 10,000, C_{D_0} is almost independent of Reynolds number and approximately equal to 0.42. These conditions reduce Equation 2.96 to

$$\frac{r}{a} \quad 6.349\left[(1-C)\left(\frac{V_\theta}{V_r}\right)^2\left(\frac{\rho_s}{\rho_L} - 1\right) - 1\right](1-C)^{3.78} \qquad (2.97)$$

Figure II.7 is a graph of Equation 2.97. The net result is that for a given geometry there is an equilibrium radius with zero concentration. As the concentration increases, the equilibrium radius decreases.

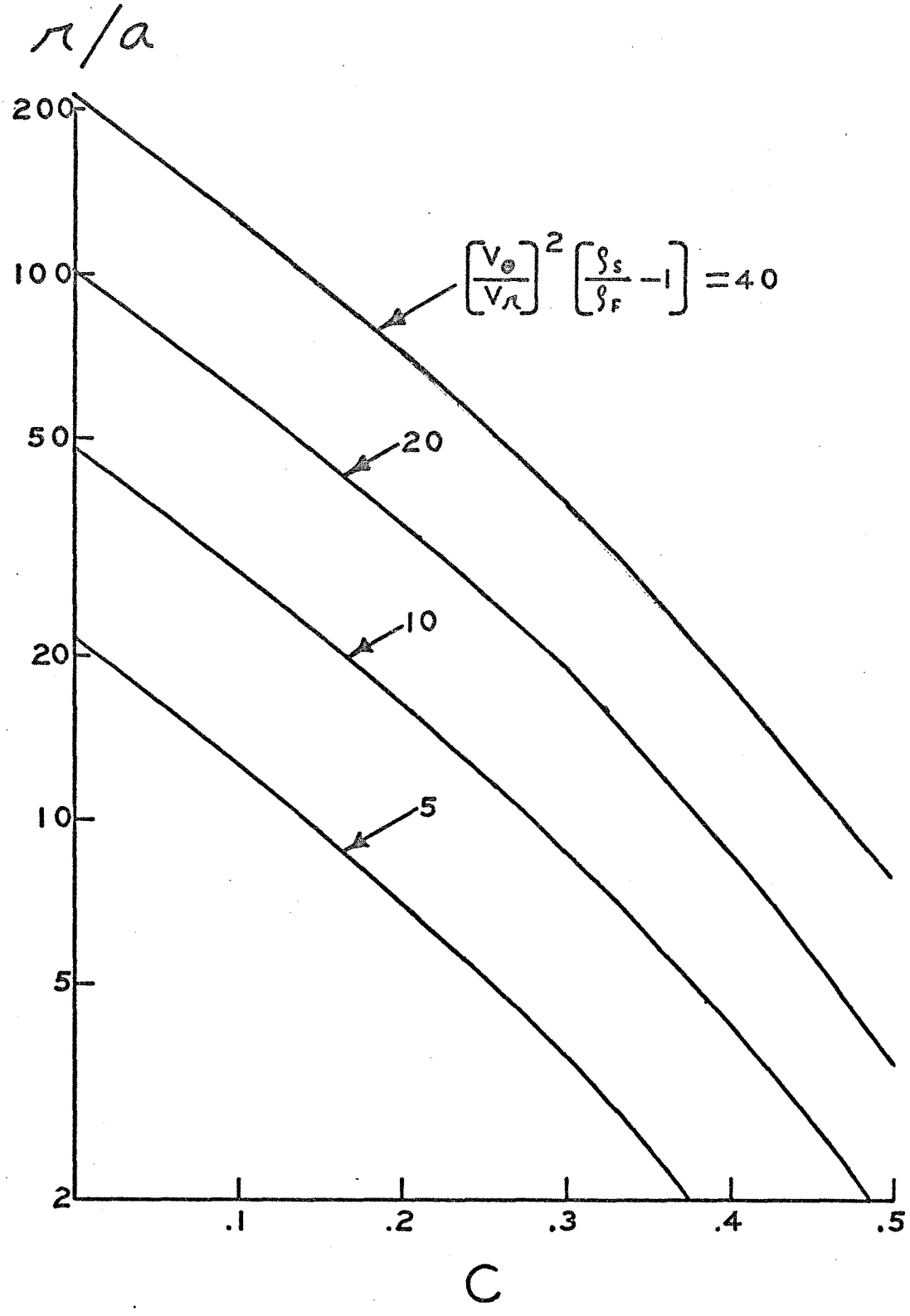

Figure II.7. Equilibrium Orbits for Non-Zero Concentrations.

This analysis has assumed that the viscous and particle-particle interaction shear stresses are zero and that because of this the fluid flow is an irrotational vortex-sink. In reality, these assumptions are not quite correct. Nevertheless, these results can be used to determine concentration distribution if the actual value of $\frac{V_\theta}{V_r}$ is used locally in the calculation.

As in the case of low concentrations, the boundary layer should have an effect on particle movement. However, it is expected that its effects will be much smaller for high particle concentrations. Certainly the equations developed for the boundary layer with no particles present must be greatly altered if the particles are of the same order of magnitude in diameter as the thickness of the boundary layer. In effect, the particles will inhibit the radial secondary flow. Any radial flow of particles will cause large shear stresses due to the interaction of particles in the boundary layer with their neighbors outside the boundary layer. The boundary layer will thus be quite thin compared to the pure fluid case.

This analysis has shown that if a vortex-sink is established between two flat plates and particles are introduced to the flow, the first few particles should have orbits at the single particle radius. Additional particles will have orbits at smaller radii for higher concentration. Figure II.8 graphs this relationship for $\left(\frac{V_\theta}{V_r}\right)^2\left(\frac{\rho_s}{\rho_f}-1\right) = 20$. The theory predicts that there will be a radius such that there is a sharp change in concentration. This is the only way that a continuous distribution of particles can be achieved. However, the model used here neglects the effects of turbulent diffusion, and the side-wall

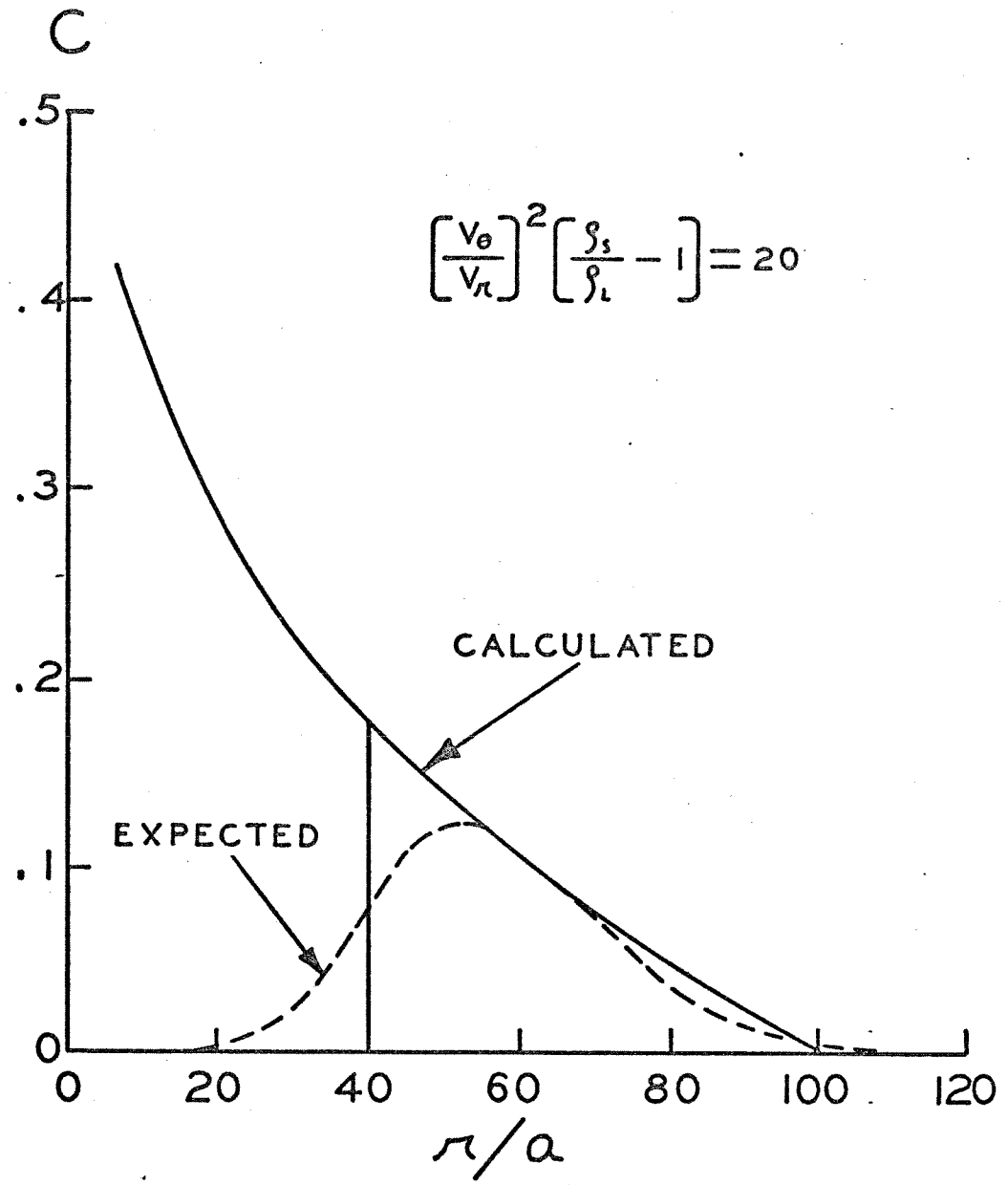

Figure II.8. Equilibrium Orbits for a Given Volume of Particles.

boundary layers. Diffusion can be expected to carry some of the particles out further than the single particle orbit and also to round off the discontinuity in concentration at the inner edge.

It can be argued that the boundary layer is unimportant where the concentration of particles is high, but in the pure fluid region at small radii, the boundary layer will start to grow again. Consequently some of the particles will be swept inward in the boundary layer as described before. Thus, the sharp discontinuity in concentration will in reality be quite rounded.

2. Circulation Reduction

The above analysis assumed that the viscous forces and particle-particle interaction forces were zero. In this section the effects of these forces on the flow will be discussed. It has been shown that the boundary layer, in the presence of high concentrations of particles, will be thin. However, the shear stress will not be zero. The shear stress will have components in both the radial and tangential directions.

The procedure used here will be to take the equations of motion describing this configuration, allow the flow to be turbulent and integrate the equations in the axial direction.

The equations of motion are:

Continuity

$$\frac{\partial V_r}{\partial r} + \frac{V_r}{r} + \frac{\partial V_x}{\partial x} = 0 \qquad (2.98)$$

Radial Momentum

$$\rho_2 V_r \frac{\partial V_r}{\partial r} + \rho_2 V_x \frac{\partial V_r}{\partial x} - \rho \frac{V_\theta^2}{r} = -\frac{\partial P}{\partial r} + \mu_1 \left[\frac{\partial^2 V_r}{\partial r^2} + \frac{1}{r}\frac{\partial V_r}{\partial r} - \frac{V_r}{r^2}\right] + \mu_2 \frac{\partial^2 V_r}{\partial x^2} \qquad (2.99)$$

Tangential Momentum

$$\rho_L V_r \frac{\partial V_\theta}{\partial r} + \rho_L V_x \frac{\partial V_\theta}{\partial x} + \rho_L \frac{V_r V_\theta}{r} = \mu_1 \frac{\partial^2 V_\theta}{\partial x^2} + \mu_2 \left(\frac{\partial^2 V_\theta}{\partial r^2} + \frac{1}{r} \frac{\partial V_\theta}{\partial r} - \frac{V_\theta}{r^2} \right) \tag{2.100}$$

Since the shear stresses are due to the effects of particles as well as the fluid, different effective viscosities have been used for each component of shear stress.

The continuity equation can be used to simplify the other two equations.

Radial

$$\rho_L \frac{\partial}{\partial r}(V_r^2) + \rho_L \frac{\partial}{\partial x}(V_x V_r) + \frac{\rho_L}{r} V_r^2 + \frac{\rho}{r} V_\theta^2 = \mu_2 \frac{\partial^2 V_r}{\partial x^2} - \mu_1 \frac{\partial^2 V_r}{\partial r \partial x} - \frac{\partial P}{\partial r} \tag{2.101}$$

Tangential

$$\rho_L \frac{\partial}{\partial r}(V_r V_\theta) + \rho_L \frac{\partial}{\partial x}(V_x V_\theta) + 2 \frac{V_\theta V_r}{r} = \mu_2 \frac{\partial^2 V_\theta}{\partial x^2} + \mu_2 \left[\frac{1}{r} \frac{\partial}{\partial r}(r V_\theta) \right] \tag{2.102}$$

Now let the pressure and velocities be turbulent and average the equations with respect to time. Defining:

$$\begin{aligned} V_r &= \bar{V}_r + V_r' \\ V_\theta &= \bar{V}_\theta + V_\theta' \\ P &= \bar{P} + P' \end{aligned} \tag{2.103}$$

where the bars refer to time average and the primes denote the fluctuating part. Thus the equations become:

Radial $$\rho_L \frac{\partial}{\partial r}\left(\bar{V}_r^2 + \overline{V_r'^2} \right) + \rho_L \frac{\partial}{\partial x}\left(\bar{V}_r \bar{V}_x + \overline{V_r' V_x'} \right) + \frac{1}{r}\left\{ \rho_L \left(\bar{V}_r^2 + \overline{V_r'^2} \right) + \rho \left(\bar{V}_\theta^2 + \overline{V_\theta'^2} \right) \right\} =$$

$$\mu_2 \frac{\partial^2 \bar{V}_r}{\partial x^2} - \mu_1 \frac{\partial^2 \bar{V}_x}{\partial r \partial x} - \frac{\partial \bar{P}}{\partial r} \tag{2.104}$$

Tangential

$$\rho_L\left[\frac{\partial}{\partial r}\left(\bar{V}_r\bar{V}_\theta+\overline{V_r'V_\theta'}\right)+\frac{\partial}{\partial x}\left(\bar{V}_x\bar{V}_\theta+\overline{V_x'V_\theta'}\right)+\frac{2}{r}\left(\bar{V}_r\bar{V}_\theta+\overline{V_r'V_\theta'}\right)\right]= \mu_3\frac{\partial^2\bar{V}_\theta}{\partial x^2}+\mu_4\frac{\partial}{\partial r}\left[\frac{1}{r}\frac{\partial}{\partial r}\left(r\bar{V}_\theta\right)\right] \tag{2.105}$$

Now assume that the axial length between side walls is $\mathcal{L}$ and integrate these equations from 0 to $\mathcal{L}$ in the axial direction. Note that the shear stresses on each wall are the same, and that at the walls all the velocities are zero. The final equations are,

Radial

$$\rho_L\frac{1}{r}\frac{\partial}{\partial r}\left(r\bar{\bar{V}}_r^2\right)-\rho_L\frac{1}{r}\bar{\bar{V}}_\theta^2=\frac{-2\mu_2}{\mathcal{L}}\frac{\partial\bar{V}_r}{\partial x}\Big|_0-\rho_L\frac{1}{r}\frac{\partial}{\partial r}\left(r\overline{\overline{V_r'^2}}\right)-\frac{\partial\bar{P}}{\partial r} \tag{2.106}$$

Tangential

$$\rho_L\frac{1}{r^2}\frac{\partial}{\partial r^2}\left(r^2\bar{\bar{V}}_r\bar{\bar{V}}_\theta\right)=-\frac{2\mu_3}{\mathcal{L}}\frac{\partial\bar{V}_\theta}{\partial x}\Big|_0+\mu_4\frac{\partial}{\partial r}\left[\frac{1}{r}\frac{\partial}{\partial r}\left(r\bar{\bar{V}}_\theta\right)\right]+\frac{\partial}{\partial r}\left(\overline{\overline{V_r'V_\theta'}}\right) \tag{2.107}$$

where the second bar refers to average over X .

It has been argued above that the boundary layers are thin. This means that conditions are essentially uniform in the X direction except very close to the wall. Hence,

$$\begin{aligned}\bar{\bar{V}}_r^2&\simeq\left(\frac{Q}{2\pi r}\right)^2\\ \bar{\bar{V}}_\theta^2&\simeq\bar{V}_\theta^2\\ \bar{\bar{V}}_r\bar{\bar{V}}_\theta&\simeq\frac{-Q}{2\pi r}\bar{V}_\theta\end{aligned} \tag{2.108}$$

Equation 2.106 can then be rewritten as:

$$(r\bar{V}_\theta)^2 = \frac{1}{\rho} r^3 \frac{d\bar{P}}{dr} - \frac{\rho_L}{\rho}\left(\frac{Q}{2\pi}\right)^2 + \frac{2}{A} r^3 \frac{\mu_2}{\rho} \frac{d\bar{V}_r}{dx}\Big|_0 + \frac{\rho_L}{\rho} r^2 \frac{d}{dr}\left(r\overline{\overline{V_r'^2}}\right) \qquad (2.109)$$

The third term on the right is the wall shear stress in the radial direction. The fourth term on the right is the dynamic pressure corresponding to $\overline{\overline{V_r'^2}}$. Since the average velocity in the radial direction is much smaller than the average tangential velocity, the radial wall shear stress will be small compared to the pressure drop. A similar argument holds for the dynamic pressure associated with $\overline{\overline{V_r'^2}}$. Assuming that $\overline{\overline{V_r'^2}}$ goes roughly as $\bar{V}_r^2$, then both the third and fourth terms on the right hand side of Equation 2.109 will be small positive numbers. If these terms are neglected,

$$(r\bar{V}_\theta)^2 = \frac{1}{\rho} r^3 \frac{d\bar{P}}{dr} - \frac{\rho_L}{\rho}\left(\frac{Q}{2\pi}\right)^2 \qquad (2.110)$$

This equation provides a simple way of determining the tangential velocity of the flow without introducing any probes. Measurement of flow rate, Q, pressure gradient, $\frac{d\bar{P}}{dr}$, and average density, ρ, allow direct calculation of $\bar{V}_\theta$. Any small errors introduced by neglecting the extra terms in Equation 2.109 will decrease the calculated value of $\bar{V}_\theta$. This technique is used in the experimental sections to determine $\bar{V}_\theta$ from experimental data.

Using this result, Equation 2.107 may now be simplified:

$$-\frac{Q}{2\pi}\frac{\rho_L}{r^2}\frac{d}{dr}(r\bar{V}_\theta) = -\frac{2\mu_2}{A}\frac{d\bar{V}_\theta}{dx}\Big|_0 + \mu_2 \frac{d}{dr}\left[\frac{1}{r}\frac{d}{dr}(r\bar{V}_\theta)\right] - \frac{d}{dr}\left(\overline{\overline{V_r' V_\theta'}}\right) \qquad (2.111)$$

Now the first term on the right hand side of this equation is the wall shear stress in the tangential direction. Designating this by τ_w we have:

$$\tau_w = \mu_3 \left.\frac{d\bar{V}_\theta}{dx}\right|_0 \tag{2.112}$$

The second and third terms on the right hand side of Equation 2.111 are shear stress terms. The first is pseudo-laminar in that it is a function of the viscosity of the fluid and also particle-particle interactions. The second is a turbulent shear stress term. These two terms can be written in the form

$$\frac{d}{dr}\left[\mu_T \frac{1}{r}\frac{d}{dr}\left(r\bar{V}_\theta\right)\right] = \mu_3 \frac{d}{dr}\left[\frac{1}{r}\frac{d}{dr}\left(r\bar{V}_\theta\right)\right] - \frac{d}{dr}\left(\overline{V_r' V_\theta'}\right) \tag{2.113}$$

where μ_T is an effective turbulent viscosity for the systems. Thus, Equation 2.111 becomes:

$$\frac{d}{dr}\left(r\bar{V}_\theta\right) = \frac{r^2}{\frac{Q}{2\pi}}\left\{\frac{2}{t}\frac{\tau_w}{\rho} - \frac{d}{dr}\left[\mu_T \frac{1}{r}\frac{d}{dr}\left(r\bar{V}_\theta\right)\right]\right\} \tag{2.114}$$

This equation shows that a decrease in circulation can come from either the wall shear stress or the internal shear stresses on cylindrical surfaces. The two effects seem to be inextricable. Thus, it is not possible to determine from experimental measurements of $\bar{V}_\theta$ (through $\frac{d\bar{P}}{dr}$) the actual mix of wall shear and shear on cylindrical surfaces. However, since the shear on cylindrical surfaces term involves $\frac{d}{dr}\left(r\bar{V}_\theta\right)$, it is clear that this force goes to zero if the flow is irrotational. In addition, the wall shear stress term is expected to be proportional to $\bar{V}_\theta^2$ so that it will become proportionately larger for higher velocity flows. Assuming that only wall shear affects the flow:

$$\frac{d}{dr}(r\bar{V}_\theta) = \frac{r^2}{\frac{Q}{2\pi}} \frac{2}{\rho} \frac{\tau_w}{\rho} \tag{2.115}$$

A wall shear stress coefficient, f , may be defined as

$$\tau_w = f \frac{1}{2} \rho \bar{V}_\theta^2 \tag{2.116}$$

Thus,

$$f = -r \frac{d}{dr}\left(\frac{\bar{V}_r}{\bar{V}_\theta}\right) \tag{2.117}$$

This equation may be used to calculate the wall shear stress coefficient from experimental data. Since $\bar{V}_\theta$ may be calculated from pressure tap data, and $\bar{V}_r$ is known from the flow rate and continuity, f may be determined by differentiation. However, $\bar{V}_\theta$ was also calculated by differentiation of the side-wall pressure data so that the calculation of f requires a second derivative. The difficulties in this procedure have been described above. Nevertheless, this does provide a way of determining wall shear stress without direct measurement.

CHAPTER III

APPARATUS AND PROCEDURE

A. Small Annular Fluidized Bed

The annular fluidized bed work was done in two test facilities. The first utilized most of the vertical fluidized bed flow circuit described in Part I-A with the addition of a new annular test section. It was constructed as a preliminary step in order to answer some questions regarding the feasibility of a larger scale apparatus. The second apparatus is substantially larger, more complex, and utilizes a completely new flow circuit.

The first annular chamber was designed to directly replace the vertical test section described in Part I-A. Figure III.1 is a photograph showing the essential details. Flow enters the unit through two 4-inch plastic pipes. These pipes are routed on opposite sides of the test section so as to provide dual entrance paths for the fluid. There is a nozzle inside the end of each pipe to accelerate the flow. The test section itself is circular and 12 inches in inside diameter. It is constructed mostly of acrylic plastic with $\frac{1}{2}$-inch thick side walls. The axial length between side walls is 1.6 inches. The flow enters tangentially and swirls around the chamber many times before passing radially into the exit section located at the center. The exit section is 2.0 inches in diameter, and has two layers of fine screen (80 mesh brass over 10 mesh stainless steel) to hold the beads in the test section and to smooth any axial variations in flow rate. Within the exit section, the flow is turned and finally passes out axially. A flexible piece of plastic tubing carries the

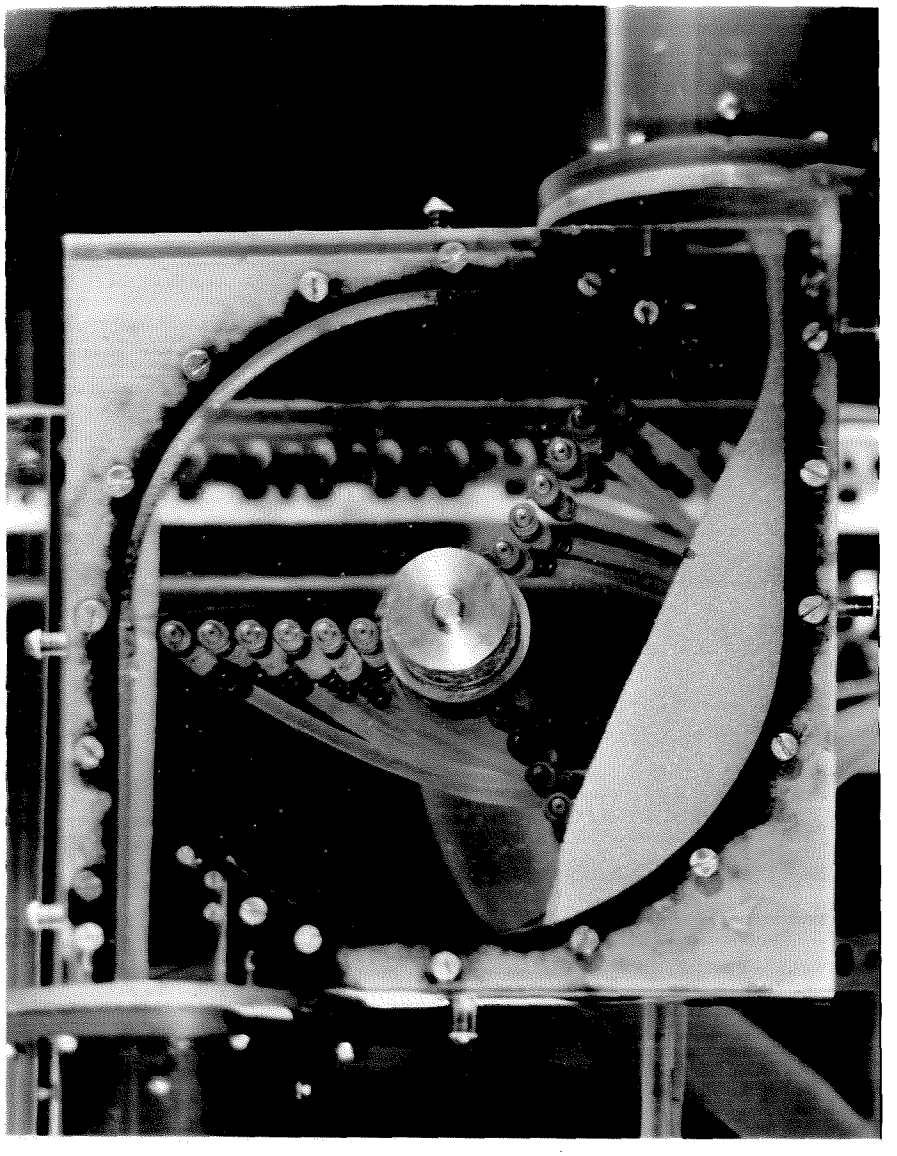

Figure III.1. Photograph of Small Annular Chamber.

flow back to the rest of the circuit.

The annular chamber is mounted with the axis horizontal, thus introducing a non-axisymmetric gravitational force. The effects of this force will be discussed later. The size of the slits through which the flow enters were designed to provide for the ratio of tangential to radial velocity to be about 10.0.

Eighteen pressure taps were arranged along 3 radial lines at 120° intervals to provide information as to axial symmetry and radial pressure gradient. These pressure taps were connected to the manometer board described in Part I-A.

Two different types of particles were used in experiments. Glass beads of 1 millimeter diameter and specific gravity about 2.2 relative to water were used for the first test. Subsequent tests were run with ground nylon balls. These balls are 1/8-inch diameter, with a tolerance of $\pm$ 0.001 inch, and are almost perfect spheres. Their specific gravity is 1.14 relative to water.

The experiments done with this apparatus were mostly qualitative. Since the side walls were transparent, the movement of single particles in the flow could easily be observed. When high concentrations of particles were used, it was difficult to see more than a short distance into the suspension. But with lower concentrations of particles, visibility was improved. Dye injection tests were conducted to visualize the side wall boundary layers. Concentrated red and blue food coloring was injected through the side walls at various rates. A comparison of the direction of the plume at a high dye flow rate to the direction at a low dye flow rate was used as an indication of secondary flow.

Quantitative experiments were also performed. These consisted of measuring the pressures at the side wall pressure taps with and without particles. The experimental procedure used here was quite similar to that used in the vertical fluidized bed. Flow rate was measured with the orifice plate, and the manometer board was read to determine the pressure as a function of radius. Because of the generally high turbulence level of the system and the need for very accurate pressure measurements, two methods were used to reduce error. The first method consists of placing small flow-restricting orifices in each manometer line to increase the time constant of the manometer system to about 2 seconds. The second method was to photograph the manometer board and read the manometer levels from the negatives. This allowed simultaneous readings of all tubes at once.

Data runs were taken with and without particles over a range of flow rates. The average concentration of particles for the runs with glass beads was 14.2 percent. The average concentration is the ratio of volume of the particles to total volume of the annulus open to the particles. The average concentration for the runs with nylon balls was 1.16 percent.

The results of these experiments showed that for several reasons accurate data could only be obtained with a substantially larger apparatus. First, in this small test section, the centripetal acceleration was not large enough to totally swamp the effects of gravity. Increasing the centripetal acceleration could only be accomplished by an increase in flow rate beyond the capacity of the test loop. Second, the calculations performed earlier indicate that the ratio of equilibrium

radii for particles at zero concentration and at, say, 40 percent concentration can easily be a factor of 10 or more. However, in the small apparatus, the ratio of radii at the outside to the radius at the screen is only 6. Increasing this ratio by decreasing screen size is impractical due to cavitation considerations, increased pressure losses, and at small radii, the ratio of equilibrium radius to particle radius becomes very large, thus introducing errors in the approximations used above. Third, two inlets are not enough to produce axisymmetric flow. The symmetry would be improved by a larger number of flow inlets, and a smoothing chamber or plenum outside the test section. Fourth, accurate pressure gradient measurements require a large number of small pressure taps quite close together. The larger the apparatus, the smaller the pressure tap holes appear relative to the device, and the more room is available for locating them.

In this apparatus, the pump, motor, and piping system are operating at their maximum capacity. Replacing any one of these components would increase the available head and flow rate, but only slightly. It was decided that the gains possible by modifications of the system would not be great enough to eliminate the problems mentioned above and that a new test section and flow circuit were required for more accurate measurements.

B. Large Annular Fluidized Bed

An entirely new and much larger test loop was designed and constructed. Figure III.2 is a schematic of the flow circuit drawn approximately to scale, and Figure III.3 is a photograph of the completed apparatus.

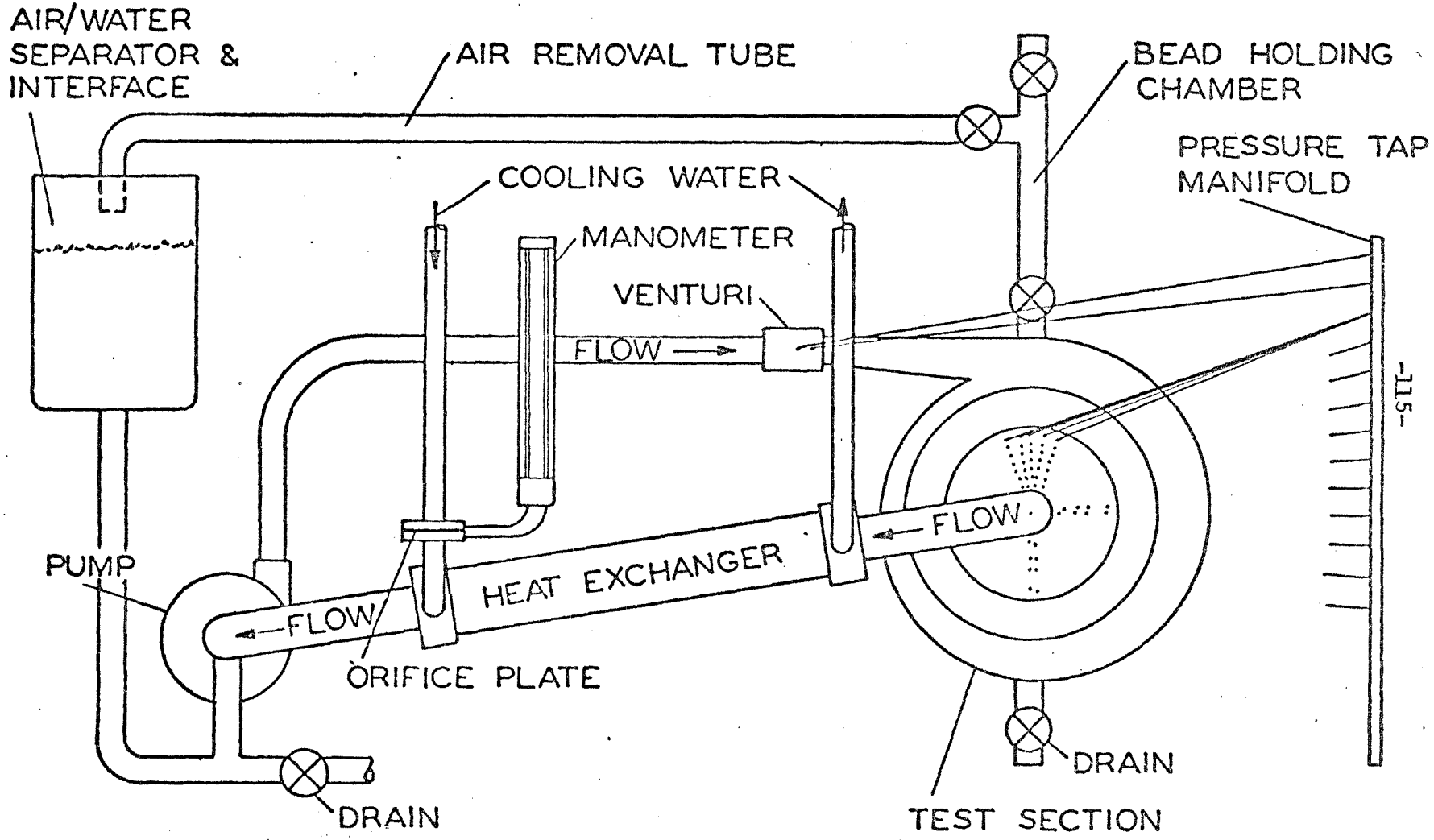

Figure III.2. Schematic Diagram of Flow Circuit.

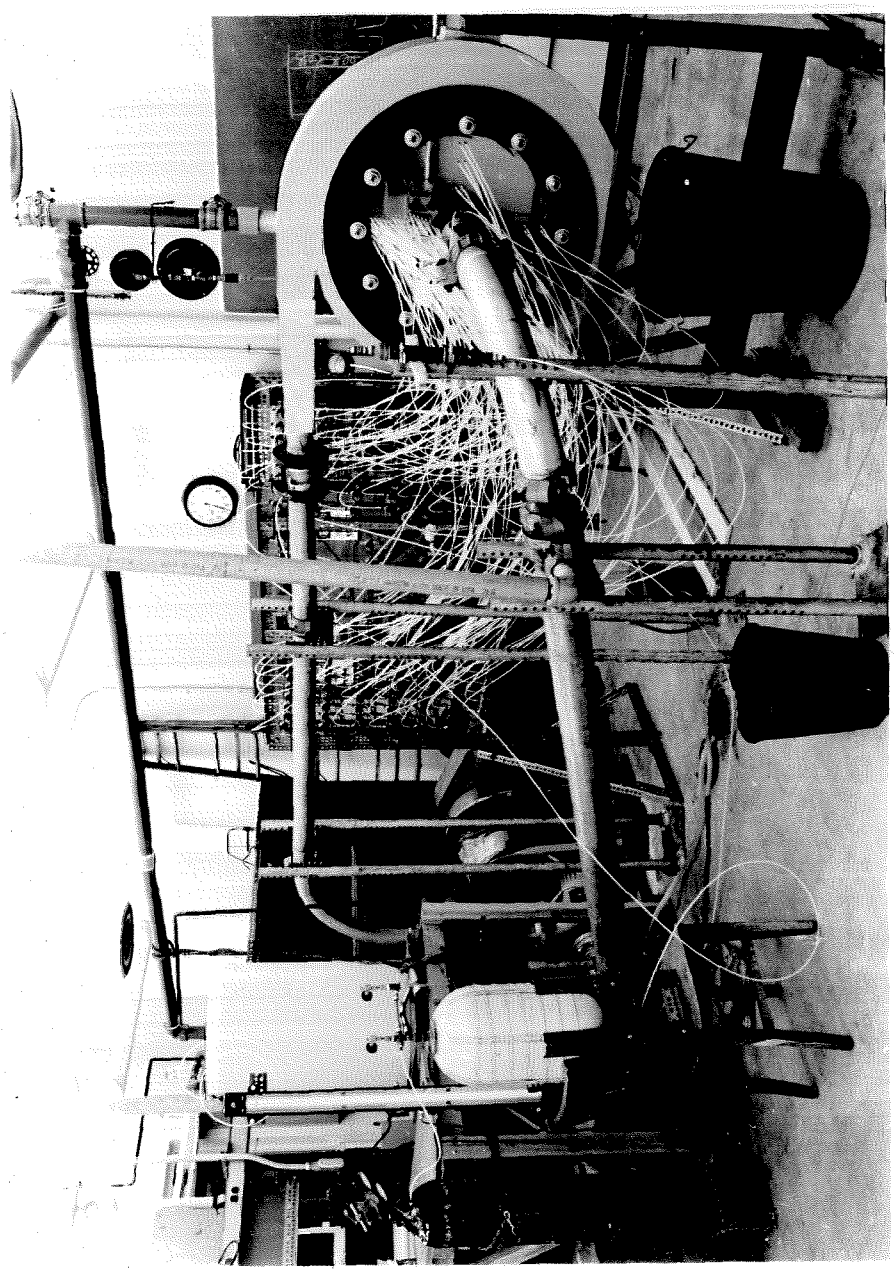

Figure III.3. Photograph of Large Annular Fluidized Bed Apparatus.

The pump is of the centrifugal type and is rated at 170 foot head at 500 gallons per minute flow rate. The pump requires 27 horsepower at 3500 r.p.m. (The pump for the old system rated at 40 foot head at 120 gallons per minute flow rate and required 3 h.p.) The pump is driven by a 30 h.p. shunt wound D.C. electric motor with a 2 x 1 triple chain drive speed increaser to give 4000 r.p.m. maximum speed for the pump. Power is supplied to the motor by a control system, drawing current from a 440 volt, 3 phase line. A control system supplies armature current through 4 three phase manually adjustable autotransformers with full wave rectification. The armature current is a maximum of 100 amps at 300 volts. Field current adjustment is manual or automatic with proportional-integral feedback control of shaft speed. The piping loop is designed for low head loss and is constructed mostly of galvanized steel with 3-inch steel pipe on the high pressure side and a 4-inch steel pipe on the low pressure side. There are no valves in the main flow path. Flow regulation is through the variable speed motor. The elbows are of large radius, 20 inches for the 3-inch line, and 15 inches for the 4-inch line.

The flow rate was measured with a venturi meter ($\beta = 0.65$). An air-water interface is maintained off the main circuit in a 55-gallon plastic drum. This interface provides a reference atmospheric pressure. Provision is also made, though not shown in Figure III.2, for isolating the interface and pressurizing the system with high pressure water. A second loop is provided to bleed off a small amount of flow from the main circuit and pass it into the 55-gallon drum. This loop serves to

separate air bubbles present in the flow on start-up and is normally inoperative during a data run.

A heat exchanger is incorporated around a straight section of pipe to maintain a uniform temperature of the water in the primary circuit during operation. The primary flow is unrestricted through a 4-inch inside diameter tube. (This section of the primary circuit is all brass.) Cooling water flowing through an outer jacket is supplied through an auxiliary pump and cooling tower on the roof. The cooling capacity is sufficient to keep the temperature of the primary circuit at less than 10° F. above ambient. The cooling water flow rate is measured with an orifice plate.

A diagram of the test section is shown in Figure III.4, and photographs showing the essential parts in Figures III.5 and III.6. The outer part of the test section is a galvanized steel plenum chamber in the form of scroll with flow entering tangentially through a diffuser attached to the high pressure piping. The scroll was designed to provide uniform flow through the 12 brass vanes at the entrance of the working section. Located above the plenum, see Figure III.2, is a bead holding chamber which allows easy filling of the apparatus with particles. At the bottom of the plenum, a drain allows removal of both water and particles.

The working section is bounded by two large acrylic plastic side walls supported by the plenum. The 12 brass vanes are adjustable in pitch so that the ratio of tangential to radial velocity within the working section may be varied. The vanes are supported by stainless steel shafts which may be clamped in any angular position. The vane

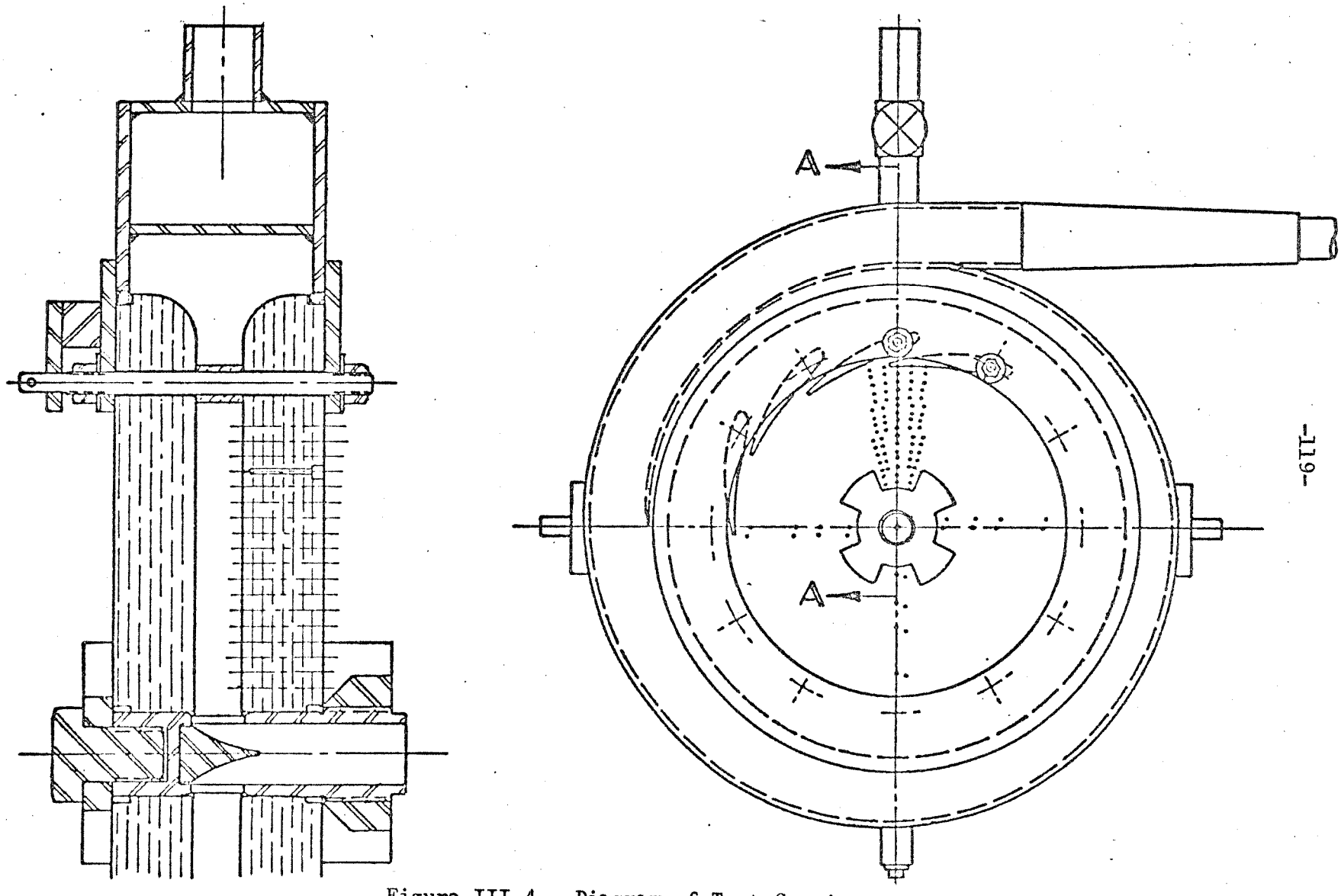

Figure III.4. Diagram of Test Section.

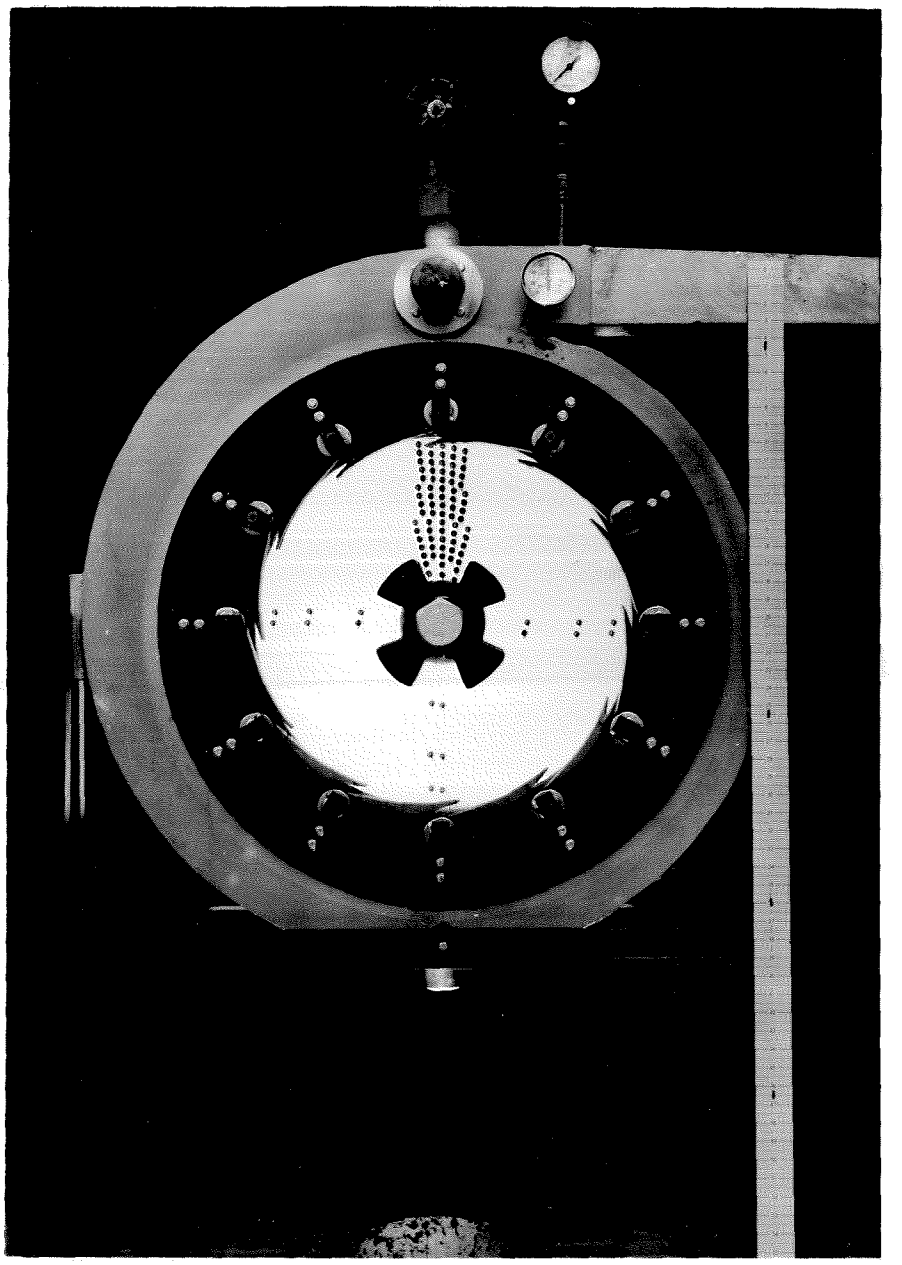

Figure III.5. Photograph of Test Section.

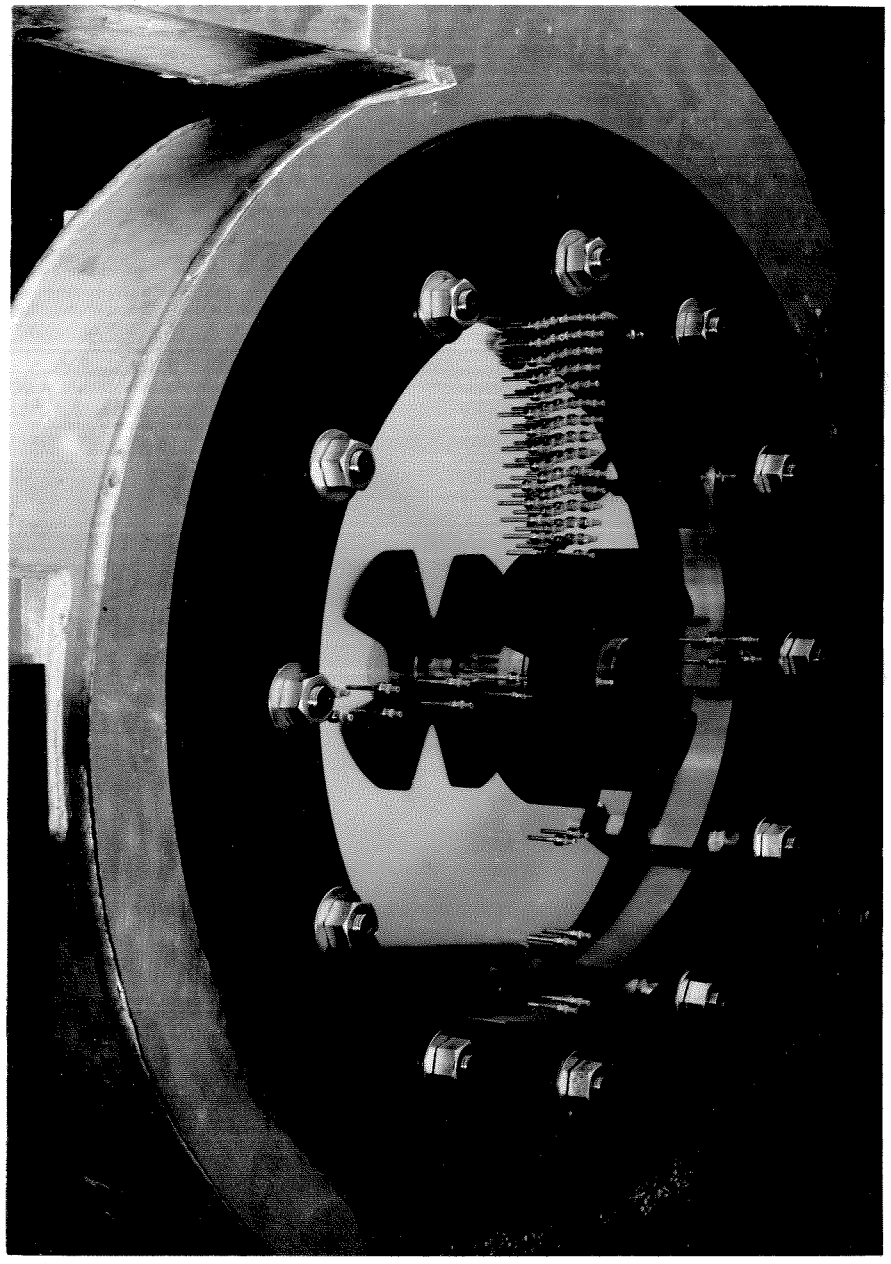

Figure III.6. Photograph of Test Section.

pitch is set by aligning the vane tip with a transparent gauge, not shown, which may be moved from vane to vane. The rounded circumferences of the acrylic side walls act as a nozzle for the entering flow.

The flow passes out of the working section radially into a stainless steel exit section. This exit section is similar to the one in the small apparatus and contains a screen of high solidity to make the velocity distribution uniform and prevent loss of the beads. The photograph in Figure III.6 was taken before the screen was installed and shows the supporting part of the exit section. Installation of the screen consisted of winding a wire spacer around the exit section and soldering the screen to this spacer. After passing through the screen, the liquid flows through the slots shown in the photograph and then out axially through the exit section. The exit section is supported by large steel flanges notched to allow observation of the flow near the screen. The flow passes out of the exit section and into a diffuser with 15° included angle and then into the piping loop. Separation in the diffuser is hindered by the presence of a perforated plate at the large end and a cross-shaped flow divider.

Because of the high pressure in this device (100 psi maximum), the load-bearing members (the vane shafts and exit section) were made of hardened stainless steel. The large steel flanges on the exit section were required to distribute the load across a section of each side wall. The acrylic plastic side walls were 2.6 inches thick to support the bending loads imposed by fluid pressure.

Provision was made for placing the axis of the working section either horizontally or vertically. However, because of the expected

difficulties of viewing the flow and removing the particles with the axis vertical, experiments were only performed with the axis horizontal.

A total of 103 pressure taps are located in one of the acrylic side walls, arranged in groups in each 90° quadrant. One group of 79 taps is located at 0.2-inch radial intervals from 2.0-inch radius to 3.6-inch radius and at 0.1-inch radial intervals from 3.6-inch radius to 10.6-inch radius. The other three quadrants have 8 taps each located at the same radii as selected taps from the first group. The first group provides information on pressure variation with radius; the other groups provide a check of flow symmetry. Each pressure tap has a 0.016-inch diameter orifice at the wall and is connected to a pressure measuring system with quick disconnect fittings and semi-rigid nylon tubing.

The pressure measuring system consists of a complex solenoid valve network, a single differential pressure transducer, and a sequencing computer to operate the system. Appendix C contains a more detailed description of the system and its operation.

Values of some of the major parameters of this entire apparatus are listed in Table III.1.

This entire apparatus was designed around the characteristics of 1/8-inch diameter nylon balls. These balls, identical to the ones used in the smaller annular bed, are readily available and have excellent tolerances. With these balls, the theoretical equilibrium radius for a single particle can be varied over the entire working section by setting $\frac{V_e}{V_r}$ at values within the range of 5 to 17.

TABLE III.1

LARGE ANNULAR CHAMBER CHARACTERISTICS

motor capacity	30	H.P.
maximum operating pressure	100	P.S.I.
maximum operating flow rate	500	G.P.M.
working fluid	Water	
vane circle radius	12.0	inches
exit section outside radius	1.375	inches
test section axial length	1.6	inches
acrylic side wall thickness	2.6	inches
$\frac{V_\theta}{V_r}$ in plenum	30.0	
$\frac{V_\theta}{V_r}$ at vane entrance	8.0	
$\frac{V_\theta}{V_r}$ in working section	5 to 25 (by adjustment)	
number of pressure taps	103	
pressure tap orifice diameter	0.016	inches

A laser concentration meter was developed to provide a means of measuring concentration gradient with radius. It operates on the principle that a beam of light will be attenuated a predictable amount while passing through a cloud of known properties. A complete description of this device is provided in Appendix D.

The experiments performed here included visual studies of the orbits of single particles including nylon balls of various sizes and other plastic balls. In addition, dye injection tests were performed at various radii to confirm the boundary layer characteristics. Several data runs were performed with various concentrations of 1/8-inch nylon balls. In each data run, a pressure survey was made, and the local concentration of beads was measured as a function of radius. (For comparison, several data runs were made without particles.)

Each data run took a minimum of two days to perform. One day was required for the pressure measurements and a second was required for concentration measurements. The procedure was started by aligning each vane with the optical gauge and tightening all of the test section seals. Next, the pressure measuring system was cleaned out and all air purged from the system. Each pressure tap was checked for clogging individually and purged with clean water at least 4 times. The test loop was filled and drained and then filled again to provide a clean working fluid. The flow was then started. Any air entrained during start-up was eliminated at the air-water interface. The air-eliminating process took a minimum of 2 hours to accomplish. After a final check for air in the pressure measuring system, a data run was started. The pump was brought up to speed and the control system was locked in at

the desired flow rate. After allowing several hours for thermal equilibrium, the pressure measuring sequence was started. The sequencing computer cycled through 74 pairs of pressure taps measuring the pressure difference between each pair. For each measurement the pressure transducer was integrated over a period of 20 seconds. All of the measurements were completed in about one hour.

The apparatus was then shut down and some beads were added to the plenum chamber. After allowing another two hours for the beads to absorb water, the system was started up and run for an hour to obtain thermal equilibrium. The same pressure measuring sequence was used again. Visual observations of the flow were also made.

The concentration measurements were usually made on a different day due to the time required for the pressure measuring part. After the usual preliminaries, the pump was brought up to speed and the measurements started. For each measurement the laser was carefully aligned so that the beam passed through the chamber parallel to the axis. The photodiode assembly was positioned on the other side of the test section and carefully aligned with the beam. The reading was integrated over a period of 20 seconds and then recorded. The laser was then moved to the next position and the procedure repeated. About 40 measurements were taken at different radii. The radii were taken in approximately $\frac{1}{2}$-inch steps and then interlaced so that no time-wise variations would appear in the data.

The volume of beads used for each experiment was measured by water displacement in a calibrated cylinder. The beads were dried before measurement so that no water adsorbed on the surface was measured

erroneously. They were also dried afterward so that they could be poured into the test section smoothly.

The venturi meter pressure taps were connected to the pressure measuring system and thus the flow rate was monitored during the experiments. Typically, the venturi pressure drop was measured once before, twice during, and twice after each data run.

The data were manually recorded from the integrating digital voltmeter and punched onto cards for data reduction on a large computer.

CHAPTER IV

RESULTS AND COMPARISON WITH ANALYSIS

A. Small Annular Chamber

1. Qualitative Results

The experiments on the small annular fluidized bed showed that the basic operating principle of the device was valid and that particles could be hydrodynamically supported. However, they also demonstrated the difficulty of obtaining axisymmetric flow.

The dye injection through pressure taps in the side wall was of limited utility in visualizing the secondary flow. The flow was highly turbulent and the plume dispersed so rapidly that only large variations in plume direction could have been seen. As the flow rate of dye was varied from zero up to quite large values, the direction of the plume remained roughly the same both with and without particles in the flow. (In the tests with particles it was difficult to see the plume at all.)

In order to compare the single particle orbits calculated in Chapter II with experiment, a few particles were placed in the flow. For the nylon balls, the equilibrium radius of the particle orbit was calculated to be about 10 inches. Since the outside radius of the chamber was only 6 inches, the balls were expected to scrape along the outer cylindrical wall. However, the actual particle orbits were greatly different. The particles were seen to traverse the entire chamber. Sometimes they would even strike the screen on the exit section. This behavior was due to the asymmetry of the flow created by the two flow inlets. As the particles moved through the chamber they passed

through regions of both high and low circulation. Thus, they never reached equilibrium.

Tests were also done with higher loads of particles, but the head rise of the pump limited the experiments to relatively low concentrations. As the flow was started, the particles moved immediately to the screen and formed a packed bed with very high flow resistance. As the flow increased, the particles on the outside were pulled away and the pressure drop across the packed bed decreased. This allowed a higher flow rate and even more particles were pulled away. The process continued until all of the beads were suspended. However, with higher loads of particles, the flow resistance of the initial packed bed was too great to allow this process to progress. Consequently, the packed bed remained on the screen and the fluidized bed was not formed. The highest concentrations which could be used without a packed bed on the screen were 15 percent for the glass beads and 2 percent for the nylon balls. If slightly higher concentrations were used, a small packed bed formed on the screen. As the concentration was increased further, the packed bed increased in thickness and the flow slowed down.

Figure IV.1 is a photograph of the system in operation with glass beads. There is a region of low concentration of beads near the screen. Outside of this region the concentration appears to be substantially higher. The problems of symmetry can be seen in the vicinity of the flow inlets. In addition, there is a small area of low concentration along the upper boundary of the chamber. This shows that gravity is still important in determining the particle behavior. The ratio of centripetal acceleration to gravitational acceleration on the outside

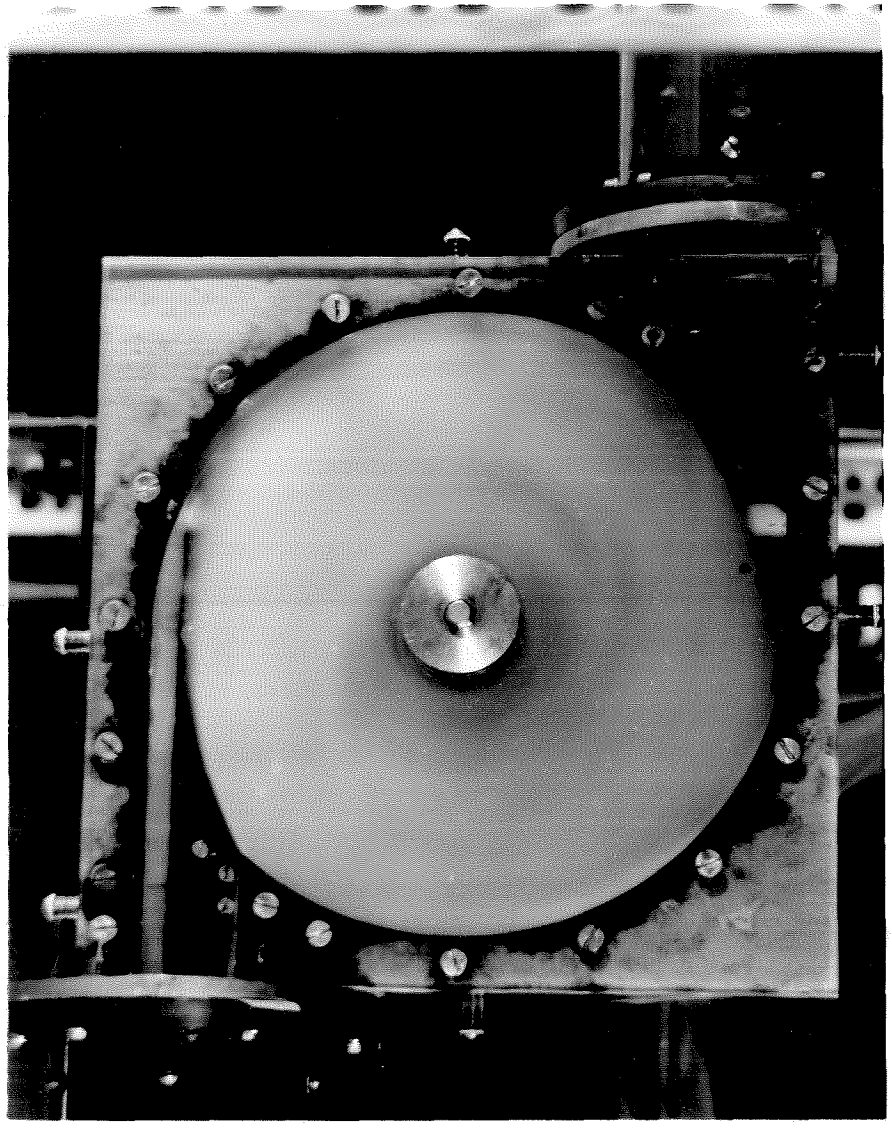

Figure IV.1. Photograph of Small Annular Chamber in Operation.

radius of the chamber is about 1.7. Substantially higher centripetal acceleration is necessary to eliminate this asymmetry.

After several data runs, the screen on the exit section was severely damaged. In addition, the nylon balls were abraded. The velocity of the water near the screen was about 35 ft./sec. The component in the tangential direction was about 34.9 ft./sec. Thus, if the particles move at the same tangential velocity as the fluid, they scrape along the screen at very high velocity. This phenomenon produced the abrasion of the screen and particles.

2. Quantitative Results

The quantitative experiments consisted of the measurement of the static wall pressure as a function of radius for flow of water and for suspensions of glass beads and nylon balls in water. The pressure taps on each of the three radial lines were located at $\frac{1}{2}$-inch intervals from 2.5 inches to 5.0 inches radius. If the flow were axisymmetric, the pressures would be the same at corresponding pressure taps along each radial line. However, the results showed significant differences between the 3 groups of pressures measured. Although the pressure gradients for each group were about the same, the magnitudes of pressures measured did not agree well. At the outside pressure taps the differences in pressures from one radial line to the next were the same order of magnitude as the pressure differences between radially adjacent pressure taps.

The presence of the particles had a pronounced effect on the pressures. Figure IV.2 is a plot of pressure against the inverse of the radius squared for flow of water, and suspensions of glass beads

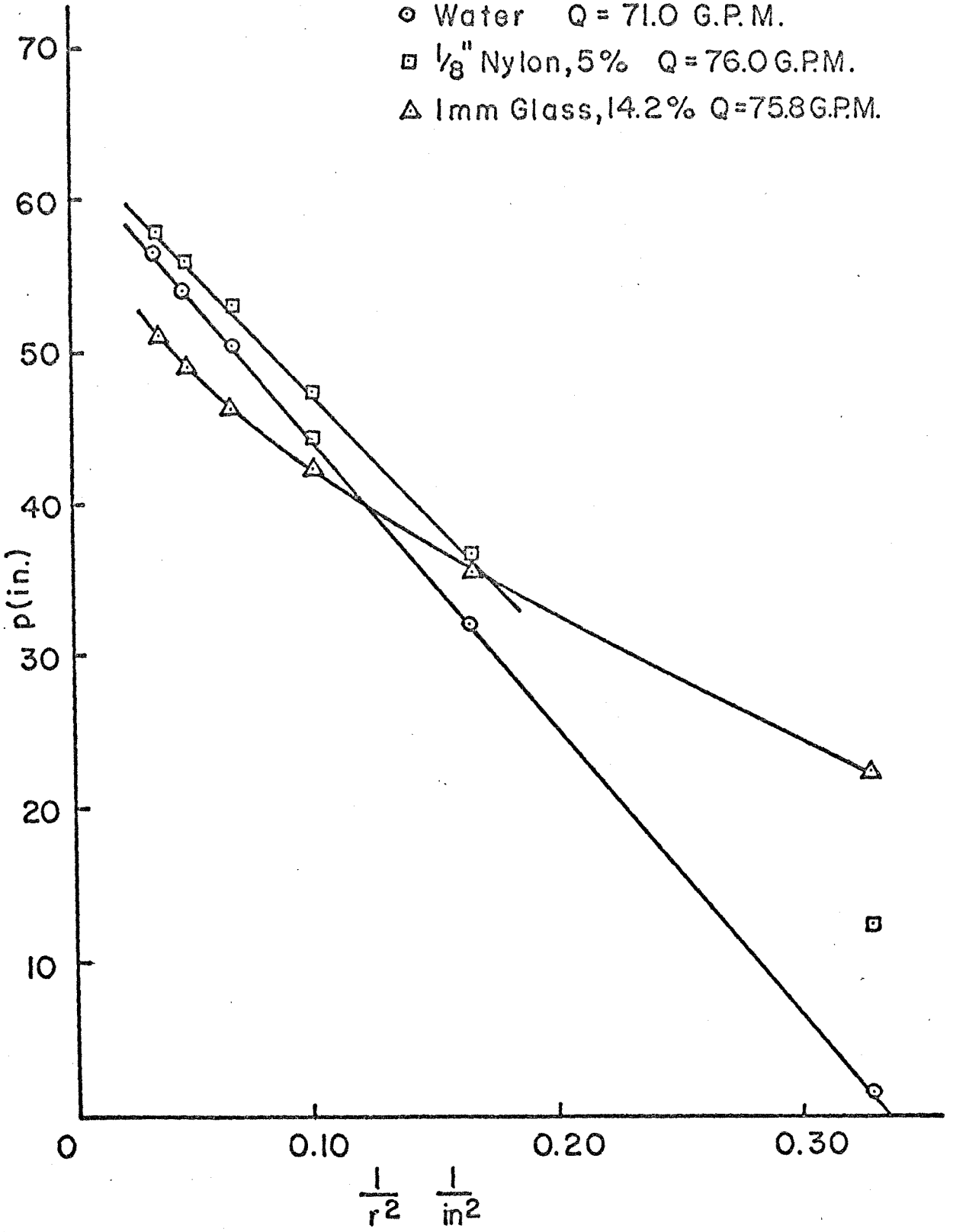

Figure IV.2. Plot of Pressure Against the Inverse of the Radius Squared--Small Annular Chamber.

and nylon balls. The data shown were taken from one group of pressure taps in a radial line. The data for water fit a straight line almost perfectly. A straight line on these coordinates is equivalent to constant circulation. Thus, the viscous effects are negligible. The data for the suspensions show that there is an appreciable loss of circulation due to shear stresses.

The ratio of tangential to radial velocity can be determined from the slope of the line drawn through the data. This ratio is about 14 for water flow, and it varies with radius for the suspensions. The chamber was designed to produce a ratio of 10. It was assumed that the flow entered tangentially over the entire area of the inlet channels. However, it is apparent from Figure IV.1 that the vortex flow in the chamber reduces the effective area of the inlets thus raising the ratio of tangential to radial velocity.

B. Large Annular Chamber

1. Observations

Flow of Water

In the course of the experiments, the apparatus was operated over a range of flow rates and inlet blade angles. The system was found to have pressure oscillations, as measured by a gauge attached to the plenum. At low flow rates, the pressure was essentially constant. At higher flow rates the needle on the pressure gauge indicated variations in pressure which increased with flow rate. When the plenum pressure was 60 P.S.I., the pressure fluctuations were about $\pm$ 5 P.S.I. as read on the gauge.

These pressure fluctuations were the result of several phenomena. First, at high flow rates the pressure in the exit section dropped below atmospheric pressure. This is a result of the diffuser mounted downstream. When the pressure dropped far enough beneath atmospheric pressure, cavitation bubbles were produced causing oscillations. Pressure measurements at both ends of the diffuser confirmed that at high flow rates the pressure was indeed less than atmospheric. At high flow rates the sound of the collapse of the cavitation bubbles could be heard as a hissing sound emanating from the exit section. To confirm the presence of cavitation, the air-water interface was isolated from the system and the static pressure was raised with a nitrogen bottle. As the pressure was raised, the noise decreased, thus confirming the cavitation.

The second reason for these pressure fluctuations is separation of the diffuser. There are two diffusers in the system. The diffuser downstream of the exit section has an included angle of 15 degrees and a ratio of areas at either end of the diffuser of 4. Differential pressure measurements over the diffuser length showed that the recovery was about 25 percent indicating separation. A cross-shaped flow divider was placed in the diffuser and a perforated plate was added at the downstream end. This increased the pressure recovery to about 50 percent and significantly reduced the pressure fluctuations. The other diffuser is located on the inlet to the plenum. It has an included angle of 10 degrees, a square cross-section, and a ratio of areas of 3. The diffuser is mounted on the downstream side of the venturi meter and has a transition from a round pipe to the square diffuser shape at the inlet.

The performance of the diffuser near the exit section has a greater effect on the flow than the other diffuser because of the smaller cross-sectional area and corresponding larger recoverable head.

At 300 G.P.M. flow rate, the total recoverable head for the exit section diffuser is 5.93 P.S.I. while for the other diffuser it is 1.14 P.S.I.

Dye was injected into the chamber to visualize the secondary flow. Unlike the tests in the small annular chamber, these tests gave definite indication of secondary flow. Dye was injected from some of the side wall pressure taps. The tests were done at $\frac{V_\theta}{V_n} = 15$ as determined from the vane setting. The angle that the plume made with a tangent to a circle with center at the axis was measured approximately. At a pressure tap near the outside of the chamber (9.9-inch radius), the angle was 10° regardless of the flow rate of dye. However, at a pressure tap closer to the axis (4.9-inch radius), the angle was 40° for low flow rates and 20° for high flow rates. This indicates that the fluid within the boundary layer does have a substantial radial component. It should be noted that the flow was highly turbulent and that the angles quoted are only approximate.

As a test of symmetry, the chamber was filled with a mixture of dye and water. When the flow was started, the interface of the colored water and clear water coming in from the plenum was observed. The starting vortices could easily be seen. Flow was observed to come through each inlet evenly and the interface reached the screen at the same time around the entire circumference. It was found that the optical tool used to position the vanes produced a vane to vane

variation of as much as 0.010 inch. Since the width of each inlet varied from .260 to .49 inch for these experiments, the widths of each channel can be assumed to be essentially equal.

Single Particle Orbits

Tests were run with a few 1/8-inch diameter balls over the full range of flow rates and vane angles. Although the calculated equilibrium orbits ranged from 9.0 to 22.5 inches, the actual behavior of the particles was the same for each test. Like the tests in the smaller annular chamber, the balls moved over the entire volume of the chamber. Occasionally they would collide with the vanes and the screen on the exit section. These collisions produced audible clicks. Figure IV.3 is a photograph of the movement of the beads. A strobed light source produced pulses at the rate of 400 per second. The vanes were set to give $\frac{V_\theta}{V_r} = 15$ and the flow rate of water was about 200 G.P.M. The direction of flow is counterclockwise. There are several balls moving in essentially circular orbits. However, there are also particles moving in oblique orbits. Note that the particles that are moving inward are decreasing in radius rapidly.

In Chapter II the side-wall boundary layer was analyzed for laminar flow. The results indicated that the maximum boundary layer thickness for $\frac{V_\theta}{V_r} = 15$ and 100 G.P.M. flow was the order of 0.06 inch. Here the flow rate is greater and since the boundary layer thickness is related to the flow rate the thickness can be calculated to be about 0.04 inch. Inside the boundary layer, the ratio of tangential to radial velocity is much lower than in the main flow. This boundary layer thickness is valid only for laminar flow. Nevertheless, the thickness

Figure IV.3. Photograph of Particles at Low Concentration.

calculated is of the same order of magnitude as the particle radius. If a particle moved near the wall, it would be affected by the boundary layer and swept rapidly into the center. Near the screen the flow is uniform because of the high solidity of the screen. Thus, a particle in this region will spiral outward seeking its equilibrium position. This seems to fit the photographic observations.

During high speed operation, the movement of the particles was difficult to follow by eye. When the flow rate was slowed down to 100 G.P.M., the individual particles could be easily tracked. The particles were observed to have near circular orbits at about a 4-inch radius. The particles were seen to move in these orbits many times, say 50, slowly increasing their radius before darting in toward the center.

The nylon balls were examined after running the apparatus for several hours. The surfaces of the balls were severely abraded. This, again, is a result of their high velocity movement along the screen. At 200 G.P.M., the tangential velocity at the screen surface was almost 70 ft./sec.

Tests were also run with larger nylon balls (3/16 and 1/4-inch diameters) and a large plastic ball (5/8 inch in diameter). The behavior of these balls was similar to the smaller balls and no equilibrium circular orbits were obtained. It is again suspected that the boundary layer is responsible for the instability. However, the other possibility is that in turbulent flow, circular orbits are not stable. The stability was studied only for laminar flow and may not be indicative of turbulent flow.

High Concentration

Tests were run with overall concentrations ranging from 0 up to about 12 percent over a range of flow rates. The behavior at start-up was similar to that observed with the smaller chamber. At low flow rates the particles packed against the screen, and as the flow rate increased, they were pulled off and became hydrodynamically suspended. The problem of the bed failing to spin up, however, was not observed. It should be noted that in the tests with the small chamber the bed did not spin up for overall concentrations greater than 2 percent with nylon balls.

Once the bed reached steady state, the concentration of particles appeared to vary with radius. Figure IV.4 is a photograph of the apparatus operating with a packed bed at the inner screen. It was taken with a strobe light with very short duration to stop the motion. At the outside, near the vanes, the concentration is near zero. The concentration increases as the radius decreases in a smooth manner to a packed bed several particle diameters in thickness at the inner screen. Outside the packed bed, the next row of balls is moving very slowly along the surface. They move in unison as they inch along the packed bed surface. The next several rows of balls are moving at very high speed, although the rows are clearly discernible.

For lower bed loads, the concentration reached a maximum and then decreased toward the screen. In the vicinity of the screen the concentration appeared almost zero with a few rapidly moving particles scraping along the screen. It was found that sustained operation in this mode resulted in severe abrasion of the particles and destruction

Figure IV.4. Photograph of Particles at High Concentration.

of the screen. During several runs the screen was destroyed, allowing particles to pass out of the chamber.

Since the flow rate and vane angles could be varied, the ratio of centripetal acceleration to gravitational acceleration could also be varied. This ratio was a maximum of 3 at 12-inch radius, and a maximum of 24 at 6-inch radius. (This compares to a ratio of 1.7 for the small chamber at 6-inch radius.) At high speeds, there was no discernible gravitational effect anywhere in the bed. This maximum value of the ratio of centripetal to gravitational acceleration could be obtained with all vane angles used due to the pump characteristics. However, at lower flow rates the same gravitational effects on particle orbits were noted as in the smaller chamber.

Occasionally near the outside of the chamber, a clump of particles at higher than the local concentration would form. This clump was visually discernible and made several revolutions around the axis before disappearing. The concentration of this clump was only slightly larger than the rest of the suspension, and its linear dimensions were of the order of 2 inches. It was common for several clumps to be present at the same time at different points along the circumference.

A possible explanation of these clumps is that if, due to turbulent fluctuations, several particles in the suspension were closer together than the rest, the radial component of flow would be diverted around rather than through the clump. This would result in a lower drag force on the clump and it would move outward. This same phenomenon exists in vertical fluidized beds.

Aside from the clumps of particles, there was no sign of any asymmetry due to the finite number of flow inlets.

2. Pressure Measurements

The first measurements were of the differential pressures across 0.1 or 0.2-inch radial increments. It was found that slight mislocation of the pressure taps resulted in large scatter in the data. The pressure taps were drilled on a machine capable of positioning the drill bit with ± 0.001 inch. However, since the drill bit was small, some wandering is expected. If each pressure tap were located within 0.005 inch of the ideal position, the error in the difference in radii could be as much as 10 percent. This error was reduced in subsequent experiments by measuring the pressure differences between pressure taps 0.5 to 0.6 inch apart.

The data were reduced by application of Equation 2.110. The flow rate was determined from the calibration curve supplied by the venturi manufacturer. The first derivative of pressure with respect to radius was assumed to be the differential pressure divided by the radial distance between pressure taps. The average density for the suspension was taken equal to that of water. This is a good assumption since the particles were only slightly more dense than water. (For instance, at 30 percent concentration, much higher than considered here, the error introduced by this assumption is only 4 percent.)

A digital computer was used to perform the arithmetic and to plot the results. The results were expressed as a plot of $\frac{V_\theta}{V_r}$ against radius. This format was chosen because it allows easy comparison of runs at the same vane angle but different flow rates.

Twenty-eight runs were performed at various blade angles, flow rates, and concentrations of particles. For 13 of these runs both pressure and concentration measurements were made. For some of these runs measurements were also performed without particles. The remaining 15 data runs were quite similar to the others except that they were either pressure or concentration measurements alone, or were performed merely for calibration purposes.

The results for the 13 complete data runs appear in Appendix E. Table E.1 summarizes the operating parameters for each run. Some of the parameters listed require explanation.

The vane gap is the minimum clearance between two adjacent vanes. It determines the ratio of $\frac{V_\theta}{V_r}$ for the annular chamber. It was determined by measuring the distance with a hole gauge and thus calibrating the optical gauge. These measurements were performed prior to assembly of the test section.

The nominal value of $\frac{V_\theta}{V_r}$ was calculated from momentum considerations assuming the flow entered the chamber at the tangential velocity corresponding to the flow rate divided by the total area of the inlet channels. The observed values of $\frac{V_\theta}{V_r}$ were deduced from the pressure measurements. Although agreement of these numbers is better than for the small chamber, the deviations at small vane gaps are substantial. The deviation is of opposite sign to the deviation noted in the small bed. Appendix E also contains the plots of $\frac{V_\theta}{V_r}$ against radius and the calculated concentration distribution for each of the 13 runs. The following discussion will refer to several of these figures.

Figure E.26 contains the results of Run 11 without any particles present and is typical of the behavior of many of the tests without particles. The ratio of tangential to radial velocity is proportional to the circulation for a given flow rate. Consequently, Figure E.26 may be interpreted as a plot of circulation against radius. The large fluctuations at large radii are produced by non-uniformities of the flow introduced by the finite number of vanes. These fluctuations die out in a short distance. It is expected that the wall shear stress will reduce the circulation as the flow moves inward toward the screen and most of the data confirms this. The peak values occur at a radius of about 8 inches. The reduction in circulation amounts to 15 percent (from the peak to the smallest value measured). In the small annular chamber there was no perceptual loss in circulation with water alone. However, due to the inaccuracies in the data, a reduction in circulation of only 15 percent would not have been measurable.

For radii greater than 8 inches, the slope of the curve is the opposite of the slope at smaller radii. This surprising phenomenon was present in all of the measurements taken without particles and indicates, on face value, a wall shear stress in the opposite direction as the velocity. It was expected that $\frac{V_\theta}{V_r}$ would decrease monotonically as the flow passed through the chamber. The explanation is found in the boundary layer analysis. As shown in Chapter II, the local pressure gradient is determined by the square of the mean velocity averaged across the cross-section. Although the inlets to the chamber are designed for continuously accelerating flow, there is still appreciable boundary layer build-up in the channels. The flow in the boundary

layer enters the chamber at lower tangential velocity than the main flow. Thus, the flow at very large radii contains a core of fast moving fluid and two boundary layers with fluid moving slower. As shown in the boundary layer calculation, the growth of the boundary layer occurs mostly in the outer region. Consequently, this low velocity fluid becomes the secondary flow in the boundary layer. This has the effect of increasing the average value of the tangential velocity in the chamber at smaller radii and produces the rise in the $\frac{V_\theta}{V_r}$ curve noted.

Figures E.30 and E.32 are the results for Run 13 with and without particles respectively. In the test with particles, the fluidized bed was operating with no packed bed at the screen and the concentration of beads at large radii was near zero. The concentration rose to a maximum of 12 percent at about 8-inch radius and then decreased near the screen. The results of this run are typical of annular bed performance without a packed bed at the screen. The difference between the behavior with and without particles is substantial. In the region of highest concentration the slope of the data is quite steep indicating high wall shear stress.

Figure E.13 is the plot obtained for Run 6 with particles. In this run there was a packed bed against the screen extending out to 2.25 inches radius. Outside of the packed bed there were several rows of beads moving in unison at very slow speed. The remainder of the beads were moving at high speed. The concentration for this run rose monotonically with decreasing radius to the packed bed condition at the screen. The slope of $\frac{V_\theta}{V_r}$, which is an indication of wall shear

stress, becomes greater with decreasing radius and is at its steepest at about 3.3 inches. The values of $\frac{V_\theta}{V_r}$ for smaller radii appear large because of the large pressure losses in the dense suspension near the packed bed. The data reduction program which plotted the data in Appendix E depends on pressure drop alone and attributes the increased pressure drop in the stationary packed bed to increased circulation. The circulation is actually reduced in this region reaching essentially zero near the surface of the packed bed. The dotted curve shows the expected actual values of $\frac{V_\theta}{V_r}$. This response is typical of the runs with a packed bed at the screen.

3. Concentration Measurements

Appendix E also contains the results of the concentration measurements. The data were reduced using the calibration curve obtained for the vertical fluidized bed of square cross-section (see Appendix D). As a check of the accuracy of the data, the volume of balls in a radial increment was integrated across the chamber to obtain an estimate of the total. This was compared with the volume actually measured by water displacement. The difficulty with this procedure is that concentration measurements could not be made very close to the screen because of the high concentration of particles. (The concentration meter could only measure concentration less than 30 percent.) Thus, the measured concentrations were extrapolated to obtain the total volume of beads in the chamber. Despite the limitations of the method, the results agreed fairly well. The deviation was at most 20 percent, and was usually within 5 percent.

The analysis in Chapter II predicts that the concentration should be a monotonically decreasing function of radius for all annular fluidized beds where the particles are hydrodynamically supported and the Reynolds number based on superficial velocity and particle diameter is greater than 500. The Reynolds numbers for all of the runs was greater than 500 at 9.4-inch radius. For most cases it was greater than 500 over the entire bed.

Figure E.31 in Appendix E contains the results for Run 13. For this run there were no beads packed against the screen. Since the concentration goes to zero at large radii, it can be assumed that the particles are hydrodynamically supported. However, the concentration does not increase monotonically for decreasing radius. It first increases rapidly from zero as the radius decreases reaching a maximum at a radius of 8.5 inches. For smaller radii, the concentration decreases monotonically reaching a relatively low level at the screen. As stated in Chapter II, this behavior is indicative of the formation of side-wall boundary layers. The discontinuity in concentration predicted by the theory cannot exist in a real annular bed because the particles near the discontinuity become caught in the secondary flow developing at the discontinuity and are swept into the center. Thus, in the outer region the particles are hydrodynamically supported by the fluid in the manner presented in Chapter II, and in the inner region they are strongly influenced by the secondary flow in the boundary layer. It is expected, though not verified by experiment, that the particles in the inner region were circulating inward in the boundary layers and outward in the center. Run 13 is the only run presented in which

particles were not packed against the screen. The high velocity movement of particles moving near the screen in this run caused severe damage to the screen and greatly abraded the particles. This precluded other runs without a packed bed at the screen.

Figure E.9 contains the results for Run 4 where there was a packed bed at the screen. As predicted by analysis, the concentration rises monotonically with decreasing radius. The analysis, however, was for particles totally suspended by the fluid. Since there was a packed bed against the screen, at least some of the particles were not hydrodynamically supported.

To examine the effect of the packed bed on the suspension of particles at larger radii compare Runs 4 and 5 which are identical except that Run 5 has a heavier load of particles (750 ml. versus 507 ml.) and hence a slightly smaller flow rate (since the pump speed was maintained constant). Figure E.12 contains the results for Run 5. The concentration plots are identical for large radii and only diverge at radii less than 4.0 inches. It is apparent that the effect of the packed bed on the hydrodynamic suspension of the particles is limited to the region near the packed bed. Thus, the equations used to calculate equilibrium orbits as a function of concentration should produce reasonable results for radii more than 4.0 inches in this run. The only evidence of this phenomenon in the plots of concentration against radius is the rapid increase of concentration and change in slope of the data in this region.

Run 9 illustrated in Figure E.21 demonstrates another phenomenon of the behavior of annular fluidized beds with packed beds at the screen.

The plotted data for concentration versus radius are similar to the data from Runs 4 and 5 except for the flat spot from 4.0 to 6.0 inches radius. The ratio of tangential to radial velocity for this run is higher than for Runs 4 and 5 and results in a more rapid increase of concentration with decreasing radius at large radii. For small radii the concentration rises rapidly approaching the packed bed. The flat spot is probably a result of two effects. First, as in the case with no packed bed at the screen, a discontinuity in concentration predicted by analysis results in the leveling off of the concentration. However, the pressure drop of the flow through the packed bed tends to hold particles in the bed. In between the packed bed and the hydrodynamically supported particles there is a region where particles are moved about by the secondary flow. Again the extent of the effect of the packed bed on the other particles may be determined by examining a similar run with more particles.

Run 11 is similar to Run 9 except that it has a bead load of 1102 ml. as opposed to 900 for Run 9. Figure E.25 contains the results of Run 11. The plot of concentration against radius is quite similar to Run 9 except that the point at which the concentration rises rapidly has been shifted outward from 3.5 to 4.5 inches. Thus it appears that the extent of the region of constant concentration is merely decreased by the addition of particles.

These results can be generalized to explain the concentration distribution for an annular fluidized bed as the load of particles is varied. Figure IV.5 shows the expected relationships. At very light loads the concentration of particles is almost independent of radius.

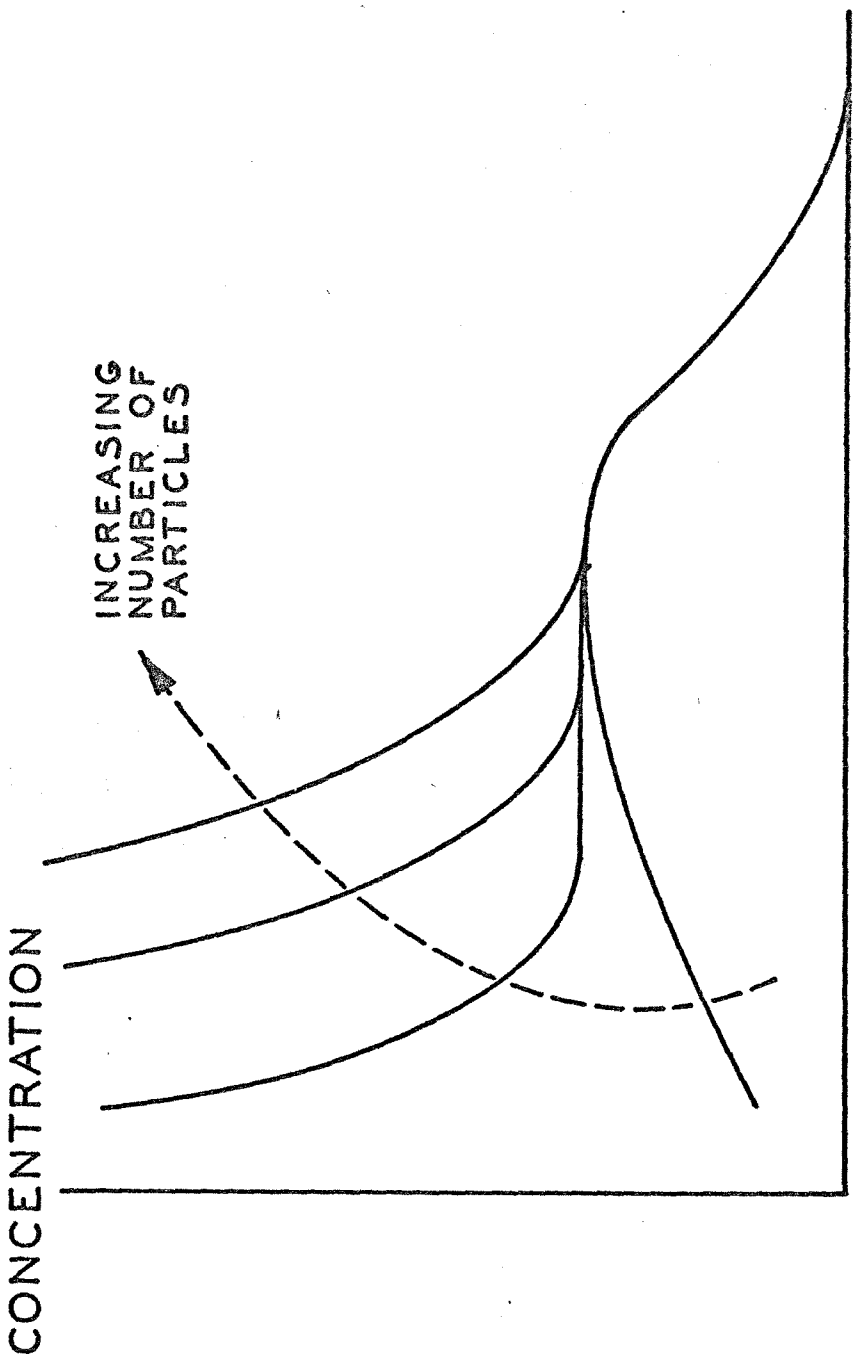

Figure IV.5. Expected Concentration Distribution in an Annular Fluidized Bed.

The boundary layer dominates the flow and particles can be found everywhere. As the load of particles rises, the effects of the secondary flow decrease and the particles in the outside of the bed become hydrodynamically supported as described in Chapter II. The particles at smaller radii are still affected by the secondary flow. As the load increases further, the additional particles form a packed bed at the screen and the area between the outside region where the particles are hydrodynamically supported and the packed bed becomes a region of uniform concentration where the particles are influenced by the secondary flow. If the load of particles is increased even more, the additional particles increase the thickness of the packed bed and decrease the extent of the region of uniform concentration.

The flow rate of liquid through the chamber seems to have little effect on the positions of the particles. This is probably due to the fact that the Reynolds number is so high that the drag coefficient of the particles is almost independent of Reynolds number. (In the Reynolds number range of 500 to 7500, the drag coefficient varies less than 10 percent from 0.42.) Several of the runs described in Appendix E were identical except for the flow rate. The differences in the $\frac{V_\theta}{V_r}$ and concentration data for those runs are negligible. However, the value of $\frac{V_\theta}{V_r}$ does have an important effect.

Runs 8 and 13 are identical except that in Run 8 $\frac{V_\theta}{V_r} = 16$, and in Run 13 $\frac{V_\theta}{V_r} = 20$. The results for these runs are shown in Figures E.19 and E.31 respectively. Although both runs have the same load of particles, Run 8 with the lower value of $\frac{V_\theta}{V_r}$ has a packed bed while Run 13 does not. The effect of increasing $\frac{V_\theta}{V_r}$ is to increase

the equilibrium radius of the particles at a given concentration. However, note that the equilibrium radius for zero concentration is hardly changed at all. This may be due to the finite size of the bed and the interaction of the particles with the inlet flow streams. The next section will discuss an attempt to correlate these data with the analysis in Chapter II.

4. Correlation of Wall Shear Stress and Drag Coefficient With Concentration

Wall Shear Stress

In Chapter II it was demonstrated that the wall shear stress coefficient for an annular fluidized bed could be calculated from the static pressure measurements through the equation

$$f = -\pi \frac{d}{dr}\left(\frac{V_r}{V_\theta}\right) \tag{4.1}$$

This procedure is equivalent to a second derivative of the pressure with respect to radius and hence is almost impossible to do accurately. In order to calculate the derivatives in a systematic manner, the data were fitted to polynomials of powers of radius for each data run. The polynomials were of the form

$$\frac{V_r}{V_\theta} = a_0 + a_1 r + a_2 r^2 + \cdots \tag{4.2}$$

where the coefficients a_i were determined from a least-squares analysis. For each data run polynomials of order 2 through 6 were tried. The best fits were obtained with fifth order polynomials for all data runs except Run 13, for which a sixth order polynomial was the best fit. The order of the polynomial was selected by plotting the data and curves of best

fit of each order and choosing the curve which seemed to give the best approximation. The differentials of the polynomials give wall shear stress coefficient directly.

The concentration of particles for each run was known for a selected number of radii as shown in Appendix E. In order to correlate the shear stress coefficient with concentration, both were evaluated at $\frac{1}{4}$-inch intervals over the range of available data. (The concentration was evaluated by interpolation.) Since the slope of measured values of $\frac{V_\theta}{V_r}$ shown in Appendix E become zero or even negative at large radii, some of the wall shear stress coefficients calculated from the polynomials at large radii were negative. Negative values have no significance in this calculation and hence they were neglected.

Figure IV.6 shows the correlation on logarithmic coordinates. Note that the abscissa is the voidage (one minus the concentration) and a different symbol has been used for each data run. The arrow shows the approximate wall shear stress coefficient for turbulent flow in a pipe at Reynolds number $R_\ell = \frac{V_\theta \ell}{\nu}$.

The correlation is not very good. Although there is a trend toward higher shear stress at higher concentration for all of the runs collectively, the trend is not borne out for the individual data runs. All that can be said is that the level of the wall shear stress coefficient is within the same order of magnitude as the coefficient for flow in a pipe at the same Reynolds number.

It should be noted that wall shear stress coefficients could also be determined for the flow without particles. However, the slopes

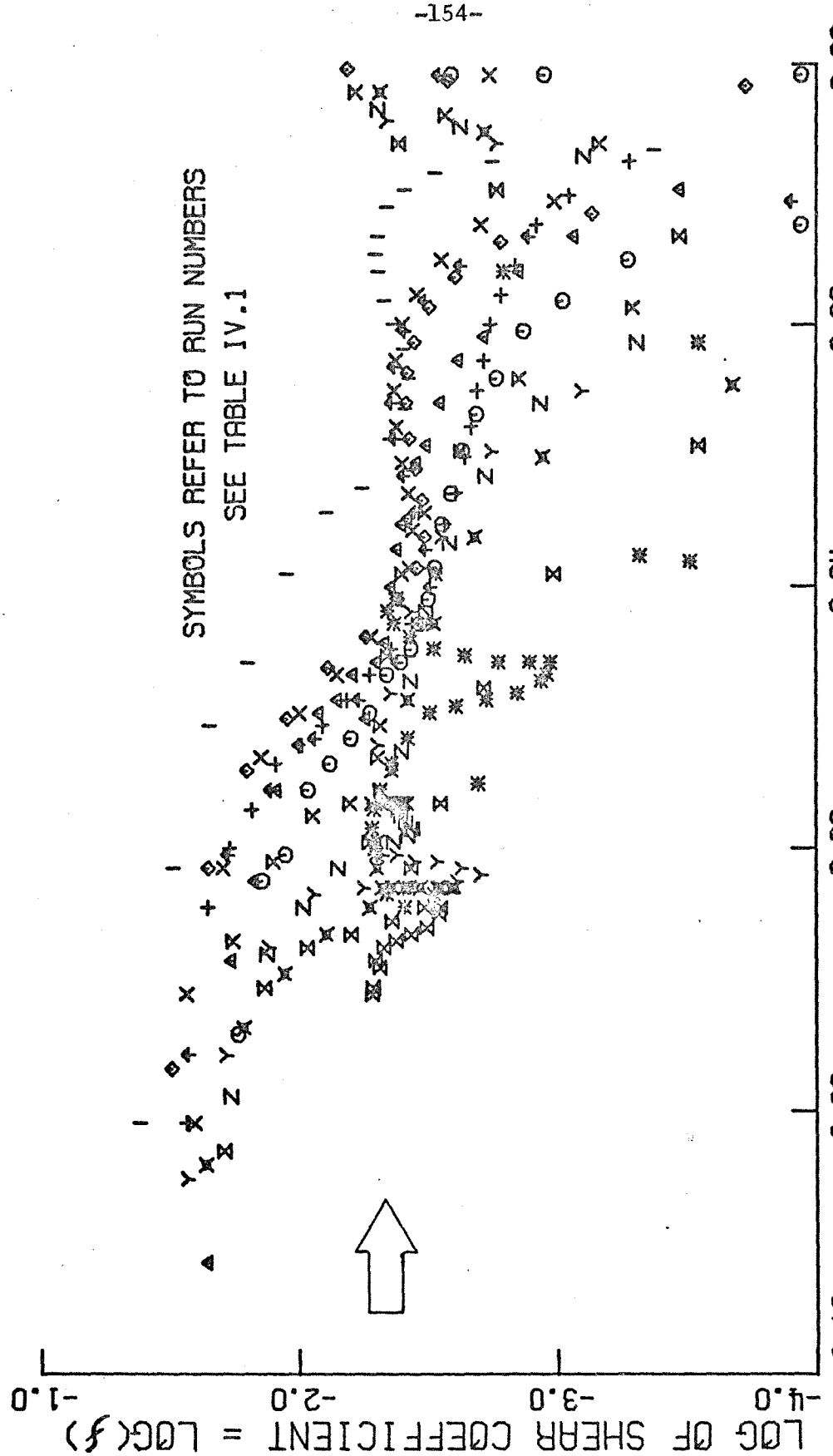

Figure IV.6. Correlation of Wall Shear Stress with Concentration.

TABLE IV.1

SYMBOLS FOR FIGURES IV.6 AND IV.7

I	RUN NUMBER 1
△	RUN NUMBER 2
+	RUN NUMBER 3
⊙	RUN NUMBER 4
X	RUN NUMBER 5
◇	RUN NUMBER 6
⊕	RUN NUMBER 7
Y	RUN NUMBER 8
⊠	RUN NUMBER 9
X	RUN NUMBER 10
Z	RUN NUMBER 11
⧖	RUN NUMBER 12
✳	RUN NUMBER 13

of the curves of $\frac{V_\theta}{V_r}$ (or $\frac{V_r}{V_\theta}$) are smaller for the water alone and are more difficult to evaluate accurately.

Drag Coefficient

In Chapter II it was demonstrated that the drag coefficient for the particles in an annular fluidized bed could be calculated from the equation,

$$C_{D_s} = \frac{8}{3}\frac{a}{r}\left[(1-\epsilon)\left(\frac{V_\theta}{V_r}\right)^2\left(\frac{\rho_s}{\rho_l}-1\right)-1\right] \tag{4.3}$$

where the drag coefficient is based on the superficial velocity. This drag coefficient was calculated for each run in the same manner as the wall shear stress coefficient. The best fit polynomials were used for $\frac{V_r}{V_\theta}$, and the concentration was determined by interpolation of the data in Appendix E.

The correlation of drag coefficient with voidage is shown in Figure IV.7. This correlation has much less scatter than the previous one principally because only a single differentiation of the pressure with respect to radius was necessary. (Some of the scatter in both of these correlations may be due to the variation of other parameters not considered.) The correlation indicates an increase of drag coefficient with concentration.

It was shown in Chapter II that the drag coefficient should be of the form

$$C_{D_s} = C_{D_0}(1-\epsilon)^{1-2m} \tag{4.4}$$

for fully suspended particles. Where C_{D_0} is the drag coefficient of a single particle based on Reynolds number, $R_e = \frac{V_r 2a}{\nu}$, and m is also

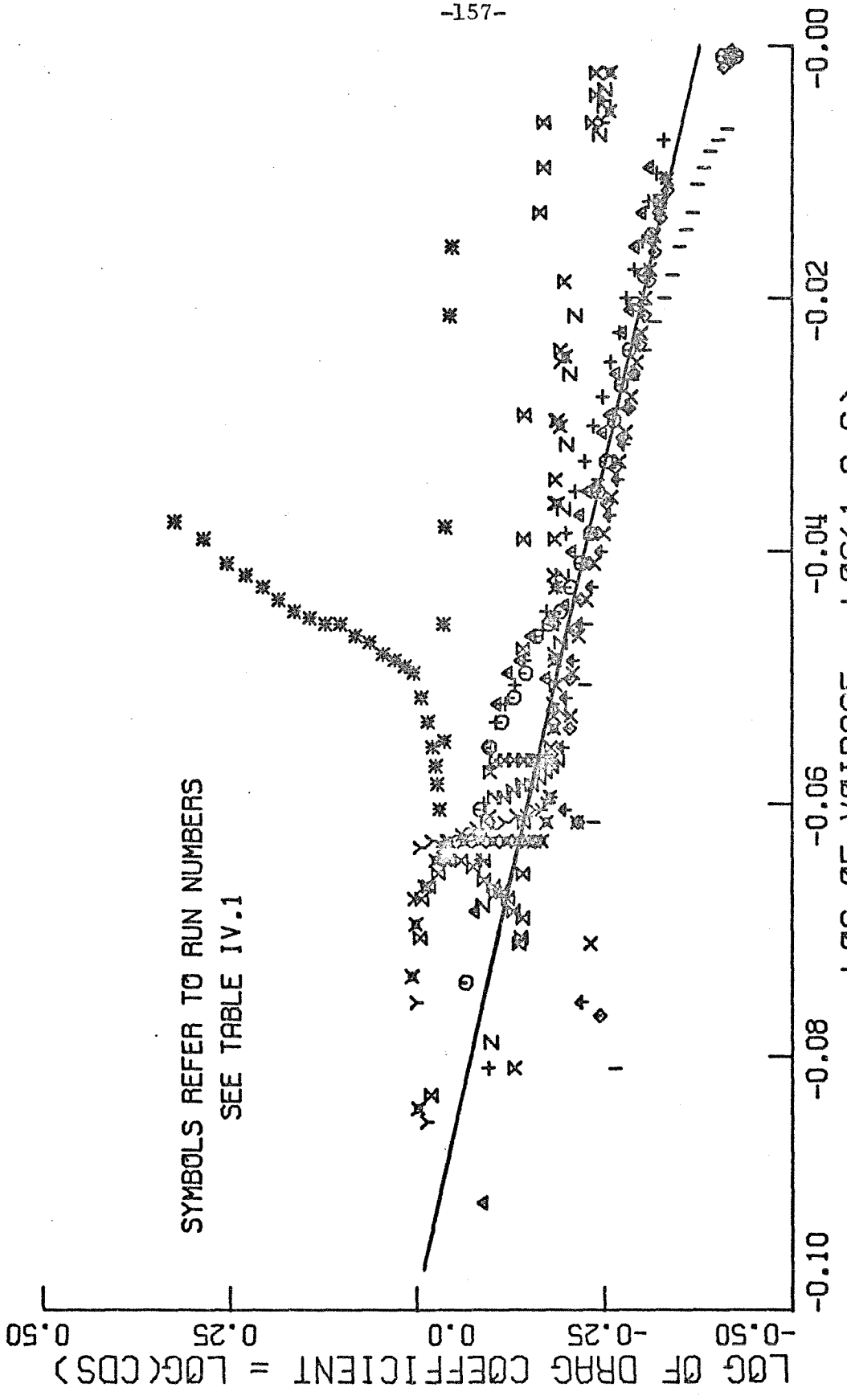

Figure IV.7. Correlation of Drag Coefficient With Concentration.

a function of Reynolds number. The Reynolds number range for each run was calculated from the data in Appendix E. The result is that all of the experiments fall in the range $460 < \mathcal{R}_e < 7200$. The drag coefficient for a single sphere in an infinite quiescent fluid, for this Reynolds number range, is almost constant (Zenz and Othmer, 1960). The average value of drag coefficient for this range is 0.42. The maximum value is 0.55 and the minimum is 0.385. Also, since for most of the experiments $\mathcal{R}_e > 500$, the exponent should be 2.39. This yields the expected relationship:

$$C_{D_s} = 0.42\,(1-\epsilon)^{-3.78} \tag{4.5}$$

This is a straight line on logarithmic coordinates and has been drawn in Figure IV.7.

The fit is quite good for most of the data runs. The notable exception is Run 13. This is the run with no packed bed at the screen. The data points that are furthest from the predicted relationship represent the region in which the particles are supported by the secondary flows in the boundary layers. As stated earlier, the relationships developed for fully suspended particles do not apply in this region. Neglecting this region, all of the data points are within a factor of two of the predicted relationship, and many are within a few percent.

Although this correlation fits the data quite well, it is still difficult to predict the detailed performance of an annular fluidized bed. Using Equation 4.5 in Equation 4.3, the equilibrium radius for zero concentration can be calculated. For Run 4 the radius is 9.0

inches. For Run 13, it is 22.5 inches. However, in both runs the actual value as measured was between 9 and 11 inches. Thus, the relationship expressed by Equation 4.5 should be used more as a guide than a detailed specification.

CHAPTER V

CONCLUSIONS AND SUGGESTIONS FOR FURTHER WORK

A. Conclusions

The analyses and experiments reported above have led to several conclusions concerning vortex-sink flow with particles.

It is possible to design a chamber to produce relatively axisymmetric flow at a specified ratio of tangential to radial velocity. For axisymmetric flow it is necessary to have a large number of flow inlets. With only two inlets, the flow is quite asymmetric resulting in unsatisfactory pressure measurements. With 12 flow inlets, the region of asymmetry is limited to the region close to the vanes. The ratio of tangential to radial velocity may be calculated approximately by considering the angular momentum introduced into the chamber by the flow in each inlet channel.

The flow without particles may produce large secondary flows in the boundary layers. In the analysis performed to calculate the characteristics of the boundary layers for laminar flow it was found that the ratio of tangential to radial velocity in the main flow had a minor effect on the boundary layer thickness. Dye injection experiments confirmed the presence of secondary flow in the large annular chamber. Additional experiments indicated some reduction in circulation due to side-wall boundary layers.

The orbits for individual particles suspended in the flow were calculated to be circular. A stability analysis showed the orbits to be stable for laminar flow. However, the actual orbits as measured appeared to be unstable. Individual particles were seen to traverse the entire

volume of the chamber. This behavior is thought to be due to turbulence and the entrainment of the particles in the secondary flow.

Data from vertical fluidized beds were extended to provide a prediction of the concentration distribution in an annular fluidized bed for hydrodynamically suspended particles. The drag coefficient as calculated by the analysis matched the actual drag coefficients measured in the experiments quite well. However, the agreement was not good enough to allow prediction of particle orbits at a given concentration closer than a factor of two.

The annular fluidized bed could be operated either with a packed bed at the screen or with a relatively low concentration of particles in that region. The influence of the packed bed on the suspension of the other particles was found to be limited to a region close to the surface of the packed bed. Without the packed bed some particles were swept inward and impacted the screen at high velocity resulting in severe damage to the screen and the surface of the particles.

The particles were found to have an effect on the wall shear stresses and, as a result, the circulation distribution. The shear stress calculations were difficult to perform due to the requirement of a second derivative of the measured data with respect to radial position. Although the results contained substantial scatter, the wall shear stress coefficient was found to be of the same order of magnitude as for fully developed flow through a smooth pipe with the Reynolds number based on the tangential velocity and axial length of the bed.

B. Suggestions for Further Work

The analyses and experiments presented in this thesis are only a beginning of study in this field. Several other experiments could be performed.

Most of the experiments reported here used only one kind of particle and fluid (1/8-inch diameter nylon balls and water). Other experiments could be done using different sizes and densities of particles and different fluids including gases. The apparatus for such experiments should be designed so that the calculated equilibrium orbits for single particles are within the chamber. Experiments could also be done with a range of particle sizes. Separation of the various sizes may occur as in vertical fluidized beds.

Experiments could also be performed to further minimize the effects of gravity. If the axis of the chamber were oriented vertically, the gravitational force would no longer affect axial symmetry. However, it would tend to cause particles to settle into a side-wall boundary layer. An apparatus designed for higher flow rates would minimize the effect of gravity by making the other forces larger in comparison.

An apparatus could be designed to operate through a wider range of $\frac{V_\theta}{V_r}$. The experiments here were limited by the characteristics of the particles. At lower values of $\frac{V_\theta}{V_r}$ the beads remained packed against the screen, and at higher values of $\frac{V_\theta}{V_r}$ the equilibrium orbit for a single particle was much larger than the chamber. Operation at low values of $\frac{V_\theta}{V_r}$ would tend to minimize the effects of the secondary flow but would require much larger flow rates to maintain high centripetal acceleration.

Finally, the wall shear stress should be measured more accurately. The effect of wall shear stress on circulation could be increased by using a shorter axial length. This would increase the accuracy of the measurements obtained from pressure surveys. Alternately, wall shear stress might be measured directly by measuring the forces on a small isolated section of the chamber wall.

APPENDICES

PART I

APPENDIX A

ELECTROMAGNETIC VELOCITY PROBE

This Appendix describes the electromagnetic velocity probe used in the experiments on the vertical fluidized bed. Both the operating principle and the specific application will be discussed.

Although the principle of the electromagnetic flowmeter was conceived by Faraday in the nineteenth century, it has only recently been made workable by Kolin (Kolin (1944, 1945, 1954, 1969, 1970), Kolin and Wisshaupt (1963)). It is now a commercially produced device and is currently employed to measure the flow rates of liquids and slurries in pipes; it also finds application in the measurement of blood flow.

The electromagnetic velocity probe, developed here, operates on the same principle, magnetic induction. A conducting fluid moving through a magnetic field generates a voltage in the direction normal to the velocity and magnetic field directions. This voltage may be measured with suitable electrodes. The voltage is proportional to the product of the velocity, the magnetic field strength, and the distance between the electrodes.

An electromagnetic flowmeter consists of a section of pipe with a powerful magnet arranged to produce a uniform magnetic field normal to the direction of fluid flow. The pipe has an insulating liner, and electrodes in the tube walls on a line normal to the magnetic field and direction of flow. Thus, the flow of a conducting fluid (such as tap water) will generate a voltage directly proportional to the velocity.

Due to problems associated with electrolysis, it is necessary to use an alternating magnetic field and generate an alternating voltage.

The electromagnetic flowmeter requires an electrically conductive medium. In the case of a slurry of insulating particles in a conducting fluid, the electromagnetic flowmeter measures only the velocity of the fluid. If the particles are moving at the same velocity as the liquid, then the flowmeter is sensitive to the volumetric flow rate of the suspension.

This principle can be used to measure local velocities rather than overall flow rates. Kolin presented two methods for doing this. Both methods involve placing a small tubular probe in the flow. While this is satisfactory for pure liquid flow, it results in clogging in solid, liquid flow.

The electromagnetic velocity probe developed here is based on a blood flowmeter developed by Mills (1966). Although Mills's device was designed for measuring the flow rate of blood in an artery, it can be modified to measure local velocities. Figure A.1 is a schematic diagram showing the configuration used here, and Figure III.1 in Part I-A is a photograph of the probe and associated electronics.

The probe is constructed of plastic and contains a miniature electromagnet oriented to produce a magnetic field in a direction perpendicular to the probe axis. The magnet generates a voltage in the fluid flowing axially over the probe. The voltage is measured with two electrodes imbedded in the probe surface. The wires are brought out along the probe stem and are connected to the electronics shown in Figure III.1. The electronic system provides current to excite the magnet

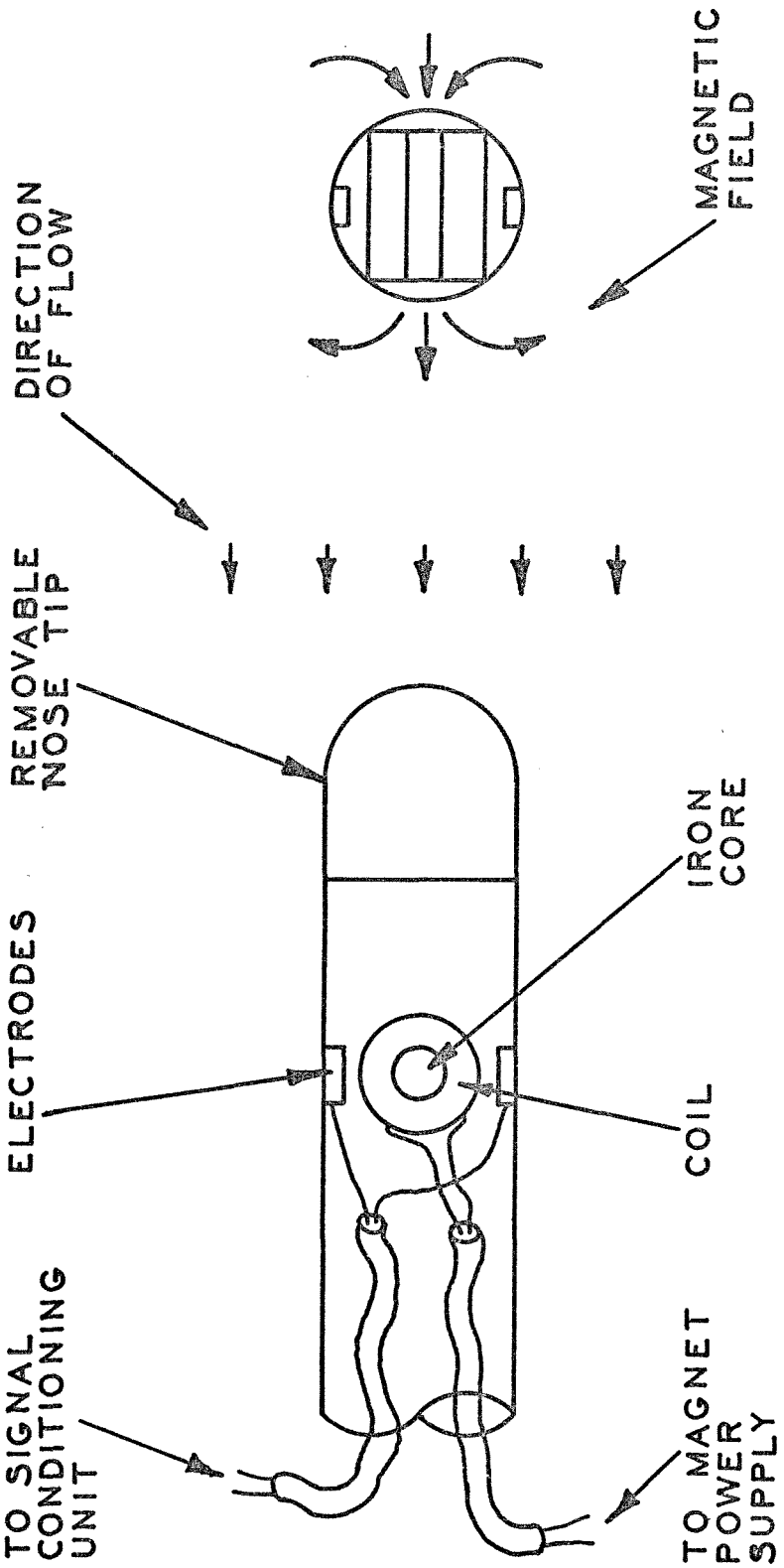

Figure A.1. Schematic Diagram of Electromagnetic Velocity Probe.

and transforms the alternating voltage measured into a well-buffered D.C. signal proportional to the local velocity. The probe is $\frac{1}{4}$ inch in diameter and is equipped with a removable nose cone to vary the length of the probe upstream of the sensing area.

In operation, the probe is immersed in the flow with the nose pointing upstream. The fluid velocity flowing over the probe in the vicinity of the magnet is sensed; if particles are present, they should not affect the measurement.

APPENDIX B

DRAG COEFFICIENT FOR PARTICLES IN A CLOUD

Many two-phase flow problems involve the determination of the force exerted on the particles in a cloud by the motion of a fluid through the cloud. In general, one would expect that the force would be determined by the relative velocity between particles and the fluid, the concentration of the particles, and the properties of the fluid. If the concentration of particles is low enough, the particles can be assumed to act independently and behave as if they were immersed individually in the moving fluid. As the concentration increases, a point is reached where the disturbances generated by any one particle affects others. As the concentration is increased even further, particles may collide. At a volume concentration of 1 percent, the minimum distance between uniformly distributed spheres is less than 3 diameters. At 7 percent, this distance is less than 1 diameter. Thus, even at quite low concentrations, particle-particle interaction can be expected to occur. The drag force exerted on a cloud of concentration greater than a few tenths of a percent by volume cannot be determined by extrapolating data obtained for individual particles.

A vertical fluidized bed is one example of flow through a cloud. When a bed is fully fluidized, the pressure drop across the bed is very nearly equal to the weight of the particles plus the liquid in the bed. This implies that in the fluidized state the particles are totally supported by the fluid and that, on the average, the particles experience zero lift from collisions. If this were not so, some of the particles would be supported by the walls (by friction) or by the bottom plate

so that the net pressure drop would be less than the weight of the solids and liquid. When such pressure measurements are made, one usually finds that the pressure drop is slightly higher than the hydrostatic calculated value. The increase is probably due to fluid friction. The pressure loss due to fluid friction is expected to be small because the velocity head in most beds is only a few percent of the hydrostatic head in 1 pipe diameter.

Measurements on a fluidized bed can be used to determine the drag coefficient for particles in a cloud. Assuming that uniform spherical particles are, on the average, totally supported by the liquid and that collisions have no average lift effect, one can write a force balance for a typical single particle.

There are three forces acting on the particle: the force of gravity, the buoyancy force, and the fluid drag force. The force of gravity, F_G , is:

$$F_G = -\frac{4}{3}\pi a^3 \rho_s g \tag{B.1}$$

where ρ_s is the particle density, g is the gravitational acceleration, and a is the particle radius.

The buoyancy force is F_B , and assuming that the particles are small,

$$F_B = -\frac{4}{3}\pi a^3 \frac{dP}{dx} \tag{B.2}$$

where $\frac{dP}{dx}$ is the pressure gradient in the vertical direction. Since the particles are totally fluidized,

$$\frac{dP}{dx} = \left[-\rho_s c + \rho_l (1-c)\right] g \tag{B.3}$$

$$F_B = -\frac{4}{3}\pi a^3 \left[\rho_s c + \rho_l (1-c)\right] g \tag{B.4}$$

The fluid drag force is F_D,

$$F_D = C_D \frac{1}{2} \rho_l v^2 \pi a^2 \tag{B.5}$$

where C_D is the drag coefficient based on a reference velocity, v.

In steady state, the sum of the forces is zero.

$$F_G + F_B + F_D = 0 \tag{B.6}$$

$$-\frac{4}{3}\pi a^3 \rho_s g + \frac{4}{3}\pi a^3 \left[\rho_s c + \rho_l (1-c)\right] g + C_D \frac{1}{2} \rho_l v^2 \pi a^2 = 0 \tag{B.7}$$

Simplifying:

$$C_D = \frac{8}{3} a g (1-c)\left(\frac{\rho_s}{\rho_l} - 1\right) \frac{1}{v^2} \tag{B.8}$$

Many empirical correlations of the important parameters of fluidized beds have appeared in the literature. These correlations have been brought forward only to explain the operation of fluidized beds, not to describe the individual particle forces. Consequently, these correlations appear in the form of relationships between overall fluidized bed parameters.

One widely accepted correlation was derived empirically by Richardson and Zaki (1954). They performed many experiments in various size tubes using many different solids and liquids. They measured the fluid and particle properties and correlated them with the overall bed properties. Their result was:

$$\frac{U_s}{U_T} = (1-C)^n \tag{B.9}$$

where U_s is the superficial velocity which is defined as the volumetric flow rate through the bed divided by the bed cross-sectional area. U_T is the terminal settling velocity of the single particle in an infinite fluid, C is the volume concentration of solids and n is an exponent depending on Reynolds number of the flow and the ratio of particle diameter to tube diameter,

$$n = \left[4.35 + 17.5 \frac{2a}{D_T}\right] R_{e_s}^{-.03} \quad \text{for} \quad .2 < R_{e_s} < 1.0 \tag{B.10}$$

$$n = \left[4.45 + 18.0 \frac{2a}{D_T}\right] R_{e_s}^{-.10} \quad \text{for} \quad 1.0 < R_{e_s} < 200 \tag{B.11}$$

$$n = 4.45\, R_{e_s}^{-.10} \quad \text{for} \quad 200 < R_{e_s} < 500 \tag{B.12}$$

$$n = 2.39 \quad \text{for} \quad R_{e_s} > 500 \tag{B.13}$$

$$R_{e_s} = \frac{2aU_s}{\nu} = \text{Reynolds number } (a \text{ is the particle radius, } \nu \text{ the kinetic viscosity}) \tag{B.14}$$

U_T may be determined from Equation B.8 if C is equated to zero. Then U becomes U_T and C_D becomes C_{D_o}, the drag coefficient of a single particle.

$$C_{D_o} = \frac{8}{3} a g \left(\frac{\rho_s}{\rho_l} - 1\right) \frac{1}{U_T^2} \tag{B.15}$$

C_{D_o} may be taken from the standard drag curve and is a function of Reynolds number,

$$R_{e_T} = \frac{2aU_T}{\nu} \tag{B.16}$$

Equations B.8, B.9, and B.15 may be combined so that:

$$\frac{C_D}{C_{D_0}} = \left(\frac{U_s}{U}\right)^2 (1-\epsilon)^{1-2m} \tag{B.17}$$

Equation B.17 gives the drag coefficient of particles in a fluidized bed. It may be generalized to give the drag coefficient of particles in a cloud where the concentration is uniform and particle collisions do not affect average momentum transport.

The question arises as to what velocity, U, should be specified. If U is taken equal to U_s;

$$C_{D_s} = C_{D_0}(1-\epsilon)^{1-2m} \tag{B.18}$$

While this is useful for fluidized bed problems where U_s is easily calculated, it gives little insight into the particle-particle interaction. The local velocity of the fluid is not U_s. The superficial velocity is the velocity if there were no particles present. The presence of the particles occludes some of the area of the bed thus increasing the velocity of the liquid in the interstitial spaces. The average velocity of the liquid in the interstitial spaces will be called the average velocity and given the symbol U_A. Thus,

$$U_A = \frac{U_s}{1-\epsilon} \tag{B.19}$$

If U in Equation B.17 is taken equal to U_A, then

$$C_{D_A} = C_{D_0}(1-\epsilon)^{3-2m} \tag{B.20}$$

C_{D_A} can be used to determine particle drag on particles in a cloud where U_A is the average fluid phase velocity.

Equations B.18 and B.20 show that the drag coefficient based on either U_S or U_A is strongly dependent on concentration. The reasons for this dependence are probably two-fold.

First, the flow around a particle is both unsteady and highly turbulent. One would expect a turbulent length scale of the order of the size of the particle due to vortex shedding, and smaller wave lengths due to the decomposition of the eddies during subsequent flow over and around particles. One would also expect turbulent length scales of the order of the diameter of the pipe as well. Hence, there should be scales from many particle diameters down to much smaller than one particle diameter with a distribution quite different from that in ordinary pipe flow. Also, from the estimates described in Part I-A, the turbulence level may be 40 percent or larger.

Some work has been done on the drag coefficient for a sphere immersed in turbulent flow by Torobin and Gauvin (1961) with wave lengths small compared to the diameter of the sphere. The results of these papers are unclear, and even if the level of turbulence is known, it is very difficult to determine the drag coefficient from these published correlations. The main effect seems to be a lowering of the Reynolds number at the transition point for turbulent flow rather than an increase in drag coefficient for all Reynolds numbers.

On the other extreme, Hill (1973), at this institution, has done some work on spheres falling through an oscillating liquid where the wave lengths of the disturbances thus generated were very large. The results

indicate an increase in some cases. However, the increase is less than a factor of two and, in addition, the turbulence level was only about 2 percent.

A second reason for dependence of drag coefficient on concentration is the proximity of one particle to another. Since the wake of a particle moving in a stationary liquid can be more than one diameter in length, in a fluidized bed of concentration greater than a few percent the particles will greatly interfere with each other's flow pattern. In fluidized beds of concentration even less than 6 percent, the clicking noise of colliding particles is very noticeable if the Reynolds number of the particle motion is sufficiently high.

These two variables, the turbulence level and the proximity of one particle to the other, must certainly be related to the concentration. So the strong dependence of drag coefficient on concentration is reasonable.

A new effective velocity, U_E, can be defined such that the drag coefficient based on this velocity is independent of concentration. Then Equation B.17 can be rearranged as follows:

$$\frac{U_E}{U_S} = \frac{C_D}{C_{D_o}} (1-\epsilon)^{\frac{1-2m}{2}} \tag{B.21}$$

Now in the limit of zero concentration, $U_E = U_S$, which implies that $C_{D_E} = C_{D_o}$. Therefore,

$$U_E = U_S (1-\epsilon)^{\frac{1-2m}{2}} \tag{B.22}$$

Thus, the drag force between fluid and particles can be assumed to be due to a velocity past the particles, v_f, resulting in the same drag coefficient as the terminal settling velocity case.

As shown in Part I-A, a total head probe, or electromagnetic velocity probe immersed in the bed measures v_f approximately.

APPENDIX C

PRESSURE MEASURING SYSTEM

The experiments in the large annular fluidized bed required the measurement of differential pressures between 103 pressure taps in the working section and 2 pressure taps on the venturi meter. A manometer bank would have been unsatisfactory because of the wide range of magnitudes of the pressures at various pressure taps. In addition, since the second derivative of pressure was required, less error would be introduced by measuring the pressure differences between adjacent pressure taps and hence the gradient directly.

The alternatives then were installation of a pressure transducer for each pair of pressure taps to be measured or a means of switching from one pair of pressure taps to the others. The latter could be done much more cheaply.

The pressure measuring system thus consists of a differential pressure transducer, a complex solenoid valve network, a sequencing computer, and an integrating digital voltmeter to read the pressure transducer output. This elaborate system is necessary because of the large number of differential pressure readings that are required. To attempt to make connections manually would be quite impractical. Figure C.1 is a schematic diagram of the system.

The pressure transducer is a Datametrics Type 538-72 high accuracy variable capacitance pressure transducer. It has a full scale pressure range of 20 P.S.I. and a line pressure rating of over 150 P.S.I.G. It is powered and demodulated by a Type 104-56 electronic manometer. This transducer was chosen because it is of the variable capacitance

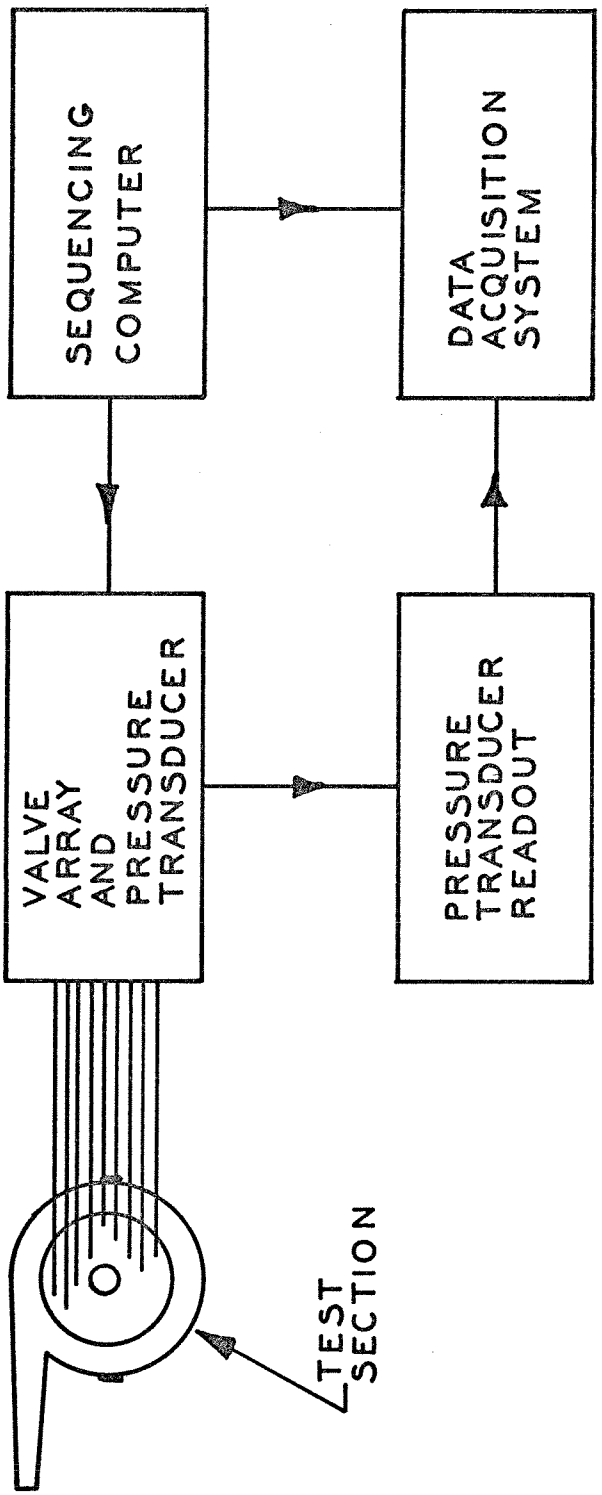

Figure C.1. Schematic Diagram of Pressure Measuring System.

type and retains its accuracy at low percentages of full scale differential pressure. The manufacturer claims accuracy of the order of $\pm$ 0.03 percent of reading down to 10^{-3} times full scale. The working medium of the transducer is silicone oil.

The pressure taps on the test section are connected to individual solenoid valves in the network by rigid nylon tubing. A schematic of the valve array is shown in Figure C.2 and a photograph in Figure C.3. One half of the valves are manifolded to one plenum and the other half to a second plenum. The plenums are connected through four reversing solenoid valves to a pair of Ametek isolators, which are thin Viton diaphragms. The other sides of the diaphragms are connected to the pressure transducer. The isolators are necessary to separate water in the lines from the pressure taps from the silicone oil in the pressure transducer. Two more solenoid valves admit clean pressurized water to the system to purge the pressure taps of dirt and air. Three pressure relief valves protect the pressure transducer against pressure surges, and two needle valves limit the flow through the relief valves.

The sequencing computer is a solid-state electronic controller that performs all of the details of taking a measurement. It acts as an interface between the experimenter and the valving system. Its capability includes the storage of a sequence of up to 120 different data points and the storage of a sub-sequence of 10 steps per data point. In operation the computer can start on any of the 120 steps and perform the 10 steps of the sub-sequence, then index to the next step and again perform the sub-sequence, and so on. The computer can operate automatically for any preset number of data points and stop automatically

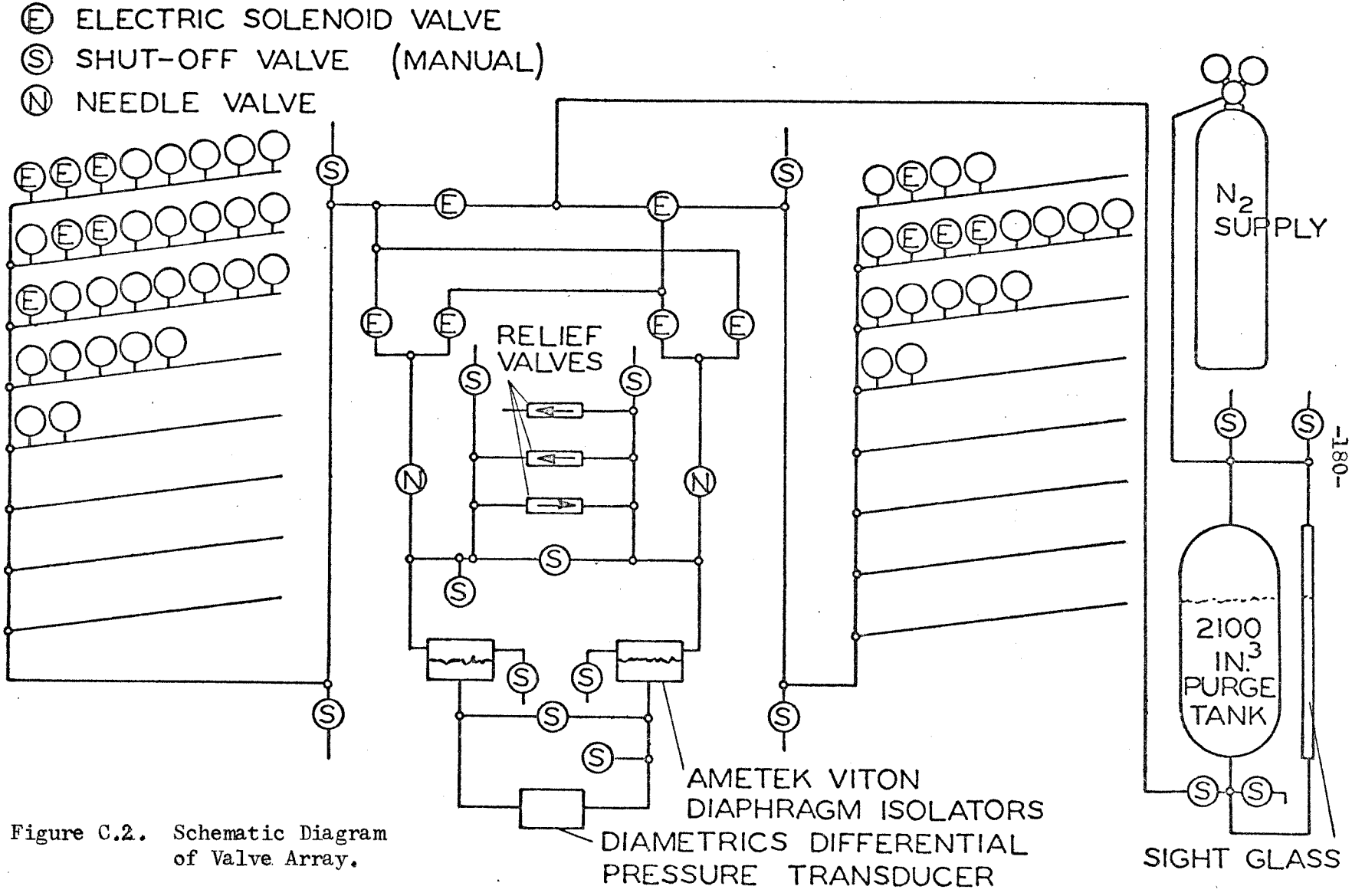

Figure C.2. Schematic Diagram of Valve Array.

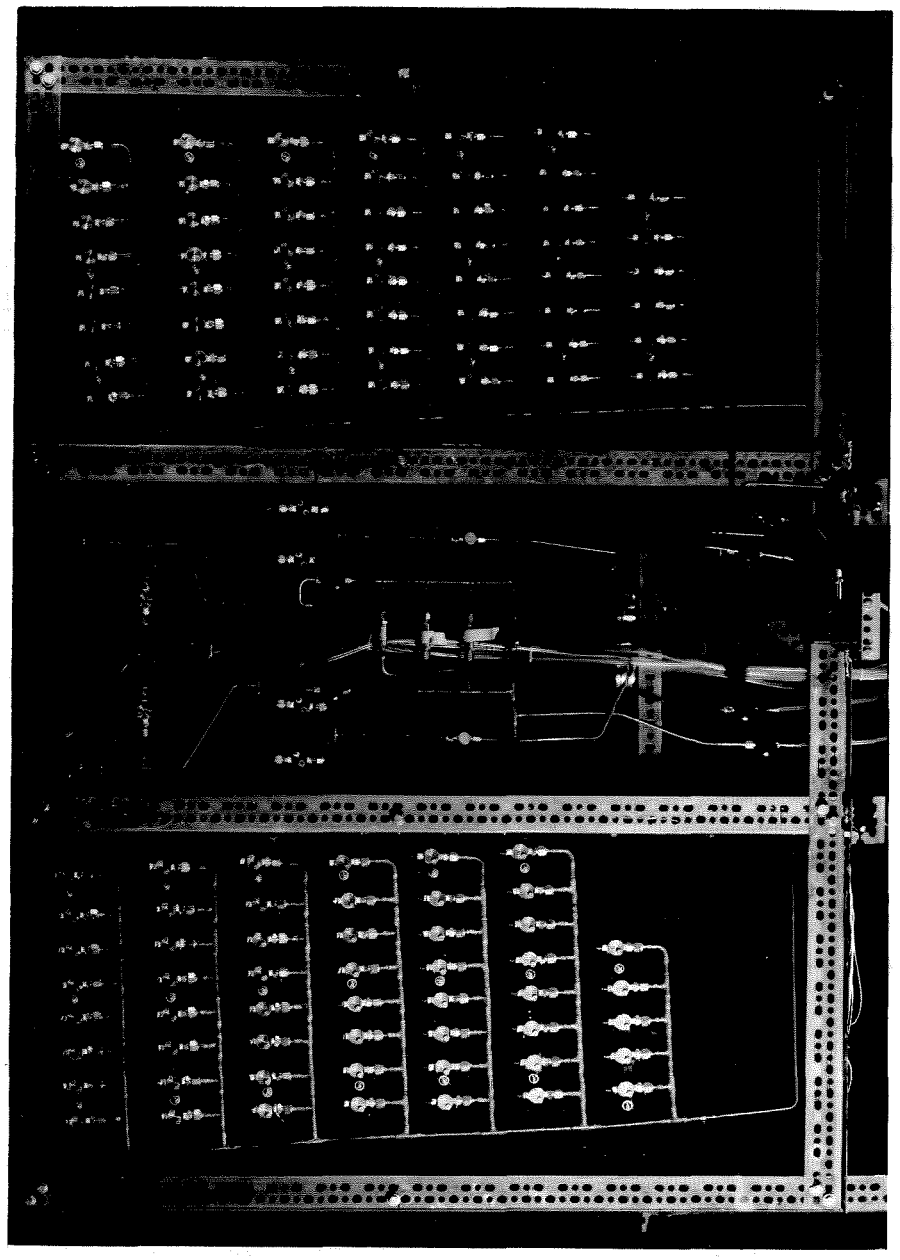

Figure C.3. Photograph of Valve Array.

at the end, thus freeing the experimenter to monitor and control other aspects of the system operation. Each step in the 120-step sequence specifies two valve numbers which select a pair of pressure taps and a sign indicating which pressure tap should be connected to the high pressure side of the pressure transducer.

The sub-sequence of 10 steps determines what happens during each of the 120 steps of the measurement sequence. For each of the 10 steps there are 10 possible functions. The time that the computer spends on each step is adjustable from a few nano-seconds up to over one minute. The functions that can be chosen to be performed during each step are as follows:

1. blow out left bank of pressure taps with high-pressure clean water
2. blow out right bank of pressure taps with high-pressure clean water
3. open pressure taps
4. open measuring valves so that the proper pressure tap is on the high side of the pressure transducer
5. zero pressure transducer
6. uncommitted
7. uncommitted
8. index 120-step sequence one step
9. skip this step and go on to next
10. stay on this step until manual command is given.

Any combination of the above can be programmed in each step except that the 'skip' step overrides all others. The uncommitted choices could be

used to control a data acquisition system or for any other function desired. However, in these experiments they were not used.

The sub-sequence is programmed by the insertion of pins in the proper holes on the front panel and indicating lights show which step is currently in operation. A selector switch is provided to select a stopping point for the 120-step sequence. Twelve possible stopping points are provided. Switches are also provided to select manually a pair of pressure taps. The binary coded valves selected and the sign are available in digital form on the rear of the unit. This may be connected to a data-acquisition system if desired. Additional controls are provided to control manually all other functions, such as manual rotation of the drum, manual stopping of the sub-sequence, etc.

The following is an example of a typical operation. The drum is programmed for 120 different data points. For this experiment, say, only points 11-103 are needed. The 120-step sequence is manually advanced to step 11 and the stop selector switch is set to stop at step number 103. A data-acquisition system with 2 channels is connected to the pressure transducer output (first channel) and the valve number output of the computer (second channel). The 'initiate measurement' command wire is connected to uncommitted output #7. The sub-sequence is programmed to provide the following functions: zero pressure transducer, blow out left pressure tap, blow out right pressure tap, measure differential pressure, and index to the next measurement. The times for each step may be chosen at random.

To operate, the experimental apparatus is put into operation and the 'start' button is pushed. The computer starts with step 11, performs

all measurements, indexes to step 12, and so on. At the end of step 103, the computer stops with the sub-sequence in step 1. The data-acquisition system will contain the numbers of the two valves, which one was at higher pressure, and the actual differential pressure for each of the 92 data points. This information may be fed, if desired, into a computer for data reduction.

Although the system described above can operate very rapidly, it was found that the turbulent fluctuations in pressure were so great in the experiments that a true average pressure could only be determined by integrating the transducer output for many seconds. Thus, with the integration time for pressure measurement long compared to valve operation time, the value of recording data on a data-acquisition system was reduced.

Consequently, an integrating digital voltmeter was used. A $4\frac{1}{2}$ digit Data Precision Model 2400 digital voltmeter was chosen. This instrument uses the dual slope technique to obtain integrated values of a D.C. signal. The integration time built into the instrument is 0.1 seconds. To modify this value, circuitry was added to both attenuate the input signal and increase the integration time in the proper ratio. This circuit allowed operation of the digital voltmeter in either its original state or with integration times of .2, .4, .8, 1.0, 2.0, and so on up to 80 seconds. The circuitry was calibrated against a precision voltage source on each range.

In the experiments performed here it was found that most of the turbulent fluctuations were eliminated at 20 second integration time. Repeatability at this setting was within .1 percent.

This system has been designed as a separate unit so that it may be used for many other experiments. All of the tubing connections have been made with quick disconnecting fittings, and the sequencing computer is equipped with multi-pin connectors for rapid set-up. Although the system was designed for a water system, it can be used equally as well with any fluid noncorrosive to brass and stainless steel where the line pressure is less than 150 pounds per square inch and the differential pressures to be measured are less than 20 pounds per square inch.

APPENDIX D

LASER CONCENTRATION METER

A major part of the experiments discussed above involved the measurement of the local value of concentration in an annular fluidized bed. This was accomplished by the development of a laser concentration meter. It operates on the principle that a light beam incident on a cloud of particles, moving randomly, will be attenuated in a predictable manner. This Appendix contains the theoretical considerations which make the device possible, a detailed description of its construction and operation, and the calibration curve obtained for a vertical fluidized bed.

Attenuation of a Light Beam by a Cloud

Suppose that there is an empty box of dimensions $L \times L \times d$ and that an infinitesimally thin light beam is shining through the box. Now put one spherical particle of radius a at an arbitrary location. Neglecting edge effects, the probability that the light beam will not be occluded by the particle is

$$P_{OPEN} = 1 - \frac{\pi a^2}{L^2} \tag{D.1}$$

Similarly, if N spheres are placed in the box at random,

$$P_{OPEN} = \left(1 - \frac{\pi a^2}{L^2}\right)^N \tag{D.2}$$

If the spheres are allowed to move randomly in the box, the intensity of the beam reaching the far side of the box relative to its original intensity would be the same as P_{OPEN} on the average. Thus, the intensity, I, is:

$$I = \left(1 - \frac{\pi a^2}{L^2}\right)^N \tag{D.3}$$

The number of particles in the box may be represented as a concentration, C.

$$C = \frac{4\pi a^3 N}{3L^2 d} \tag{D.4}$$

The cross-section of the box, L^2, may then be eliminated from Equation D.3, leaving:

$$I = \left(1 - \frac{3Cd}{4Na}\right)^N \tag{D.5}$$

$$\ln I = N \ln\left(1 - \frac{3Cd}{4Na}\right) \tag{D.6}$$

Now, holding the concentration fixed and letting N become very large:

$$\ln I \approx -\frac{3Cd}{4a} \tag{D.7}$$

$$I \approx e^{-\left(\frac{3d}{4a}\right)C} \tag{D.8}$$

Equation D.8 is the basic equation of the laser concentration meter. It determines the relationship between concentration and beam intensity for a given configuration.

Construction and Operation

The complete meter is shown schematically in Figure D.1. The light source for this concentration meter was chosen as a 1 milliwatt helium-neon laser. However, a laser is by no means necessary. It was used here because it is a handy source of a mono-chromatic, and essentially parallel, thin beam of light. The coherency of the light is not necessary for the experiment, and in fact is a liability in that

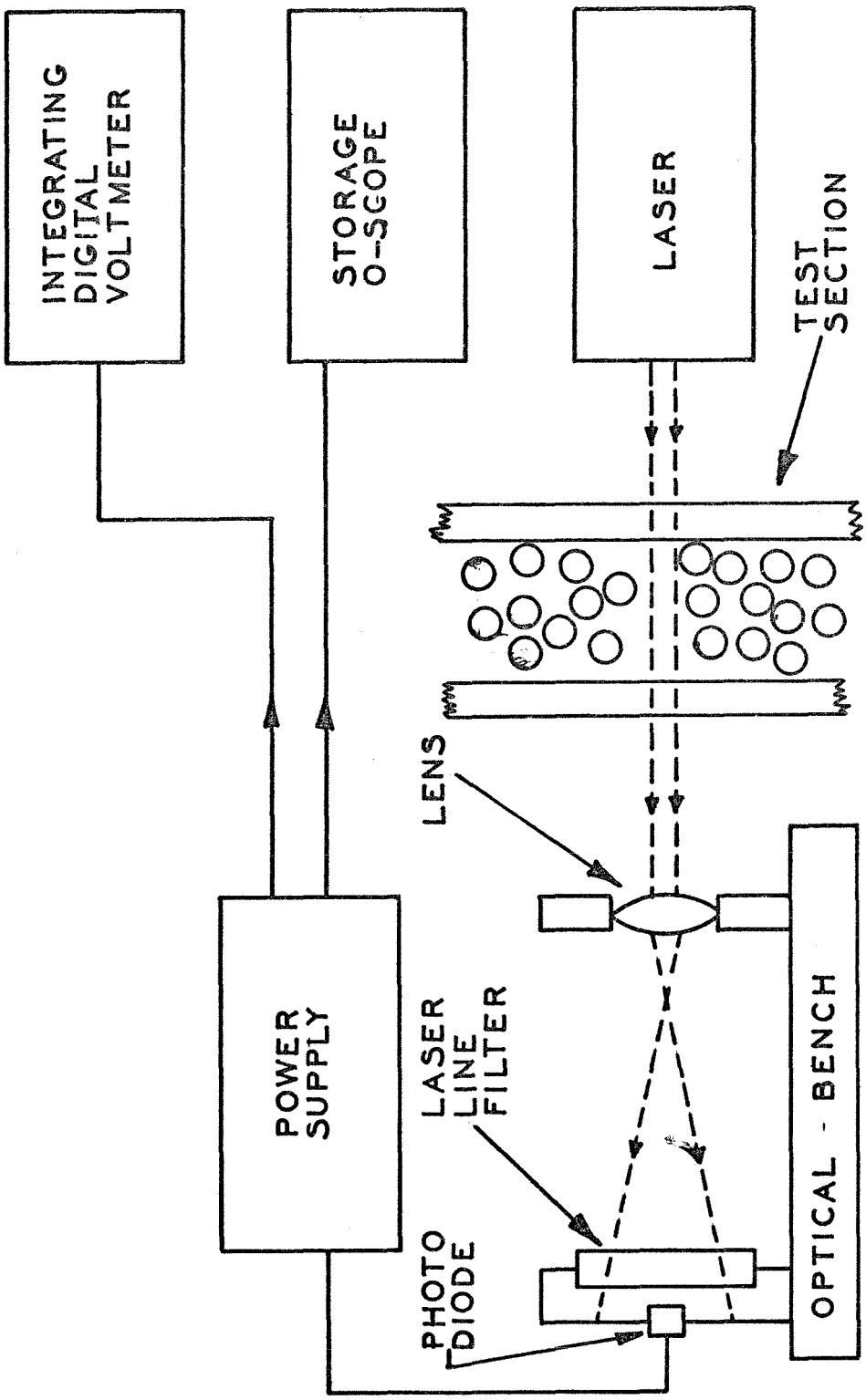

Figure D.1. Schematic Diagram of Laser Concentration Meter.

the laser light produces an interference pattern if passed through a lens. A mono-chromatic light source is convenient because it allows measurements to be performed in a well-lit room, providing a laser line filter is used to protect the photosensitive device.

The theory assumes an infinitesimally thin beam of light. The actual laser beam diameter is 1.0 mm. Because of the possible change in calibration due to beam width, the beam diameter was maintained fixed throughout the experiments.

The light beam passes through a transparent test section containing the cloud of particles to be measured, and the transmitted part impinges upon a lens. The lens diverges the beam and the resultant beam passes through a laser line filter to a photodiode. Because the beam leaving the photodiode is diverging, relative movement of the photodiode assembly and the lens results in changes in intensity of the light falling on the photocell. The photodiode is powered by a 5-volt voltage supply. A resistor in series with the photodiode provides a voltage drop proportional to the intensity of light striking the photodiode. This voltage is measured with the integrating digital voltmeter described in Appendix C and also monitored on an oscilloscope. The photodiode used here is a Clairex Model 4020. It has a sensing diameter of 0.06 inch and a rise time of 1.5 microseconds.

In operation the device is set up with the test section clear of beads. The apparatus is optically aligned and the position of the photodiode varied until the voltage across the photodiode is 1.0 volt. When particles are then introduced, the digital voltmeter reads the average intensity of the beam directly. In the annular fluidized bed

the walls of the test section moved as the particles were introduced so that the alignment was off. The oscilloscope was monitored so that the maximum value of instantaneous intensity was adjusted to 1.0 volt while the apparatus was in operation.

For the calibration in a fluidized bed, the integrating digital voltmeter was not available, so a resistor-capacitor network was used to provide a 75 second time constant to smooth the output.

Calibration

As a check of the linearity of the output reading with average intensity, a 10-inch diameter paper disc with holes around the circumference was rotated at high speed. The system was aligned so that the laser beam could only reach the photodiode by passing through the holes in the paper disc. The average intensity could be calculated directly from the number of holes.

The voltmeter reading was directly related to the calculated intensity. The voltmeter read 7 to 15 percent low over the range from 0.008 to 0.212. Utilizing the calibration curve obtained below, it will be seen that this corresponds to a concentration error of about 0.4 percent.

The calibration was done in a fluidized bed chamber of square cross-section (1.6 x 1.6 inches inside). 1/8-inch nylon beads were used as the particles and water as the fluid. The water was supplied by an additional loop on the flow circuit developed by Willus. The concentration was determined by dividing the volume of the beads by the total volume of the fluidized bed. The laser beam was passed through the approximate center of the bed to obtain an average concentration.

129 data points were taken, covering a range of concentrations from 2.5 percent to 35 percent. The data are shown in Figure D.2. A straight line fits these data remarkably well. A least-squares fit weighting each data point equally yields the relation

$$I = \ell^{-25.3033\,C} \tag{D.9}$$

Using the values of $\alpha = 1.6$ inches and $a = 0.0625$ inch in Equation D.8 yields the prediction:

$$I = \ell^{-19.2\,C} \tag{D.10}$$

The difference in the exponents in Equations D.9 and D.10 is probably due to several effects. One problem is that the centers of the particles are not free to go all the way to the wall. Thus, the concentration calculated by dividing the volume of beads by the total fluidized bed volume may be less than the actual value locally. Another problem is that the theory assumes that many particles can line up in one row. However, only 12 particles may be lined up in the direction of the laser beam without interfering with the walls.

Equation D.10 may be applied directly to other configurations providing the geometry is the same as in the calibrating fluidized bed. Consequently, the thickness of the annular fluidized bed was chosen as 1.6 inches to avoid recalibration.

Most of the calibration data points fall within a concentration range of $\pm$ 2 percent. This corresponds to an intensity range of $\pm$ 40 percent. Thus, accuracy in the intensity measurement is not critical.

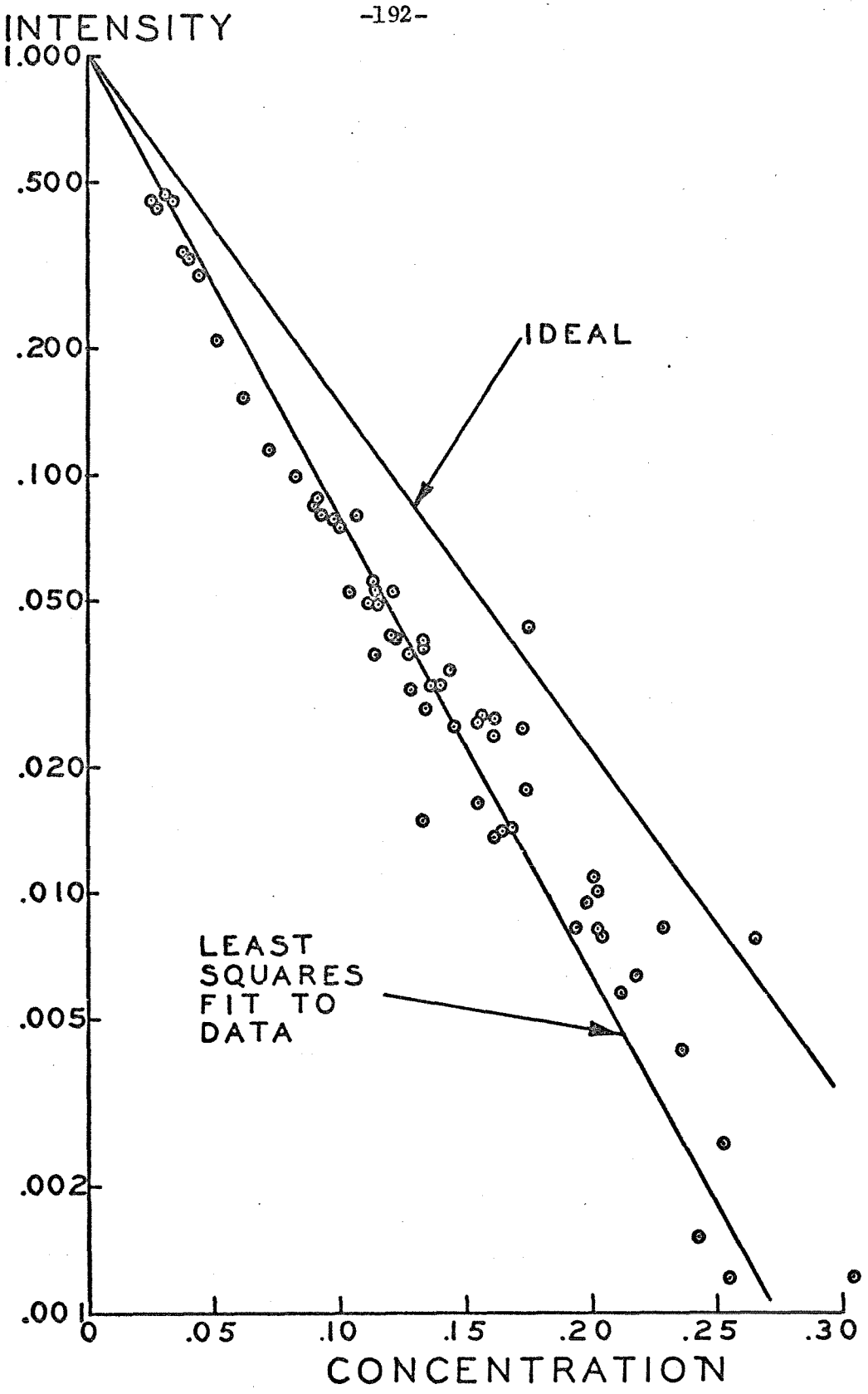

Figure D.2. Calibration Curve for Laser Concentration Meter.

One limitation of the meter is that the upper limit for concentrations is about 30 percent. At this concentration, only about 0.1 percent of the incident light actually strikes the photodiode. At lower intensities the leakage current of the photodiode and finite band width of the laser line filter combine to produce erroneous readings.

APPENDIX E

This Appendix contains the reduced data from the experiments described in Chapter IV. There are 13 data runs described. Table E.1 lists the major parameters for each data run and may be used as a guide in examining the remaining data.

The remainder of this Appendix contains plots of $\frac{V_\theta}{V_r}$ and concentration against radius. The plots are arranged in order of increasing run number and are also listed in the list of illustrations for Part I.

TABLE E.1
SUMMARY OF DATA RUNS

RUN NUMBER	VANE GAP	V_e/V_n NOMINAL	PUMP SPEED RPM	TESTS WITHOUT PARTICLES		TESTS WITH PARTICLES			
				FLOWRATE GPM	V_e/V_n MAXIMUM OBSERVED	FLOWRATE GPM	V_e/V_n MAXIMUM OBSERVED	PARTICLE VOLUME Cm^3	PACKED BED
1	0.487	13.0	2500	292.7	12.8	233.2	11.7	400	YES
2	0.411	15.3	1500			149.4	13.2	507	"
3	0.411	15.3	1750			172.6	13.0	507	"
4	0.411	15.3	2000	181.3	14.0	180.8	13.0	507	"
5	0.411	15.3	2000			165.1	13.1	750	"
6	0.411	15.3	2250			185.4	13.1	750	"
7	0.411	15.3	2500	265.0	14.5	203.7	130	750	"
8	0.338	18.7	2000			170.4	16.0	900	"
9	0.338	18.7	2500			218.8	15.7	900	"
10	0.338	18.7	2000			152.7	16.0	1102	"
11	0.338	18.7	2500	242.8	17.0	192.7	15.8	1102	"
12	0.301	21.0	2500	229.7	17.3	192.7	17.5	1192	"
13	0.260	24.4	2000	213.5	20.4	178.7	20.3	900	NO

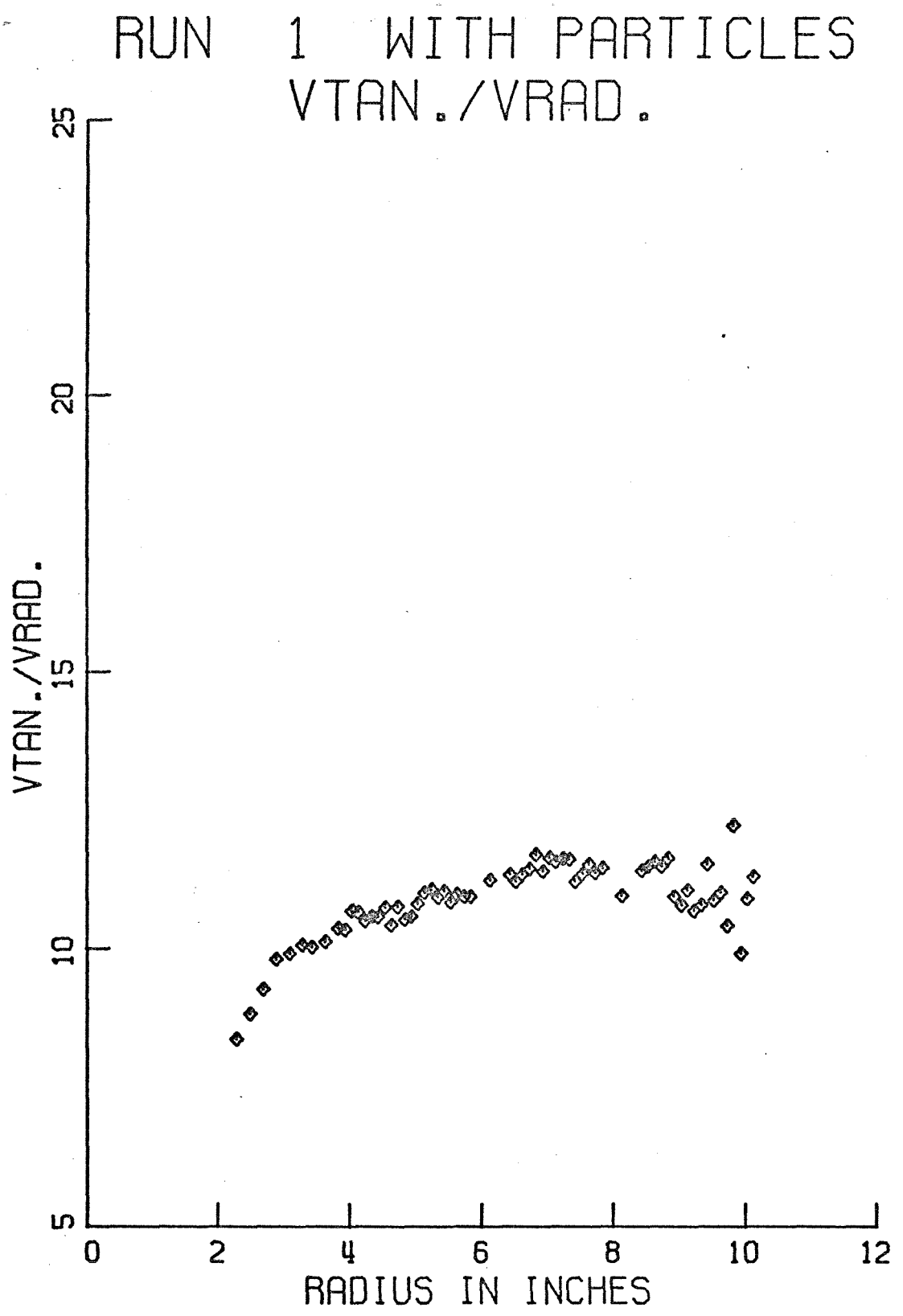
RUN 1 WITH PARTICLES
VTAN./VRAD.
VTAN./VRAD.
25
20
15
10
5
0
2
4
6
8
10
12
RADIUS IN INCHES

Figure E.1

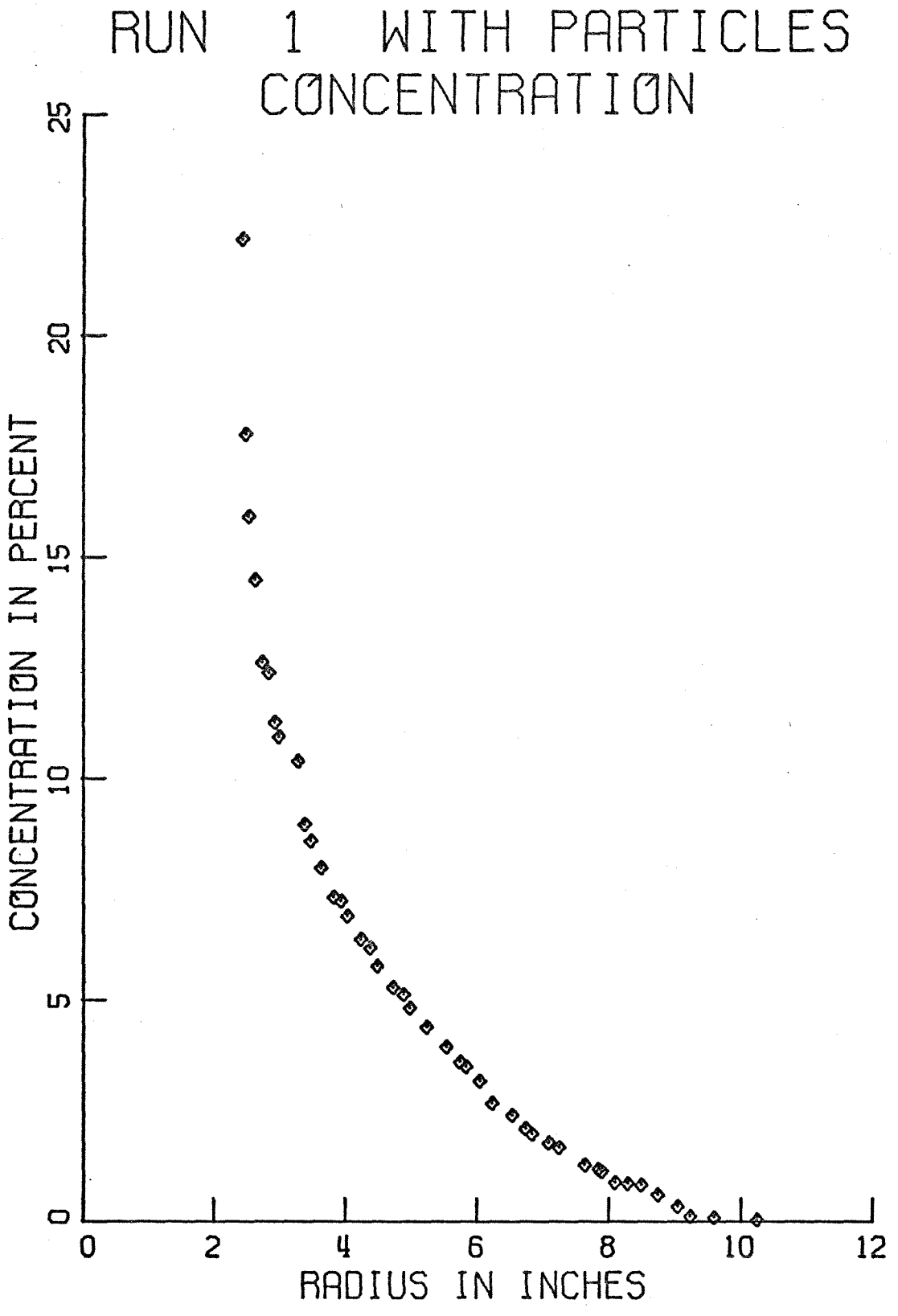
RUN 1 WITH PARTICLES
CONCENTRATION
CONCENTRATION IN PERCENT
0
5
10
15
20
25
0
2
4
6
8
10
12
RADIUS IN INCHES

Figure E.2

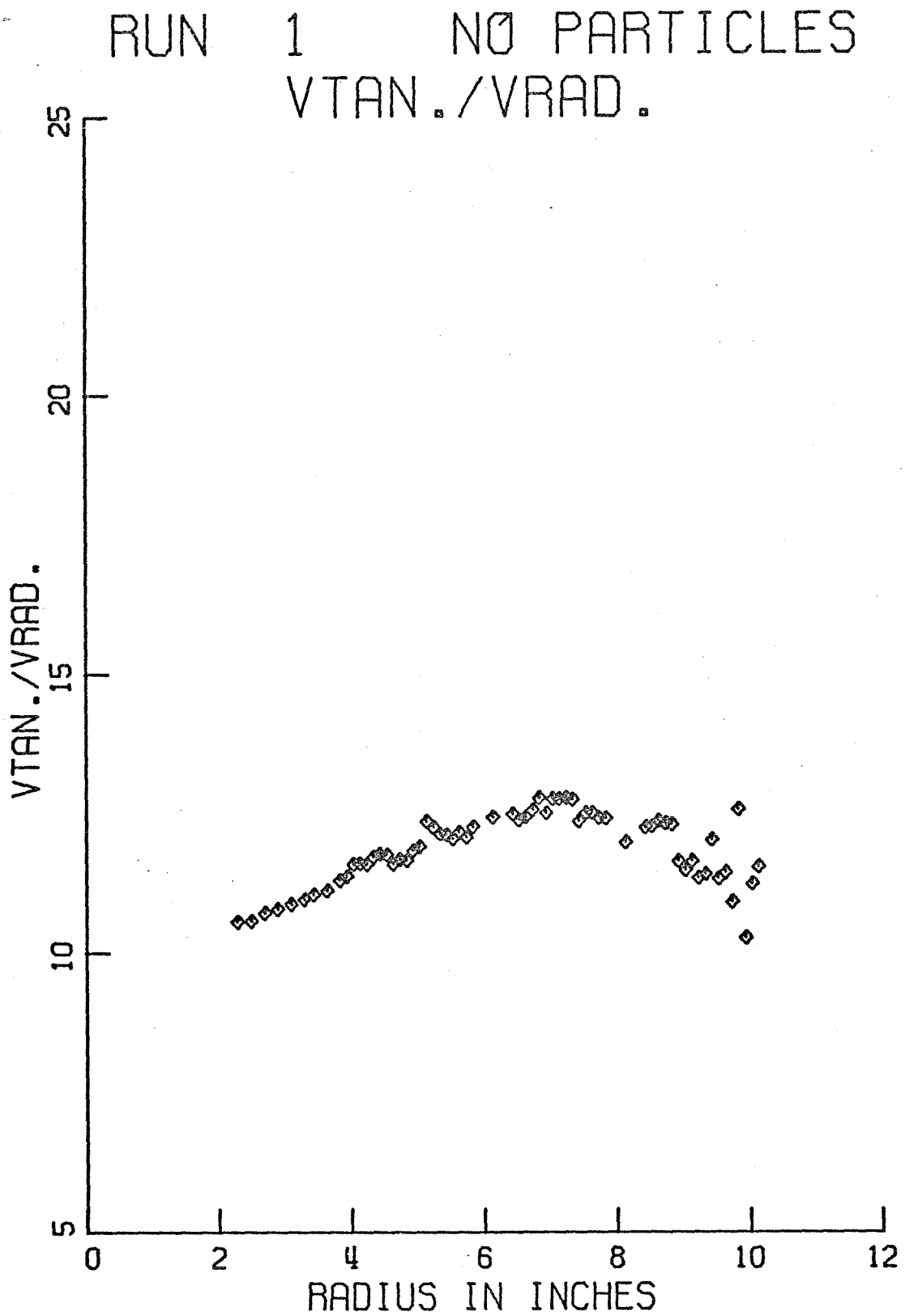
RUN 1 NØ PARTICLES
VTAN./VRAD.
VTAN./VRAD.
25
20
15
10
5
0
2
4
6
8
10
12
RADIUS IN INCHES

Figure E.3

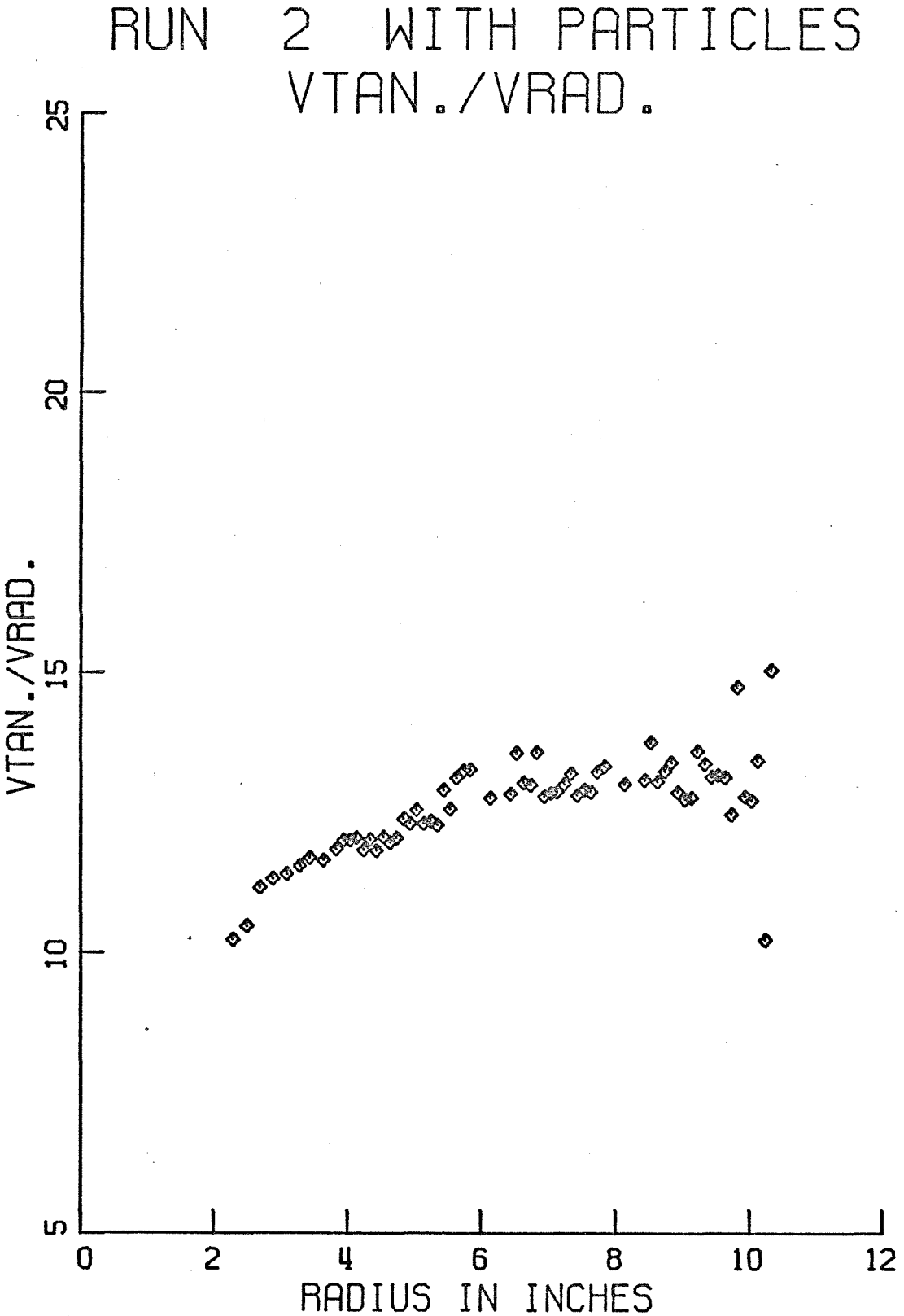
RUN 2 WITH PARTICLES
VTAN./VRAD.
VTAN./VRAD.
25
20
15
10
5
0
2
4
6
8
10
12
RADIUS IN INCHES

Figure E.4

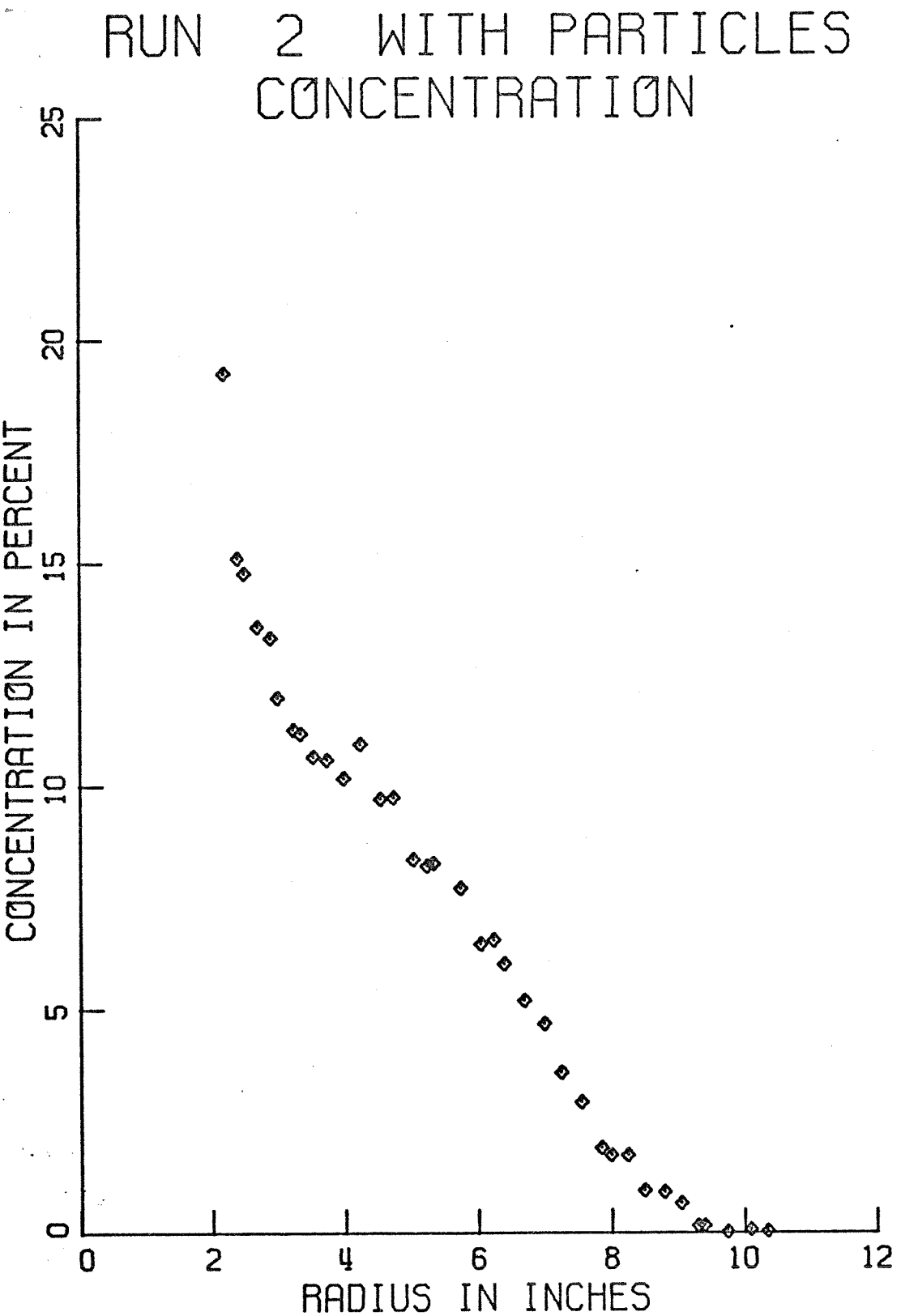
RUN 2 WITH PARTICLES
CONCENTRATION
CONCENTRATION IN PERCENT
0
5
10
15
20
25
0
2
4
6
8
10
12
RADIUS IN INCHES

Figure E.5

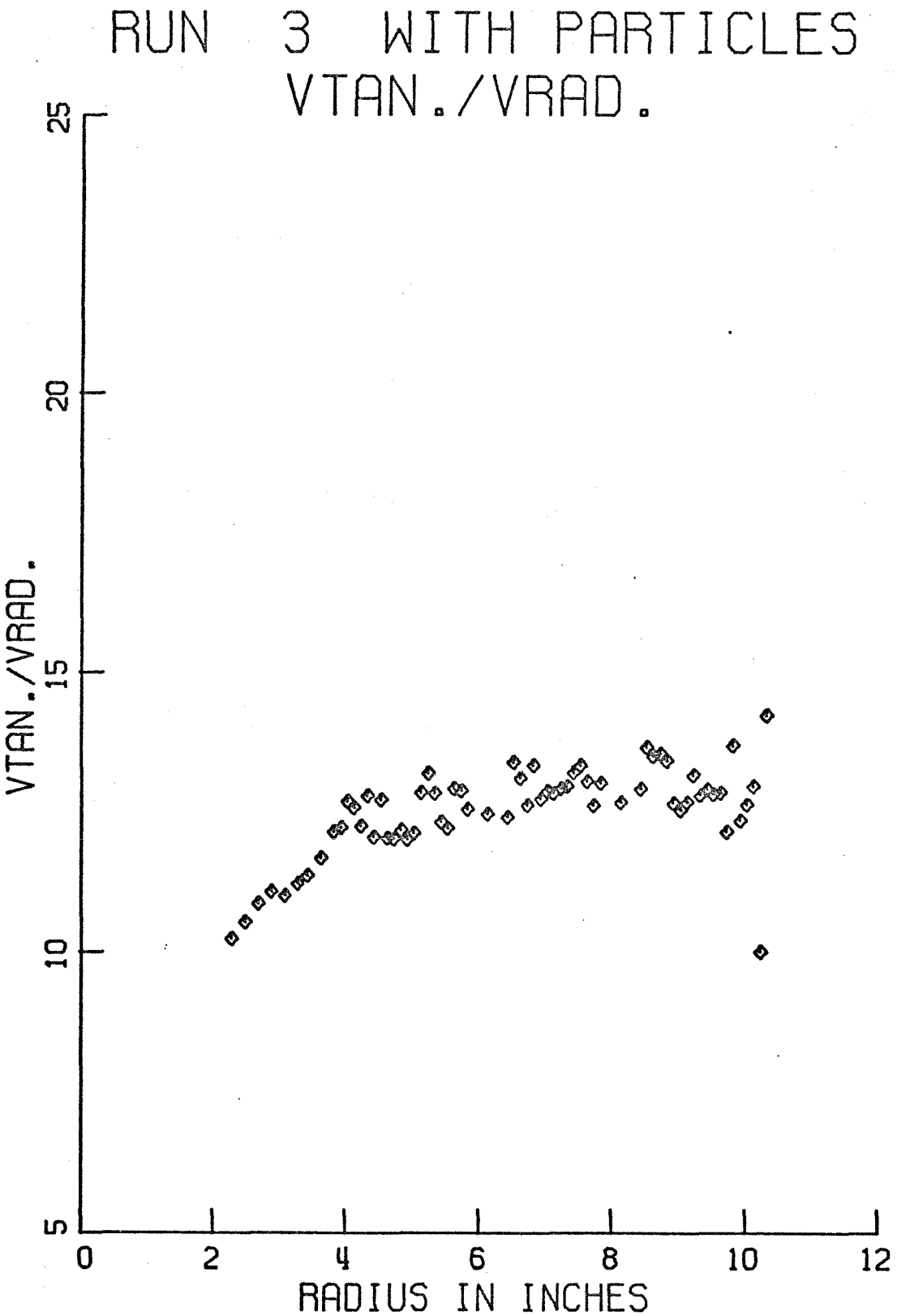
RUN 3 WITH PARTICLES
VTAN./VRAD.
VTAN./VRAD.
25
20
15
10
5
0
2
4
6
8
10
12
RADIUS IN INCHES

Figure E.6

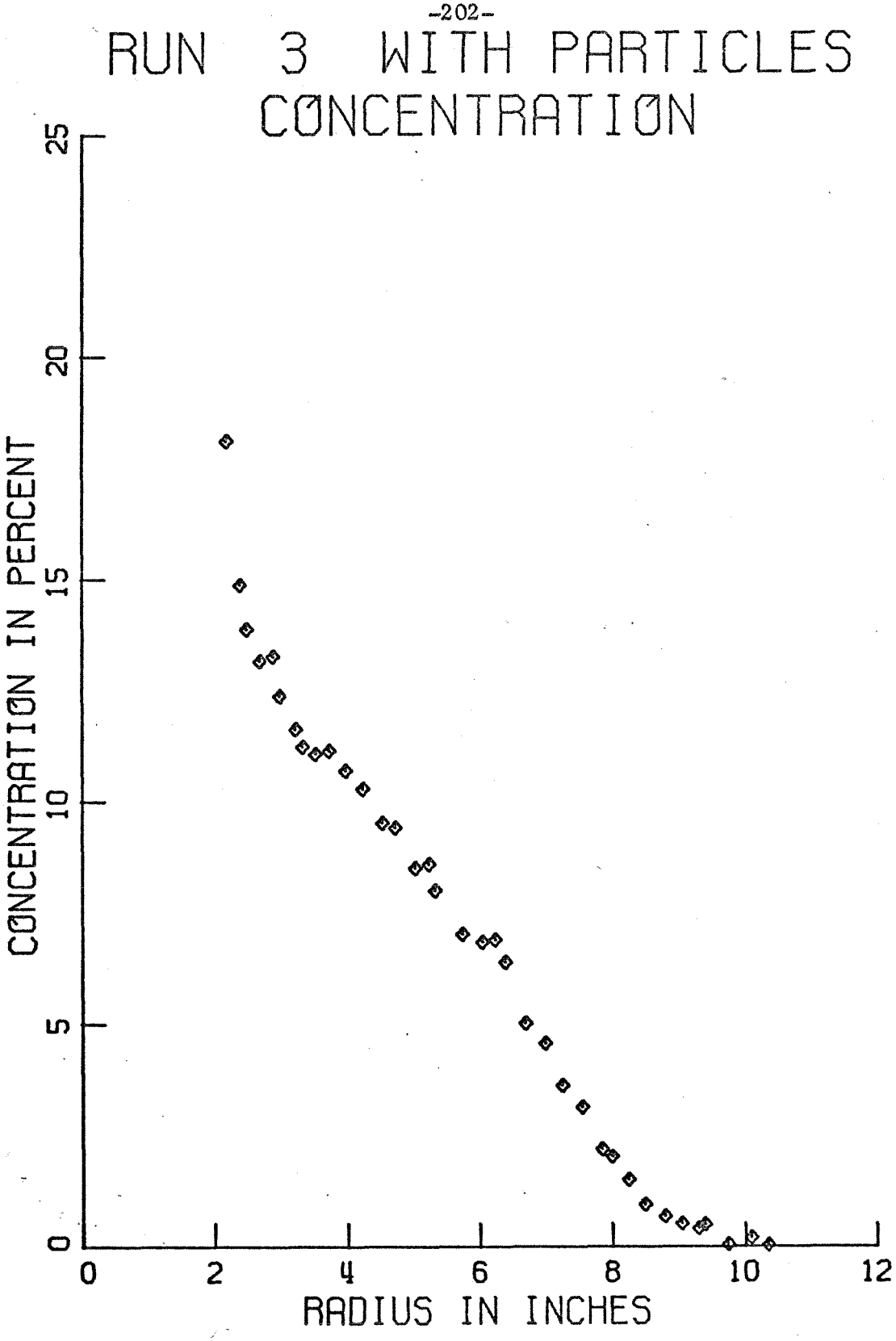
RUN 3 WITH PARTICLES
CONCENTRATION
CONCENTRATION IN PERCENT
0
5
10
15
20
25
0
2
4
6
8
10
12
RADIUS IN INCHES

Figure E.7

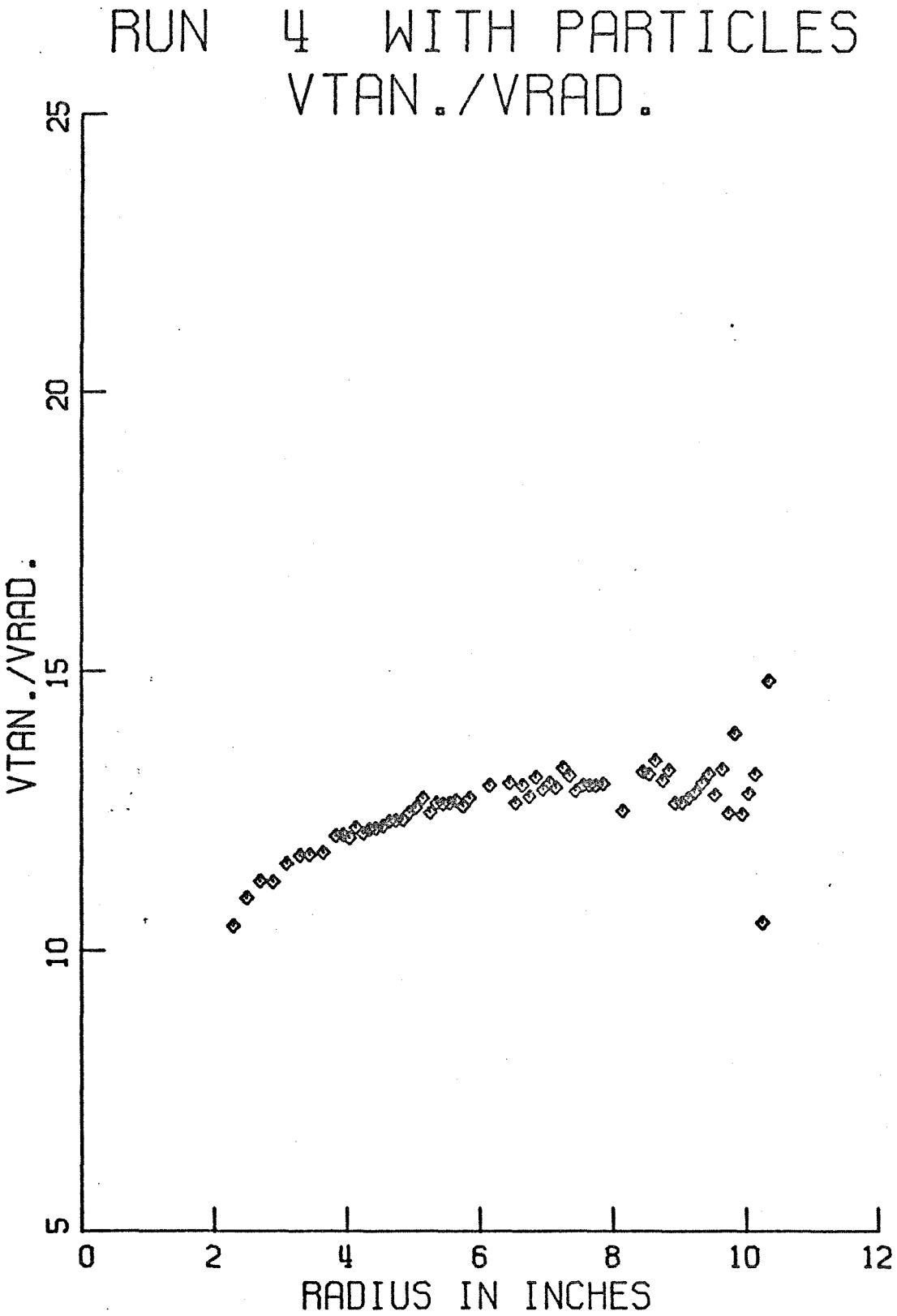
RUN 4 WITH PARTICLES
VTAN./VRAD.
VTAN./VRAD.
25
20
15
10
5
0
2
4
6
8
10
12
RADIUS IN INCHES

Figure E.8

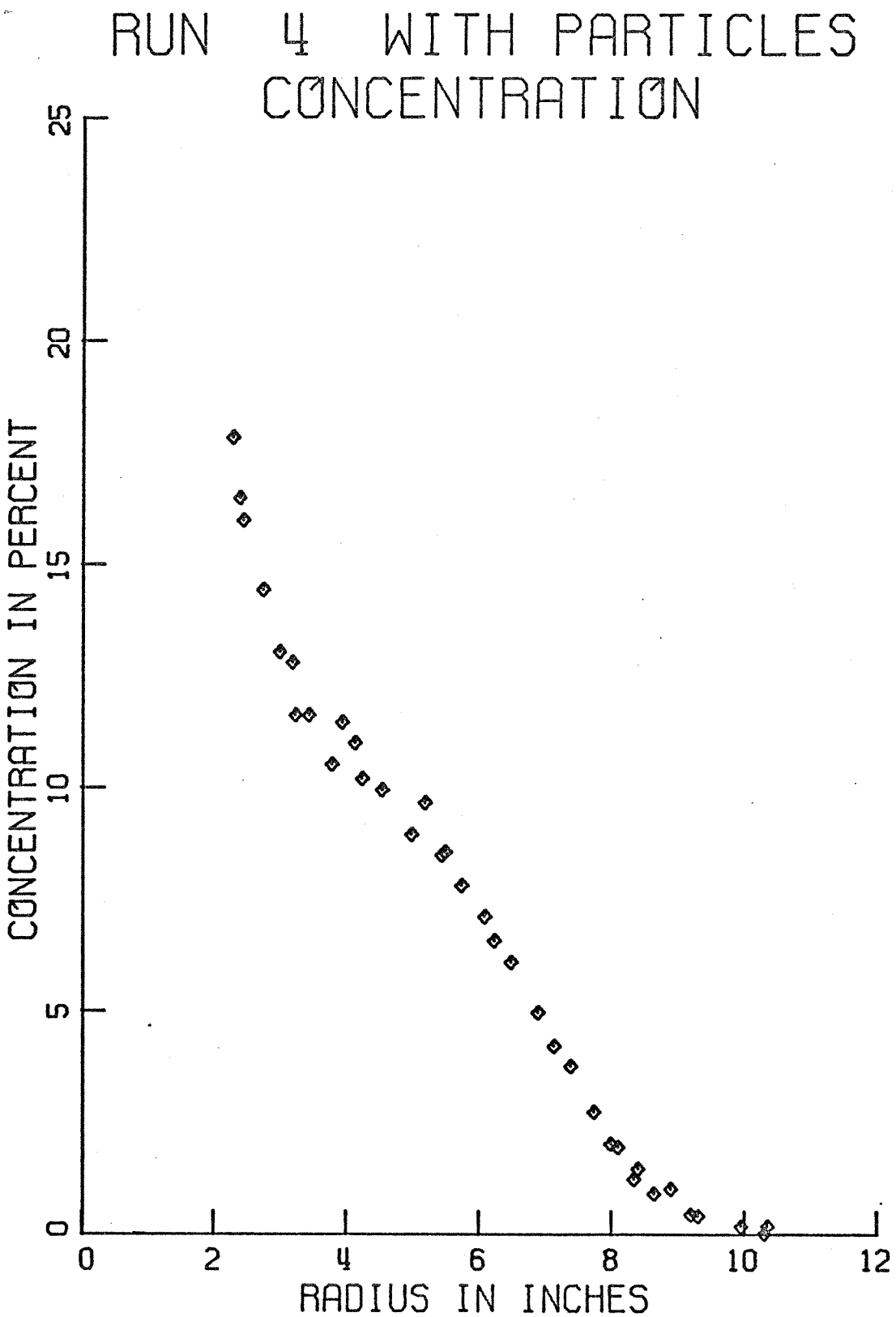
RUN 4 WITH PARTICLES
CONCENTRATION
CONCENTRATION IN PERCENT
0
5
10
15
20
25
0
2
4
6
8
10
12
RADIUS IN INCHES

Figure E.9

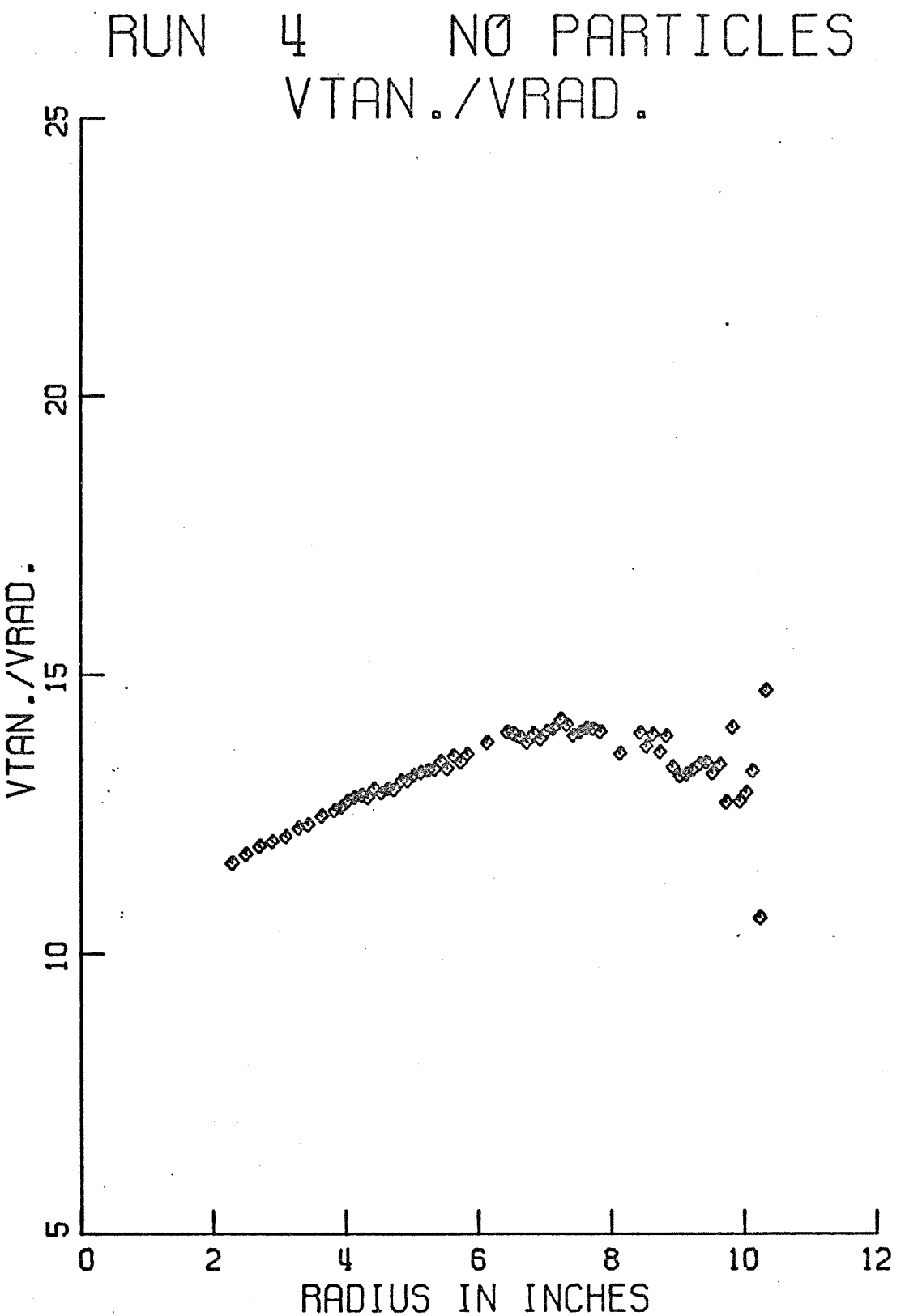
RUN 4 NØ PARTICLES
VTAN./VRAD.
VTAN./VRAD.
25
20
15
10
5
0
2
4
6
8
10
12
RADIUS IN INCHES

Figure E.10

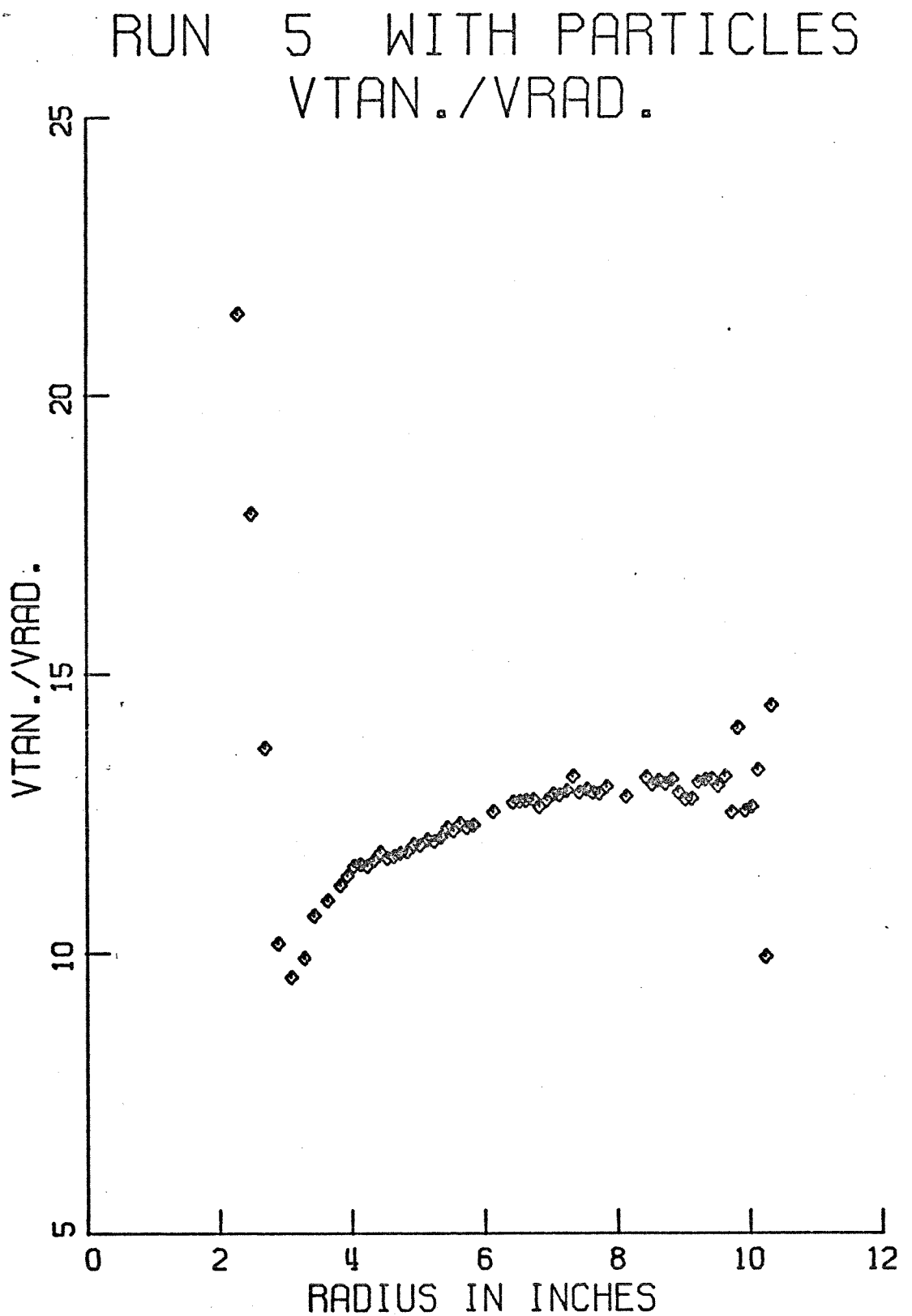
RUN 5 WITH PARTICLES
VTAN./VRAD.
VTAN./VRAD.
25
20
15
10
5
0
2
4
6
8
10
12
RADIUS IN INCHES

Figure E.11

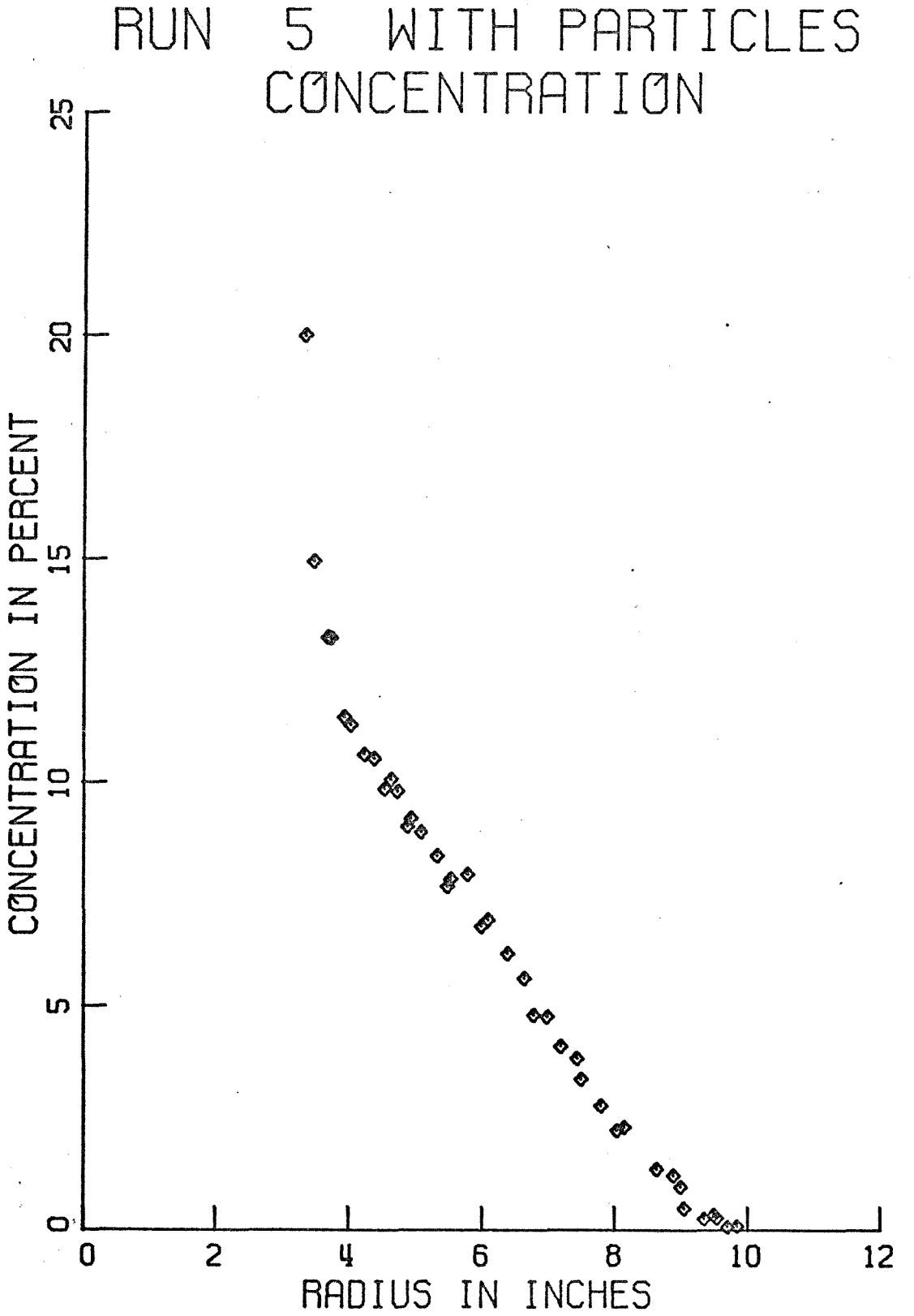
RUN 5 WITH PARTICLES
CONCENTRATION
CONCENTRATION IN PERCENT
0
5
10
15
20
25
0
2
4
6
8
10
12
RADIUS IN INCHES

Figure E.12

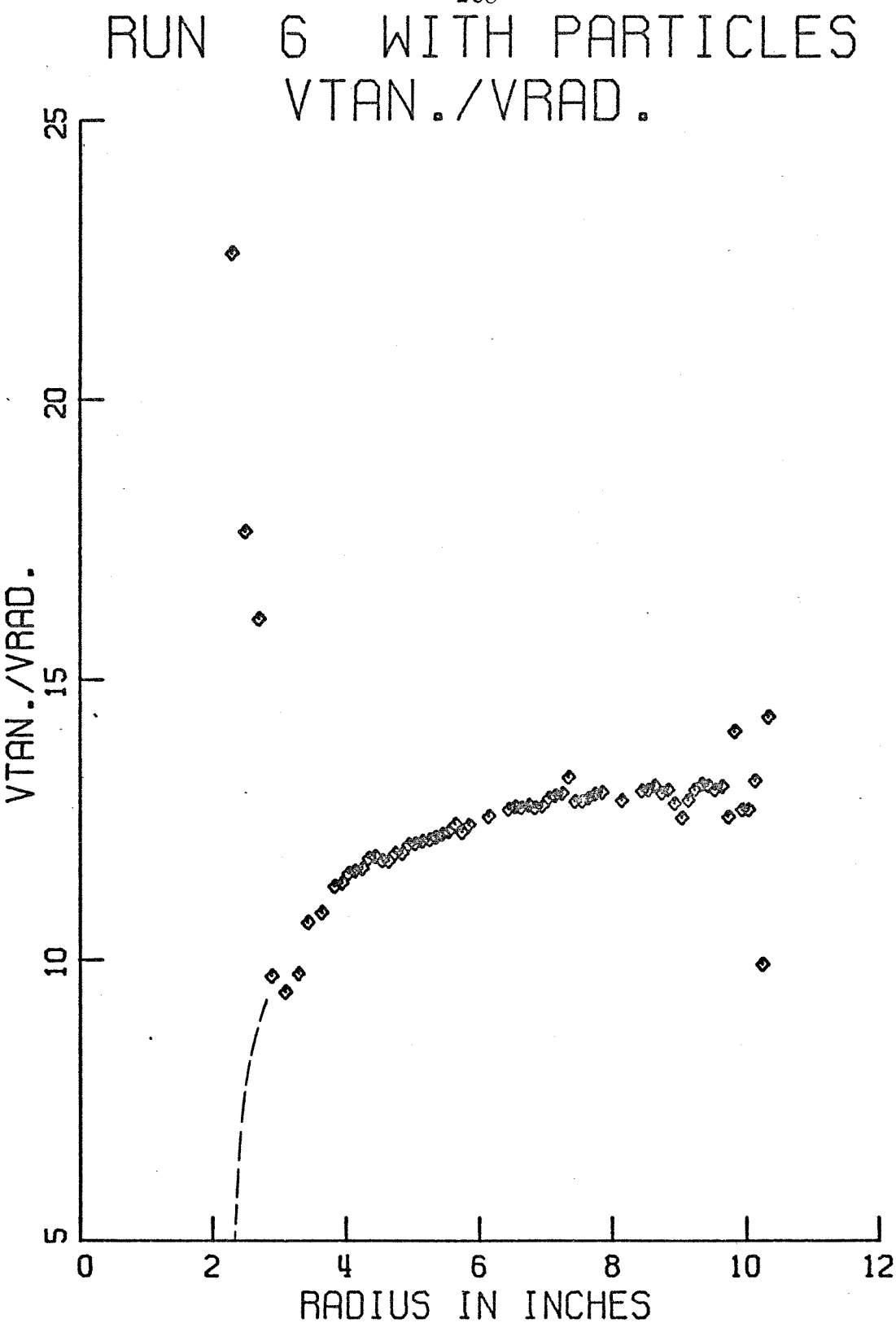
RUN 6 WITH PARTICLES
VTAN./VRAD.
VTAN./VRAD.
25
20
15
10
5
0
2
4
6
8
10
12
RADIUS IN INCHES

Figure E.13

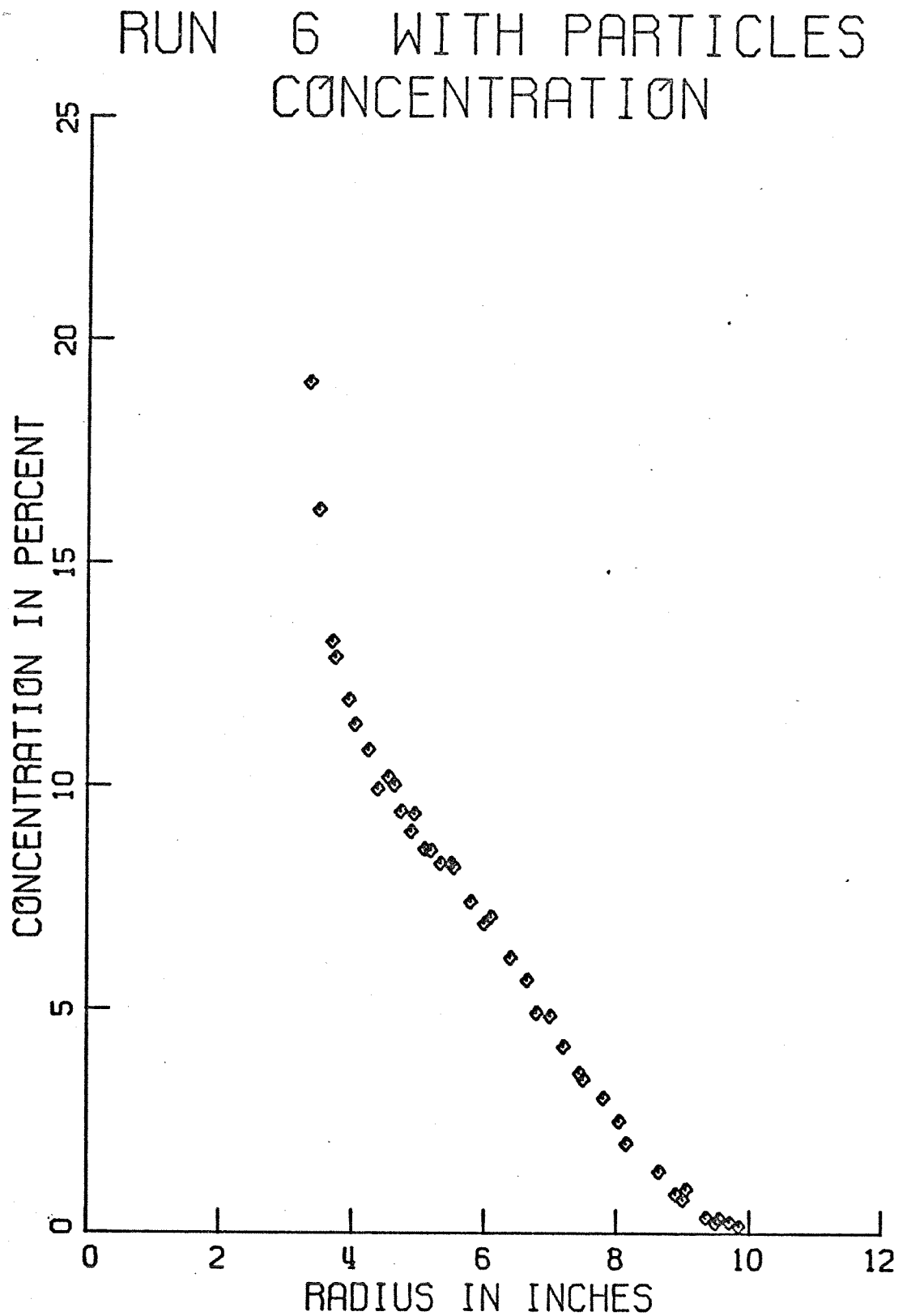
RUN 6 WITH PARTICLES
CONCENTRATION
CONCENTRATION IN PERCENT
0
5
10
15
20
25
0
2
4
6
8
10
12
RADIUS IN INCHES

Figure E.14

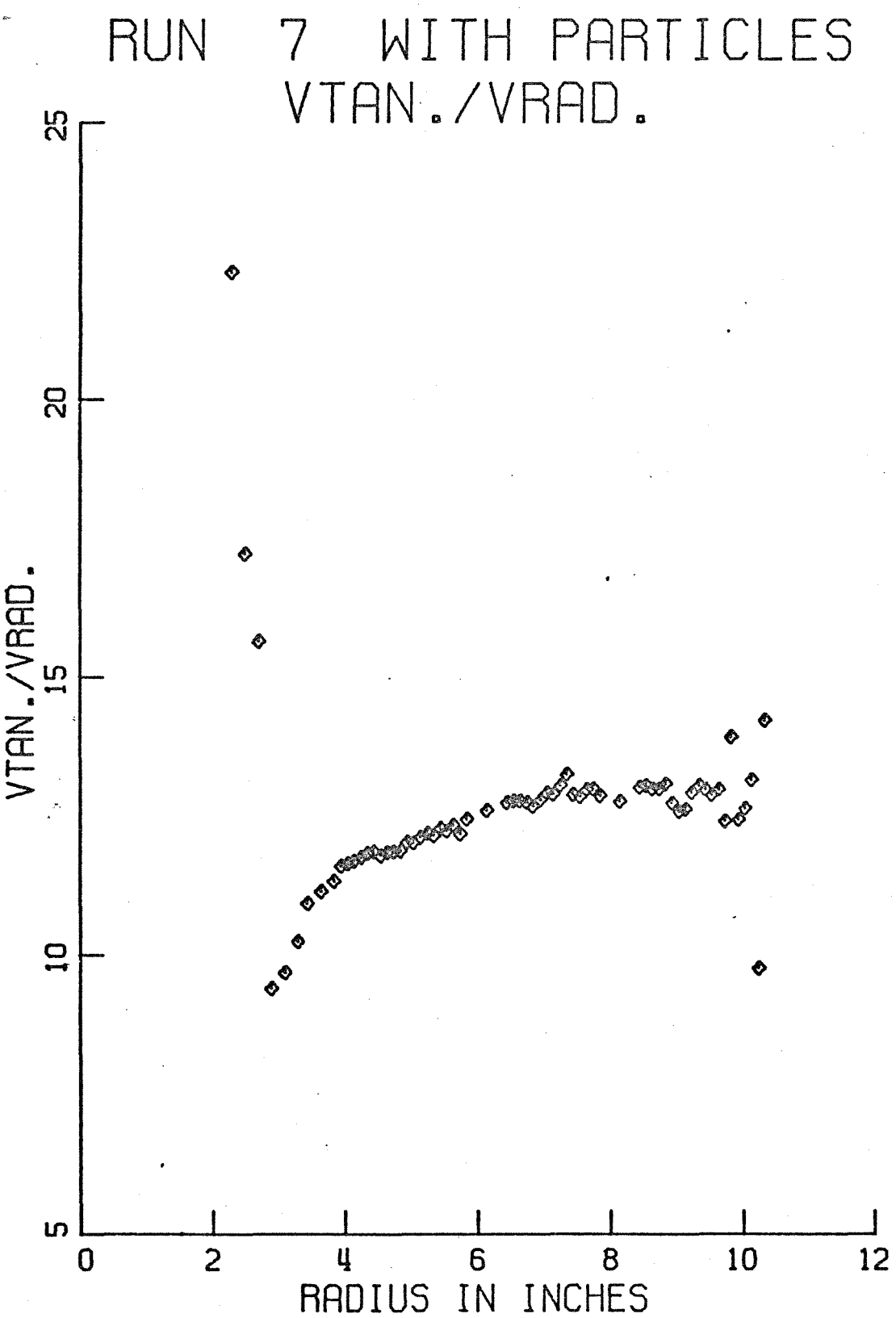
RUN 7 WITH PARTICLES
VTAN./VRAD.
VTAN./VRAD.
25
20
15
10
5
0
2
4
6
8
10
12
RADIUS IN INCHES

Figure E.15

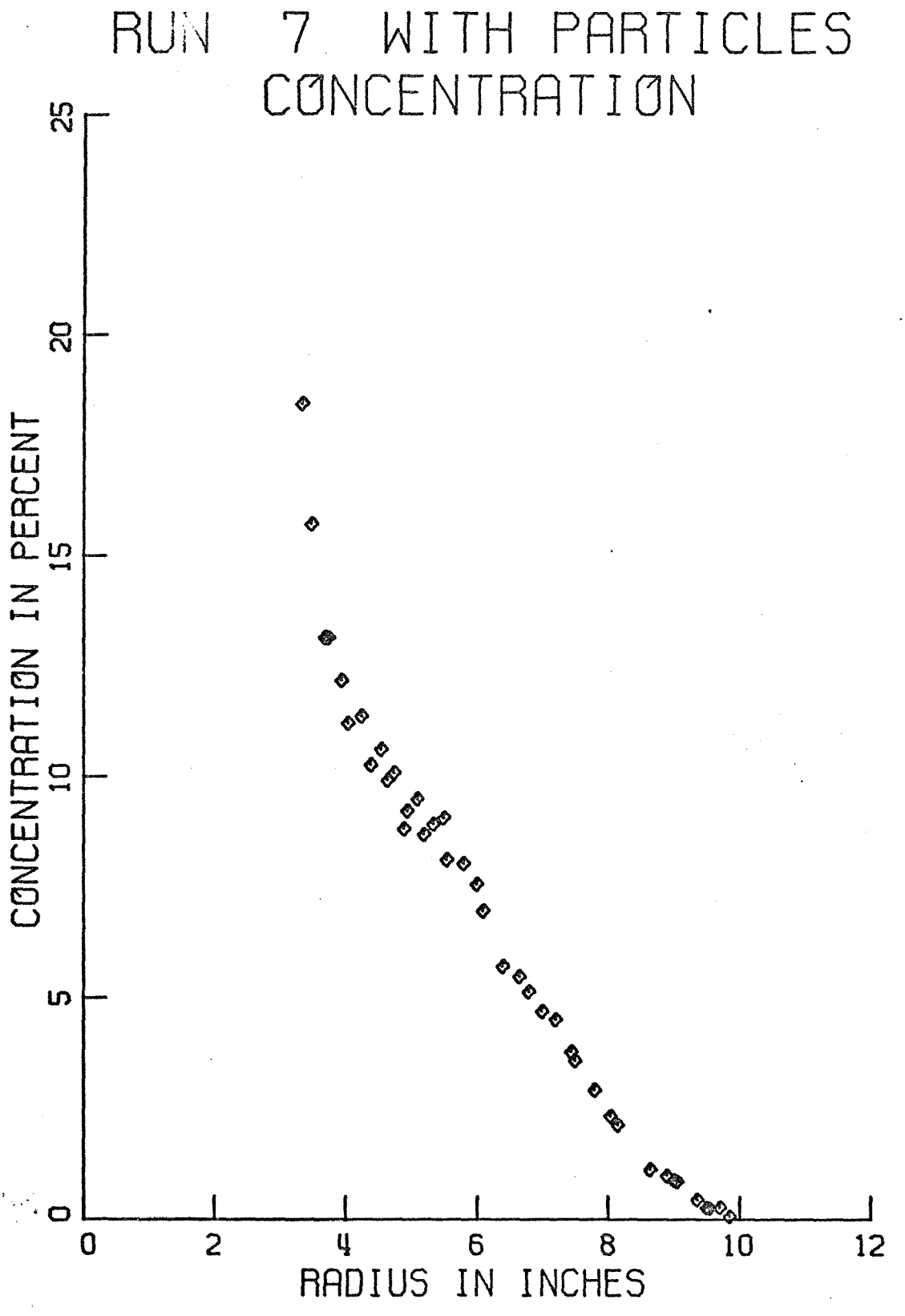
RUN 7 WITH PARTICLES
CONCENTRATION
CONCENTRATION IN PERCENT
0
5
10
15
20
25
0
2
4
6
8
10
12
RADIUS IN INCHES

Figure E.16

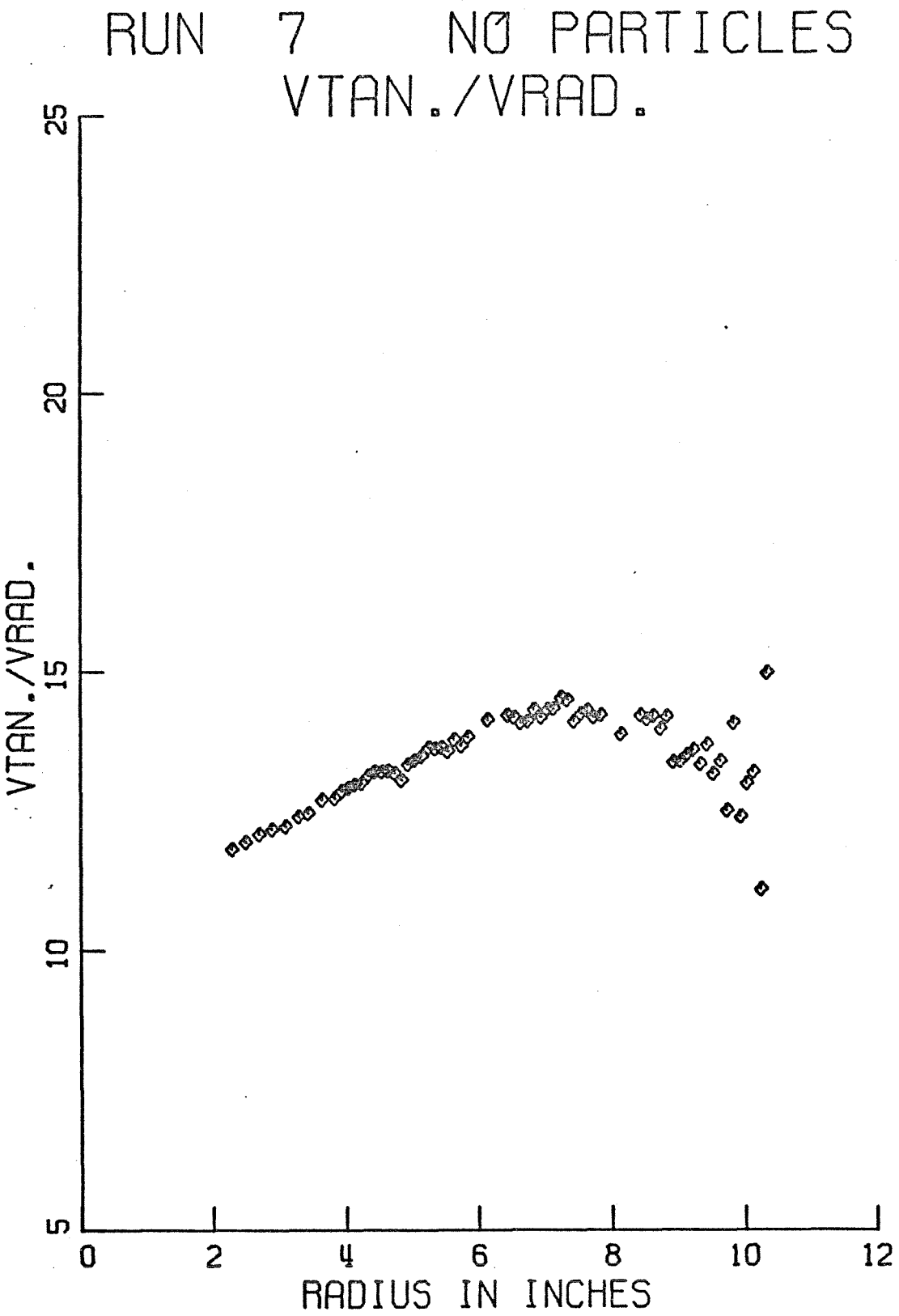
RUN 7 NØ PARTICLES
VTAN./VRAD.
VTAN./VRAD.
25
20
15
10
5
0
2
4
6
8
10
12
RADIUS IN INCHES

Figure E.17

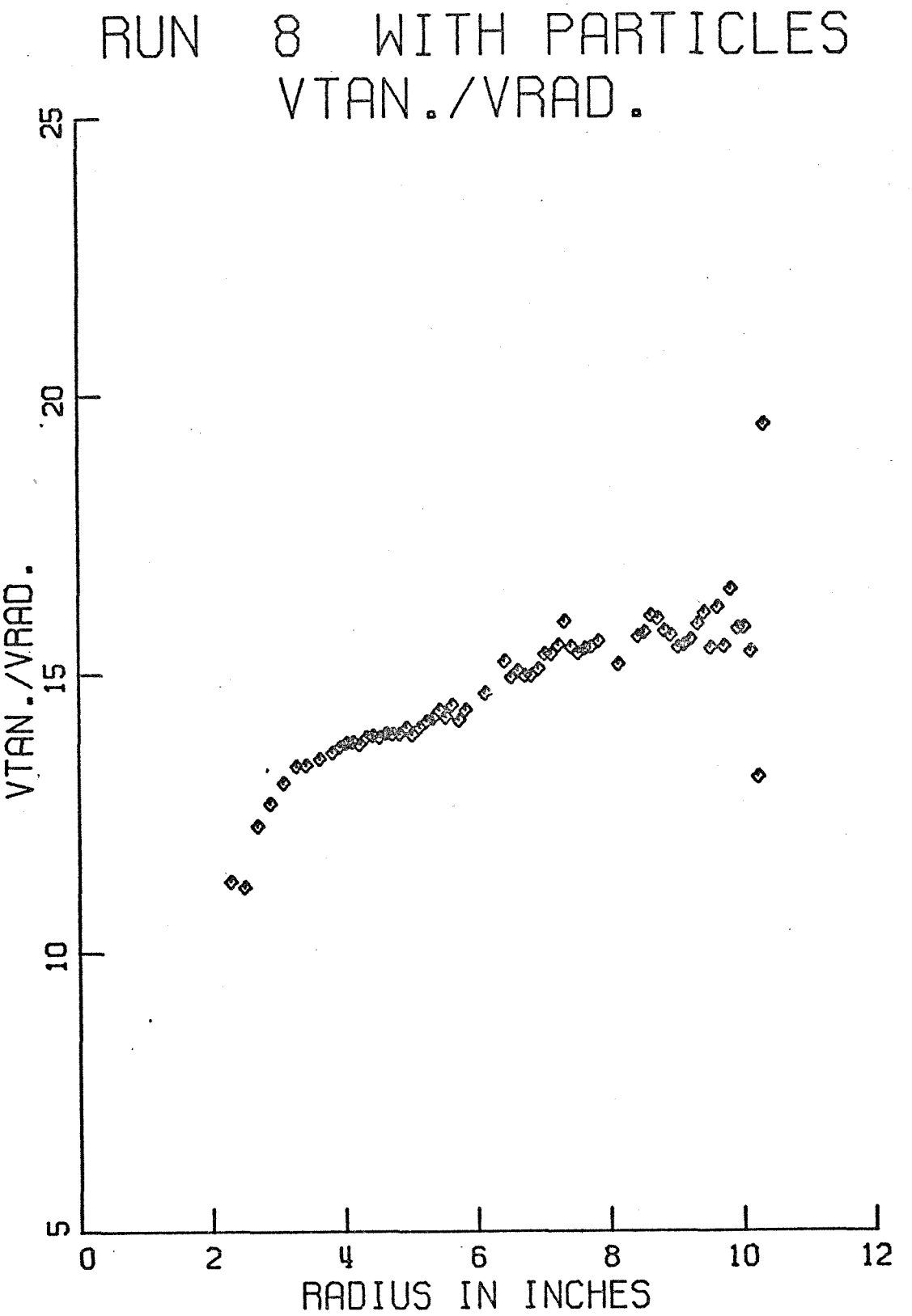
RUN 8 WITH PARTICLES
VTAN./VRAD.
VTAN./VRAD.
25
20
15
10
5
0
2
4
6
8
10
12
RADIUS IN INCHES

Figure E.18

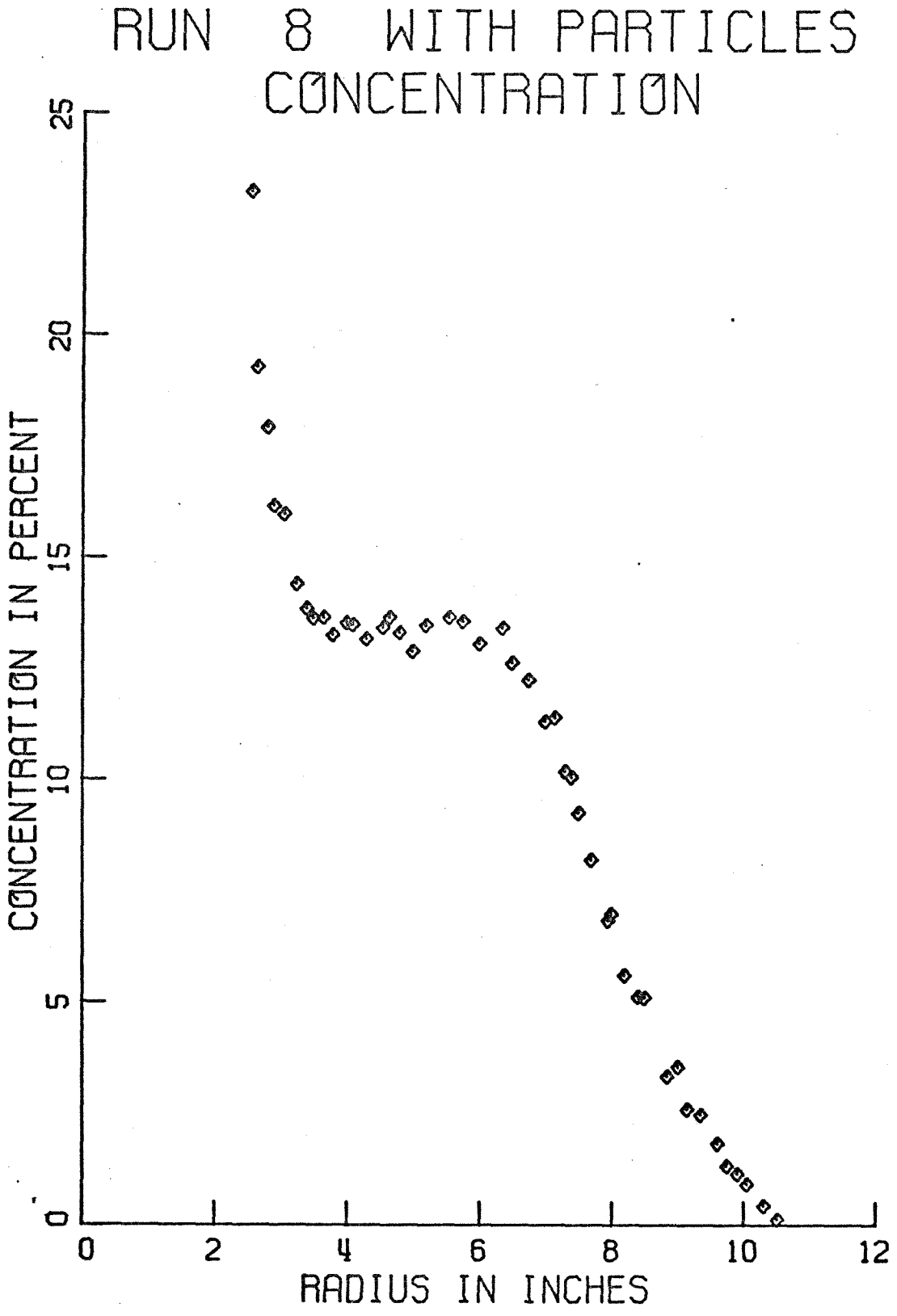
RUN 8 WITH PARTICLES
CONCENTRATION
CONCENTRATION IN PERCENT
0
5
10
15
20
25
0
2
4
6
8
10
12
RADIUS IN INCHES

Figure E.19

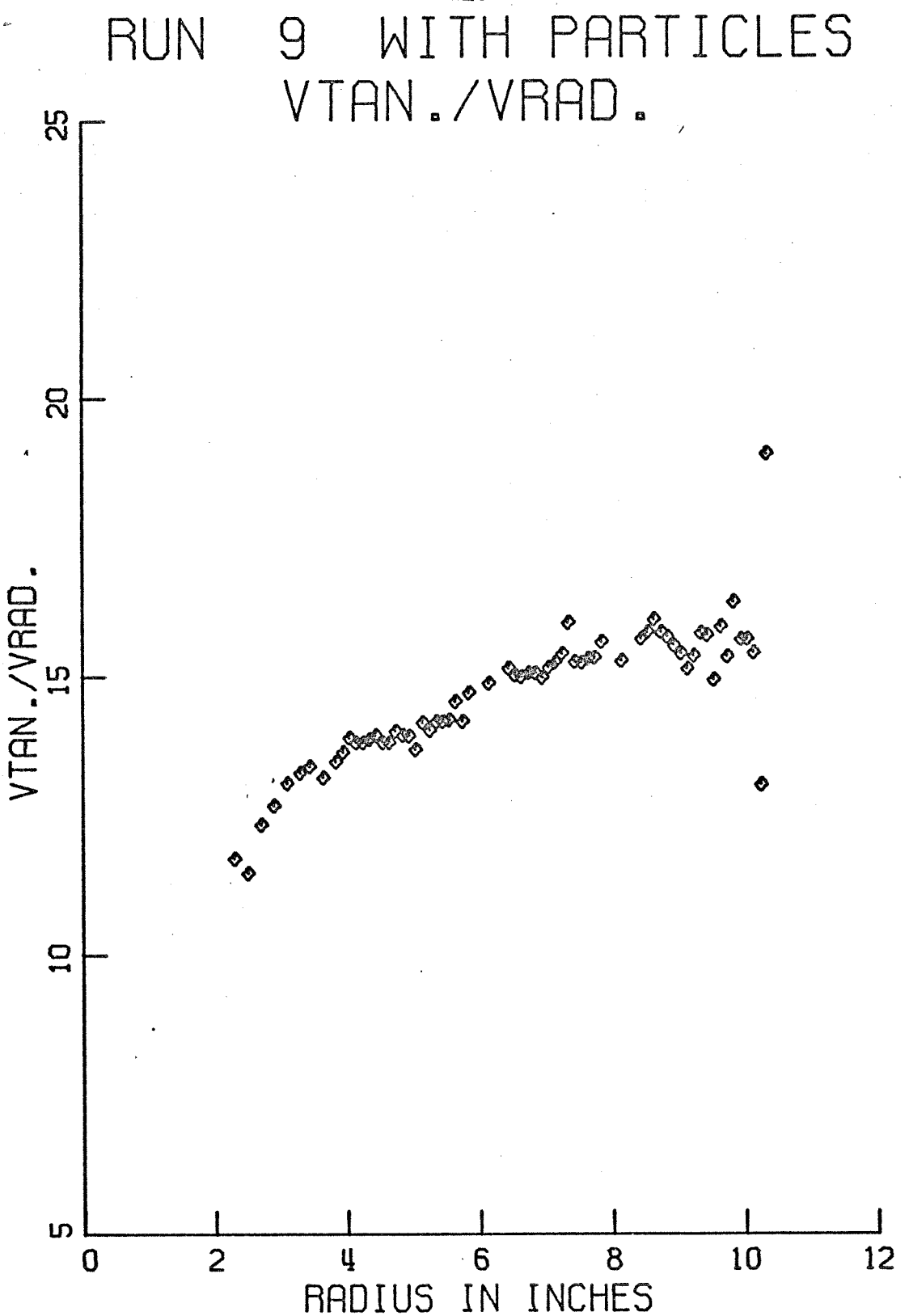
RUN 9 WITH PARTICLES
VTAN./VRAD.
VTAN./VRAD.
25
20
15
10
5
0
2
4
6
8
10
12
RADIUS IN INCHES

Figure E.20

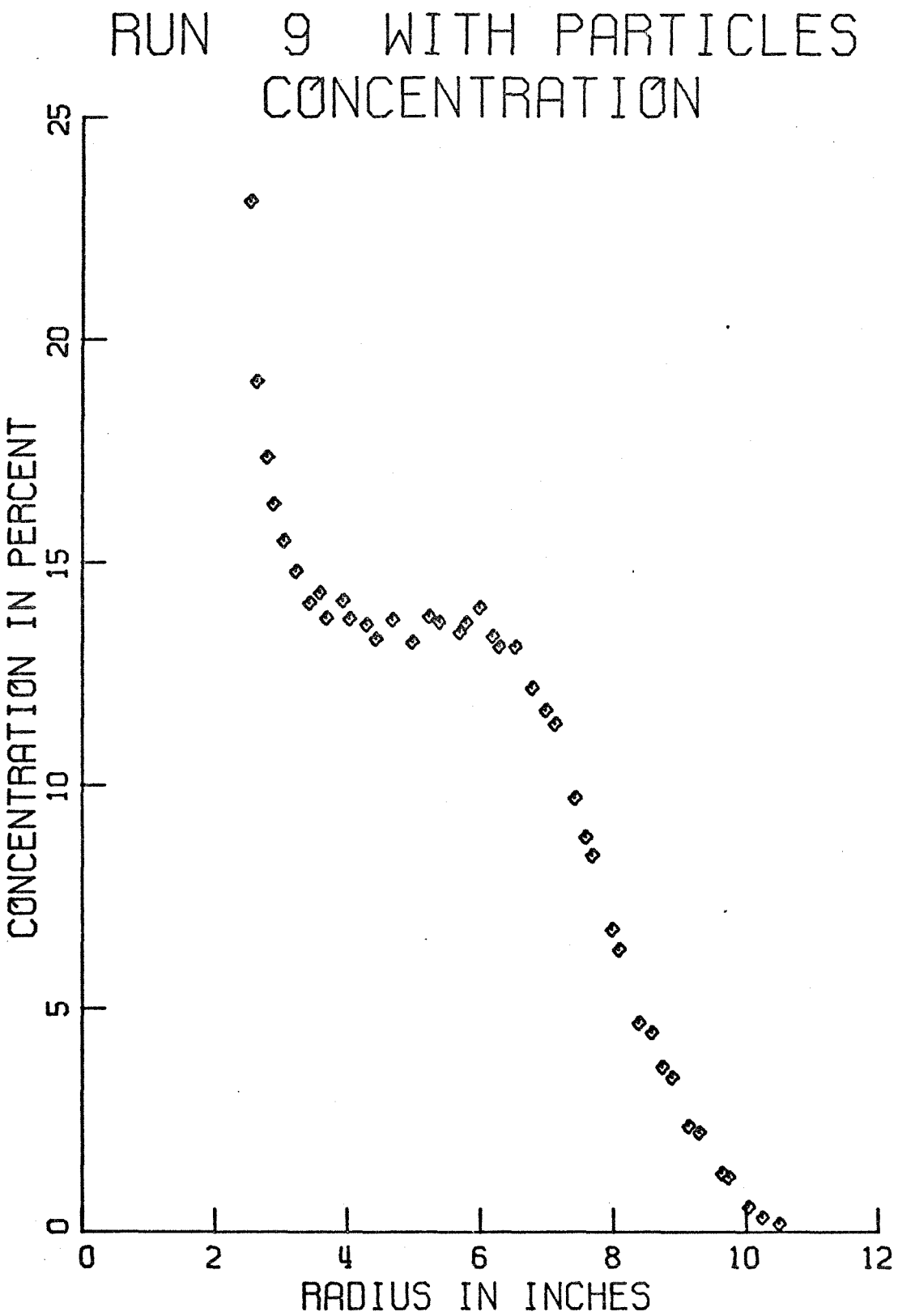
RUN 9 WITH PARTICLES
CONCENTRATION
CONCENTRATION IN PERCENT
0
5
10
15
20
25
0
2
4
6
8
10
12
RADIUS IN INCHES

Figure E.21

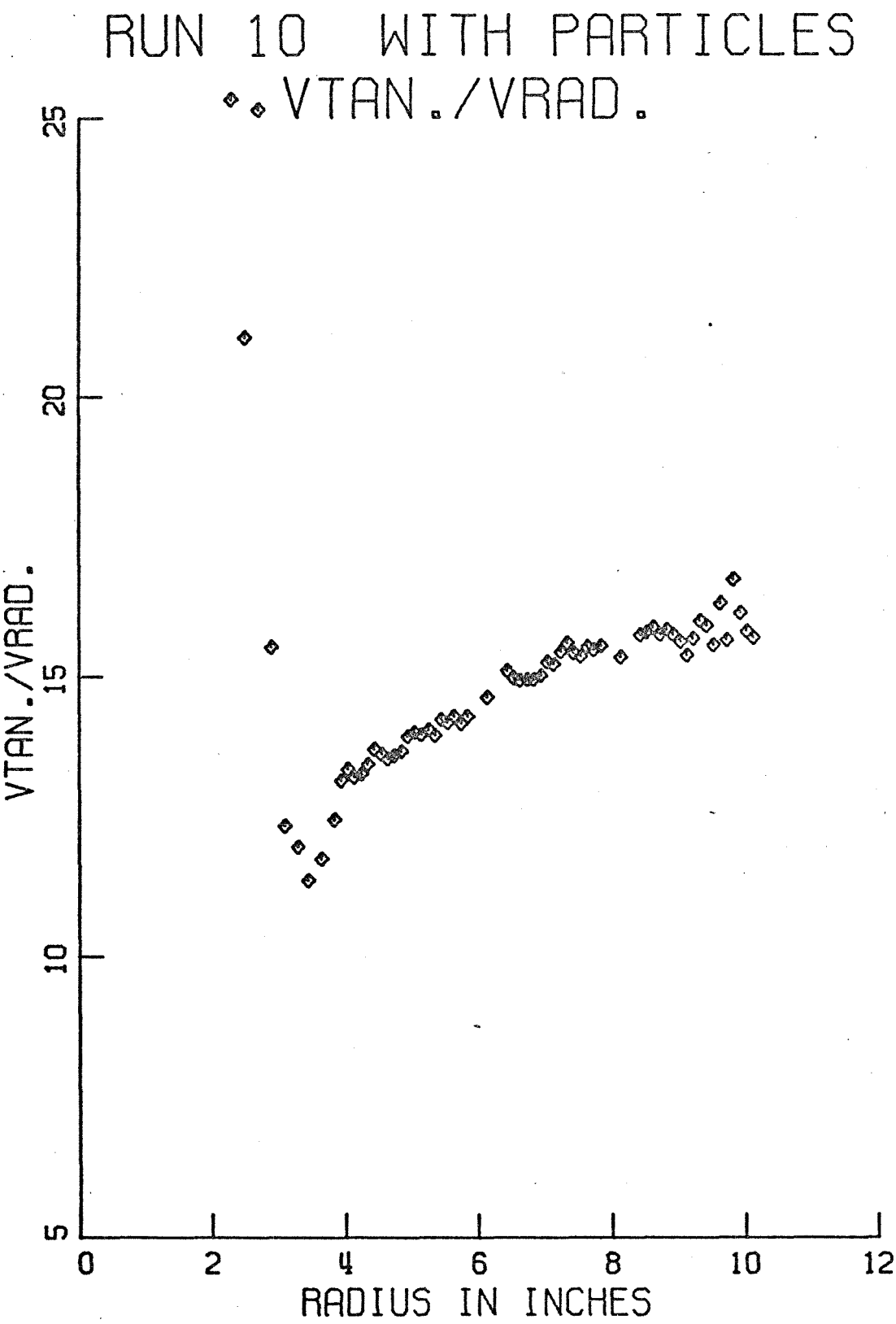
RUN 10 WITH PARTICLES
VTAN./VRAD.
VTAN./VRAD.
25
20
15
10
5
0
2
4
6
8
10
12
RADIUS IN INCHES

Figure E.22

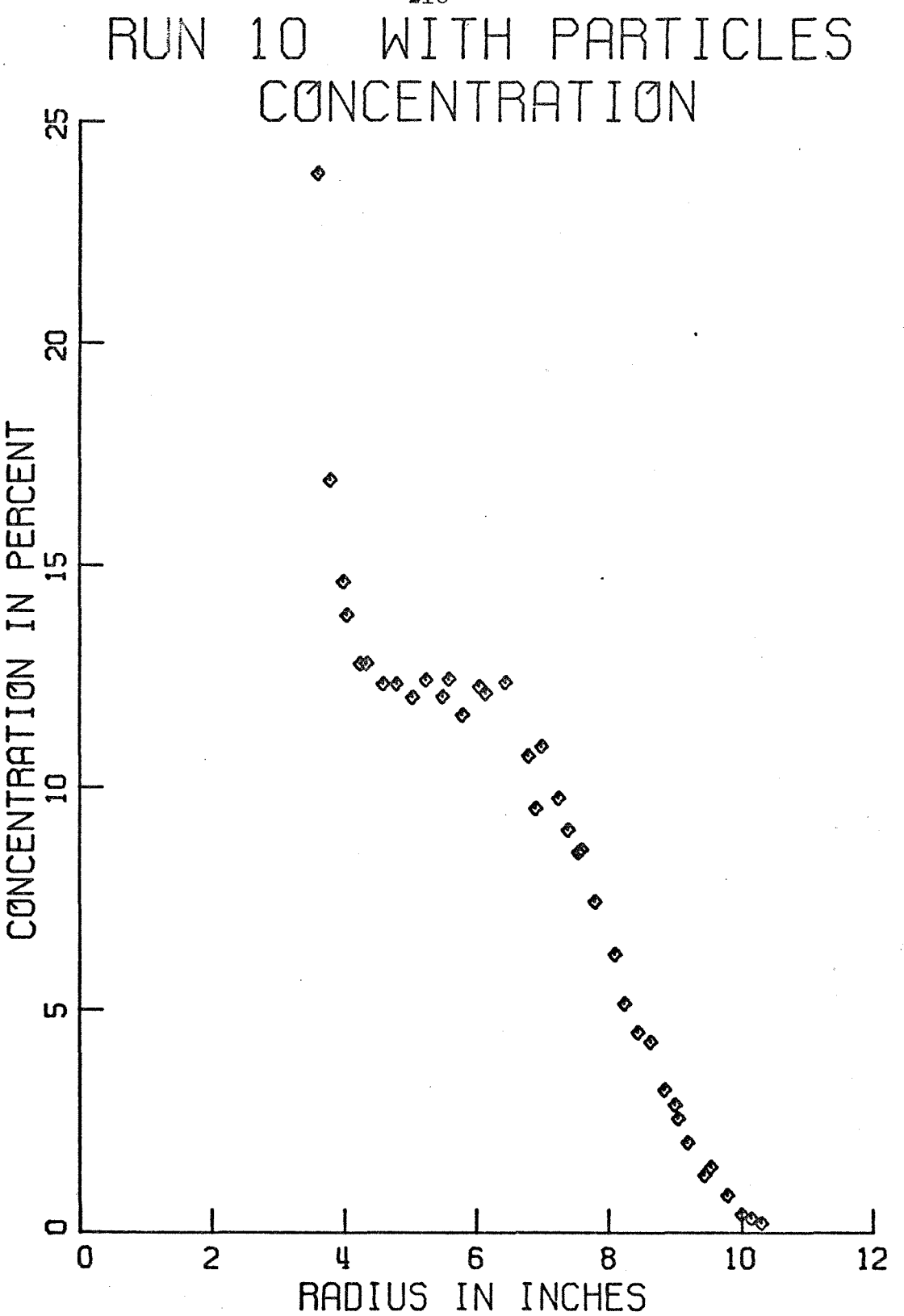
RUN 10 WITH PARTICLES
CONCENTRATION
CONCENTRATION IN PERCENT
0
5
10
15
20
25
0
2
4
6
8
10
12
RADIUS IN INCHES

Figure E.23

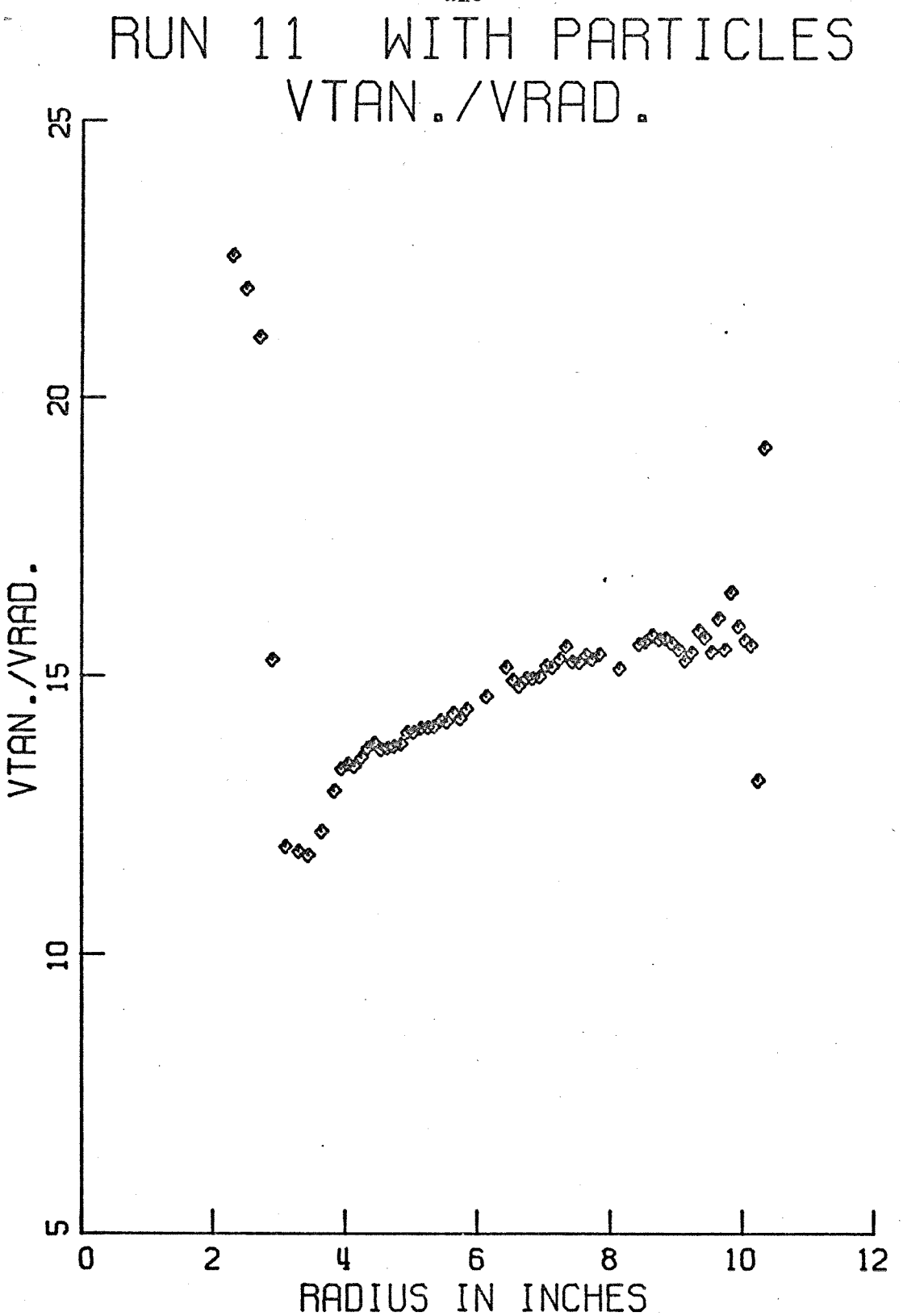
RUN 11 WITH PARTICLES
VTAN./VRAD.
VTAN./VRAD.
25
20
15
10
5
0
2
4
6
8
10
12
RADIUS IN INCHES

Figure E.24

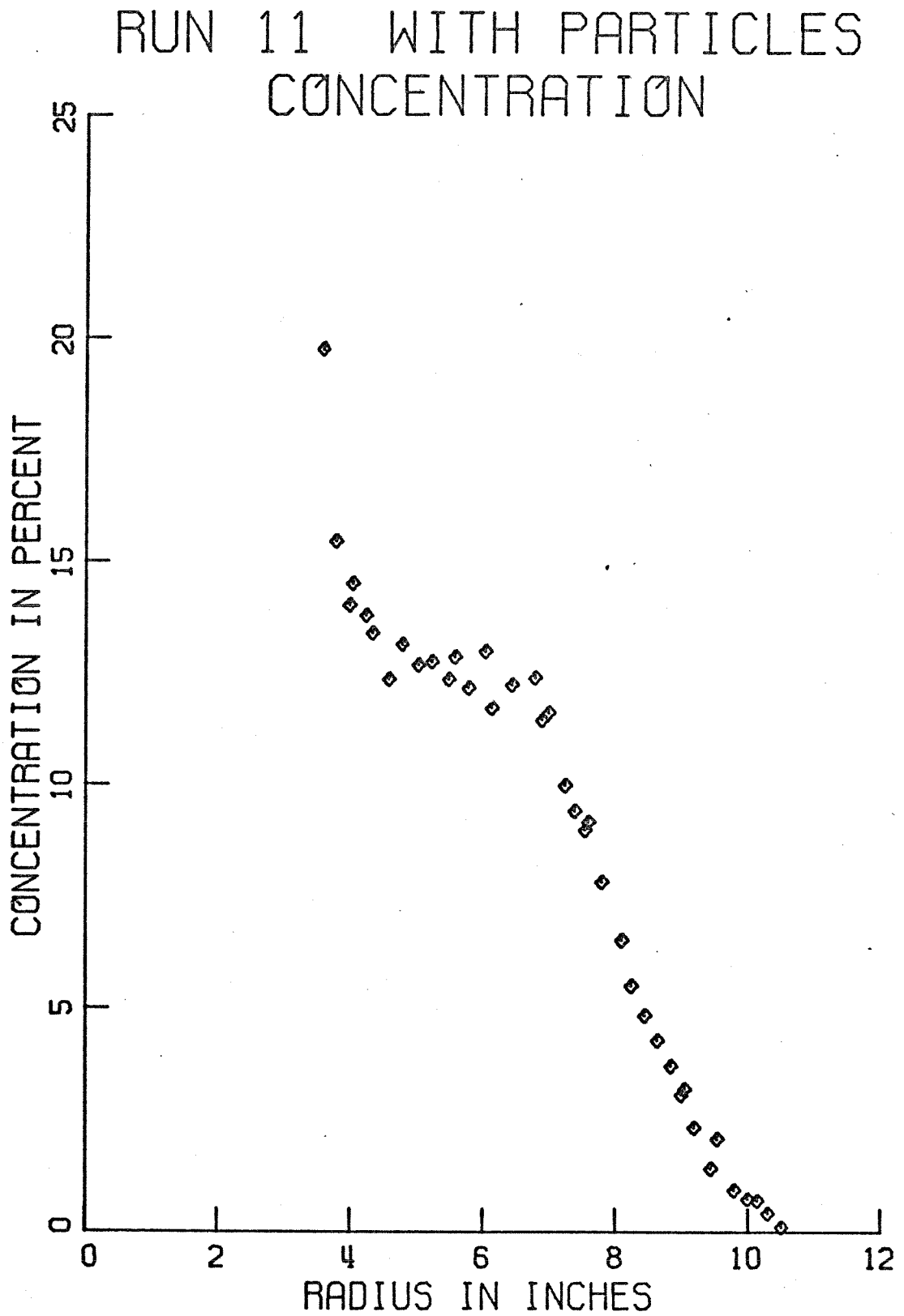
RUN 11 WITH PARTICLES
CONCENTRATION
CONCENTRATION IN PERCENT
0
5
10
15
20
25
0
2
4
6
8
10
12
RADIUS IN INCHES

Figure E.25

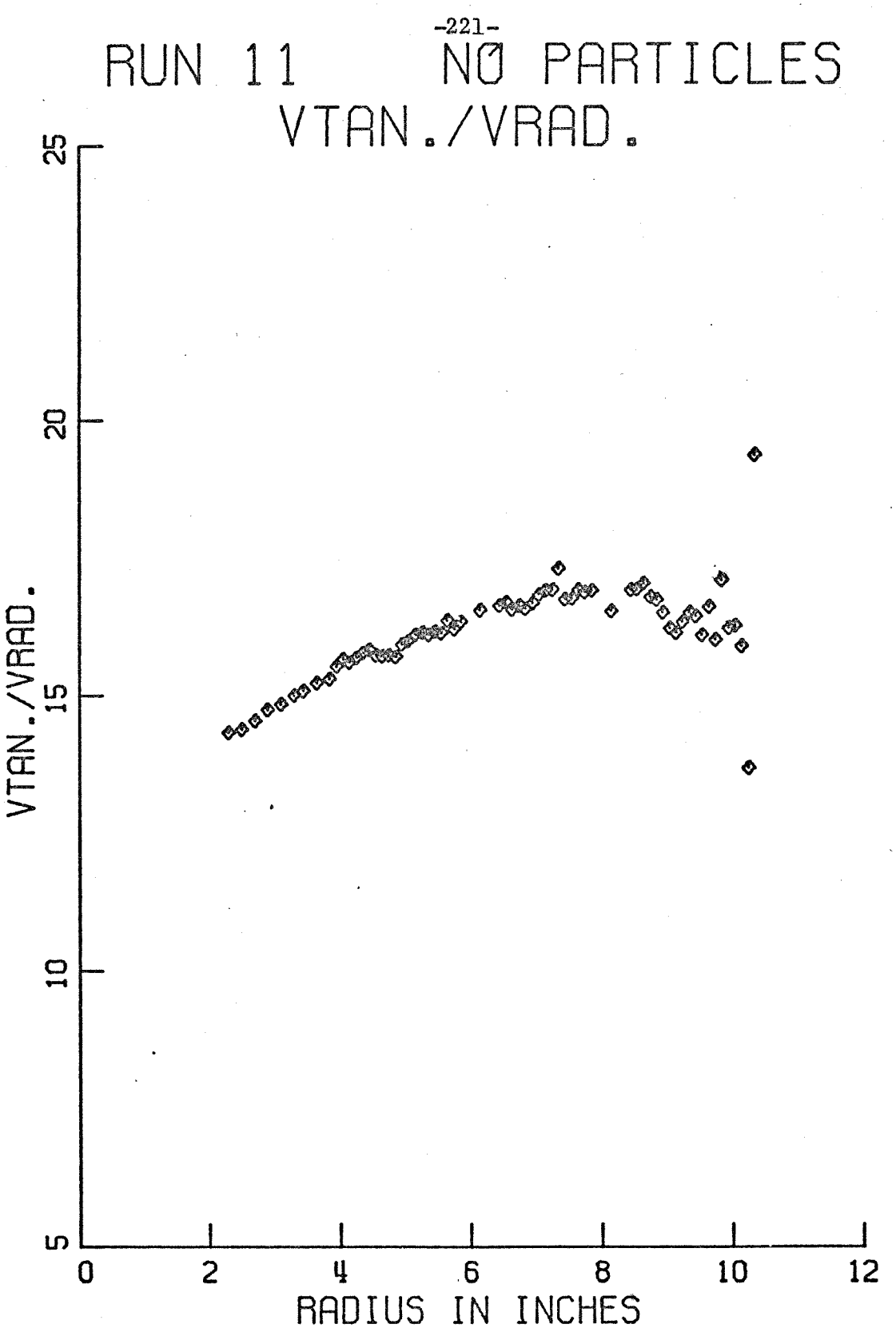
RUN 11 NØ PARTICLES
VTAN./VRAD.
VTAN./VRAD.
25
20
15
10
5
0
2
4
6
8
10
12
RADIUS IN INCHES

Figure E.26

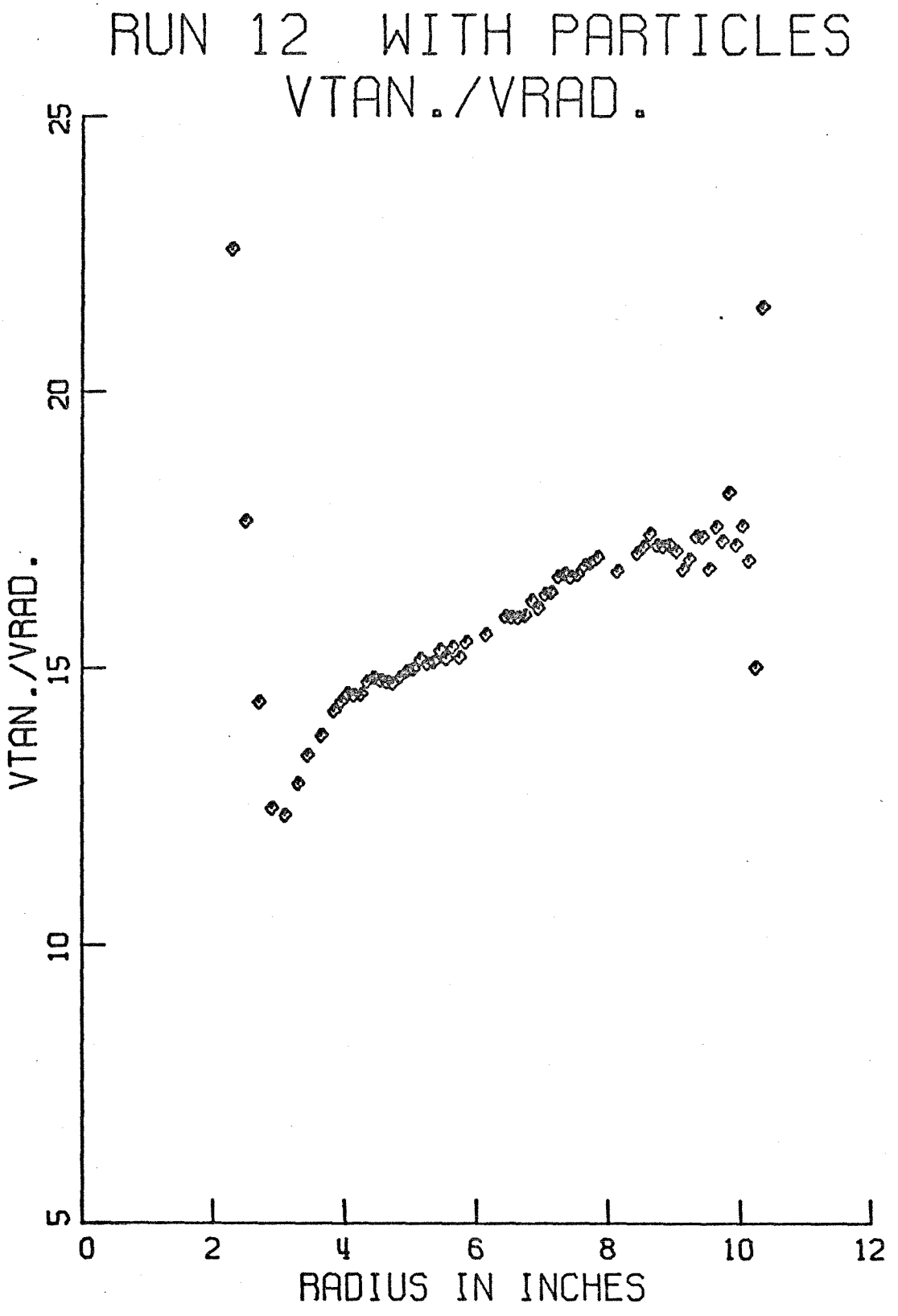
RUN 12 WITH PARTICLES
VTAN./VRAD.
VTAN./VRAD.
25
20
15
10
5
0
2
4
6
8
10
12
RADIUS IN INCHES

Figure E.27

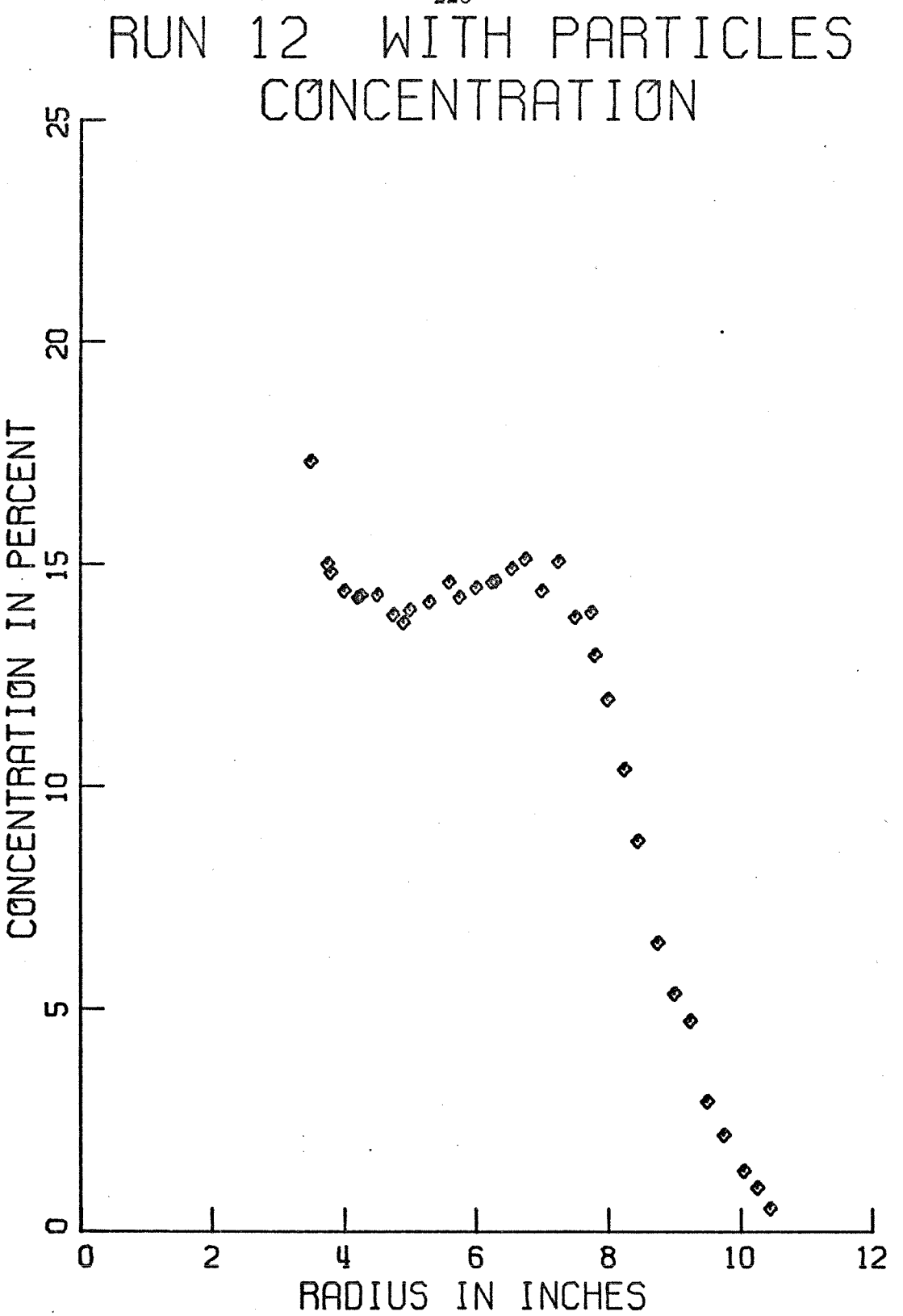
RUN 12 WITH PARTICLES
CONCENTRATION
CONCENTRATION IN PERCENT
0
5
10
15
20
25
0
2
4
6
8
10
12
RADIUS IN INCHES

Figure E.28

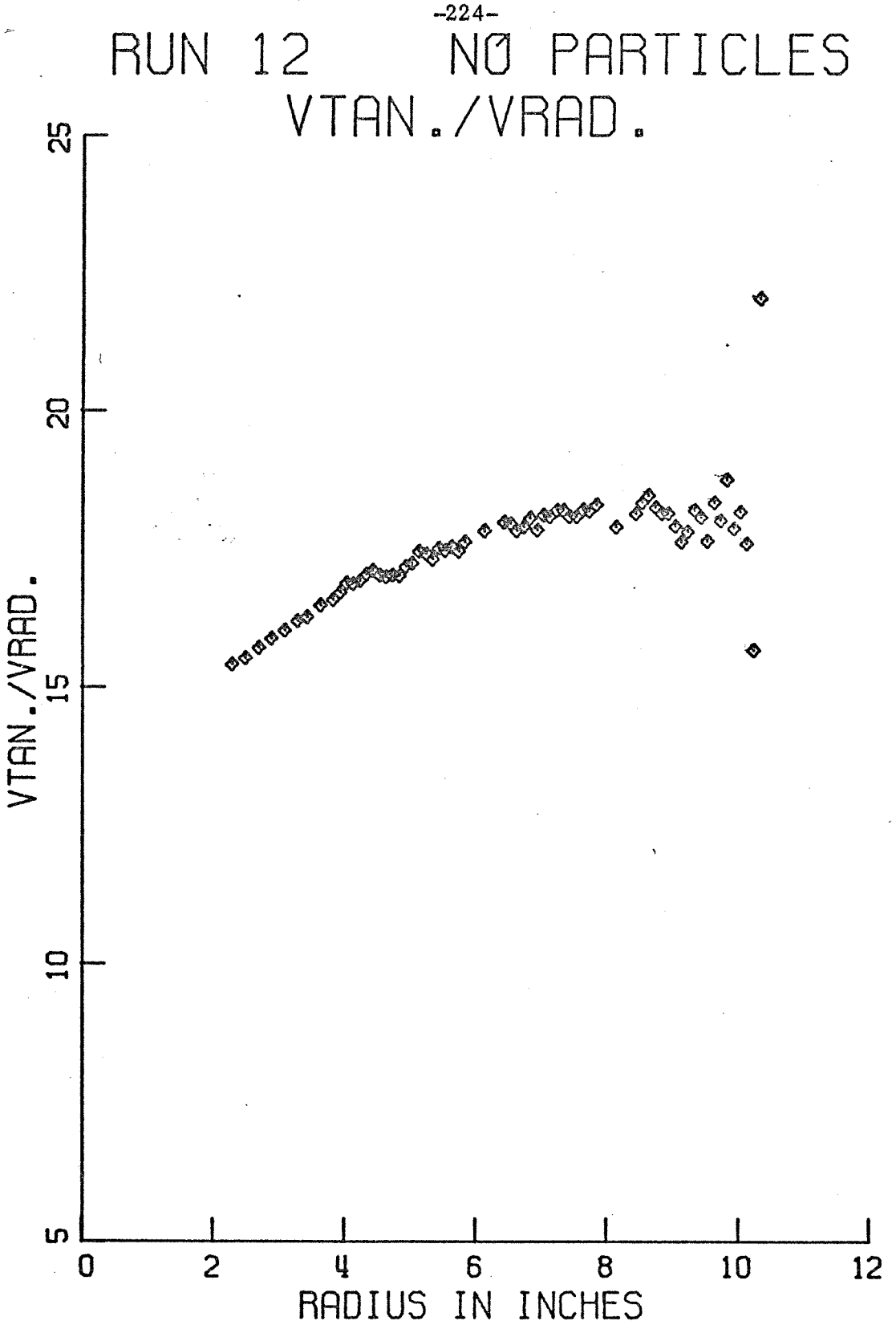
RUN 12 NØ PARTICLES
VTAN./VRAD.
VTAN./VRAD.
25
20
15
10
5
0
2
4
6
8
10
12
RADIUS IN INCHES

Figure E.29

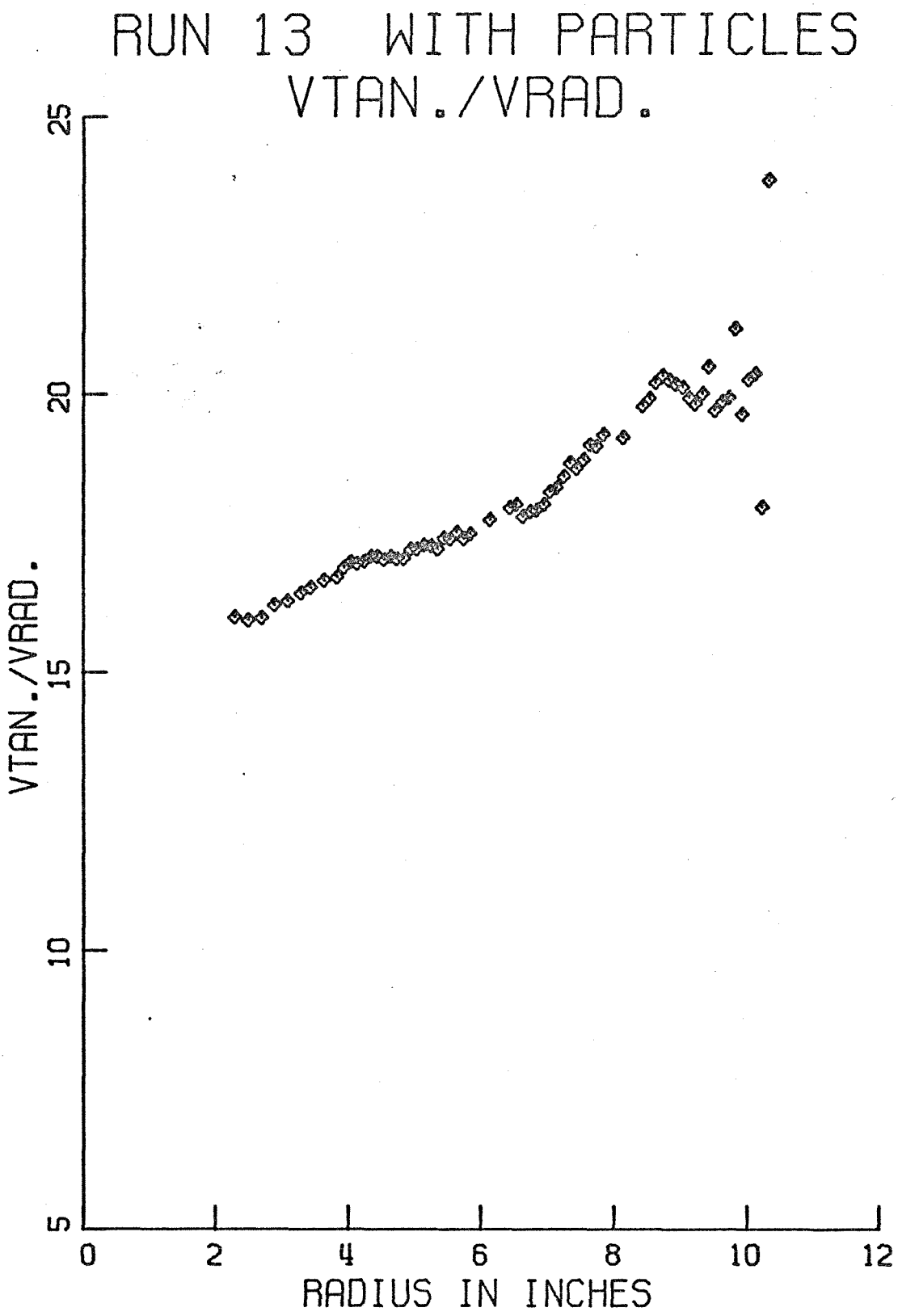
RUN 13 WITH PARTICLES
VTAN./VRAD.
VTAN./VRAD.
25
20
15
10
5
0
2
4
6
8
10
12
RADIUS IN INCHES

Figure E.30

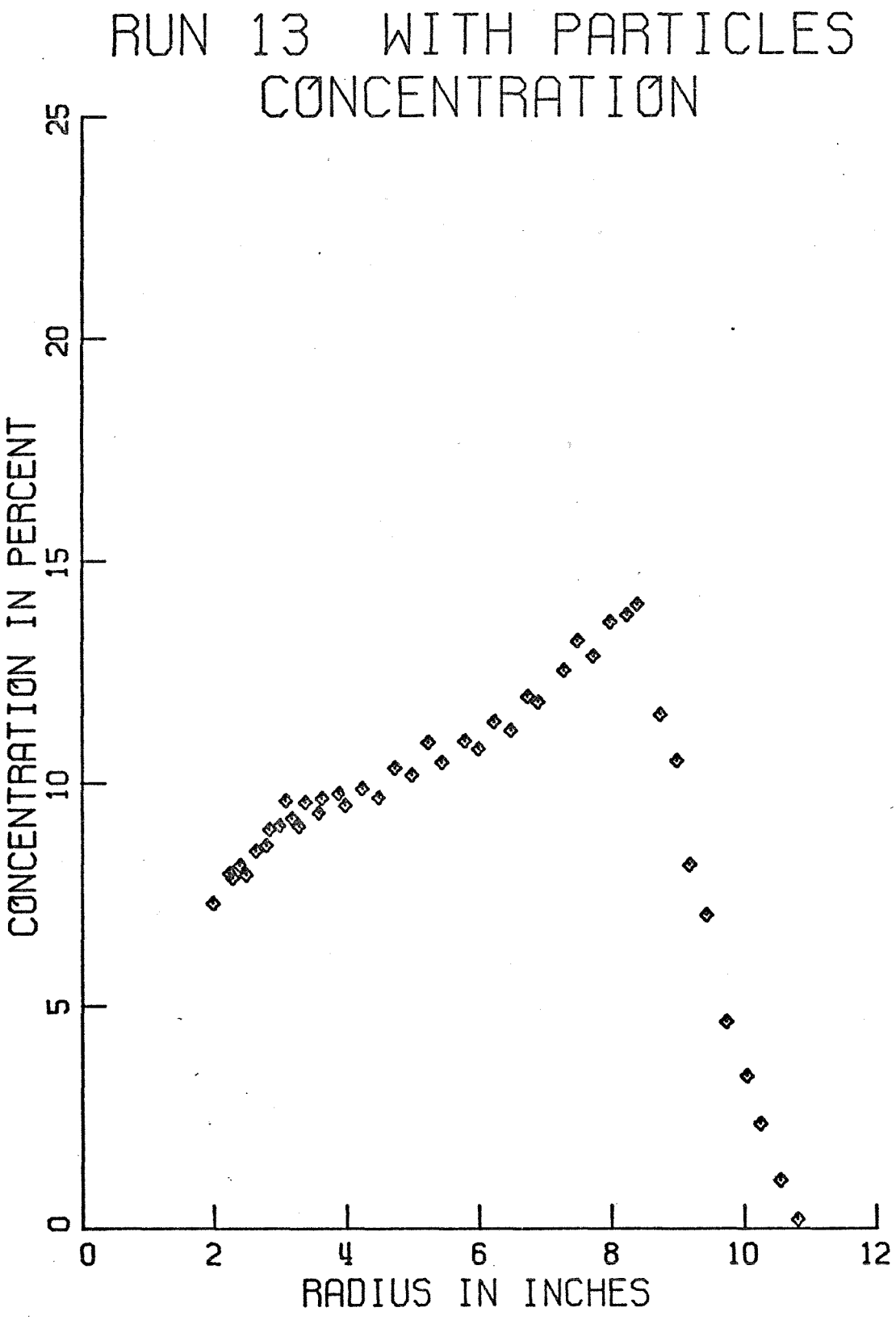
RUN 13 WITH PARTICLES
CONCENTRATION
CONCENTRATION IN PERCENT
0
5
10
15
20
25
0
2
4
6
8
10
12
RADIUS IN INCHES

Figure E.31

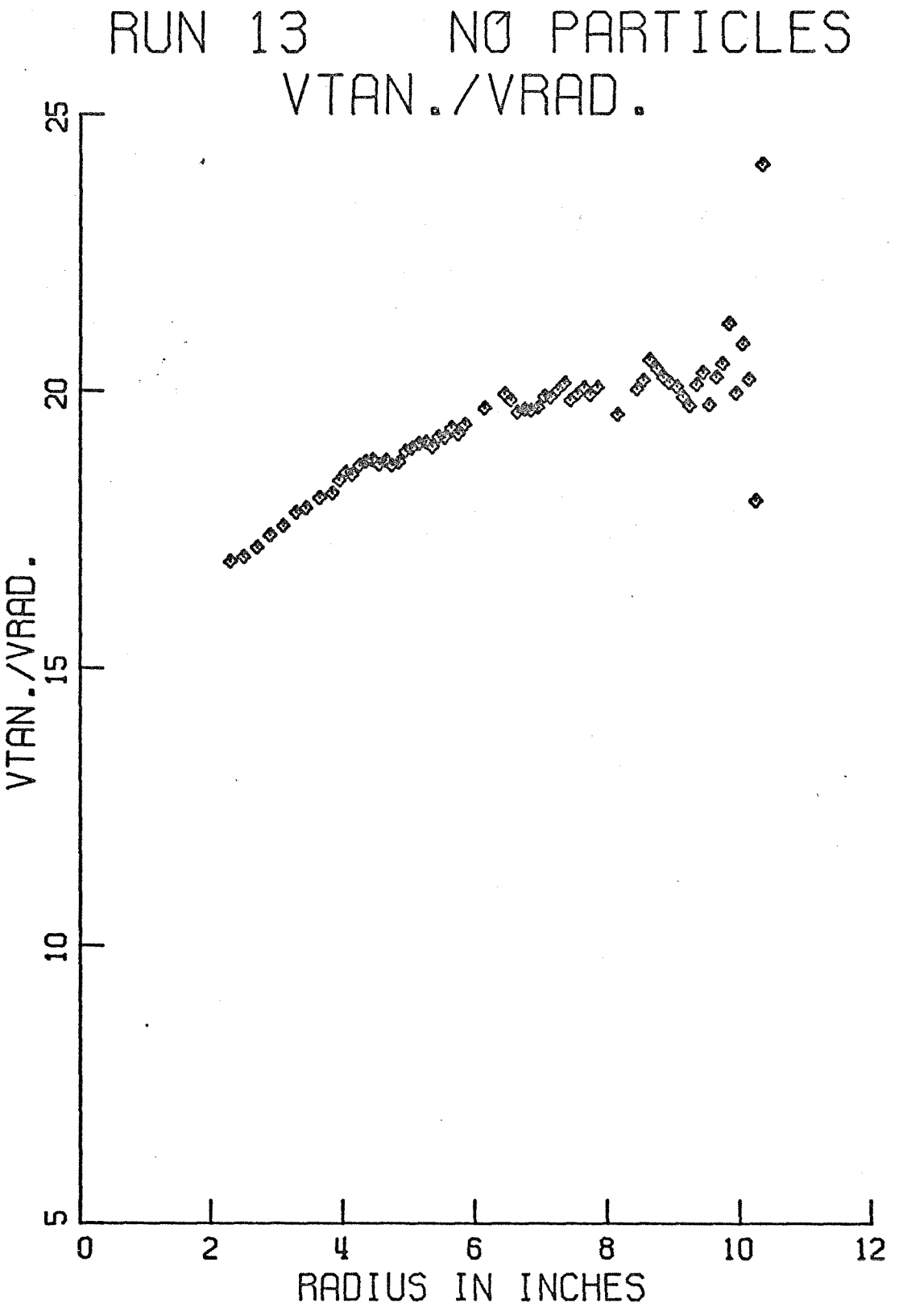
RUN 13 NØ PARTICLES
VTAN./VRAD.
VTAN./VRAD.
25
20
15
10
5
0
2
4
6
8
10
12
RADIUS IN INCHES

Figure E.32

REFERENCES

1. Anderson, L. A., Hasinger, S. and Turman, B. N., "Two Component Vortex Flow Studies, with Implications for the Colloid Core Nuclear Rocket Concept", A.I.A.A. Paper No. 71-637, June, 1971.

2. Cooke, J. C., "On Poulhausen's Method with Application to a Swirl Problem of Taylor", Journal of Aeronautical Science, vol. 19, p. 486, 1952.

3. Daily, J. W. and Chu, T. K., "Rigid Particle Suspensions in Turbulent Shear Flow: Some Concentration Effects", Massachusetts Institute of Technology Hydrodynamics Laboratory Report No. 48, October, 1961.

4. Daily, J. W. and Roberts, C. P. R., "Rigid Particle Suspensions in Turbulent Shear Flow: Size Effects with Spherical Particles", M. I. T. Hydro. Lab. Report No. 69, June, 1964.

5. Daily, J. W. and Shen, C. C., "Rigid Particle Suspensions in Turbulent Shear Flow: An Improved Flow Facility and Measurements with 0.0255 Inch Spheres", M. I. T. Hydro. Lab. Report No. 68, May, 1964.

6. Davidson, J. F. and Harrison, D., Fluidised Particles, Cambridge University Press; Cambridge, England, 1963.

7. Elata, C. and Ippen, A. T., "The Dynamics of Open Channel Flow with Suspensions of Neutrally Buoyant Particles", M. I. T. Hydrodynamics Laboratory, Dept. of Civil and Sanitary Engineering, Technical Report No. 45, January, 1961.

8. Fletcher, E. C., Gyarmathy, G. and Hasinger, S., "Separation of Submicron Condensate Particles in a Vortex Chamber", U. S. Air Force Aerospace Research Laboratories, No. ARL-0218, November, 1966.

9. Goldstein, S., "A Note on the Measurement of Total Head and Static Pressure in a Turbulent Stream", Proceedings of the Royal Society of London Series A, vol. 155, pp. 570-575, May-June, 1936.

10. Hill, M. K., "Behavior of Spherical Particles at Low Reynolds Number in a Fluctuating Translational Flow", Ph.D. Thesis, California Institute of Technology, 1973.

11. Jackomis, W. N. and Turman, D. N., "The Colloid Core Nuclear Reactor Concept", U.S. Air Force Aerospace Research Laboratories Report, No. ARL-70-0167, September, 1970.

12. Kolin, A., "Alternating Field Induction Flowmeter of High Sensitivity", Review of Scientific Instruments, vol. 16, no. 5, pp. 109-116, May, 1945.

13. Kolin, A., "Approaches to Blood-Flow Measurement by Means of Electromagnetic Catheter Flow Meters", I.E.E.E. Trans. on Magnetics, vol. Mag-6, no. 2, pp. 308-314, June, 1970.

14. Kolin, A., "Electromagnetic Velometry. I. A Method for the Determination of Fluid Velocity Distribution in Space and Time", Journal of Applied Physics, vol. 15, pp. 150-164, February, 1944.

15. Kolin, A., "Electromagnetic Velometry. II. Elimination of the Effects of Induced Currents in Explorations of the Velocity Distribution in Axially Symmetrical Flow", Journal of Applied Physics, vol. 25, no. 4, pp. 409-423, April, 1954.

16. Kolin, A., "A New Principle for Electromagnetic Catheter Flow Meters", Proceedings of the National Academy of Science, vol. 63, pp. 357-363, 1969.

17. Kolin, A., "A Radial Field Electromagnetic Intravascular Flow Sensor", I.E.E.E. Transactions on Bio-Med. Engr., vol. BME-16, no. 3, pp. 220-221, July, 1969.

18. Kolin, A. and Wisshaupt, R., "Single-Coil Coreless Electromagnetic Blood-Flow Meters", I.E.E.E. Transactions on Bio-Med. Electronics, vol. 10, pp. 60-67, April, 1963.

19. Leva, Max, Fluidization, McGraw-Hill Book Co., New York, 1959.

20. Lewellen, W. S., "A Review of Confined Vortex Flows", NASA Report, CR 1772, July, 1971.

21. Lewellen, W. S. and Rott, N., "Boundary Layers and their Interaction in Rotating Flows", Progress in Aeronautical Science, vol. 7, p. 111, 1966.

22. Mack, L. M., "The Laminar Boundary Layer on a Disc of Finite Radius in a Rotating Flow. Part I: Numerical Integration of the Momentum--Integral Equations and Application of the Results to the Flow in a Vortex Chamber", Jet Propulsion Laboratory, Calif. Institute of Technology, Technical Report No. 32-224, May 20, 1962.

23. Mack, L. M., "The Laminar Boundary Layer on a Disc of Finite Radius in a Rotating Flow. Part II: A Simplified Momentum Integral Method.", Jet Propulsion Laboratory, Calif. Institute of Technology, Technical Report No. 32-366, January 31, 1963.

24. McMichael, F. C., "Suspensions of Granular Particles Generated by Upward Flow", Ph.D. Thesis, California Institute of Technology, 1963.

25. Mills, C. J., "A Catheter Tip Electromagnetic Velocity Probe", Phys. Med. Biol., vol. 11, p. 323, 1966.

26. Pinchak, A. C., "A Review of State of the Art of Cyclone-Type Separators", U.S. Air Force Aerospace Research Laboratories, No. 67-0047, March, 1967.

27. Poblawski, R. and Toms, H. L., Jr., "Experimental Investigation on the Maximum Mach Number in a Confined Compressible Vortex", U.S. Air Force Aerospace Research Laboratories, No. ARL-0018, January, 1971.

28. Richardson, J. F. and Zaki, W. N., "Sedimentation and Fluidisation: Part I", Trans. Instn. Chem. Engrs. 32, p. 35-53, 1954.

29. Rosenhead, L., Laminar Boundary Layers, Clarendon Press, Oxford, England, 1963.

30. Taylor, G. I., "The Boundary Layer in the Converging Nozzle of a Swirl Atomizer", Quarterly Journal of Mechanics and Applied Mathematics, vol. 3, pp. 129-239, 1950.

31. Torobin, L. B. and Gauvin, W. H., "The Drag Coefficients of Single Spheres Moving in Steady and Accelerated Motion in a Turbulent Fluid", A.I.Ch.E. Journal, vol. 7, pp. 615-619, 1961.

32. Willus, C. A., "An Experimental Investigation of Particle Motion in Liquid Fluidized Beds", Ph.D. Thesis, California Institute of Technology, 1970.

33. Zabrodsky, S. S., Hydrodynamics and Heat Transfer in Fluidized Beds, The M. I. T. Press, Cambridge, 1966.

34. Zenz, F. A. and Othmer, D. F., Fluidization and Fluid-Particle Systems, Reinhold Publishing Co., New York, 1960.

PART II

UNSTEADY DISTURBANCES IN AXIAL COMPRESSORS

CHAPTER I

INTRODUCTION

A. Background

If the angle of attack of an airfoil is increased from zero, the lift of the airfoil will increase. However, at high angles of attack, a point is reached where the lift drops rapidly for small increases of angle of attack. At this point the airfoil is said to be stalled. Recovery from the stall and the restoration of lift can only be accomplished by reducing the angle of attack.

However, in contrast with an airplane wing which has its best ratio of lift/drag at a moderate angle of attack, well removed from the stall, the compressor produces the best lift/drag at heavy loading, very close to the stall. Small disturbances from the design condition for normal operation can produce stalling.

The angle of attack for the blades in a compressor is a function of blade geometry and of the ratio of the axial velocity to the rotor speed. For the high solidity blades commonly used in modern compressors, the direction of flow leaving any blade row is essentially constant, independent of the inlet conditions. Consequently, if the rotor speed is maintained constant, the angle of attack on both rotor and stator increases as the axial velocity of the gas through the compressor decreases. Similarly, holding the gas velocity constant, the angle of attack increases with rotor speed. In general, these two variables are related and in steady state, changing one variable specifies a new operating point for the machine. If the compressor is operating at design point near stall, it is conceivable that small

variations of gas velocity could cause stalling.

There are several possible sources of variation of these parameters that could cause stall. The first source is improper operation of the compressor off design. Off design analysis of compressors is discussed in the literature. The reader is referred to several of the recent books on turbomachines (Wislicenus (1965), Dixon (1966), Dzung (1970)).

A second possible source is gas velocity variations due to inlet flow distortion. This may be caused by separation of the inlet diffuser when at an angle of attack. Several investigators have studied this problem for steady incompressible flow both for high hub-to-tip ratio where the radial variations are neglected, and for low hub-to-tip ratios including radial effects. Two methods of analysis have been used; the more common treats each blade row as an actuating disc with infinitesimal thickness in the axial direction (Horlock, 1966); the other distributes the blade forces continuously along the length of the compressor. The latter is simpler for a multistage compressor (Plourde and Stenning (1968), Callahan and Stenning (1971)).

A third type of disturbance, unsteady flow variation, has not been investigated thoroughly. This study is limited to the simplest form of unsteady disturbances, planar oscillations with no variation circumferentially or radially. Such disturbances may occur when an airplane passes through a rapidly varying temperature or pressure field such as the exhaust from a rocket or when unsteady burning in the combustion chamber produces downstream pressure disturbances.

B. Method of Solution

In contrast to the work described above, this study includes time varying flow. In addition, the disturbances may be incident from either the front of the rear of the compressor.

The method is similar to the second method for calculating inlet flow distortion described above in that the forces exerted by the blades are distributed uniformly over the length of the compressor. The difference is that the earlier studies involved steady incompressible asymmetric flow while this analysis treats unsteady compressible axisymmetric flow with no radial variation. However, the method presented here can be extended to treat both radial and circumferential variations with some added complexity.

The method of solution consists of writing the equations of motion for flow through the compressor including the time varying terms. The body forces representing the blades are determined from the overall total temperature rise of the compressor, and the efficiency, assumed constant for each stage. The pressure, density, and velocity in the compressor are taken to have small fluctuating perturbations superimposed upon the mean values. The equations are then linearized in the usual manner. The flow outside the compressor is taken to be uniform with small disturbances superimposed. The solution obtained inside the compressor is matched to the solutions obtained outside the compressor at each end. The solution inside the compressor is obtained by a numerical finite difference technique.

The performance specifications of a typical large multistage axial flow compressor were used as an example. It will be seen that the added factors of variation with time and compressible flow greatly complicate the analysis over the relatively simple closed form analysis of Plourde and Stenning. However, if the axial velocity and the average axial Mach number are assumed constant over the length of the compressor, a closed form solution can be obtained. This simplification is examined briefly in the Appendix.

There are several factors not considered in this analysis which may have measurable effect. First, it has been assumed that the only way that the compressor interacts with the flow is through the cumulative blade forces. In a real compressor, the forces alternate in direction from stator to rotor. Strictly, these forces should be taken into account.

Second, the flow through the compressor has been assumed unrestricted. In reality there is a reduction in cross-sectional area open to the flow due to the presence of the blades. The effects of this reduction of area on the propagation of the perturbations are discussed in Chapter II.

Third, the variation of flow direction in the compressor has been assumed small. In reality, the flow is turned from axial to some flow angle at the front of the compressor and moves through the compressor in a helix. The flow angle varies little through each blade row. It is again straightened out at the rear of the compressor by straightening vanes. The effects of this turning of the flow will be discussed in Chapter III.

It must be remembered that although the goal of this study is to predict the velocity fluctuations which cause stall, the analysis performed is linearized. The equations presented here would not properly represent the blade forces at the magnitude of velocity fluctuations necessary for stall. Stall is essentially a non-linear effect. Nevertheless, the analysis does give some insight into the phenomena involved and at least estimates of the actual relationships.

The perturbations examined here are taken to be plane waves propagating in the axial direction only. The interactions of acoustical waves traveling at an angle to the axis with flow straightening vanes of zero thickness and turning angle has been examined by Kaji and Okazaki in 1970. Their analysis incorporates a modified actuator disc theory. Such oblique waves could be incorporated in the analysis presented here if the tangential variations were considered.

CHAPTER II

AXIAL FLOW VARIATIONS IN A COMPRESSOR

A. Steady State Equations

This analysis will be carried out representing the blade rows as distributed body forces. The effect of the variation in cross-sectional area in the blade rows will be neglected here and treated separately in Chapter III.

The undisturbed flow is assumed to be one-dimensional. This means that radial variations are neglected and the compressor may be considered unwrapped in the circumferential direction. The configuration is equivalent to one-dimensional flow through a passage of varying height h, a function of X. The Mach number of the axial component of velocity is assumed subsonic everywhere.

The equations of motion may be written down directly.

Continuity
$$\frac{\partial}{\partial t}(\rho h) + \frac{\partial}{\partial x}(\rho U h) = 0 \tag{2.1}$$

Momentum
$$\rho\left(\frac{\partial U}{\partial t} + U\frac{\partial U}{\partial x}\right) + \frac{\partial p}{\partial x} = \frac{\rho \bar{U}^2}{a} X \tag{2.2}$$

Energy
$$\rho c_p\left(\frac{\partial T}{\partial t} + U\frac{\partial T}{\partial x}\right) - \left(\frac{\partial p}{\partial t} + U\frac{\partial p}{\partial x}\right) = \rho U \frac{\bar{U}^2}{a} F \tag{2.3}$$

where $\rho, U, p, T,$ AND c_p are the density, velocity, pressure, temperature, and specific heat at constant pressure. X is the equivalent body force which represents the blades. F is the non-isentropic component of force due to losses, $\bar{U}$ is a velocity independent of time to be defined later, and a is the compressor length. The factor $\frac{\rho \bar{U}^2}{a}$ is the appropriate normalizing factor for the body forces so

X and F are non-dimensional.

These body forces will now be evaluated in terms of the compressor parameters for steady state operation. The stagnation temperature rise for two-dimensional flow through a single axial stage is given by:

$$c_p \Delta T = V_R^2 \left[1 - \frac{U}{V_R} (\tan \beta_2 + \tan \gamma_2) \right] \tag{2.4}$$

where V_R is the rotor blade speed, and β_2 and γ_2 are the leaving angles relative to the rotor and stator respectively. It is assumed that the flow angle entering the stage is the same as that leaving the stage, and that there is no change in axial velocity through the stage. (See Figure II.1 below.)

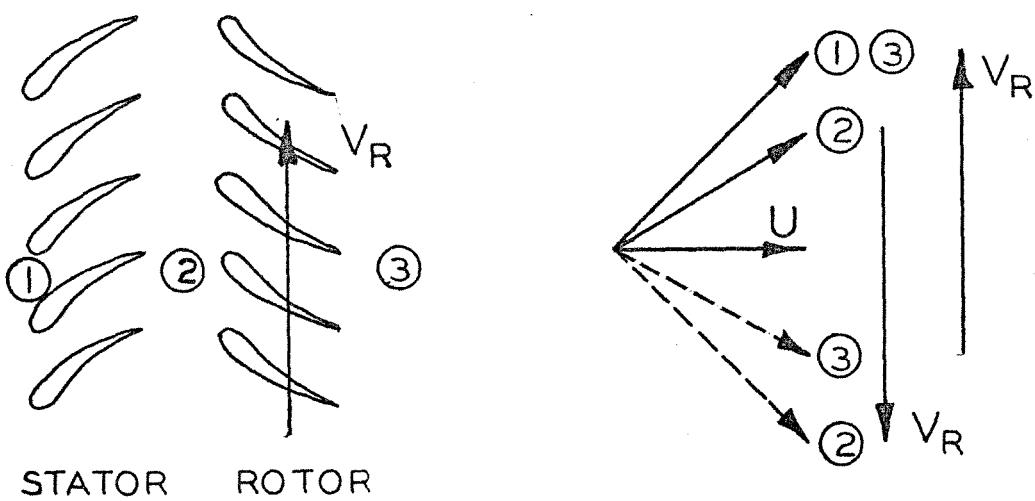

Figure II.1. Axial Stage Geometry

If β_ℓ and γ_ℓ are independent of incoming angles to the blade rows, then:

$$C_p \Delta T = V_n^2 \left(1 - \alpha \frac{U}{V_n}\right) \tag{2.5}$$

where,

$$\alpha = \tan \beta_\ell + \tan \gamma_\ell = \text{constant}. \tag{2.6}$$

Now assume that the compressor is made up of many stages so that the increase in stagnation temperature for each stage may be uniformly distributed over the length of the stage. The equivalent temperature distribution for N stages (with the same α and V_n) is:

$$C_p \frac{dT}{dx} = \frac{N}{a} V_n^2 \left(1 - \alpha \frac{U}{V_n}\right) \tag{2.7}$$

If further, ζ is the infinitesimal stage efficiency,

$$\frac{1}{p}\frac{dp}{dx} = \frac{\gamma}{\gamma - 1}\zeta \frac{1}{T}\frac{dT}{dx} \tag{2.8}$$

where the working fluid has been taken as an ideal gas. That is:

$$p = \rho R T \tag{2.9}$$

The temperatures and pressures in Equations 2.7 and 2.8 are strictly stagnation conditions. However, if the velocity changes through a complete stage are small, the equations are almost identical whether static or stagnation conditions are implied.

Equations 2.7, 2.8, and 2.9 may be combined to yield:

$$\frac{dp}{dx} = \rho \zeta \frac{N}{a} V_n^2 \left(1 - \alpha \frac{U}{V_n}\right) \tag{2.10}$$

For steady state, and assuming $\frac{dv}{dx} = 0$, Equations 2.2 and 2.10 may be combined to find the axial force X.

$$X = N\left(\frac{V_n}{v}\right)^2 \gamma\left(1 - \alpha\frac{v}{V_n}\right) \tag{2.11}$$

X may also be evaluated by combining Equations 2.2, 2.8, and 2.9 to yield:

$$X = \gamma\,\frac{c_p a}{v^2}\,\frac{dT}{dx} \tag{2.12}$$

Similarly, for steady state, Equations 2.3, 2.7, and 2.10 can be combined to find F.

$$F = \frac{1-\gamma}{\gamma} X \tag{2.13}$$

Equation 2.3 may be combined with Equation 2.9 to eliminate T.

$$\frac{\rho}{\gamma-1}\left(\frac{d}{dt} + v\frac{d}{dx}\right)\left(\ln\rho - \gamma\ln\rho\right) = \rho v\frac{\bar{v}^2}{a} F \tag{2.14}$$

B. Perturbed Equations

Now examine Equations 2.1, 2.2, and 2.14 where the pressure density and velocity are allowed to be time varying such that:

$$\begin{aligned} \rho &= \bar{\rho}\left(1 + \frac{\rho'}{\bar{\rho}}\right) \\ \rho &= \bar{\rho}\left(1 + \frac{\rho'}{\bar{\rho}}\right) \\ v &= \bar{v}\left(1 + \frac{v'}{\bar{v}}\right) \end{aligned} \tag{2.15}$$

The barred quantities in this equation refer to the unperturbed steady state conditions, and the primed quantities are small perturbations. Note that $\bar{v}$ in Equation 2.15 defines v in Equations 2.2 and 2.3.

For simplicity assume that $\bar{U}$ is constant through the compressor and define the dimensionless variables ξ and τ such that:

$$\xi = \frac{x}{a}$$
$$\tau = \frac{\bar{U}}{a} t \tag{2.16}$$

Substituting Equations 2.15 and 2.16 into Equations 2.1, 2.2, and 2.14,

$$\frac{\partial}{\partial \tau}\left(\frac{\rho'}{\bar{\rho}}\right) + \frac{\partial}{\partial \xi}\left(\frac{\rho'}{\bar{\rho}} + \frac{U'}{\bar{U}}\right) = 0 \tag{2.17}$$

$$\frac{\partial}{\partial \tau}\left(\frac{U'}{\bar{U}}\right) + \frac{\partial}{\partial \xi}\left(\frac{U'}{\bar{U}}\right) + \bar{X}\left(\frac{p'}{\bar{p}} - \frac{\rho'}{\bar{\rho}}\right) - X'\left(\frac{U'}{\bar{U}}\right) + \frac{R\bar{T}}{\bar{U}^2}\frac{\partial}{\partial \xi}\left(\frac{p'}{\bar{p}}\right) = 0 \tag{2.18}$$

$$\frac{R\bar{T}}{\bar{U}^2}\left(\frac{\partial}{\partial \tau} + \frac{\partial}{\partial \xi}\right)\left(\frac{p'}{\bar{p}} - \gamma\frac{\rho'}{\bar{\rho}}\right) - (\gamma - 1)\frac{1-\eta}{\eta}\left[\bar{X}\left(\frac{\rho'}{\bar{\rho}} - \frac{p'}{\bar{p}}\right) + X'\frac{U'}{\bar{U}}\right] = 0 \tag{2.19}$$

where only the first order terms have been kept. The zero order terms all drop out because they are identically satisfied in steady state. $\bar{X}$ is the same as X in Equations 2.11 and 2.12, and is the steady state value of the force X. X' is the derivative of X with respect to velocity fluctuations in the stage so that at any time,

$$X = \bar{X} + X'\left(\frac{U'}{\bar{U}}\right) \tag{2.20}$$

It is assumed that the rotor speed is not changed in the presence of the perturbations. This is a good assumption if its moment of inertia is large and the disturbances have sufficiently high frequency.

It is also assumed that the efficiency, η, remains the same in the presence of the perturbations. This is true to first order only

if the unperturbed flow is at peak efficiency.

The factor $(\gamma-1)\frac{1-\zeta}{\zeta}$ approaches zero as ζ approaches 1.0. Hence define the small parameter ϵ such that:

$$\epsilon = (\gamma-1)\frac{1-\zeta}{\zeta} \tag{2.21}$$

Also, the temperature in Equations 2.18 and 2.19 always occurs in the form $\frac{R\bar{T}}{\bar{U}^2}$. So define the Mach number based on average axial velocity as $\bar{M}$,

$$\frac{R\bar{T}}{\bar{U}^2} = \frac{1}{\gamma \bar{M}^2} \tag{2.22}$$

Since Equations 2.17, 2.18, and 2.19 are linear and first order with respect to τ, they have solutions of the form

$$\begin{aligned} \frac{\rho}{\bar{\rho}} &= \rho(\xi) e^{-\lambda\omega\tau} \\ \frac{s}{\bar{s}} &= s(\xi) e^{-\lambda\omega\tau} \\ \frac{u}{\bar{U}} &= U(\xi) e^{-\lambda\omega\tau} \end{aligned} \tag{2.23}$$

Thus the equations become:

$$\frac{d\,s(\xi)}{d\,\xi} + \frac{d\,U(\xi)}{d\,\xi} = \lambda\omega\, s(\xi) \tag{2.24}$$

$$\gamma\bar{M}^2 \frac{d\,U(\xi)}{d\,\xi} + \frac{d\,P(\xi)}{d\,\xi} = \tag{2.25}$$

$$\gamma M^2\left\{\lambda\omega U(\xi) - \bar{X}\left[P(\xi) - s(\xi)\right] + X' U(\xi)\right\}$$

$$\frac{d\,P(\xi)}{d\,\xi} - \gamma\frac{d\,s(\xi)}{d\,\xi} = \tag{2.26}$$

$$\lambda\omega P(\xi) - \lambda\omega\gamma s(\xi) - \epsilon\gamma\bar{M}^2\left\{\bar{X}\left[P(\xi) - s(\xi)\right] - X' U(\xi)\right\}$$

These equations are linear in ζ, but have non-constant coefficients due to $\bar{M}^2$. If $\bar{M}^2$ were taken as constant and equal to, say, the mean value in the compressor, then solutions of the form

$$v(\zeta) = K_v \, e^{i\lambda\zeta} \tag{2.27}$$

would satisfy the equations. This assumption leads to a simple closed form solution. However, a compressor with both $\bar{v}$ and $\bar{M}$ constant can have no temperature rise and hence the working fluid must be incompressible. This solution is discussed in the Appendix. For the present, $\bar{M}$ will be taken as a variable.

Equations 2.24, 2.25, and 2.26 may be rearranged so the derivatives are expressed as functions of the variables themselves.

$$\frac{dv(\zeta)}{d\zeta} = \frac{1}{(1-\bar{M}^2)} \left\{ \frac{i\omega p(\zeta)}{\gamma} \right. \tag{2.28}$$

$$\left. - \bar{M}^2 \left[i\omega v(\zeta) + (1-\epsilon)\left[X' v(\zeta) + \bar{X}\left[p(\zeta) - s(\zeta) \right] \right] \right] \right\}$$

$$\frac{ds(\zeta)}{d\zeta} = i\omega s(\zeta) - \frac{dv(\zeta)}{d\zeta} \tag{2.29}$$

$$\frac{dp(\zeta)}{d\zeta} = \gamma \bar{M}^2 \left\{ i\omega v(\zeta) \right. \tag{2.30}$$

$$\left. - \frac{dv(\zeta)}{d\zeta} + X' v(\zeta) - \bar{X}\left[p(\zeta) - s(\zeta) \right] \right\}$$

C. Numerical Solution

These equations lend themselves to a "marching" type numerical integration where if the values of the parameters are given at one point, the derivatives can be calculated assuming

$$v(\zeta + \Delta\zeta) = v(\zeta) + \frac{dv(\zeta)}{d\zeta} \Delta\zeta \tag{2.31}$$

and so on. Thus, the solution may be "marched" from one end of the compressor to the other if the conditions at one end are known.

Outside the compressor, both up and downstream, the flow is one-dimensional in a tube of constant cross-sectional area. The solution for this problem may be obtained in the same manner where the body forces vanish in Equations 2.1, 2.2, and 2.14 and the Mach number is constant. For small perturbations, a closed form solution can be expressed as

$$\frac{\rho'}{\bar{\rho}} = \left[A\, e^{i\frac{\bar{M}}{1+\bar{M}}\omega\xi} + B\, e^{-i\frac{\bar{M}}{1-\bar{M}}\omega\xi}\right] e^{-i\omega\tau} \tag{2.32}$$

$$\frac{s'}{\bar{s}} = \frac{1}{\gamma}\left[A\, e^{i\frac{\bar{M}}{1+\bar{M}}\omega\xi} + B\, e^{-i\frac{\bar{M}}{1-\bar{M}}\omega\xi}\right] e^{-i\omega\tau} + C\, e^{i\omega(\xi-\tau)} \tag{2.33}$$

$$\frac{u'}{\bar{u}} = \frac{1}{\gamma\bar{M}}\left[A\, e^{i\frac{\bar{M}}{1+\bar{M}}\omega\xi} - B\, e^{-i\frac{\bar{M}}{1-\bar{M}}\omega\xi}\right] e^{-i\omega\tau} \tag{2.34}$$

The terms involving A correspond to a pressure wave propagated downstream relative to the mean flow, at the local velocity of sound. The terms involving B correspond to a pressure wave propagated upstream, relative to the mean flow, at the local velocity of sound. The term involving C corresponds to an entropy wave moving with the same velocity as the mean flow.

Since the compressor extends from $\xi = 0$ to $\xi = 1$, the solutions outside the compressor must match the solution inside the compressor at $\xi = 0$ and $\xi = 1$. Denoting the conditions upstream by the subscript 1 and those downstream by the subscript 2:

$$
\begin{aligned}
p(0) &= A_1 + B_1 \\
s(0) &= \frac{1}{\gamma}(A_1 + B_1) + C_1 \\
v(0) &= \frac{1}{\gamma \bar{M}_1}(A_1 - B_1)
\end{aligned}
\tag{2.35}
$$

$$
\begin{aligned}
p(1) &= A_2 e^{i\frac{\bar{M}_2}{1+\bar{M}_2}\omega} + B_2 e^{-i\frac{\bar{M}_2}{1-\bar{M}_2}\omega} \\
s(1) &= \frac{1}{\gamma}\left[A_2 e^{i\frac{\bar{M}_2}{1+\bar{M}_2}\omega} + B_2 e^{-i\frac{\bar{M}_2}{1-\bar{M}_2}\omega}\right] + C_2 e^{i\omega} \\
v(1) &= \frac{1}{\gamma \bar{M}_2}\left[A_2 e^{i\frac{\bar{M}_2}{1+\bar{M}_2}\omega} - B_2 e^{-i\frac{\bar{M}_2}{1-\bar{M}_2}\omega}\right]
\end{aligned}
\tag{2.36}
$$

Since Equations 2.28, 2.29, and 2.30 constitute a set of three independent equations, three of the constants A_1, B_1, C_1, A_2, B_2, C_2 must be evaluated from boundary conditions, and the other three may be determined from the numerical integration of Equations 2.28, 2.29, and 2.30. Also, since the equations are linear, the solutions may be added or subtracted to give additional solutions.

In order to integrate the equations, it is necessary to specify all of the constants at one end of the compressor. The three independent sets of boundary conditions used for the integration are:

$$
\begin{array}{lllll}
1. & A_2 = 1.0 & B_2 = 0.0 & C_2 = 0.0 \\
2. & A_2 = 0.0 & B_2 = 1.0 & C_2 = 0.0 \\
3. & A_2 = 0.0 & B_2 = 0.0 & C_2 = 1.0
\end{array}
\tag{2.37}
$$

While these boundary conditions make the integration easy to perform, the solutions generated are not particularly significant. For instance, the first set is the solution that results in only a transmitted pressure wave downstream of the compressor. In order to

obtain this, the solution includes a complex combination of incident and reflected waves at the front of the compressor.

Physically more meaningful are the cases where the waves incident on the compressor are the unknowns and the reflected and transmitted waves are determined in terms of these unknowns. Such solutions can be found from a linear combination of the above three cases. The three independent solutions are then:

$$\begin{array}{lllll} 1. & A_1 = 1.0 & C_1 = 0.0 & B_2 = 0.0 & \\ 2. & A_1 = 0.0 & C_1 = 1.0 & B_2 = 0.0 & (2.38) \\ 3. & A_1 = 0.0 & C_1 = 0.0 & B_2 = 1.0 & \end{array}$$

Because the integration is numerical, a separate calculation must be done for each set of compressor parameters, and for each value of ω . As an example, the calculations were performed for a single set of parameters typical of a large subsonic compressor over a range of frequencies, ω . Table II.1 lists the essential parameters for this compressor. The temperature rise is taken as linear with ζ , and as stated before, the efficiency, η , and axial velocity, $\bar{U}$, are assumed constant throughout the compressor.

A computer was utilized to perform the arithmetic. One thousand steps were used to "march" across the compressor. Solutions were obtained for the range $\omega = 0.0$ to $\omega = 64$.

The frequency of the perturbations is directly proportional to ω . However, the associated wave lengths for the corresponding waves in a straight tube are functions of both ω and $\bar{M}$.

Table II.1. Compressor Characteristics

Parameter	Symbol	Value	Units
Working fluid		Air	
Inlet temperature	$\overline{T}_1$	500	°R
Outlet temperature	$\overline{T}_2$	900	°R
Stage efficiency	η	0.84	
Number of stages	N	8	
Tip speed	V_n	1000.	ft./sec.
Axial velocity	$\overline{U}$	600	ft./sec.
Overall efficiency		0.80	
Inlet Mach number	$\overline{M}_1$	0.55	
Outlet Mach number	$\overline{M}_2$	0.41	
Average Mach number	$\overline{M}$	0.46	
	α	1.667	
	$\overline{X}$	5.607	
	X'	-13.07	
	ϵ	.0762	

$$\frac{\lambda}{a} = \frac{2\pi}{\omega} \quad \text{For the entropy wave}$$

$$\frac{\lambda}{a} = \frac{2\pi}{\omega}\,\frac{1+\bar{M}}{\bar{M}} \quad \text{For the pressure wave propagated downstream} \qquad (2.39)$$

$$\frac{\lambda}{a} = \frac{2\pi}{\omega}\,\frac{1-\bar{M}}{\bar{M}} \quad \text{For the pressure wave propagated upstream}$$

For high values of ω, the wave lengths became so small that errors due to the finite length of integration steps may arise. As a check of the magnitude of these errors, calculations were performed for $\omega = 16$, 32, and 64 with 5000 and 9000 steps each. There were only slight changes in the results. This is expected because even with only 1000 steps at $\omega = 64.0$, one wave length of the entropy wave corresponds to about 98 steps.

D. Disturbances Outside the Compressor

Figures II.2, II.3, and II.4 show the response outside the compressor for cases 1, 2, and 3. The magnitudes of B_1, A_2, and C_2 have been plotted as a function of ω. In Figure II.2, $A_1 = 1.0$ is the incident pressure wave. The reflected pressure wave, B_1, is seen to be a maximum at low frequency and drops off rapidly as the frequency increases. The magnitude of the reflected wave can be even larger than the incident wave. Thus, the condition at the compressor inlet is strongly influenced by the reflected wave, and the net value of the perturbation may bear no resemblance to the incident wave. The transmitted wave, A_2, exhibits the same decay with increasing frequency. However, the transmitted wave is attenuated by 50 percent or more in all cases. The fact that C_2 is not zero is a result of the efficiency not being equal to 1.0. This results in some transfer of mechanical energy

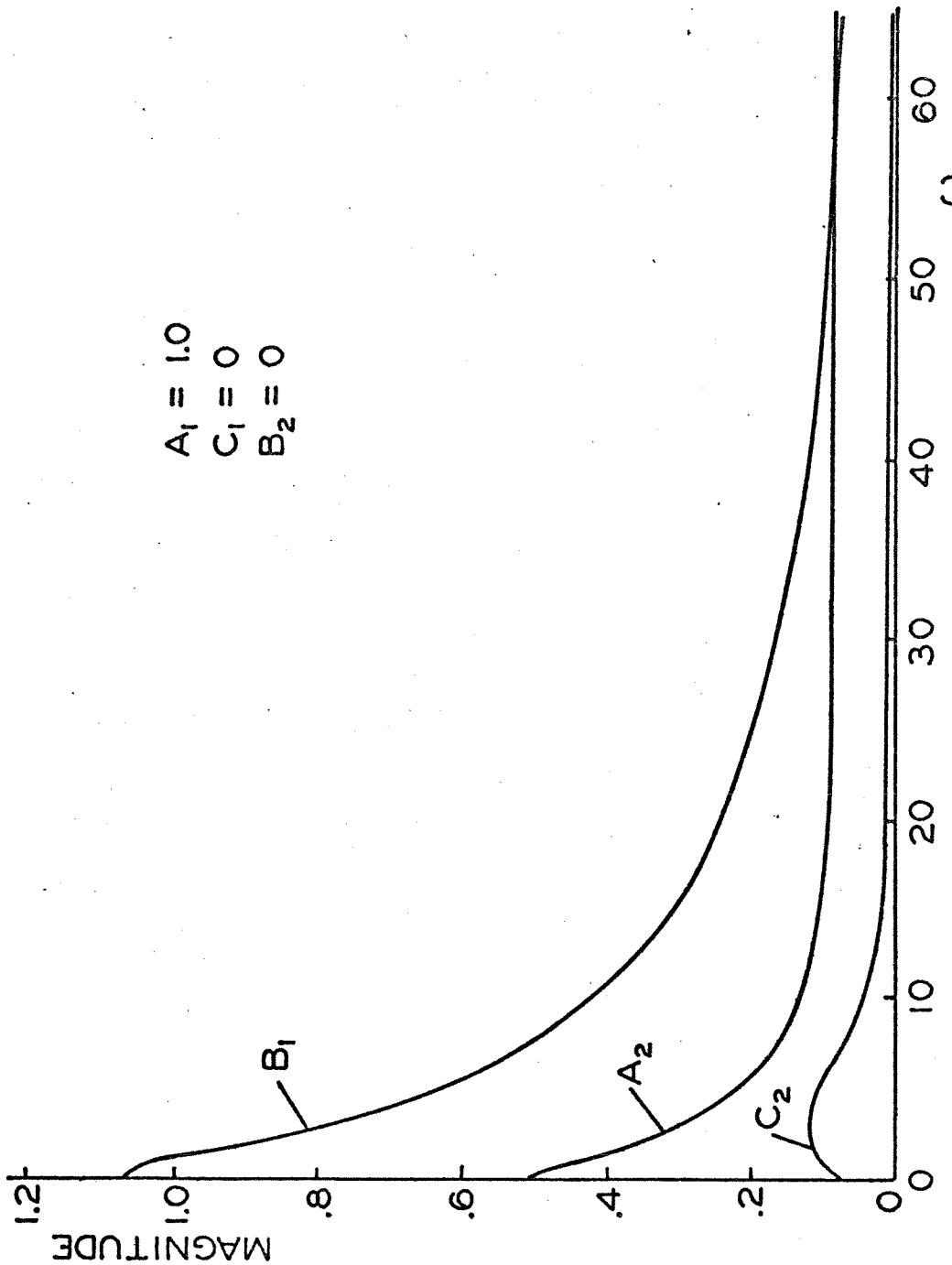

Figure II.2. Disturbances Outside the Compressor for $A_1 = 1.0$, $C_1 = 0.0$, $B_2 = 0.0$.

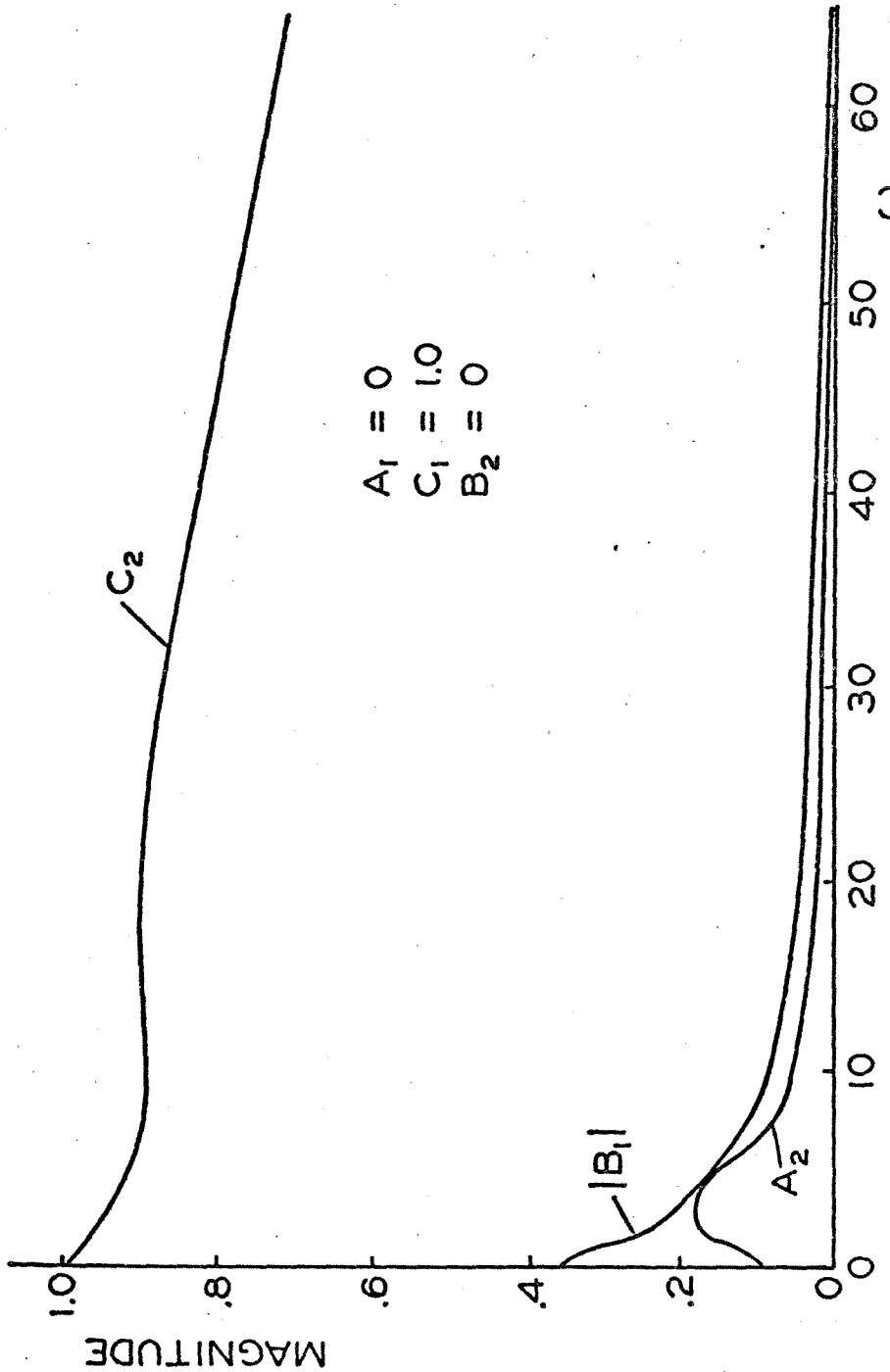

Figure II.3. Disturbances Outside the Compressor for $A_1 = 0.0$, $C_1 = 1.0$, $B_2 = 0.0$.

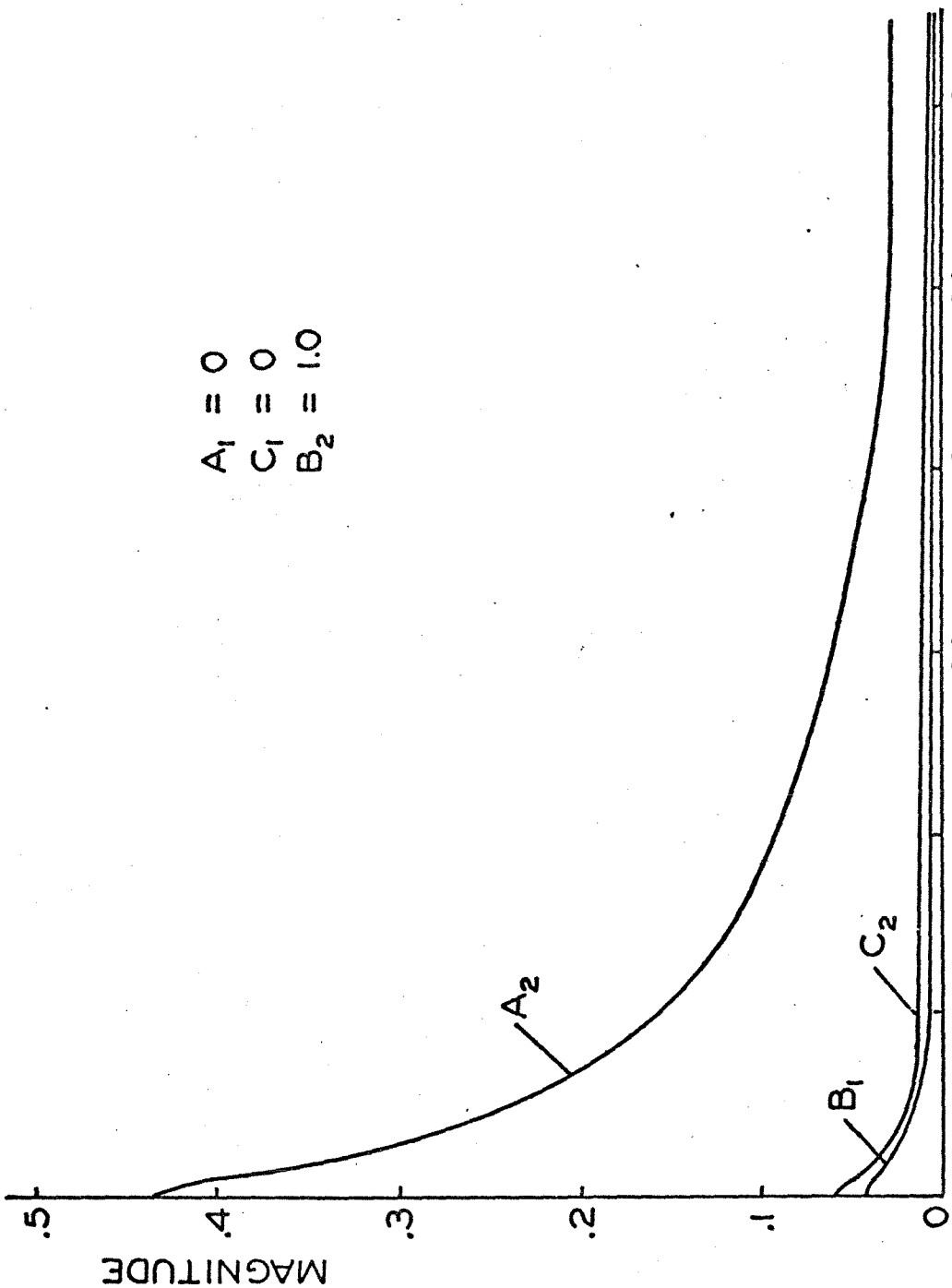

Figure II.4. Disturbances Outside the Compressor for $A_1 = 0.0$, $C_1 = 0.0$, $B_2 = 1.0$.

into non-isentropic heat energy and produces the entropy wave, C_2 .

It should be emphasized that the values plotted in Figures II.2, II.3, and II.4 are the magnitudes of the perturbations. In general, the perturbations are complex so that the phase should also be specified for complete information. Because only the magnitudes are given, simple addition of $A_1 + B_1$ will not give the pressure perturbation at $\xi = 0$, and so on.

In addition, because the mean velocity is not zero, equal magnitude pressure waves traveling in different directions are transporting different amounts of energy. For a stationary medium, the energy of a single wave length is $\frac{1}{2}\bar{\rho}A^2\omega^2\lambda$. So the energy per unit length is $\frac{1}{2}\bar{\rho}A^2\omega$. For a moving medium, this energy is carried with the local velocity of sound, C . The rate of energy transported is $\frac{1}{2}\bar{\rho}A^2\omega^2(C+U)$ if the wave is propagating downstream, and $\frac{1}{2}\bar{\rho}B^2\omega^2(C-U)$ if the wave is propagating upstream. Therefore, the ratio is

$$\frac{\text{Rate of Energy Transfer Downstream}}{\text{Rate of Energy Transfer Upstream}} = \frac{A^2(1+M)}{B^2(1-M)} \qquad (2.40)$$

Calculations show that the reflected wave B_1 , in Figure II.2 always has less energy transfer than the incident wave, $A_1 = 1.0$.

In Figure II.3, $C_1 = 1.0$ is the incident entropy wave, and C_2 is the transmitted entropy wave. Unlike the earlier case, the transmitted entropy wave is attenuated only slightly. Again, this small attenuation is an effect of the efficiency slighty less than unity. Because of this there is interchange of mechanical and non-isentropic heat energy. There is a slight attenuation of C_2 and the production of

a small reflected wave B_1, and a small transmitted pressure wave A_2.

In Figure II.4, B_2 is the incident pressure wave coming from downstream. At low frequencies it is mostly reflected in A_2 and results in a small pressure wave B_1 transmitted upstream, and a small entropy wave C_2, reflected downstream. At higher frequencies it is mostly attenuated in the compressor.

These figures treat the compressor as a transfer function so that its interaction with other components can be studied. For example, if a combustion chamber were located downstream, the transmitted waves A_2 and C_2 could be partially reflected giving rise to a B_2 wave incident on the compressor from the rear. Thus, complex problems involving many components may be analyzed treating the compressor as a transfer function.

E. Disturbances Within the Compressor

In order to indicate the stalling effect of perturbations on the compressor, it is necessary to examine the perturbations occuring inside the compressor as a function of ξ. As an example of the distribution of perturbation magnitudes inside the compressor, the parameters were plotted as functions of ξ for $\omega = 1.0$. Figures II.5, II.6, and II.7 contain the plots for cases 1, 2, and 3 respectively. Although $v(\xi)$, $p(\xi)$, and $s(\xi)$ have been plotted, only $v(\xi)$ is important in determining local angle of attack and hence an indication of stalling. The other functions have been plotted for completeness. In Figure II.5, wave $A_1 = 1.0$ is incident from the front. The small arrow marked $\left|\frac{A_1}{\gamma M_1}\right|$ shows the magnitude of $v(\xi)$ produced by A_1, at the compressor inlet. The small arrow marked $\left|\frac{B_1}{\gamma M_1}\right|$ shows the magnitude of $v(\xi)$ produced by B_1, at the same location, and so on. Note that

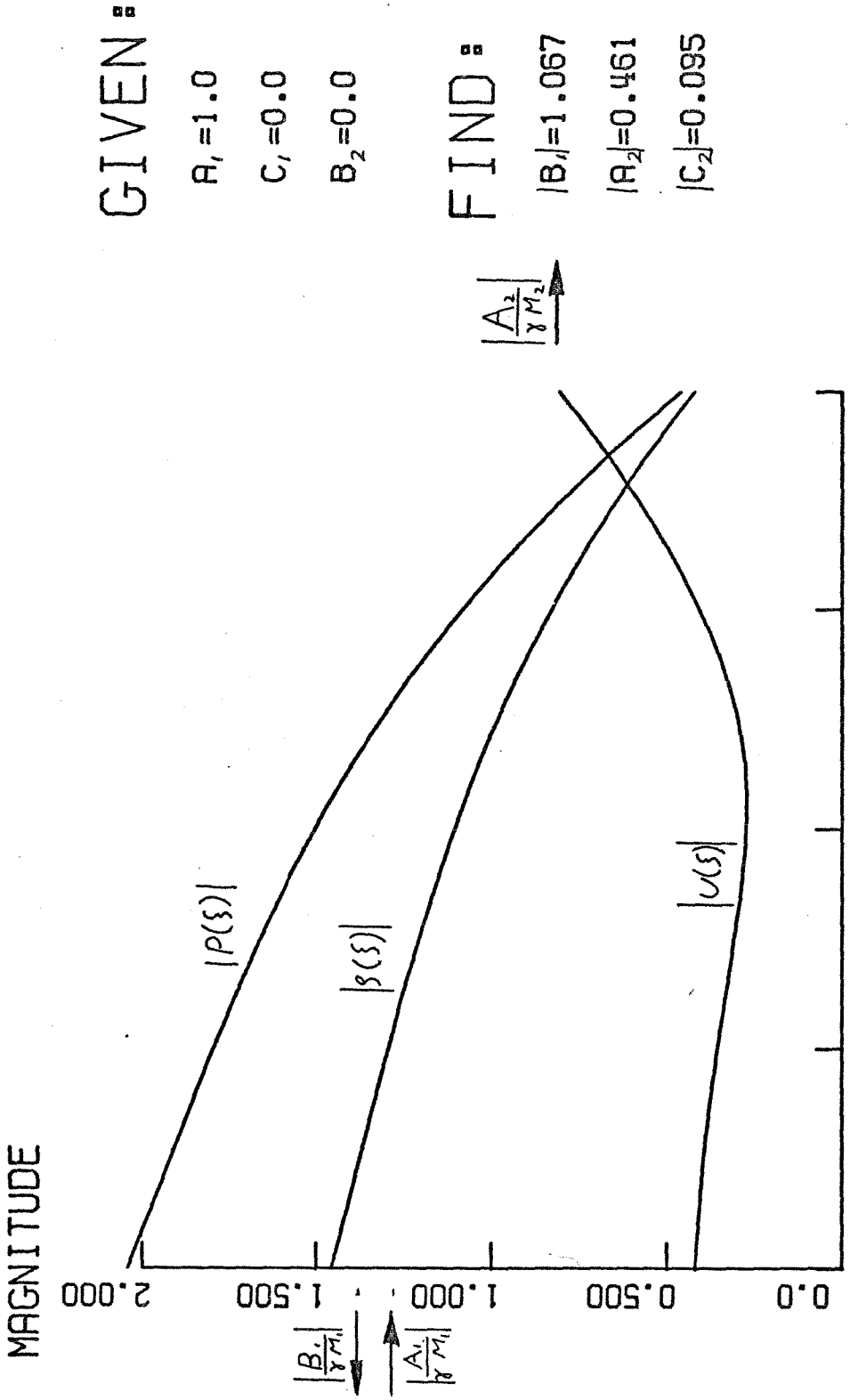

Figure II.5. Disturbances Inside the Compressor for $A_1 = 1.0$, $C_1 = 0.0$, $B_2 = 0.0$, $\omega = 1$.

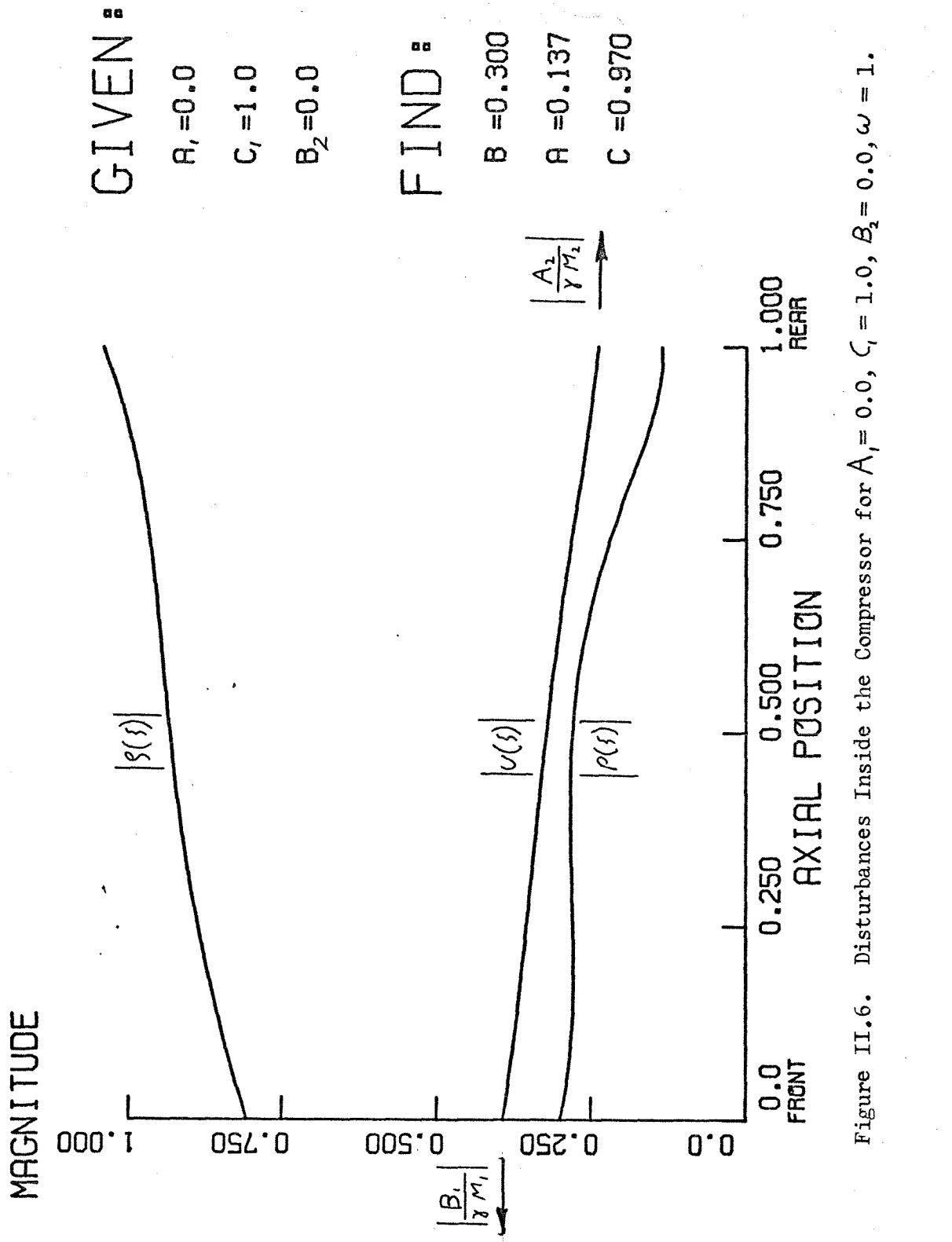

Figure II.6. Disturbances Inside the Compressor for $A_1 = 0.0$, $C_1 = 1.0$, $B_2 = 0.0$, $\omega = 1$.

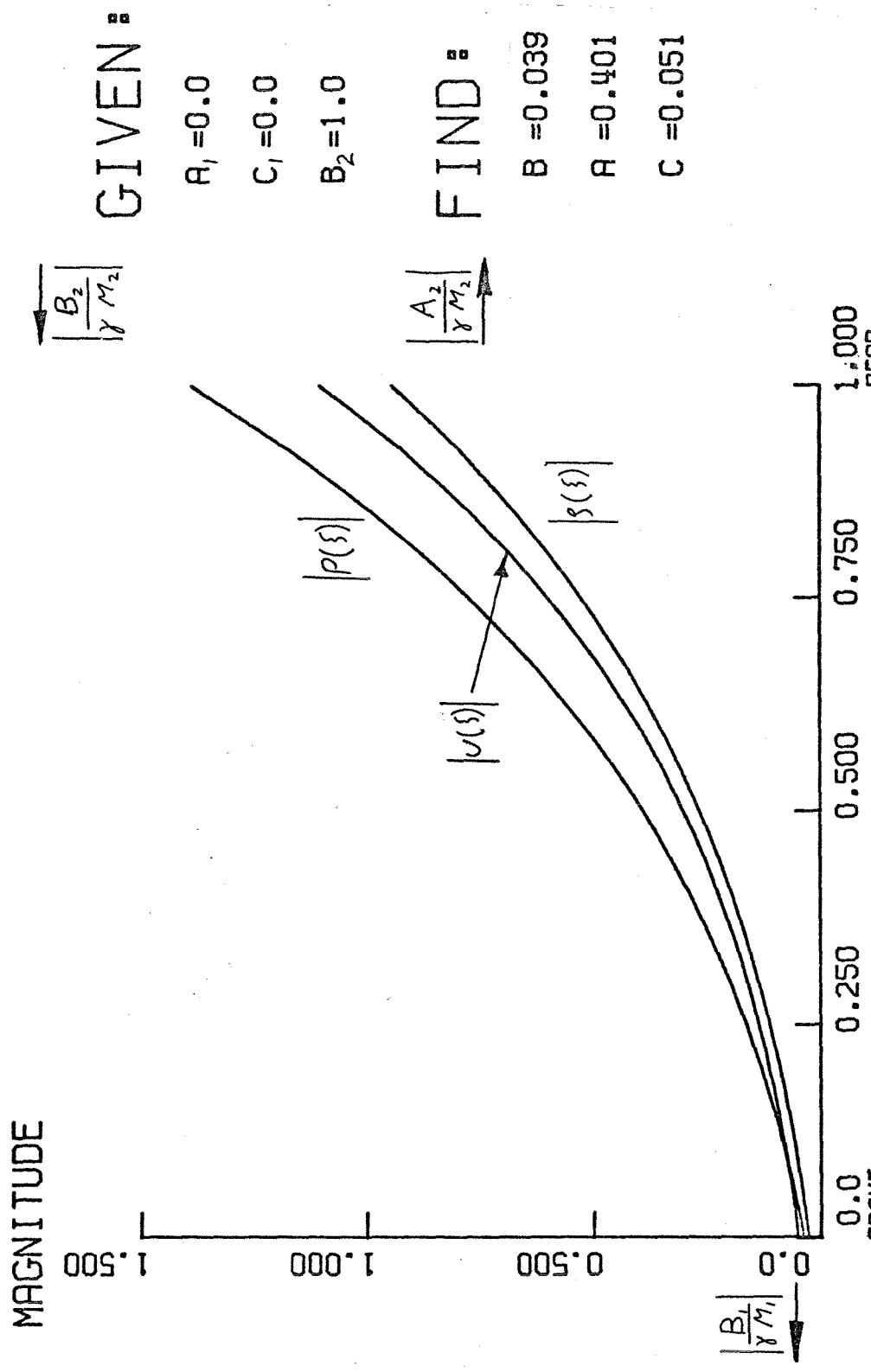

Figure II.7. Disturbances Inside the Compressor for $A_1 = 0.0$, $C_1 = 0.0$, $B_2 = 1.0$, $\omega = 1$.

the algebraic difference of the velocities due to A_1, and B_1, in Figure II.5 is much less than the actual value of $|v(0)|$. This is due to the fact that only the magnitudes of the velocities have been shown. However, at the other end of the compressor there is only one pressure wave, and hence the magnitudes of $v(1)$ and the velocity due to A_2 agree. Note that the magnitude of $v(\xi)$ varies over the length of the compressor by about a factor of 2. It first starts to decay, then rises again to reach its maximum at $\xi = 1.0$.

In Figure II.6, the incident wave is $C_1 = 1.0$, which does not contain any velocity fluctuation. However, it produces the values of $|v(\xi)|$ shown inside the compressor due to the fact that $\gamma \neq 1.0$ as discussed above and the change in Mach number through the compressor. The magnitude of $v(\xi)$ is essentially constant, only slightly larger at the inlet.

In Figure II.7, the incident wave is $B_2 = 1.0$. The net velocity perturbation dies out quite rapidly, almost to zero, at the front.

The shapes of the curves of $|v(\xi)|$ versus ξ for other values of ω are quite similar to these curves. In each case examined, $|v(\xi)|$ is a maximum either at the front or the rear of the compressor. Hence, if the compressor were operating near stall, the critical regions would be the front and the rear, and not some point in between.

The results obtained at other frequencies have been examined to determine the maximum value of $|v(\xi)|$ that occurs within the compressor. The maximum magnitude of $v(\xi)$ as a function of ω is shown in Figure II.8 for the three cases examined before.

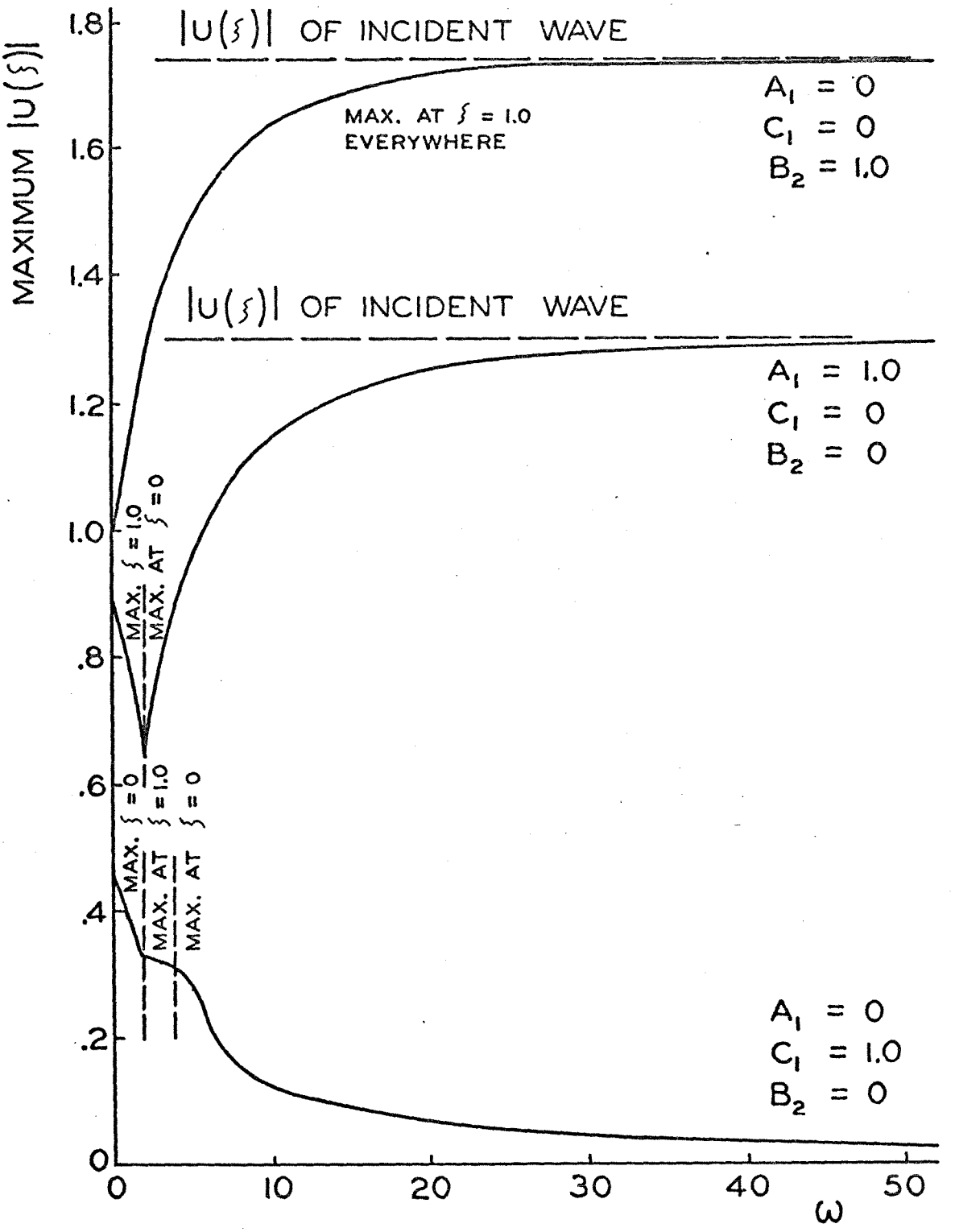

Figure II.8. Maximum Velocity Perturbation Inside the Compressor.

For the case $A_1 = 1.0$, the maximum occurs at the back of the compressor, $\xi = 1.0$, for low values of ω, and then switches to the front as ω increases. The asymptote, as ω approaches infinity is the value of $|v(\xi)|$ in the incident wave, $A_1 = 1.0$.

For the case $C_1 = 1.0$, the maximum occurs at the front, $\xi = 0$, for all ω except for the range of approximately $2 < \omega < 4$, and in that range the maximum is at the rear, $\xi = 1.0$. However, unlike the other cases, the maximum velocity approaches zero as ω approaches infinity.

For the case $B_2 = 1.0$, the maximum always occurs at the back of the compressor, and it approaches the value of $|v(\xi)|$ in the incident wave as ω approaches infinity just as the case with $A_1 = 1.0$.

The net result is that the location of the maximum velocity perturbation is dependent upon frequency, and the magnitude of the maximum ranges from about half up to the full magnitude of the velocity perturbation present in the incident pressure wave. The entropy wave gives rise to velocity fluctuation in the compressor even though the velocity fluctuation in the incident wave is zero.

The calculations performed here are intended only as an example of the method of analysis. Compressors with other characteristics would behave differently (although results given here should be typical).

Some of the assumptions used in this analysis need further discussion. The Mach number that appeared in the equations was the axial Mach number based on average axial velocity. This Mach number appeared in the calculations because axial velocity was the only

velocity considered. However, in actual operation, the Mach number of the flow with respect to the rotors will be greater due to the high tip speed of the rotor. For the compressor examined here, the Mach number relative to the rotor is 0.66 (assuming equal tangential and axial components of gas velocity). In transonic compressors, the Mach number relative to the rotor becomes unity at some radius. Outside of this radius the flow is supersonic, while inside it is subsonic. The flow in these two regions will be different, resulting in radial variations not accounted for in this one-dimensional theory.

Throughout this analysis it has been assumed that the effect of the periodic, non-cumulative forces produced by blade rows within the compressor could be neglected. These are of two types: tangential forces equal in magnitude and opposite in direction on rotor blade rows and stator blade rows, and the forces resulting from contractions and expansions of the stream tubes through the blade rows. The net value of these forces averaged over one stage length is zero, but the positive and negative components are not spread evenly over the stage length and hence affect different phases of the disturbance wave length at the same instant. Clearly, if the wave length of the disturbance is very long compared with the stage axial length the phase variation within one stage is negligible and the periodic forces within the stage tend to cancel.

In order to estimate the disturbance frequency below which the periodic forces can be neglected, the effect of a restriction in area corresponding to one stage (or blade row) alone is discussed in the next chapter. Presumably the periodic tangential forces will lead to a similar limitation.

Another assumption is that the tangential component of velocity in the compressor is zero. Actually, the equations and results remain unchanged if the value of tangential velocity is constant upstream, within, and downstream of the compressor. However, most compressors have flow coming into the compressor with no tangential component. The flow is turned by inlet guide vanes, or the first rotor to some flow angle which remains approximately constant through the compressor. Straightening vanes are then used to reduce the tangential component of velocity back to zero at the exit of the compressor. The flow inside such a compressor can be treated just as before, except the additional guide and straightening vanes must be added as separate components. These will be analyzed in Chapter IV.

CHAPTER III

RESTRICTION IN A CHANNEL

A. Basic Equations

In this chapter an analysis of flow through a tube with a smooth restriction will be presented. Since the model is to represent flow through a blade row without any cumulative blade forces, the configuration examined will be a nozzle with the same area on either end. Furthermore, the flow will be taken as entirely subsonic or entirely supersonic. The problem of the continuously accelerating nozzle with subsonic and supersonic flow at different points was examined by Candel (1972) for certain special cases. In addition, work is currently in progress by other investigators at this Institution on this problem as applied to noise production. The difference between these two configurations is that for long wave lengths the acceleration and deceleration in the entirely subsonic (or supersonic) case tend to cancel out, while there is only acceleration and no cancellation in the other case. It will be seen later that different methods must be used to obtain solutions in these two different cases.

The method of the last section applies directly to this problem. The average flow is taken as steady and one-dimensional. However, there are no body forces. The flow is then allowed to have a small fluctuating part superimposed upon the steady state solution.

The equations of motion for this problem are the same as Equations 2.1, 2.2, and 2.3 in the last section where the body forces X and F are taken as zero.

Continuity $$\frac{\partial}{\partial t}(\rho A) + \frac{\partial}{\partial x}(\rho u A) = 0 \tag{3.1}$$

Momentum $$\rho\left(\frac{\partial u}{\partial t} + u\frac{\partial u}{\partial x}\right) + \frac{\partial p}{\partial x} = 0 \tag{3.2}$$

Energy $$\rho C_p\left(\frac{\partial T}{\partial t} + u\frac{\partial T}{\partial x}\right) - \left(\frac{\partial p}{\partial t} + u\frac{\partial p}{\partial x}\right) = 0 \tag{3.3}$$

As before, it has been assumed that the flow is one-dimensional, and that any components of velocity in non-axial directions due to changing area produce negligible changes in the other variables. However, the axial velocity is not constant, and it is assumed that no losses occur. A is the cross-sectional area of the tube.

Again, the working fluid is taken as an ideal gas,

$$p = \rho R T \tag{3.4}$$

and Equation 3.3 is reduced to the form:

$$\left(\frac{\partial}{\partial t} + u\frac{\partial}{\partial x}\right)\left(\ln p - \gamma \ln \rho\right) = 0 \tag{3.5}$$

B. Perturbed Equations

Now let the parameters have a steady state average part and a small varying perturbation so that:

$$\begin{aligned} u &= \bar{u}\left(1 + \frac{u'}{\bar{u}}\right) \\ p &= \bar{p}\left(1 + \frac{p'}{\bar{p}}\right) \\ \rho &= \bar{\rho}\left(1 + \frac{\rho'}{\bar{\rho}}\right) \end{aligned} \tag{3.6}$$

where the barred quantities are the average values, and the primed quantities are the perturbations. The functions $\bar{u}$, $\bar{p}$, and $\bar{\rho}$

satisfy the equations of motion in the steady state and are known functions of X .

Substituting Equation 3.6 into Equations 3.1, 3.2, and 3.3, and examining only first order terms yields, after some simplifications,

$$\frac{\partial}{\partial t}\left(\frac{\rho'}{\bar{\rho}}\right) + \bar{U}\frac{\partial}{\partial x}\left(\frac{\rho'}{\bar{\rho}} + \frac{u'}{\bar{U}}\right) = 0 \tag{3.7}$$

$$\left(\frac{\partial}{\partial t} + \bar{U}\frac{\partial}{\partial x}\right)\left(\frac{u'}{\bar{U}}\right) + \left(\frac{\rho'}{\bar{\rho}} + 2\frac{u'}{\bar{U}} - \frac{p'}{\bar{p}}\right)\left(\frac{d\bar{U}}{dx}\right) + \frac{\bar{U}}{\gamma \bar{M}^2}\frac{\partial}{\partial x}\left(\frac{p'}{\bar{p}}\right) = 0 \tag{3.8}$$

$$\left(\frac{\partial}{\partial t} + \bar{U}\frac{\partial}{\partial x}\right)\left(\frac{p'}{\bar{p}} - \gamma\frac{\rho'}{\bar{\rho}}\right) = 0 \tag{3.9}$$

where $\bar{M}$ is the average Mach number (a function of X),

$$\bar{M} = \frac{\bar{U}}{\sqrt{\gamma R \bar{T}}} \tag{3.10}$$

Note that the average axial velocity, $\bar{U}$, is not constant so that the term involving $\frac{d\bar{U}}{dx}$ is not zero.

Equations 3.7, 3.8, and 3.9 may be converted to dimensionless notation by letting

$$\xi = \frac{x}{a}$$

$$\tau = \frac{\bar{U}_0}{a}t \tag{3.11}$$

$$\bar{V} = \frac{\bar{U}}{\bar{U}_0}$$

where $\bar{U}_0$ is the velocity in the straight portion of the tube upstream and downstream of the constriction, and a is the length of the constriction. Furthermore, Equations 3.7, 3.8, and 3.9 can be satisfied

by variables of the form,

$$\frac{v'}{\bar{V}} = v(\xi)\, e^{-i\omega\tau}$$
$$\frac{\rho'}{\bar{\rho}} = \rho(\xi)\, e^{-i\omega\tau} \qquad (3.12)$$
$$\frac{p'}{\bar{p}} = p(\xi)\, e^{-i\omega\tau}$$

Substituting these expressions in Equations 3.11 and 3.12 into Equations 3.7, 3.8, and 3.9 yield:

$$\frac{d\,v(\xi)}{d\xi} + \frac{d\,\rho(\xi)}{d\xi} = \frac{i\omega\,\rho(\xi)}{\bar{V}} \qquad (3.13)$$

$$\frac{d\,v(\xi)}{d\xi} + \frac{1}{\gamma\bar{M}^2}\frac{d\,p(\xi)}{d\xi} = \qquad (3.14)$$

$$\frac{i\omega\,v(\xi)}{\bar{V}} - \left[\rho(\xi) + 2v(\xi) - p(\xi)\right]\frac{1}{\bar{V}}\frac{d\bar{V}}{d\xi}$$

$$-\gamma\frac{d\,\rho(\xi)}{d\xi} + \frac{d\,p(\xi)}{d\xi} = \frac{i\omega}{\bar{V}}\left[p(\xi) - \gamma\,\rho(\xi)\right] \qquad (3.15)$$

These equations can be combined linearly to find the derivatives at any point in the flow.

$$\frac{d\,v(\xi)}{d\xi} = \frac{1}{\gamma(1-\bar{M}^2)\,\bar{V}}\Big\{i\omega\,p(\xi) \qquad (3.16)$$

$$-\gamma\bar{M}^2\left[i\omega\,v(\xi) - \left(\rho(\xi) + 2v(\xi) - p(\xi)\right)\frac{d\bar{V}}{d\xi}\right]\Big\}$$

$$\frac{d\,\rho(\xi)}{d\xi} = \frac{i\omega\,\rho(\xi)}{\bar{V}} - \frac{d\,v(\xi)}{d\xi} \qquad (3.17)$$

$$\frac{d\,p(\xi)}{d\xi} = \frac{i\omega}{\bar{V}}\left[p(\xi) - \gamma\,\rho(\xi)\right] + \gamma\frac{d\,\rho(\xi)}{d\xi} \qquad (3.18)$$

These equations are directly analogous to Equations 2.28, 2.29, and 2.30. They cannot be integrated in closed form for an arbitrary variation in Mach number with ξ.

If the Mach number, $\bar{M}$, is given as a function of ξ, then $\bar{V}$ and A may be found by solving Equations 3.1, 3.2, and 3.5 where the time-wise variation is taken as zero. This is quite straightforward and yields,

$$\bar{V}^2 = \frac{\left[1 + \frac{2}{\gamma-1}\frac{1}{\bar{M}_0^2}\right]}{\left[1 + \frac{2}{\gamma-1}\frac{1}{\bar{M}^2}\right]} \tag{3.19}$$

$$\frac{A}{A_0} = \left(\frac{1 + \frac{\gamma-1}{2}\bar{M}^2}{1 + \frac{\gamma-1}{2}\bar{M}_0^2}\right)^{\frac{\gamma+1}{2(\gamma-1)}} \tag{3.20}$$

where $\bar{M}_0$ and A_0 refer to conditions in the straight part of the tube.

Equations 3.16, 3.17, and 3.18 may be integrated numerically in the same manner as for the compressor. The solutions for flow in the uniform duct at either end of the nozzle are similar to the solutions obtained upstream and downstream of the compressor with Mach number the same upstream as downstream.

$$\begin{aligned} p(0) &= A_1 + B_1 \\ \rho(0) &= \frac{1}{\gamma}(A_1 + B_1) + C_1 \\ v(0) &= \frac{1}{\gamma \bar{M}_0}(A_1 - B_1) \end{aligned} \tag{3.21}$$

$$\begin{aligned} p(1) &= A_2 e^{i\frac{\bar{M}_0}{1+\bar{M}_0}\omega} + B_2 e^{-i\frac{\bar{M}_0}{1-\bar{M}_0}\omega} \\ \rho(1) &= \frac{1}{\gamma}\left[A_2 e^{i\frac{\bar{M}_0}{1+\bar{M}_0}\omega} + B_2 e^{-i\frac{\bar{M}_0}{1-\bar{M}_0}\omega}\right] + C_2 e^{i\omega} \\ v(1) &= \frac{1}{\gamma \bar{M}_0}\left[A_2 e^{i\frac{\bar{M}_0}{1+\bar{M}_0}\omega} - B_2 e^{-i\frac{\bar{M}_0}{1-\bar{M}_0}\omega}\right] \end{aligned} \tag{3.22}$$

where the subscripts 1 and 2 refer to the upstream and downstream ends respectively.

C. General Deductions

Several observations can be made before the full solution is obtained. If the flow is continuously accelerating in the nozzle, $\bar{M} = 1.0$ at the throat. This results in a singularity in Equation 3.16. This provides an additional condition to be met at the throat. If the flow is everywhere subsonic or supersonic, there is no singularity.

The second observation is that Equation 3.15 can be rewritten as

$$\frac{d}{ds}\left[p(s) - \gamma \rho(s)\right] = \frac{i\omega}{\bar{V}}\left[p(s) - \gamma \rho(s)\right] \tag{3.23}$$

$$\frac{d}{ds}\left\{\ln\left[p(s) - \gamma \rho(s)\right]\right\} = \frac{i\omega}{\bar{V}} \tag{3.24}$$

Integrating

$$\frac{p(1) - \gamma \rho(1)}{p(0) - \gamma \rho(0)} = e^{i\omega \int_{s=0}^{s=1} \frac{ds}{\bar{V}}} \tag{3.25}$$

Equations 2.32 and 2.33 may be combined to yield,

$$p(s) - \gamma \rho(s) = C e^{i\omega s} \tag{3.26}$$

outside the compressor. Now define α,

$$\alpha = \int_{s=0}^{s=1} \frac{ds}{\bar{V}} \tag{3.27}$$

Combining Equations 3.25, 3.26, and 3.27 shows that,

$$C_2 = C_1 e^{i\omega(\alpha - 1)} \tag{3.28}$$

Thus, the magnitudes of the entropy waves on either side of nozzle must be the same. This also shows that no combination of incident pressure waves can produce an entropy wave. However, the inverse is not true.

As an entropy wave passes through the nozzle, it generates pressure waves.

The third observation is in regard to the shape of the nozzle. The nozzle shape will be unimportant if the wave lengths of the perturbations are long compared to the nozzle length. The reflections across the channel, not considered in this analysis, will also be minimized.

D. Numerical Solution

Since the area of the cross-section of the channel is related to the Mach number, and since the Mach number appears directly in the equations, it is convenient to specify the Mach number as a function of ξ. A convenient Mach number variation with ξ is

$$\bar{M}(\xi) = \frac{\bar{M}_o + \bar{M}_M}{2} + \frac{\bar{M}_o - \bar{M}_M}{2} \cos(2\pi\xi) \qquad (3.29)$$

where $\bar{M}_M$ is the Mach number in the center of the nozzle. This equation represents a smooth contour where the rate of change of Mach number with ξ is zero at $\xi = 0.0$, 0.5, and 1.0. It is also symmetric with the Mach number at its minimum or maximum at $\xi = 0.5$. Equations 3.16, 3.17, and 3.18 are now integrated numerically, using the same method as in Chapter II. The same three sets of A_1, B_1, and C_2 are used as input parameters for each calculation. However, the cases with $C_1 = 0$ produce $C_2 = 0$ directly.

Three sets of values for $\bar{M}_o$ and $\bar{M}_M$ were used. The first set was $\bar{M}_o = 0.55$, $\bar{M}_M = 0.7425$. This corresponds to conditions at the inlet of the compressor assuming a 15 percent area reduction in a stationary blade row. The second and third sets are $\bar{M}_o = 0.2$ with

$\bar{M}_m = 0.3$ and 0.5. These values were chosen to show the effects of varying the area reduction of the channel. Separate integrations are necessary for each set of $\bar{M}_o$, $\bar{M}_m$, and ω evaluated. For each set of $\bar{M}_o$ and $\bar{M}_m$ used, solutions were found for the range $0 < \omega < 64$. The solutions for the higher values of ω are probably affected by the shape of the nozzle. Consequently, only the results for $\omega < 16$ are shown here. 1000 steps were used for each computation except $\omega = 64$, where 1000, 5000, and 9000 steps were used. The results for $\omega = 64$ indicated only slight changes in the magnitudes of the parameters as the number of steps was increased by a factor of 2. Since $\omega = 64$ is the case with the most rapid fluctuations in ζ, 1000 steps are quite satisfactory for lower values of ω.

E. Results

Since this calculation is being performed to check the assumption that at low values of ω the flow is unaffected by the nozzle, the results for the perturbations within the nozzle will not be presented. Only the calculated values of B_1 and A_2 will be shown, and although the solutions are complex, only the magnitudes will be shown.

Figures III.1 and III.2 show the values obtained for B_1, and A_2 for the case where $A_1 = 1.0$, $C_1 = 0$, and $B_2 = 0$ as a function of ω for all three sets of values of M_o and M_m. At $\omega = 0$, $B_1 = 0$, and $A_2 = 1.0$. This means that there is no reflection in the steady state. As ω increases the reflected wave, B_1, increases rapidly. The magnitude of the reflection is a strong function of the average Mach numbers of the flow. Holding the free stream Mach number at $\bar{M}_o = 0.2$ and increasing the Mach number at the center from 0.3 to 0.5

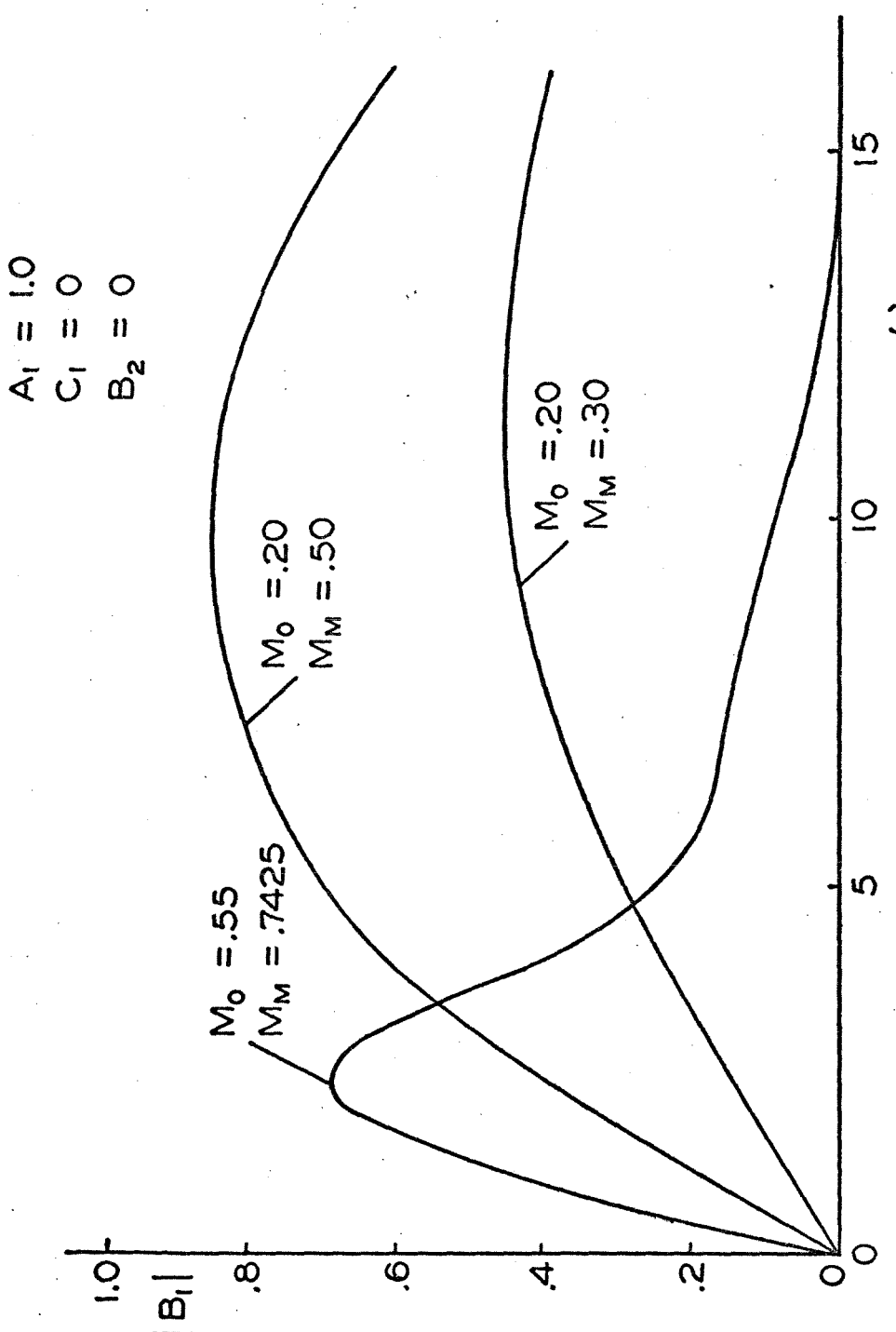

Figure III.1. Reflected Wave from a Restriction Given $A_1 = 1.0$, $C_1 = 0.0$, $C_2 = 0.0$.

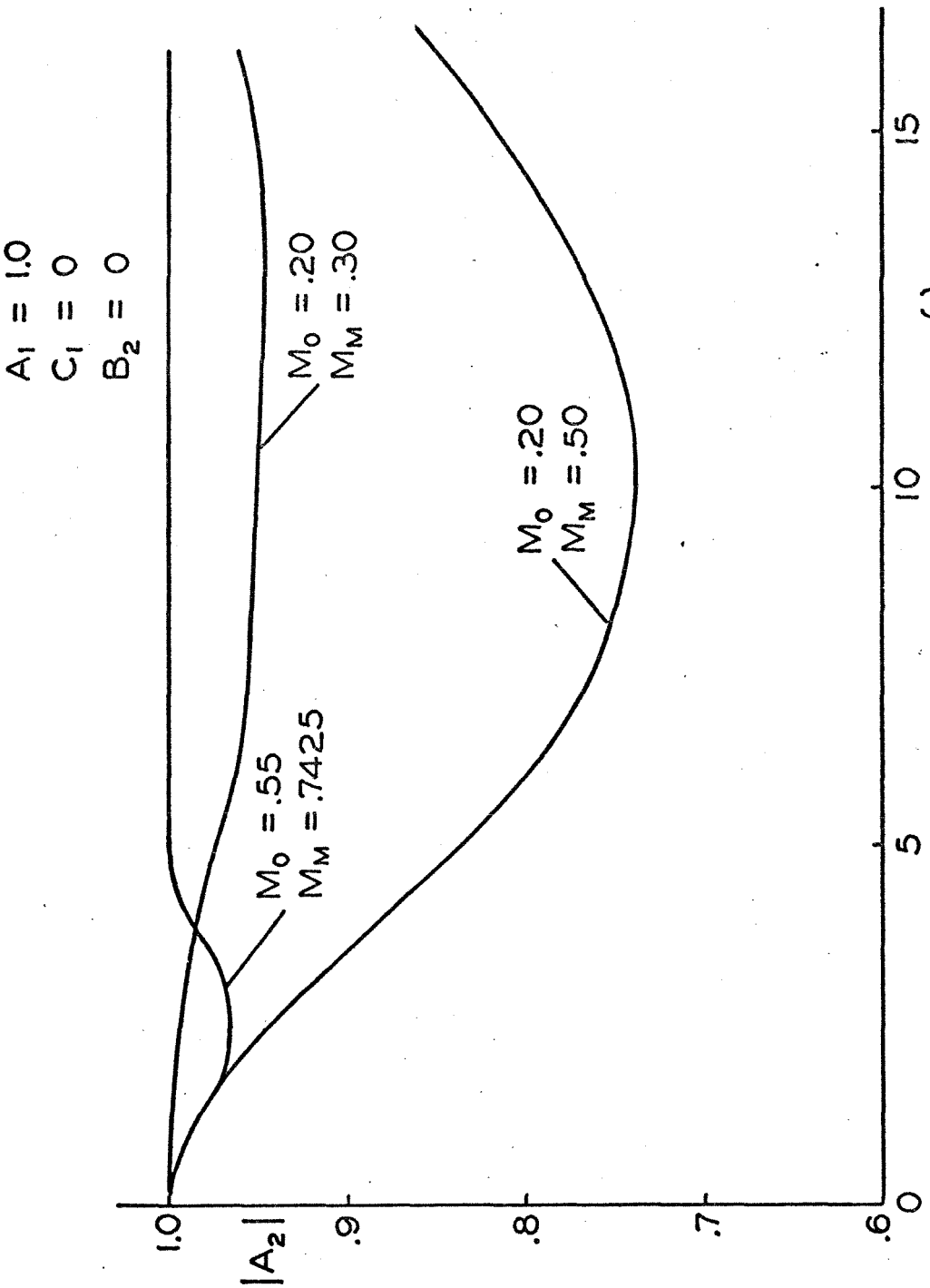

Figure III.2. Transmitted Pressure Wave from a Restriction Given $A_1 = 1.0$, $C_1 = 0.0$, $B_2 = 0.0$.

approximately doubles the rate of increase of B_1, with ω. This is expected since in the limit where $\bar{M}_M$ approaches $\bar{M}_0$, there is no reflection at all.

For the case which models the compressor blades at the front of the compressor, $\bar{M}_0 = 0.55$ and $\bar{M}_M = 0.7425$, the increase of B_1, with ω is even more rapid. For this case the magnitude of B_1, is more than 0.4 at $\omega = 2$.

The reflected wave, B_1, has a maximum for all three cases. For higher values of ω the magnitude of the reflected wave decays so that the values at $\omega = 64$ are less than 0.1 for all cases examined. As mentioned before, this behavior at high values of ω is probably inaccurate due to the one-dimensional flow assumption.

Figure III.2 shows the magnitude of the transmitted wave, for the case $A_1 = 1.0$, $C_1 = 0$, and $B_2 = 0.0$. Although the reflected waves shown in Figure III.1 were as large as 80 percent of the incident waves, the transmitted waves are always greater than 70 percent of the incident waves. It must be remembered that the energy transported by a wave is a function of both its magnitude and direction of propagation. Thus, although the reflected waves are large, they do not transport much energy. An energy balance was performed as described in Chapter II and the result showed that the energy in the reflected and transmitted waves agreed quite closely with the energy in the incident wave. For the case $\bar{M}_0 = 0.55$ and $\bar{M}_M = 0.7425$, at $\omega = 2$, almost 97 percent of the energy in the wave is transmitted and only 3 percent reflected.

Figures III.3 and III.4 show the results for the case $A_1 = 0.0$, $C_1 = 1.0$, and $B_2 = 0.0$. As stated earlier, the magnitude of C_2 must be

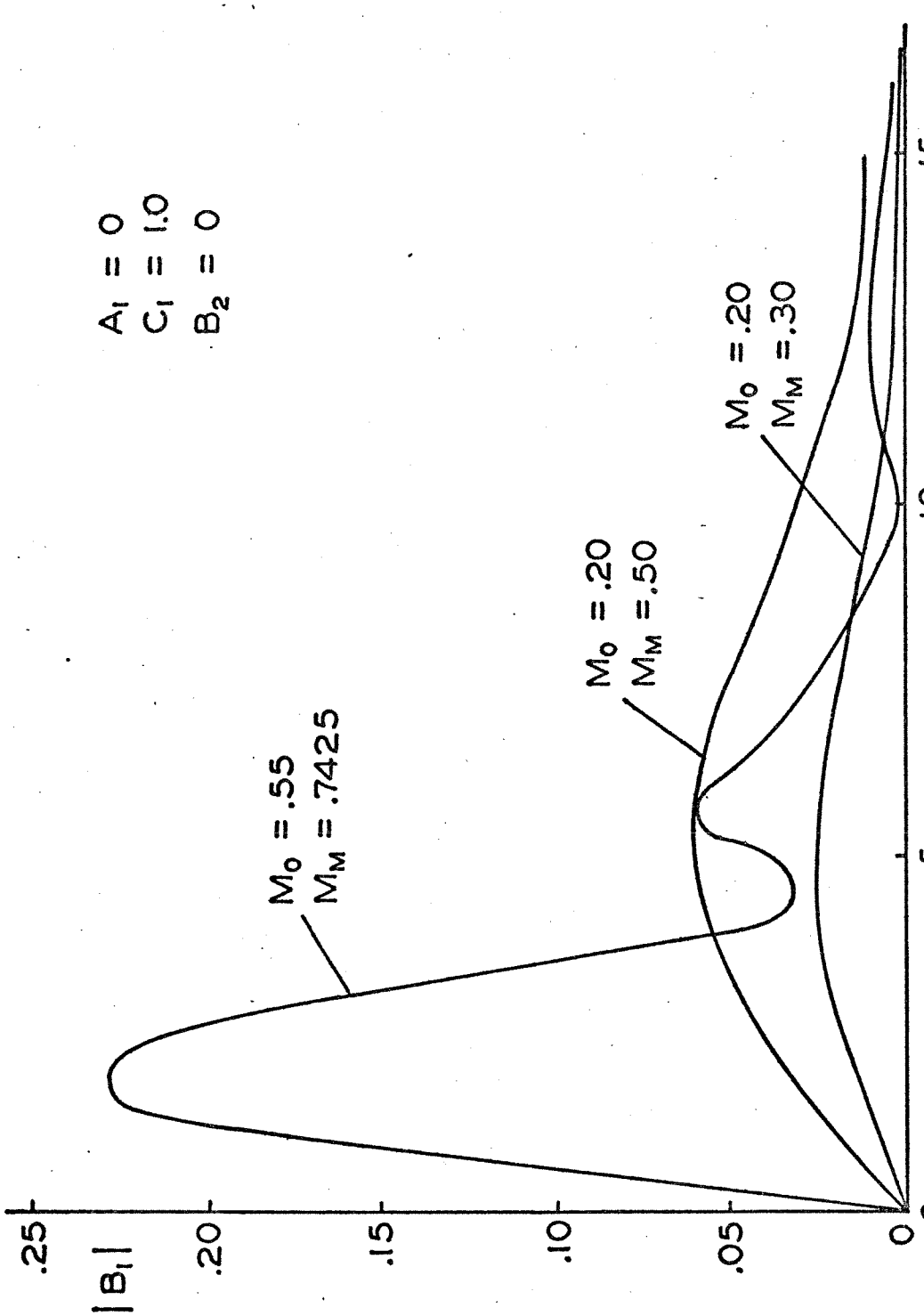

Figure III.3. Transmitted Pressure Wave from a Restriction Given $A_1 = 0.0$, $C_1 = 1.0$, $B_2 = 0.0$.

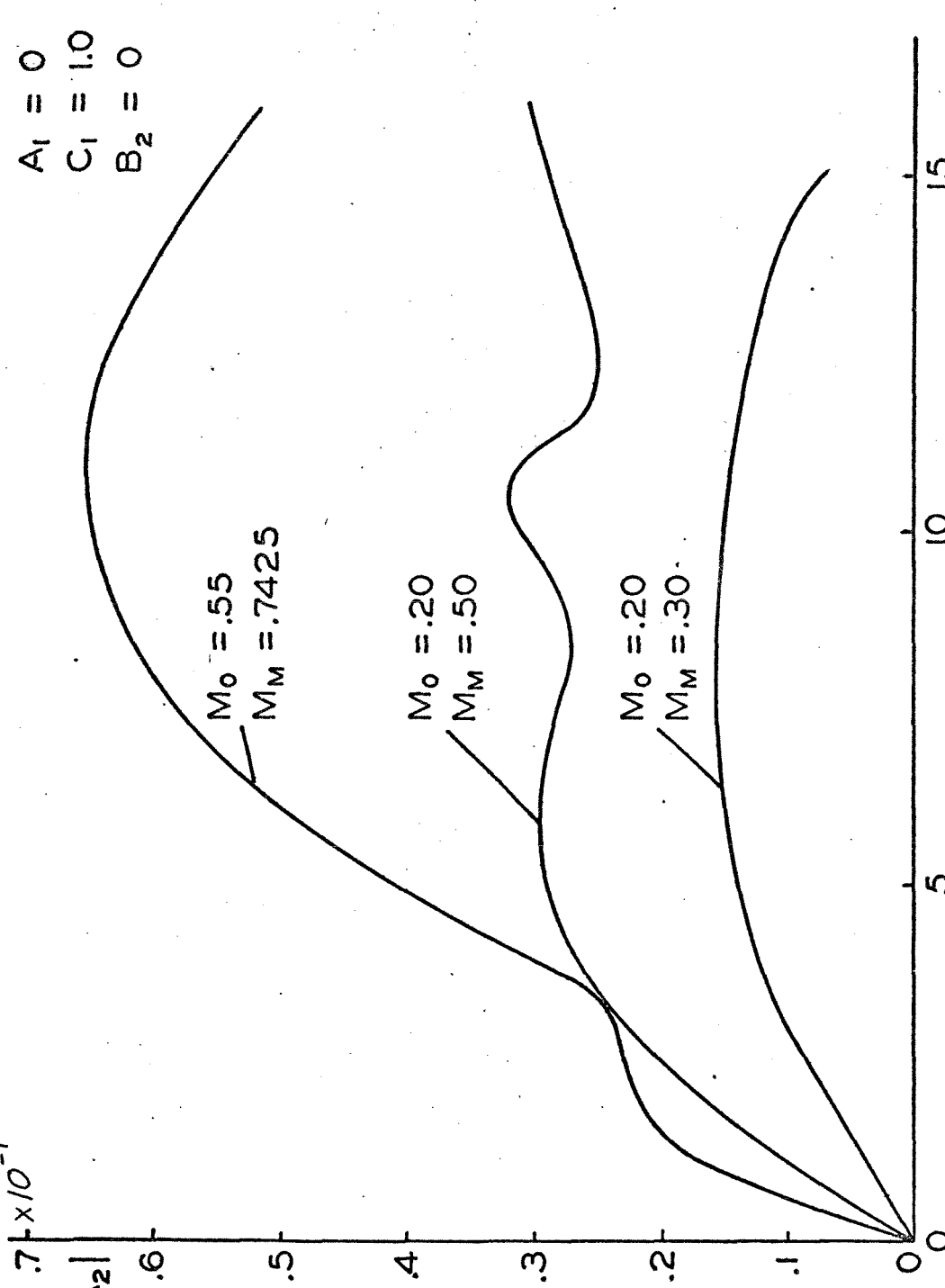

Figure III.4. Transmitted Pressure Wave from a Restriction Given $A_1 = 0.0$, $C_1 = 1.0$, $B_2 = 0.0$.

the same as C_1, for all frequencies. The incident entropy wave produces a small reflected wave, B_1, shown in Figure III.3. The rate of increase with ω at low values of ω has roughly the same dependence on Mach number as the earlier case. The magnitudes, however, are reduced. The transmitted wave, A_2, shown in Figure III.4, is quite small. The largest values are less than 7 percent of the incident wave.

Figures III.5 and III.6 show the results for the case $A_1 = 0.0$, $C_1 = 0.0$, and $B_2 = 1.0$. Here, the reflected wave is A_2. Unlike the earlier case, the set where $\bar{M}_0 = .55$ and $\bar{M}_1 = .7425$ does not produce the largest reflected wave at low values of ω. Nevertheless, the results still show that at $\omega = 0$, there is no reflection, and that the amount reflected increases as ω increases, for low values of ω.

Figure III.6 shows the transmitted wave, B_1. Again it can be seen that although the reflected wave is large, the transmitted wave is hardly affected at all. For the case $\bar{M}_0 = 0.55$ and $\bar{M}_1 = 0.7425$, the transmitted wave is more than 96 percent of the incident wave at $\omega = 2.0$.

In comparing this calculation with the compressor calculation, it is important to note that the ω values are not the same. The a used here, to reduce the problem to non-dimensional form, was the length of the nozzle. In the compressor, this length is the chord length of a blade row. Since the compressor is assumed to have 8 stages, and each stage has 2 blade rows, the length a in the nozzle calculation must correspond to about 1/16 of the compressor length. Consequently, the ω for the compressor corresponds to 16 times the ω used here. This means, for example, that to estimate the effects of the

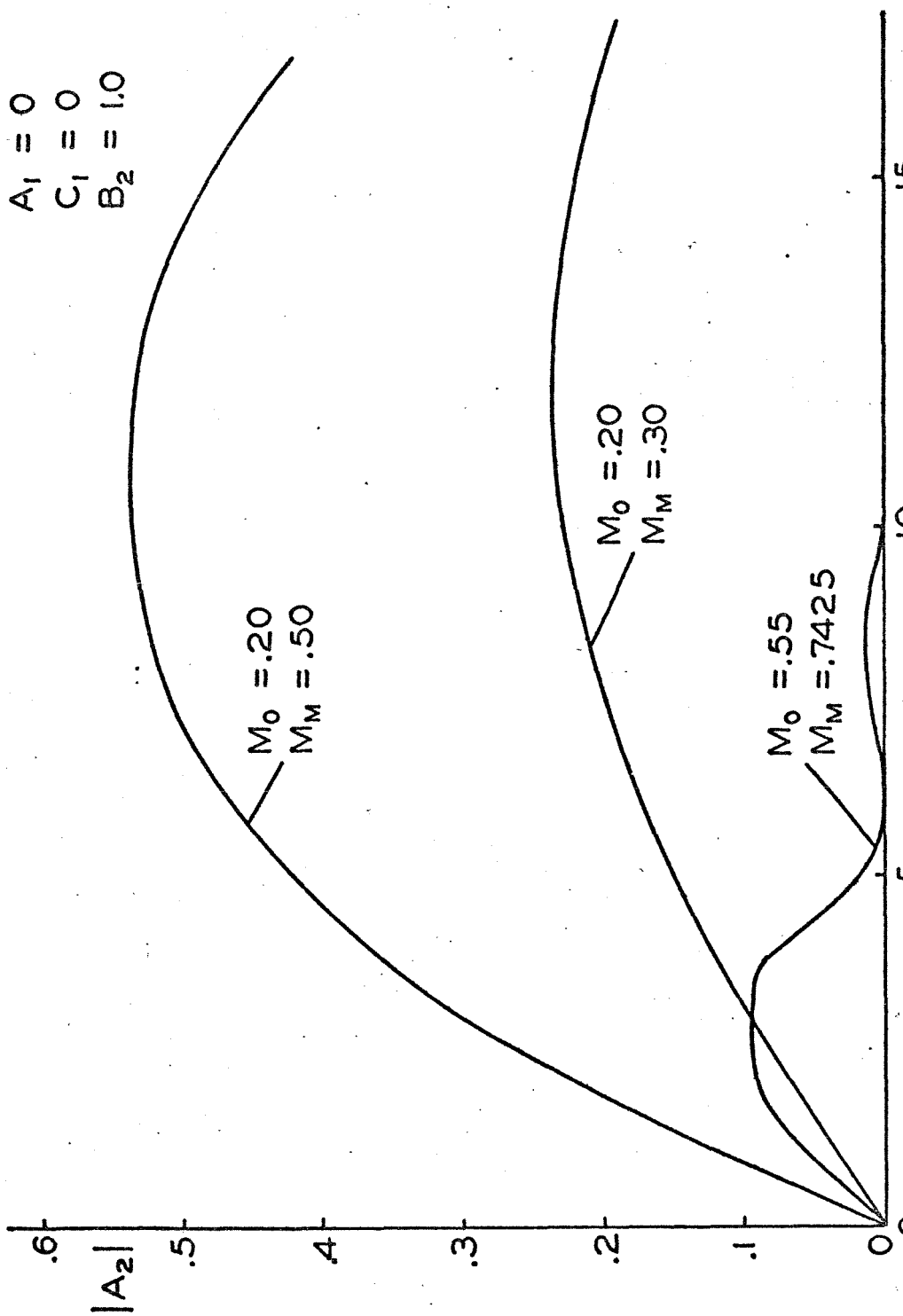

Figure III.5. Reflected Pressure Wave from a Restriction Given $A_1 = 0.0$, $C_1 = 0.0$, $B_2 = 1.0$.

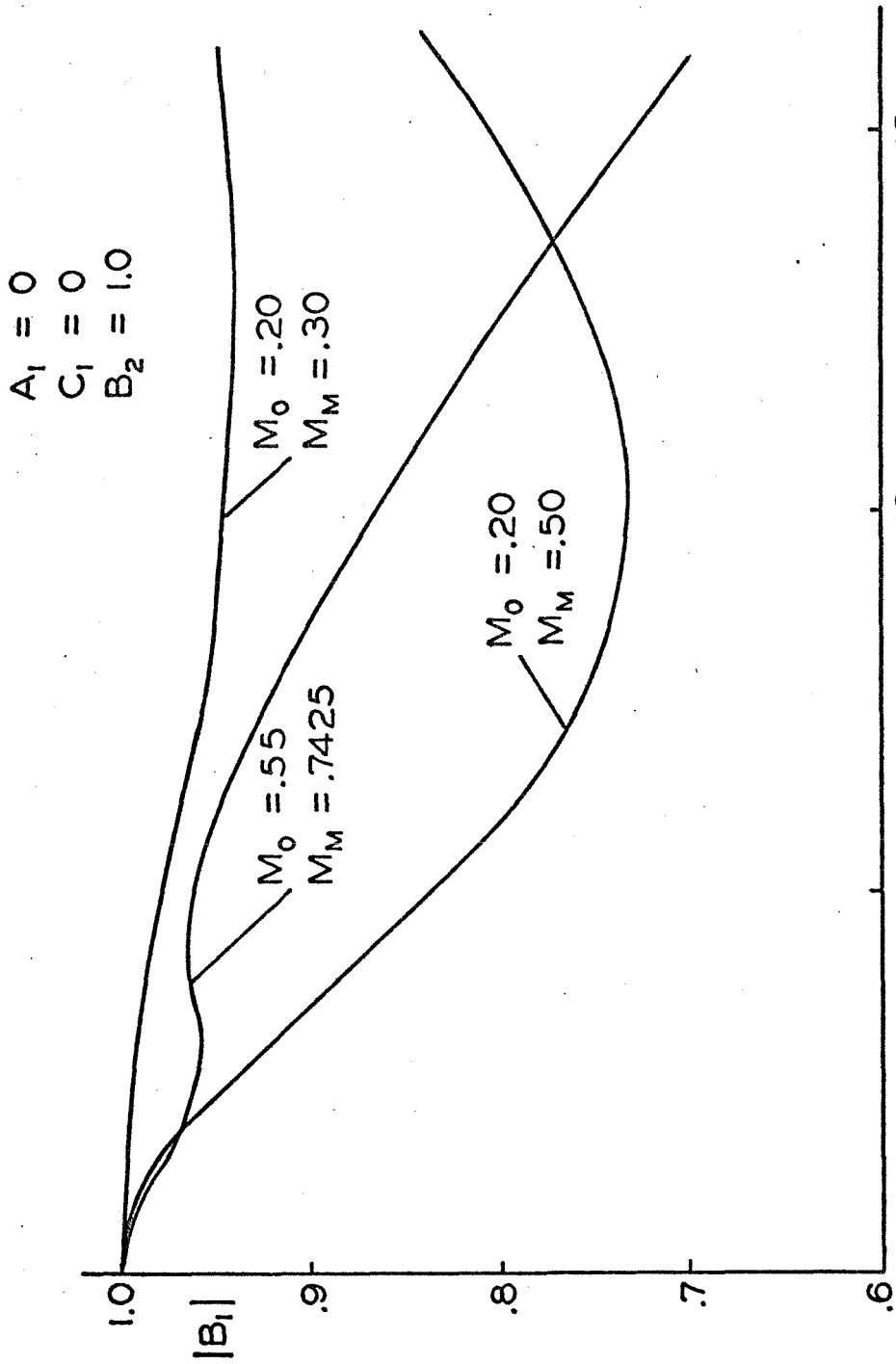

Figure III.6. Transmitted Pressure Wave from a Restriction Given $A_1 = 0.0$, $C_1 = 0.0$, $B_2 = 1.0$.

restrictions in a blade row on compressor performance at $\omega = 32$, one should examine the nozzle calculations at $\omega = 2.0$.

Since the Mach number is highest at the front of the compressor, the calculation for $\omega = 0.55$, and $\omega = 0.7425$ should give a liberal estimate of the errors introduced by this effect in the compressor.

These calculations show that substantial reflections of the pressure waves can occur for incident waves in each direction. This means that at high values of ω the reflected waves in the compressor calculation are probably in error. However, for the frequency range of interest, $\omega < 4$ in this calculation, the transmitted wave is hardly affected at all.

It must be remembered that the response of one blade row is approximately duplicated in all 16 blade rows. The point at which a pressure wave incident on a blade row from upstream is reflected only 5 percent corresponds to an ω for the compressor of 1.6. This is probably the maximum value of ω for which the reflected wave results for the compressor are accurate.

CHAPTER IV

GUIDE AND STRAIGHTENING VANES

A. Basic Equations

In this section, the flow through a direction changing blade row with perturbations will be examined. It is assumed that the blade row is stationary and the flow is isentropic. Furthermore, the effects of the blade row are concentrated in an infinitesimally thin disc. Actually, each blade row in the compressor both moving and stationary could be treated in a similar manner. The complete solution would then consist of matching the flow of these independently treated components along the compressor length. This becomes tedious for multi-stage compressors. The 8 stage compressor examined here has 16 blade rows. This analysis will be limited to one blade row and is typical of the procedure necessary for each step if the actuator disc model were to be used to study the whole compressor.

Since the blade row has zero axial extent, the equations of motion are reduced to equations relating the inlet conditions to the outlet conditions.

Continuity
$$\rho_1 U_1 h_1 = \rho_2 U_2 h_2 \tag{4.1}$$

Energy
$$\rho_1 U_1 h_1 \left(C_p T_1 + \frac{U_1^2}{2} + \frac{V_1^2}{2} \right) = \rho_2 U_2 h_2 \left(C_p T_2 + \frac{U_2^2}{2} + \frac{V_2^2}{2} \right) \tag{4.2}$$

Entropy
$$\frac{P_1}{\rho_1^\gamma} = \frac{P_2}{\rho_2^\gamma} \tag{4.3}$$

where U and V are the components of velocity in the axial and tangential directions respectively. The subscript 1 refers to upstream conditions, and the subscript 2 refers to downstream conditions. The

momentum equations are not shown here because they include the unknown forces of the blades acting on the flow and thus do not add any information necessary for the solution. Equation 4.3 is used instead. The working fluid has been assumed to be an ideal gas and so Equation 4.2 can be combined with the equation of state,

$$P = \rho R T \tag{4.4}$$

and Equation 4.1 to obtain

$$\frac{\gamma}{\gamma-1}\left(\frac{P_1}{\rho_1}\right) + \frac{U_1^2}{2} + \frac{V_1^2}{2} = \frac{\gamma}{\gamma-1}\left(\frac{P_2}{\rho_2}\right) + \frac{U_2^2}{2} + \frac{V_2^2}{2} \tag{4.5}$$

B. Perturbed Equations

The equations will be perturbed in the same manner as the earlier calculations. However, in order to compare the solution obtained here with the full compressor problem, it is assumed that the tangential components of velocity remain unperturbed. Thus, the acoustical perturbations are seen to propagate in the axial direction only. The perturbations are taken of the form

$$U_1 = \bar{U}_1\left(1+\frac{U_1'}{\bar{U}_1}\right) \qquad U_2 = \bar{U}_2\left(1+\frac{U_2'}{\bar{U}_2}\right) \tag{4.6}$$

$$\rho_1 = \bar{\rho}_1\left(1+\frac{\rho_1'}{\bar{\rho}_1}\right) \qquad \rho_2 = \bar{\rho}_2\left(1+\frac{\rho_2'}{\bar{\rho}_2}\right)$$

$$P_1 = \bar{P}_1\left(1+\frac{P_1'}{\bar{P}_1}\right) \qquad P_2 = \bar{P}_2\left(1+\frac{P_2'}{\bar{P}_2}\right)$$

$$V_1 = \bar{V}_1 \qquad V_2 = \bar{V}_2$$

Substituting these relationships into Equations 4.1, 4.3, and 4.5 and examining only the first order terms result in the following equations, after some manipulations.

$$\frac{U_1'}{\bar{U}_1} + \frac{\rho_1'}{\bar{\rho}_1} = \frac{U_2'}{\bar{U}_2} + \frac{\rho_2'}{\bar{\rho}_2} \tag{4.7}$$

$$\bar{U}_1^2\left[\frac{1}{(\gamma-1)\bar{M}_1^2}\left(\frac{p_1'}{\bar{p}_1} - \frac{\rho_1'}{\bar{\rho}_1}\right) + \frac{U_1'}{\bar{U}_1}\right] = \tag{4.8}$$

$$\bar{U}_2^2\left[\frac{1}{(\gamma-1)\bar{M}_2^2}\left(\frac{p_2'}{\bar{p}_1} - \frac{\rho_2'}{\bar{\rho}_2}\right) + \frac{U_2'}{\bar{U}_2}\right]$$

$$\frac{p_2'}{\bar{p}_2} - \frac{p_1'}{\bar{p}_1} = \gamma\left(\frac{\rho_2'}{\bar{\rho}_2} - \frac{\rho_1'}{\bar{\rho}_1}\right) \tag{4.9}$$

where the Mach numbers $\bar{M}_1$, and $\bar{M}_2$ are defined as,

$$\bar{M}_1 = \frac{\bar{U}_1}{\sqrt{\gamma R \bar{T}_1}} \tag{4.10}$$

$$\bar{M}_2 = \frac{\bar{U}_2}{\sqrt{\gamma R \bar{T}_2}} \tag{4.11}$$

Now let the perturbations be of the form given in Equations 2.32, 2.33, and 2.34. Since the blade row is collapsed to a line, the perturbations may be evaluated at $\xi = \pm 0$. In addition, since the equations used here have no derivatives with respect to time, time may be taken as constant, say $\tau = 0$ to determine the solution. Thus:

$$\begin{aligned} p_1(0) &= A_1 + B_1 & p_2(0) &= A_2 + B_2 \\ \rho_1(0) &= \frac{1}{\gamma}(A_1 + B_1) + C_1 & \rho_2(0) &= \frac{1}{\gamma}(A_2 + B_2) + C_2 \\ U_1(0) &= \frac{1}{\gamma\bar{M}_1}(A_1 - B_1) & U_2(0) &= \frac{1}{\gamma\bar{M}_2}(A_2 - B_2) \end{aligned} \tag{4.12}$$

These considerations reduce the equation of motion to:

$$A_1\left(\frac{\bar{M}_1+1}{\bar{M}_1}\right) + B_1\left(\frac{\bar{M}_1-1}{\bar{M}_1}\right) = A_2\left(\frac{\bar{M}_2+1}{\bar{M}_2}\right) + B_2\left(\frac{\bar{M}_2-1}{\bar{M}_2}\right) \tag{4.13}$$

$$A_1\left(\frac{\bar{M}_1+1}{\bar{M}_1}\right)-B_1\left(\frac{\bar{M}_1-1}{\bar{M}_1}\right)=\frac{\bar{U}_2^2}{\bar{U}_1^2}\frac{\bar{M}_1}{\bar{M}_2}\left[A_2\left(\frac{\bar{M}_2+1}{\bar{M}_2}\right)-B_2\left(\frac{\bar{M}_2-1}{\bar{M}_2}\right)\right] \tag{4.14}$$
$$+\frac{\gamma}{\gamma-1}\frac{1}{\bar{M}_1}\left(C_1-\frac{\bar{U}_2^2}{\bar{U}_1^2}\frac{\bar{M}_1^2}{\bar{M}_2^2}C_2\right)$$

$$C_1=C_2 \tag{4.15}$$

Again, the magnitude of the entropy wave remains unchanged because of the zero loss assumption implicit in Equation 4.3.

Note that the tangential velocities $\bar{V}_1$, and $\bar{V}_2$ do not appear directly in the final equations. They do have an effect, however, on the magnitudes of $\bar{U}_1$, $\bar{U}_2$, $\bar{M}_1$, and $\bar{M}_2$. This can be determined by examining the steady state equations.

If the parameters in Equations 4.1, 4.2, and 4.3 are taken as steady, the equations may be manipulated to give:

$$\left(\frac{\bar{U}_1}{\bar{U}_2}\frac{A_1}{A_2}\right)^{\gamma-1}=1+\frac{\gamma-1}{2}\bar{M}_1^2\left\{1+\frac{\bar{V}_1^2}{\bar{U}_1^2}-\frac{\bar{U}_2^2}{\bar{U}_1^2}\left[1+\frac{\bar{V}_2^2}{\bar{U}_2^2}\right]\right\} \tag{4.16}$$

$$\frac{\bar{M}_1^2}{\bar{M}_2^2}=\left(\frac{\bar{U}_1}{\bar{U}_2}\right)^{\gamma+1}\left(\frac{A_1}{A_2}\right)^{\gamma-1} \tag{4.17}$$

Now $\frac{\bar{V}_1}{\bar{U}_1}$ and $\frac{\bar{V}_2}{\bar{U}_2}$ are the tangents of the flow angles entering and leaving the blade row and must be given. Similarly, either $\frac{\bar{U}_1}{\bar{U}_2}$ or $\frac{A_1}{A_2}$ and one Mach number must be given to fully specify the problem. With this information, these equations allow computation of all the necessary average parameters to obtain a solution for the perturbations.

It should be noted that the steady state equations considered here are identical to those for flow in a one-dimensional nozzle where the velocity is given by the total actual velocity $\sqrt{\bar{U}^2+\bar{V}^2}$. Thus, the compressible flow tables for nozzles may be used to specify the average conditions.

The solution of Equations 4.13 and 4.14 is obtained in the same manner as before considering A_1, C_1, and B_2 as arbitrary. Then:

$$B_1 = \frac{A_1\left(\frac{\bar{M}_1+1}{\bar{M}_1}\right)\left(1-\frac{\bar{U}_2^2\bar{M}_1}{\bar{U}_1^2\bar{M}_2}\right)+2B_2\left(\frac{\bar{M}_2-1}{\bar{M}_2}\right)\frac{\bar{U}_2^2\bar{M}_1}{\bar{U}_1^2\bar{M}_2}-\frac{\gamma}{\gamma-1}\frac{C_1}{\bar{M}_1}\left(1-\frac{\bar{U}_2^2\bar{M}_1^2}{\bar{U}_1^2\bar{M}_2^2}\right)}{\left(\frac{\bar{M}_1-1}{\bar{M}_1}\right)\left(1+\frac{\bar{U}_2^2\bar{M}_1}{\bar{U}_1^2\bar{M}_2}\right)} \tag{4.18}$$

$$A_2 = \frac{2A_1\left(\frac{\bar{M}_1+1}{\bar{M}_1}\right)-B_2\frac{\bar{M}_2-1}{\bar{M}_2}\left(1-\frac{\bar{U}_2^2\bar{M}_1}{\bar{U}_1^2\bar{M}_2}\right)-\frac{\gamma}{\gamma-1}\frac{C_1}{\bar{M}_1}\left(1-\frac{\bar{U}_2^2\bar{M}_1^2}{\bar{U}_1^2\bar{M}_2^2}\right)}{\left(\frac{\bar{M}_2+1}{\bar{M}_2}\right)\left(1+\frac{\bar{U}_2^2\bar{M}_1}{\bar{U}_1^2\bar{M}_2}\right)} \tag{4.19}$$

$$C_1 = C_2 \tag{4.20}$$

The numerical solutions have been worked out for both inlet guide vanes and straightening vanes. The turning angle in both cases has been taken as 45 degrees. In the inlet guide vanes, the flow enters with no tangential velocity and exits with tangential velocity equal to the axial velocity. In the straightening vanes, the flow enters with tangential velocity equal to the axial velocity and exits with no tangential velocity.

For each set of vanes, the solution has been obtained both for the case of constant axial velocity and constant blade height. The constant axial velocity is easier to match up with the compressor flow, but the constant blade height is closer to the actual configurations in existing compressors, and fits better with actuator disc theory. The values of Mach numbers used are those present at the inlet and outlet of the compressor examined in Chapter II.

C. Results

Table IV.1 lists the results of the calculations. It is expected that the amount of reflection will be a monotonically increasing function of the turning angle. Clearly, if the turning angle were zero, there would be no reflection and 100 percent transmission. Since the turning angle does not appear in the final equations (4.18 and 4.19), the differences in Mach numbers and velocities on either side of the blades are responsible for the reflections. Now, because of the different assumptions chosen for each case listed in Table IV.1, the Mach numbers and velocities differ somewhat.

For the inlet guide vanes with constant axial velocity, the Mach numbers are only slightly different resulting in small reflections. As noted before, the reflection for the wave incident from downstream appears much smaller because the energy for a wave traveling downstream is greater than for a wave traveling upstream with the same magnitude.

For the inlet guide vanes with constant blade height, the angle of flow at exit produces a much smaller effective cross-sectional area resulting in a substantially higher Mach number. Thus, the reflected waves are much larger than with constant axial velocity. Another fact that must be considered is that if the velocity changes, the transmitted wave would be of different amplitude even if no reflection occurred.

The straightening vanes give similar results except that the changes in magnitude of the transmitted waves are in the opposite direction from the previous case.

TABLE IV.1.

DISTURBANCES OUTSIDE TURNING VANES

		CASE 1 $A_1 = 1.0, C_1 = 0.0, \beta_2 = 0.0$		CASE 2 $A_1 = 0.0, C_1 = 1.0, \beta_2 = 0.0$		CASE 3 $A_1 = 0.0, C_1 = 0.0, \beta_2 = 1.0$	
		A_2	B_1	A_2	B_1	A_2	B_1
Inlet Guide Vanes	$\bar{U}_1 = \bar{U}_2$ $\bar{M}_1 = .55$ $\bar{M}_2 = .567$	1.0352	-.0524	-.0690	.2332	+.00421	.9192
$\bar{V}_1 = 0$ $\bar{V}_2 = \bar{U}_2$	$h_1 = h_2$ $\bar{M}_1 = .4366$ $\bar{M}_2 = .55$	1.0779	+.1958	-.0974	.2127	-.0223	.6827
Outlet Straightening Vanes	$\bar{U}_1 = \bar{U}_2$ $\bar{M}_1 = .58$ $\bar{M}_2 = .5614$	.9635	.0613	.0719	-.2761	-.004577	1.0965
$\bar{V}_1 = \bar{U}_1$ $\bar{V}_2 = 0$	$h_1 = h_2$ $\bar{M}_1 = .58$ $\bar{M}_2 = .4464$	.9139	-.3274	.0924	-.4132	.0333	1.5635

It should be noted that the calculation done here is first order only, and that the transported perturbation energy is second order. Because of this, it is not possible to be precise about the energy balance for this problem.

Another observation is that because the blade row has been compressed into an actuating disc, there is no characteristic length to the problem. Thus, there is no frequency dependence at all.

The result here, as applied to the compressor, is that the inlet guide vanes and straightening vanes do have measurable effects. Not only do they produce reflections and either amplification or attenuation of the transmitted wave, but they also alter the Mach number and possibly the velocity of the average flow. Thus, the calculations presented in Chapter II for the compressor must be taken as descriptive only of the flow between the inlet guide vanes and straightening vanes, if any. In order to include the effects of these additional components, the boundary conditions must be matched between the three units.

CHAPTER V

CONCLUSIONS AND SUGGESTIONS FOR FURTHER WORK

A. Summary

The purpose of this study was to examine the response of a compressor to axial flow variations that might cause stalling of the compressor blades. Although the analysis was limited to small perturbations satisfying linearized equations, the results should give some indication of danger points for stalling.

The problem was attacked by representing the effects of the blades as a continuous distribution of body forces over the compressor length. The equations describing the problem could then be written directly from knowledge of the operating conditions of the compressor in steady state. The steady state solution was then perturbed by acoustical pressure waves and an entropy wave. These waves were taken as incident from either the front or back of the compressor. The equations were solved numerically using typical compressor characteristics and a range of frequencies.

The results were found dependent upon the frequency of the perturbations. In the case of pressure waves incident on the compressor, it was found that the magnitude of the velocity fluctuations induced in the compressor was always less than the magnitude of the velocity perturbations in the incident pressure wave. In the case of an entropy wave incident on the compressor, velocity fluctuations were generated inside the compressor even though none were present in the incident wave. This effect was seen to be a result of non-ideal efficiency of the blades.

The magnitudes of the velocity perturbations in the compressor were seen to be a maximum either at the front or the rear of the compressor for all cases examined. These, then, are the critical areas where stall might be expected to occur first.

Two other related problems were solved to give insight into the accuracy of the solution obtained for the compressor. First, the effect of a constriction in a duct, as in compressor blade rows, was determined using the method applied to the compressor. The results indicated that appreciable reflections could occur due to this effect. The point at which the reflected wave was 5 percent of the magnitude of the incident wave corresponded to a reduced frequency, ω , for the compressor of less than 2.0. It is known that the velocity fluctuations which cause stall are less than a frequency corresponding to two or three times the rotational frequency of the compressor. This is $\omega \approx 1$ for the compressor analyzed here.

The second related problem was the effect of inlet guide vanes and straightening vanes on the perturbations. It was found that for some geometries, very large changes could occur. Thus, the compressor analysis must be taken as indicative only of the flow between the guide vanes and straightening vanes.

B. Limitations and Further Possible Work

The most obvious limitation of this study is the requirement of small perturbations. Even if a compressor is operating quite near stall, the perturbation of velocity required to cause stall is probably quite substantial compared to the size of the perturbations required

for linearizing the equations. Analysis of the non-linearized problem is immensely more complex.

In this analysis, several parameters were taken as constant or linear in ξ . The analysis could be extended to include more complex variations in these parameters. First, the average velocity, $\bar{U}$, was taken as constant. A compressor can certainly be designed with $\bar{U}$ constant, but in general $\bar{U}$ will vary with ξ . However, several terms were dropped from the analysis when $\bar{U}$ was assumed constant. These terms were linear and could be restored without much added complexity.

Second, the temperature was assumed to be a linear function of ξ . The temperature only appeared in the form of the Mach number, and since the equations were numerically evaluated in small steps in the ξ direction, any other temperature profile could equally as well have been used. However, the change from a linear temperature rise to a constant temperature throughout the machine, as examined in the Appendix, resulted in only small changes. Consequently, the actual temperature profile is not very important.

Third, and most important, the efficiency of the blades was taken as constant independent of both velocity and position in the compressor. In general, the efficiency will be a function of position due to the changing blade height and Mach number of the flow with ξ . Again, this variation with ξ can easily be added by merely specifying the efficiency and consequently the blade force at each value of examined. This does not add much complexity. The variation of efficiency with velocity is more difficult to examine. When cascades are

operated near stall, the efficiency is strongly influenced by the angle of attack of the flow. As the blades approach the stalling condition, their efficiency drops rapidly. Since the angle of attack is related to the velocity of the gas, the efficiency must be a function of $\frac{\bar{U}+U'}{V_R}$. This type of variation may be incorporated in the same manner as the blade force. The inclusions of efficiency changes with velocity and position will probably have a major effect on the propagation of the entropy wave and a minor effect on the pressure waves.

This analysis dealt only with plane disturbances in a mean flow with axial variations. The solution method could be extended to treat radial and circumferential variations in mean flow as well. The extrapolation, however, is not straightforward. Plourde and Stenning (1968) studied steady state circumferential disturbances. They found it necessary to specify the resistance of the compressor to flow in a tangential direction. The choice was made to fit experimental data. Although the analysis of Plourde and Stenning considered only time independent variations and incompressible flow, the problems they encountered must also be solved for the time varying case.

Another problem with the extrapolation to radial and tangential variations is the boundary conditions at the ends of the compressor. Since the pressure waves can propagate in circumferential as well as axial directions, the solution requires three-dimensional solutions both inside the compressor and in the entrance and exit ducts.

APPENDIX

COMPRESSOR WITH CONSTANT VELOCITY AND MACH NUMBER

In the compressor analysis above it was found that variation in the axial Mach number precluded a closed form solution and required a numerical integration. The numerical integration gives no insight into expected wave-like propagation of perturbation inside the compressor.

In this Appendix, the compressor will be analyzed just as before, except that the Mach number will be assumed constant and equal to the value expected in the center of the compressor. This is equivalent to incompressible flow. Equations 2.24, 2.25, and 2.26 in the compressor analysis are now rewritten.

$$\frac{d\rho(s)}{ds} + \frac{du(s)}{ds} = i\omega\rho(s) \tag{A.1}$$

$$\gamma\bar{M}^2\frac{du(s)}{ds} + \frac{dp(s)}{ds} = \tag{A.2}$$

$$\gamma\bar{M}^2\left\{i\omega u(s) - \bar{X}\left[p(s) - \rho(s)\right] + X'u(s)\right\} \tag{A.3}$$

$$\frac{dp(s)}{ds} - \gamma\frac{d\rho(s)}{ds} =$$

$$i\omega p(s) - i\omega\gamma\rho(s) - \epsilon\gamma\bar{M}^2\left[\bar{X}\left(p(s) - \rho(s)\right) + X'u(s)\right]$$

Now since $\bar{M}^2$ is taken constant, the solutions to these equations are of the form:

$$
\begin{aligned}
v(\xi) &= K_v\, e^{i\lambda\xi} \\
p(\xi) &= K_p\, e^{i\lambda\xi} \\
\rho(\xi) &= K_\rho\, e^{i\lambda\xi}
\end{aligned}
\tag{A.4}
$$

where K_v, K_p, and K_ρ are constants and λ is the wave number of the perturbations inside the compressor.

Substituting these relationships into the equations and expressing the result in matrix form yields the following equation:

$$
\begin{bmatrix}
0 & \lambda-\omega & \lambda \\
\dfrac{\lambda}{\gamma\bar{M}^2}-i\bar{X} & i\bar{X} & \lambda-\omega+iX' \\
\dfrac{\lambda-\omega}{\gamma\bar{M}^2}-i\epsilon\bar{X} & -\dfrac{\lambda-\omega}{\bar{M}^2}+i\epsilon\bar{X} & i\epsilon X'
\end{bmatrix}
\begin{bmatrix} K_p \\ K_\rho \\ K_v \end{bmatrix} = 0 \tag{A.5}
$$

The condition for existence of unique solutions is that the determinant of the matrix of coefficients of the K terms is zero. The determinant results in a third order equation in λ and has three complex roots. Denoting λ_R as the real part of λ and λ_i as the imaginary part of λ, the solutions in Equation A.4 can be represented as:

$$
\frac{\rho'}{\bar{\rho}} = K_\rho\, e^{-\lambda_i \xi}\, e^{i\omega\left(\frac{\lambda_R}{\omega}\xi-\tau\right)} \tag{A.6}
$$

Thus, the imaginary part of λ corresponds to a factor which rises or decays exponentially with ξ. If the imaginary part of λ is greater than zero, the perturbation dies out as ξ increases. Similarly, if the imaginary part of λ is less than zero, the perturbations are largest at large values of ξ.

The real part of λ corresponds to a traveling wave. The wave moves in the positive ξ direction if the real part of λ is greater than zero. If $\frac{\lambda_R}{\omega} > 1.0$, the wave moves slower than the main flow, and if $\frac{\lambda_R}{\omega} < 1.0$, it moves faster.

The values of λ for ω approaching infinity can easily be evaluated by dropping the higher order terms in Equation A.5. The result is

$$\begin{aligned} \frac{\lambda_1}{\omega} &= 1.0 \\ \frac{\lambda_2}{\omega} &= -\frac{\bar{M}}{1-\bar{M}} \\ \frac{\lambda_3}{\omega} &= \frac{\bar{M}}{1+\bar{M}} \end{aligned} \tag{A.7}$$

These values are the same as for a duct with mean flow at Mach number $\bar{M}$. For $\omega \to \infty$ the wave length is very short and the disturbance is not affected by the forces acting over a very short length. The solutions for lower values of ω may be found by directly solving the equation. Using the value of $\bar{M} = 0.462$ which corresponds to the Mach number at the center of the compressor, and the other parameters listed in Table II.1, the three solutions were obtained numerically. The results are plotted in Figure A.1. Only the real part is shown. The imaginary part for each root does not change very much over the entire spectrum of ω.

One root has a real part that is positive and almost identical to ω. The imaginary part for this root is almost zero. This is a wave traveling with the mean flow at almost the same velocity as the mean flow and decaying only slightly from front to back. This wave

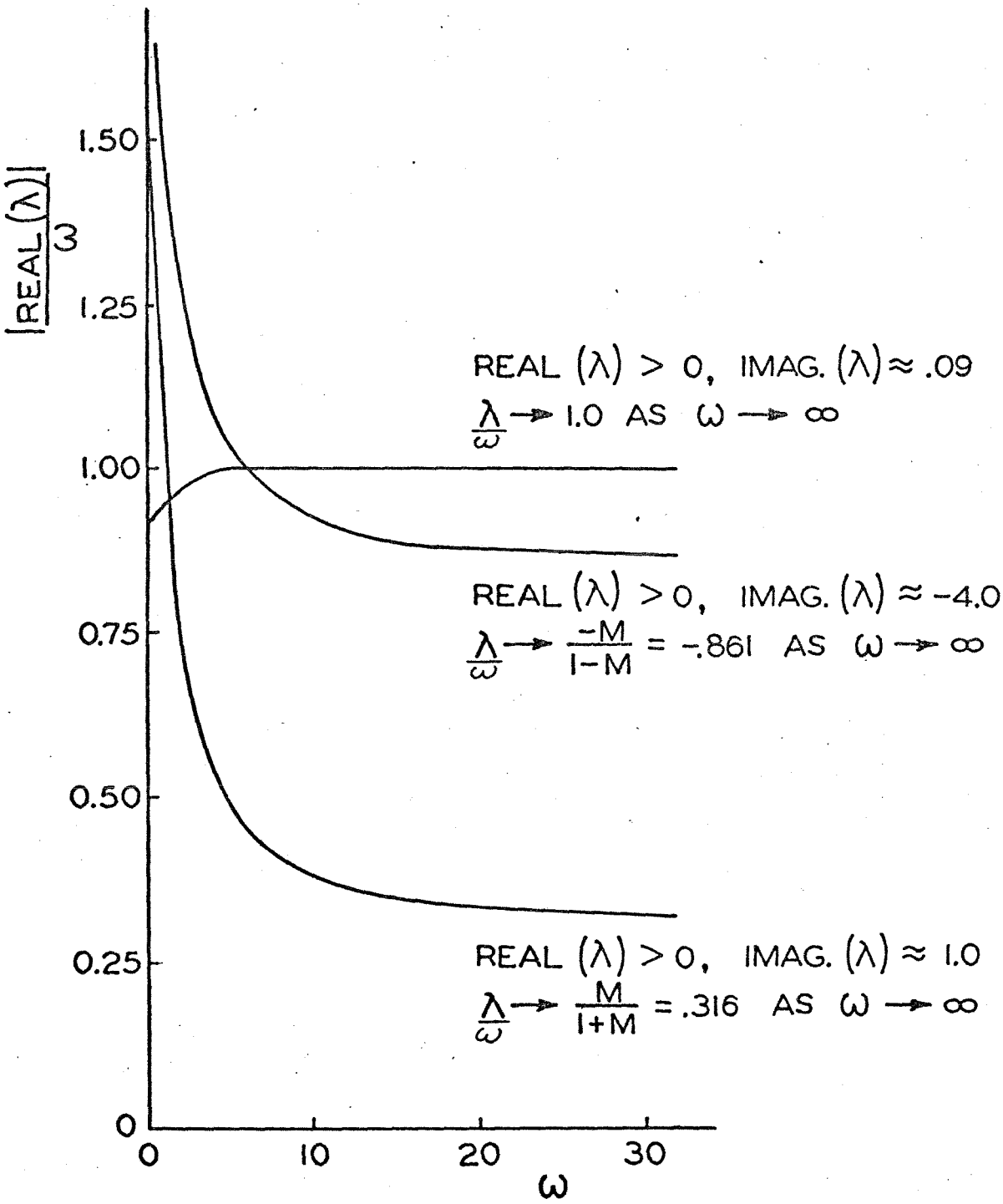

Figure A.1. Roots for Constant Velocity, Constant Mach Number Compressor.

corresponds closely to the entropy wave in a duct with mean flow. The entropy wave moves with the mean flow and does not decay at all for perfect efficiency. Since the efficiency is not perfect, a slight difference in velocity of the wave from that of the mean flow is produced along with the small decay rate.

The second root has a real part that is greater than zero and approaches $\frac{\bar{M}}{1+\bar{M}}\omega$ at high values of ω. This is a wave traveling in the positive ξ direction. This root also has a positive imaginary part which corresponds to decay in the direction the wave is moving. This root, then, corresponds closely to an acoustic wave moving in the direction of the flow. At low values of ω, the wave can move either faster or slower than the mean flow depending upon the actual value of ω.

The third root has a real part that is less than zero and approaches $\frac{-\bar{M}}{1-\bar{M}}\omega$ at high values of ω. This is a wave traveling in the negative ξ direction and corresponds closely to an acoustic wave traveling upstream. The imaginary part is a large negative number indicating rapid decay as the wave travels from the rear to the front.

The solution obtained by numerical integration of the equations for Mach number varying over the length of the compressor produced the same trends of decay as this simplified analysis. These trends are visible both within the compressor and in terms of the magnitudes of the transmitted waves.

The next step in the analysis is to use these values of λ to form the whole solution. The flow inside the compressor can be

matched to the flow outside in the straight ducts assuming the Mach number is the same upstream as downstream.

This calculation was carried out on a computer, and the results were compared with the earlier analysis. The same general trends were observed and the agreement for all parameters was reasonably good considering the assumptions involved. The results are not shown here because they are only approximations of the more accurate analysis carried out above.

Even though the Mach number is not constant in the real compressor, the basic characteristics of this analysis will still be true. The velocities of wave propagation will be changed as a function of the total Mach number. The attenuation will probably also be different due to the same phenomena discussed in conjunction with the flow through the stationary guide vanes.

REFERENCES

1. Callahan, G. M. and Stenning, A. H., "Attenuation of Inlet Flow Distortion Upstream of Axial Flow Compressors", Journal of Aircraft, vol. 8, no. 4, pp. 227-233, April, 1971.

2. Candel, S. M., "Analytical Studies of Some Acoustic Problems", Ph.D. Thesis, California Institute of Technology, 1972.

3. Dixon, S. L., Fluid Mechanics, Thermodynamics of Turbomachinery, Pergamon Press, New York, 1966.

4. Dzung, L. S., ed., Flow Research on Blading, Elsevier Publishing Co., New York, 1970.

5. Horlock, J. H., Axial Flow Turbines, Butterworth and Co., Washington, D.C., 1966.

6. Kaji, S. and Okazaki, T., "Propagation of Sound Waves Through a Blade Row: I and II", Journal of Sound and Vibration, vol. 11, pp. 339-375, March, 1970.

7. Kaji, S. and Okazaki, T., "Generation of Sound by Rotor-Stator Interaction", Journal of Sound and Vibration, vol. 13, pp. 281-307, 1970.

8. Marble, F. E., "Acoustic Disturbance from Gas Nonuniformities Convected Through a Nozzle", Proceedings of Interagency Symposium on University Research in Transportation Noise, Stanford University, Stanford, Calif., March 28-30, 1973.

9. Plourde, G. A. and Stenning, A. H., "Attenuation of Circumferential Inlet Distortion in Multistage Compressors", Journal of Aircraft, vol. 5, no. 3, pp. 236-242, May-June, 1968.

10. Wislicenus, G. F., Fluid Mechanics of Turbomachinery, Volume II, Dover Publications, New York, 1965.